Aberystwyth University

Developments in the Catalytic Graphitisation of Diamond and Silicon Carbide Surfaces

by

Benjamen P. Reed MSc BSc (Hons)

A thesis submitted in partial fulfilment of the requirements for the degree of Philosophiae Doctor in Physics

in the

Department of Physics

May 2020

To my parents, Douglas and Jennifer.

Abstract

Graphitisation of diamond and SiC surfaces to produce high-quality epitaxial graphene was developed and investigated using surface sensitive techniques, namely X-ray photoelectron spectroscopy (XPS), low-energy electron diffraction (LEED), low-energy electron microscopy (LEEM), and X-ray photoemission electron microscopy (XPEEM). The transfer of epitaxial graphene grown by catalytic graphitisation has been achieved and studied using Raman spectroscopy.

Above 930 °C, the diamond (111) surface undergoes a (2×1) reconstruction with three domains, confirmed by XPS and LEED. Previously acquired angle-resolved photoemission spectroscopy (ARPES) measurements are affirmed by modern density-functional theory (DFT) modelling along the $K\Gamma K$ reciprocal space direction which demonstrates the π-band rising above the Fermi level, indicative of a metallic surface state. Heating the diamond surface above 1000 °C produces graphene that co-exists and strongly interacts with the (2×1) reconstruction, evidenced by the emergence of Dirac cones along the K_gMK_g direction in both previously acquired ARPES and DFT modelling.

The temperature required to graphitise the diamond (111) surface is catalytically reduced to ∼500 °C in the presence of a thin iron overlayer. The purity and crystallography of the iron is vital in producing epitaxial graphene with minimal defects. Real-time electron emission spectroscopy (REES) allowed the detachment, transport, and re-crystallisation of carbon from the diamond surface into graphene to be monitored for a linear temperature ramp to 685 °C. A heavily boron-doped diamond was catalytically graphitised at 640 °C. Angle-resolved XPS and Raman measurements reveal that boron is transported through the iron and forms a boron-doped graphitic structure with a boron content of ∼5 % and p-type characteristics.

Patterned graphene is fabricated directly on the 6H-SiC (0001) surface using catalytic graphitisation. LEEM, XPEEM, and Raman spectroscopy mapping confirm that graphitised regions adhere perfectly to the catalyst pattern with a step edge <50 nm. An acid-free delamination transfer technique using a polyvinyl alcohol scaffold was developed in order to move graphene, catalytically-grown on SiC, onto silicon dioxide. This improved transfer heralds an order-of-magnitude improvement in the post-transfer defect density of graphene when compared to acid-etch transfer techniques, as well as significantly reducing polymer residues and contamination. Raman spectra with the characteristic graphene Raman peaks (D, G, and $2D$) have been measured for the first time on catalytically-grown graphene from diamond.

Acknowledgements

This work would not have been possible without the help and contributions of many important people. First and foremost, I would like to thank my supervisor Prof. Andrew Evans for giving me the opportunity to pursue this research topic and guiding me toward becoming an independent researcher with his discussions, advice, and at times, pep talks.

The contributions of Dr Simon Cooil cannot be understated. As well as providing a strong basis for my research through his original PhD work, I want to extend my sincere gratitude for his willingness to teach me, guide me, and provide many opportunities to help me advance my research. I will look back fondly on our many scientific and personal discussions. In equal measure, I would also like to thank Mr Joseph Durk, Mr Jonathan Ash, Mr Simon Astley, and Dr Di Hu, not only for their support in both the laboratory and my work, but also for making my time in the materials physics laboratory an absolute joy.

Other notable colleagues include Dr David Langstaff, Dr Matthew Gunn, Mr Les Dean, Mr David Lewis, Mr Steve Fearn and Mr John Tomes, all whom helped me with laboratory and technical support matters, as well as fruitful discussions and advice. I would also like to extent my gratitude to the staff and students of the Diamond Science & Technology Centre of Doctoral Training, as well as my colleagues at the National Physical Laboratory and the many collaborators I have worked with over the course of this investigation.

I am fortunate to have found friendship in so many people both during my time at university, and at home. These people have all indirectly contributed to this work through their encouragement, compassion, and patience. I would like to honour my friends in the 'Physics Team' and my brothers in the 'Buddy Boat'. Here's to great memories, and good times ahead.

Finally, but most importantly. Rose, you gave me the strength and the courage to complete this thesis. When I didn't believe in myself and fell into despair, you picked me back up and kept me going, even though you had to endure the same. Words cannot express how thankful I am to you, and how much you mean to me.

Contents

Dedication i

Declaration ii

Abstract iii

Acknowledgements iv

1 Introduction 1

1.1 Background & Motivation 1

1.2 Thesis Layout & Contributions 4

2 Experimental Techniques 8

2.1 Ultra-High Vacuum (UHV) 8

2.1.1 Mean Free Path of Particles 9

2.1.2 Monolayer Formation Time 10

2.2 Photoelectron Spectroscopy (PES) 12

2.2.1 Fundamentals of Photoemission 12

2.2.2 Conservation of Electron Momentum 15

2.2.3 Photoionization Cross-section 16

2.2.4 The Electron Mean-free Path 18

2.2.5 Core Level Emission 20

2.2.6 Valence State Emission 21

2.2.7 Features of Photoemission Spectra 22

2.2.8 Quantification 29

2.3 Low Energy Electron Diffraction (LEED) 32

2.4 Electron Microscopies (XPEEM & LEEM) 35
2.5 Raman Spectroscopy 39
2.6 Scanning Probe Microscopy 42

3 Instrumentation **46**
3.1 Aberystwyth UHV System 47
3.2 Photon Sources 51
3.2.1 Twin-anode X-ray Source 51
3.2.2 Ultraviolet Source 53
3.2.3 Synchrotron Radiation Facilities 55
3.3 *In-situ* Surface Processing 60
3.3.1 Sample Heating 60
3.3.2 Knudsen Cell for Metal Deposition 60
3.4 Hemispherical Photoelectron Analyser 62

4 Materials **70**
4.1 Diamond 70
4.1.1 Diamond Synthesis 71
4.1.2 Doped Diamond 77
4.2 Diamond Surfaces 79
4.2.1 The (111)(1 × 1) Surface 80
4.2.2 The (111)(2 × 1) Reconstruction 82
4.3 Graphene 86
4.3.1 Graphene Synthesis 90

5 Graphitising the (111) Diamond Surface **96**
5.1 The (111)(1 × 1) Diamond Surface 97
5.1.1 Oxygen-terminated Diamond 97
5.1.2 Hydrogen-terminated Diamond 101
5.2 The (111)(2 × 1) Reconstruction) 104
5.2.1 The Clean (2 × 1) Reconstruction 104
5.2.2 High Temperature Graphitisation of Diamond 111
5.3 Chapter Conclusion 115

6 Iron-mediated Graphitisation **118**
6.1 Iron-on-Diamond . . . 118
6.1.1 Deposition . . . 118
6.1.2 Structural and Electronic Transition . . . 122
6.2 Catalytic Graphitisation of Diamond . . . 125
6.2.1 Intrinsic Graphene Growth . . . 125
6.2.2 Boron-doped Graphene Growth . . . 129
6.3 Chapter Conclusion . . . 144

7 Toward Architectures of Catalytically-grown Graphene **147**
7.1 Patterning of Catalytically-grown Graphene . . . 148
7.1.1 Graphene dots on SiC (Aberystwyth) . . . 148
7.1.2 Graphene dots on SiC (BESSY II) . . . 154
7.2 Transfer of CVD Graphene . . . 161
7.2.1 Wet Transfer Technique (Acid Etch) . . . 161
7.2.2 Dry Transfer Technique (PVA-assisted) . . . 163
7.2.3 CVD Graphene on SiO_2 . . . 166
7.3 Catalytically-grown Graphene on SiO_2 . . . 181
7.4 Chapter Conclusion . . . 183

8 Thesis Summary **188**

References **193**

Chapter 1

Introduction

1.1 Background & Motivation

Graphene is a material that has captured the imagination of the scientific community and the wider public since it was first isolated in 2004 by Andre Geim and Konstantin Novoselov at the University of Manchester [1]. There have been significant leaps in understanding this material from numerous academic groups (which are addressed in detail in section 4.3), and due to its exciting properties, graphene has been proposed for a variety of application types from electronics [2–4], energy storage [5–7], medicine [8–10], defense, optoelectronics [11, 12], construction [13], thermal management [14], and many more. The list of potential applications is extensive, and graphene has already made its debut into some commercial applications. Small and medium-sized enterprises across the UK and internationally have already made the leap into developing and commercialising graphene, meaning that graphene-containing products are already available for purchase in 2019. As such, current predictions expect the global graphene market to be worth over £150 million by 2022 [15]. Figure 1.1 presents a roadmap for graphene applications in the 21st century as compiled

by the Graphene Flagship, a consortium of over 150 academic and industry partners in the EU [16]. The success of this roadmap is highly dependent on the development of graphene growth techniques, both for high yield (lower quality) and high quality (lower yield) routes.

In 2012, the Aberystwyth University materials research group reported a new method of growing high-quality epitaxial graphene on diamond and silicon carbide [17]. The method is essentially the reverse process of diamond formation in the Earth's crust, where non-diamond carbon is catalytically converted in diamond with the aid of transition metals under extreme temperatures and pressures [18, 19]. In UHV, a thin film of iron (a minimum of 0.75 nm thick) deposited onto a diamond surface will drastically reduce the temperature required for graphitisation from ∼1000 °C to ∼500 °C [20]. Catalytically-grown graphene resulting from this method benefits from being fabricated directly onto useful substrates with their own impressive properties. The growth method is now well-understood for both diamond and silicon carbide surfaces, with both substrates capable of producing large, high-quality, epitaxial, single crystal graphene. Another avenue of research that has been pursued by many research groups involves changing the properties of graphene via functionalisation and doping. As such, the doping of catalytically-grown graphene with boron is addressed in this thesis. Graphene often requires post-growth processing in order fabricate useful devices, such as patterning into useful architectures. In this work, the patterning of catalytically-grown graphene into useful architectures for electronic devices during growth has been considered in this work. Spatially-resolved electron spectromicroscopy techniques and Raman mapping have been key in showing that the graphene grown using this technique only exists in the region where the catalyst has been deposited. On the matter of metrology, there

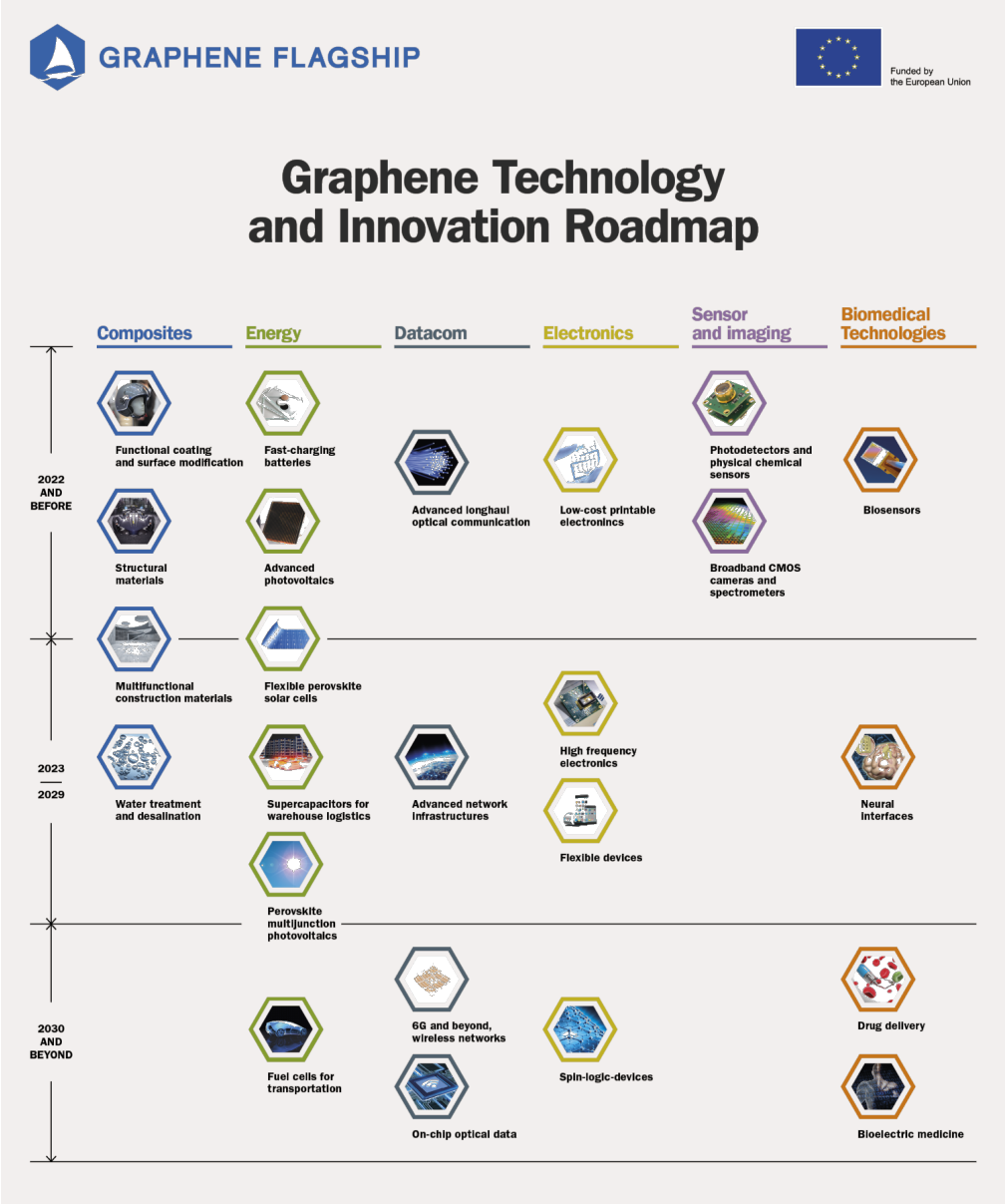

Figure 1.1. The graphene science and technology roadmap published by the Graphene Flagship extending beyond 2030 [16].

have been gaps in the characterisation of graphene grown using this method with Raman spectroscopy, the widely accepted 'fingerprint' method of graphene characterisation. The Raman scattering yield from catalytically-grown graphene on iron is extremely small, and so this has required the need to develop a suitable transfer technique to silicon wafer in order to benefit from the inherent surface enhancement effect that the silicon oxide layer provides [21, 22]. In this thesis, the first example of a characteristic Raman spectrum from graphene grown using the catalytic graphitisation technique is reported.

The primary aim of this work is to further develop an understanding of the diamond-graphene interface and the transition metal catalytic graphitisation of diamond and silicon carbide, on matters of doping, patterning, and transferring catalytically-grown graphene to arbitrary substrates.

1.2 Thesis Layout & Contributions

This thesis has been divided into 8 chapters (including this one), which contain the following content:

Chapter 2 guides the reader through the multitude of experimental techniques that have been utilised for this work, with special attention given to photoemission spectroscopy, which makes up the majority of data in this thesis. An explanation of ultra-high vacuum theory, which is synonymous with surface science, has been provided. In particular, the monolayer formation time of contamination is addressed. Other supplementary techniques such as low-energy electron diffraction, Raman spectroscopy, and atomic force microscopy are explained. Chapter 3 presents a brief explanation of equipment operated

in this work with an emphasis on the home laboratory in Aberystwyth, where the most hands-on experience was gained. The final background chapter of this thesis, chapter 4, focuses on the two carbon allotropes of interest: diamond and graphene. The structure, properties, and fabrication methods of these materials are reviewed as well as their doped forms which have different properties.

The remaining chapters present the research conducted during the project. Chapter 5 presents a study where the (111) surface of diamond is altered by heating in UHV to first drive off oxygen and create a hydrogen-terminated surface, then heated again to produce a (2×1) reconstruction, before finally creating graphene in co-existence with the (2×1) reconstruction. In the home laboratory XPS and LEED data show the various surfaces of the diamond after successive annealing cycles. Experimental angle-resolved photoemission spectroscopy (ARPES) data was acquired by Dr Simon Cooil (Aberystwyth University) at the SGM 3 beam line at the ASTRID synchrotron in Aarhus. This is compared to density-functional theory (DFT) modelling of the diamond (111) surface conducted by the author at the School of Electrical and Electronic Engineering at Newcastle University, under the guidance of Dr Jon Goss. Further application of electronic band broadening and the Fermi function was implemented by Dr Simon Cooil. At the time of writing, the results of this chapter are under preparation for publication.

Chapter 6 details the production of graphene using the iron-mediated graphitisation technique developed at Aberystwyth University. The deposition of high-quality iron thin films by evaporation from a Knudsen cell is described, and comments made on the transfer of crystallographic registry from the diamond substrate, the crystalline iron structure, and its electronic properties. Iron-

mediated graphitisation is first demonstrated on a natural moderately boron-doped diamond, confirming the reproducibility of the technique first proposed in *Carbon* in 2014. The second catalytic graphitisation has been performed on a heavily (superconducting) boron-doped diamond in an attempt to fabricate boron-doped graphene. The heavily boron-doped diamond sample was kindly provided by Dr Taisuke Kageura from the Kawarada Laboratory (School of Science & Engineering) at the Waseda University, Japan.

Chapter 7 concerns the patterning of catalytically-grown graphene into simple architectures, and also transfer to silicon oxide coated silicon wafers for further characterisation, mainly with Raman spectroscopy. Patterning graphene into dots via shadow mask deposition of iron is demonstrated in the home laboratory with XPS and Raman spectroscopy mapping. A similar experiment was also conducted at the U49 PGM SMART beam line at the BESSYII synchrotron alongside Dr Simon Cooil, Prof. Justin Wells, and Mr Frode Strand from the Norwegian University of Science and Technology (NTNU) in Trondheim, (Norway), as well as Mr Joseph Durk from Aberystwyth University. Beam line support was provided by Dr Maurico Preito and Dr Thomas Schmidt of the SMART instrument research group. XPS, LEED, and PEEM were utilised to monitor the graphitisation process, and then Raman spectroscopy mapping was conducted back at the home laboratory. The transfer of catalytically-grown graphene was also explored, first by conducting a comparison study between two differing techniques (referred to as 'wet' and 'dry') to transfer CVD graphene to silicon oxide, and then determining the structural and chemical quality of the transferred graphene with Raman spectroscopy mapping and XPS. Graphene samples grown in a hot-wall CVD reactor were kindly provided by Dr Neil Wilson from the Department of Physics at the University of Warwick. A

transfer of catalytically-grown graphene from diamond, evidenced by Raman spectroscopy, is presented in the closing of the chapter.

Finally, chapter 8 concludes by summarising the thesis and future work to be conducted.

Chapter 2

Experimental Techniques

2.1 Ultra-High Vacuum (UHV)

A vacuum is defined as a space completely devoid of matter. For all intents and purposes, such a state cannot be achieved experimentally. Instead there are defined ranges of 'vacuum', detailed in table 2.1, which are required for different applications. For any surface scientist, the use of ultra-high vacuum (UHV) systems is inescapable for two main reasons. Firstly, the reduced gas density allows the use of experimental techniques which involve electrons or ions travelling toward a sample or detector, without interference from gas phase scattering. Surface science also requires the condition of the surface to remain constant, and so UHV conditions enable the preparation of atomically clean surfaces and allow them to remain contaminant-free for the duration of an experiment. In sections 2.1.1 and 2.1.2, the justification for UHV in surface science is explored with respect to the kinetic theory of gases.

Degree of Vacuum	Pressure Range / mbar		
Low (LV)	10^{3}	$> P >$	3.3×10^{1}
Medium (MV)	3.3×10^{1}	$\geq P >$	10^{-3}
High (HV)	10^{-3}	$\geq P >$	10^{-6}
Very High (VHV)	10^{-6}	$\geq P >$	10^{-9}
Ultrahigh (UHV)	10^{-9}	$\geq P >$	10^{-12}
Extreme Ultrahigh (XHV)	10^{-12}	$> P$	

Table 2.1. Vacuum Ranges [23]

2.1.1 Mean Free Path of Particles

The gas particles in vacuum system are assumed to follow the ideal gas law, mathematically represented by

$$n = \frac{N}{V} = \frac{P}{k_B T} \tag{2.1}$$

where n is the number of gas particles N per unit volume V, i.e. the gas density (m^{-3}), P (Pa) is the base pressure, k_B is Boltzmann's constant (1.38×10^{-23} $\mathrm{J\,K}^{-1}$), and T is the temperature (K). It should be noted at this point that these equations use SI units, whereas throughout this thesis, pressure will be stated in millibar (mbar) as this is the unit convention used in the home laboratory. As gas particles are pumped away and the gas density decreases, the average distance that the remaining particles travel between collisions increases, as described by the simple hard-sphere collision model [24]. This distance is known as the mean free path λ (m) of the particles. For particles with neutral charge, the mean free path is calculated using the equation

$$\lambda = \frac{k_B T}{\sqrt{2} A P} \tag{2.2}$$

where A is the particles collisional cross-sectional area. Using equation 2.2, we can estimate the mean free path for a hypothetical vacuum system at room

Pressure P / mbar	**Mean free path λ / m**
10^{3}	$\sim 10^{-7}$
10^{1}	$\sim 10^{-5}$
10^{-3}	$\sim 10^{-1}$
10^{-6}	$\sim 10^{2}$
10^{-9}	$\sim 10^{5}$

Table 2.2. Mean free path of particles vs. pressure for N_2

temperature ($\sim$294 K) where the average particle radius is 2 Å. The results of this calculation are shown in table 2.2. In order to achieve a mean free path on the order of metres, sufficient for the use of electron/ion/molecule experiments, the vacuum system needs to be pumped down to the high vacuum range ($P < 10^{-4}$ mbar) [23].

2.1.2 Monolayer Formation Time

When considering how quickly a surface becomes contaminated by particles absorbing from the gas phase, the concept of particle flux becomes important. According to the kinetic theory of gases, the flux Γ ($m^{-2}\,s^{-1}$) of an ideal gas incident on a unit surface from one side is

$$\Gamma = \frac{1}{4} n \overline{\nu} \tag{2.3}$$

where $\overline{\nu}$ ($m\,s^{-1}$) is the average particle velocity as described by the Maxwell-Boltzmann distribution of particle velocities [25]. By substituting equation 2.1 and the equation for $\overline{\nu}$ into 2.3, we obtain

$$\Gamma = \frac{1}{4}\left(\frac{P}{k_B T}\right)\left(\sqrt{\frac{8 k_B T}{\pi m}}\right) = \frac{P}{\sqrt{2\pi m k_B T}} \tag{2.4}$$

where m (kg) is the particle mass. This clearly shows that the particle flux is directly proportional to pressure. In reality, only a fraction of these particles

Pressure P / mbar	Γ / $\mathrm{m^{-2}\,s^{-1}}$	t_{ml} / s
10^{3}	10^{27}	10^{-9}
10^{1}	10^{25}	10^{-7}
10^{-1}	10^{-23}	10^{-5}
10^{-4}	10^{-20}	10^{-2}
10^{-7}	10^{-17}	10^{1}
10^{-10}	10^{-14}	10^{4}

Table 2.3. Monolayer Formation Time vs. Pressure for N_2

will adsorb onto the surface during a unit time, while others are absorbed briefly before desorbing back into the gas phase again. The probability of adsorption is described by the sticking coefficient ξ, which is the ratio between the net rate of adsorption (adsorption minus desorption) and the rate of molecular impacts. This coefficient takes a dimensionless value between 0 and 1, and varies with coverage tending toward zero as adsorption reaches equilibrium [26]. However by assuming the sticking coefficient is unity, a lower limit for the monolayer formation time t_{ml} can be calculated as

$$t_{ml} = \frac{1}{\Gamma d_o^2} = \frac{4}{n\overline{\nu} d_0^2} \tag{2.5}$$

where d_0 is the surface area per surface site. By using equations 2.4 and 2.5, the values for Γ and t_{ml} have been calculated for a vacuum system containing diatomic nitrogen particles at room temperature. The results are presented in table 2.3, from which it becomes clear that to maintain a contamination-free surface long enough for an experiment that uses surface sensitive techniques, the pressure in the chamber must be pumped down to the ultra high vacuum range ($P < 10^{-9}\,\mathrm{mbar}$) [23].

2.2 Photoelectron Spectroscopy (PES)

The photoelectric effect is the phenomenon where electrons are ejected from a material when electromagnetic radiation is incident upon it. The effect was first observed in 1887 by Heinrich Hertz [27], and it brought into question the nature of light. Before Albert Einstein's quantized theory of light in 1905 [28], physicists did not understand why photoelectrons were emitted by high-frequency low intensity light, but not by low-frequency high-intensity light. Fundamentally it is the frequency-dependant energy per photon, not the total number of photons (i.e. intensity), that dictates whether or not photoelectrons are produced. The phenomenon of photoemission presents an opportunity to study the elemental composition, chemical environment, and electronic properties at the surface of a material via the powerful techniques of photoelectron spectroscopy (PES). These techniques probe the binding energies of electrons in the valence electronic structure and core levels of atoms, molecules, and various materials. The two main PES methods use ultraviolet and X-ray radiation to probe these binding energy regimes respectively, and give rise to the two main derivative forms of PES, both of which will be discussed in further detail in this chapter.

2.2.1 Fundamentals of Photoemission

The process of photoelectron emission has been extensively studied with many theoretical models being proposed, which are discussed in detail by Stephan Hüfner's work [29]. A three-stage process is described which distinguishes between the initial excitation and the transfer of excited electrons to the material's surface:

1. The electron absorbs a photon with energy greater than the electron's binding energy E_b, and is excited to a higher energy state greater than

the vacuum energy level.

2. The electron travels through the material until it reaches the surface/vacuum interface. The electron may undergo inelastic scattering events, losing energy with each interaction. The electron may also undergo elastic scattering meaning that the electron takes a longer path to reach vacuum without losing kinetic energy.

3. The principal photoelectron is ejected into the vacuum with kinetic energy E_k. Electrons that lost energy due to inelastic scattering events are ejected with less kinetic energy and are known as secondary electrons.

The photoelectric effect observed by Hertz is the simplest case, where the incident photons have enough energy to liberate electrons at the Fermi level. The kinetic energy of these electrons is

$$E_k = hv - \phi_s \tag{2.6}$$

where ϕ_s is the sample work function, h is Planck's constant ($6.626 \times 10^{-34}\,\mathrm{J\,s}$), and v is the photon frequency. A more general form of equation 2.6 includes the electron binding energy E_b relative to the Fermi level. This equation,

$$E_k = hv - E_b - \phi_s \tag{2.7}$$

applies to electrons in all energy states, valence or core. A final E_k correction must be made with regards to the analyser, which has a work function different to that of the sample, ϕ_A, which is a known value depending on the analyser. This difference of work function between the analyser and sample is resolved by forming a contact potential ($\phi_s - \phi_A$) through electrical connection, which

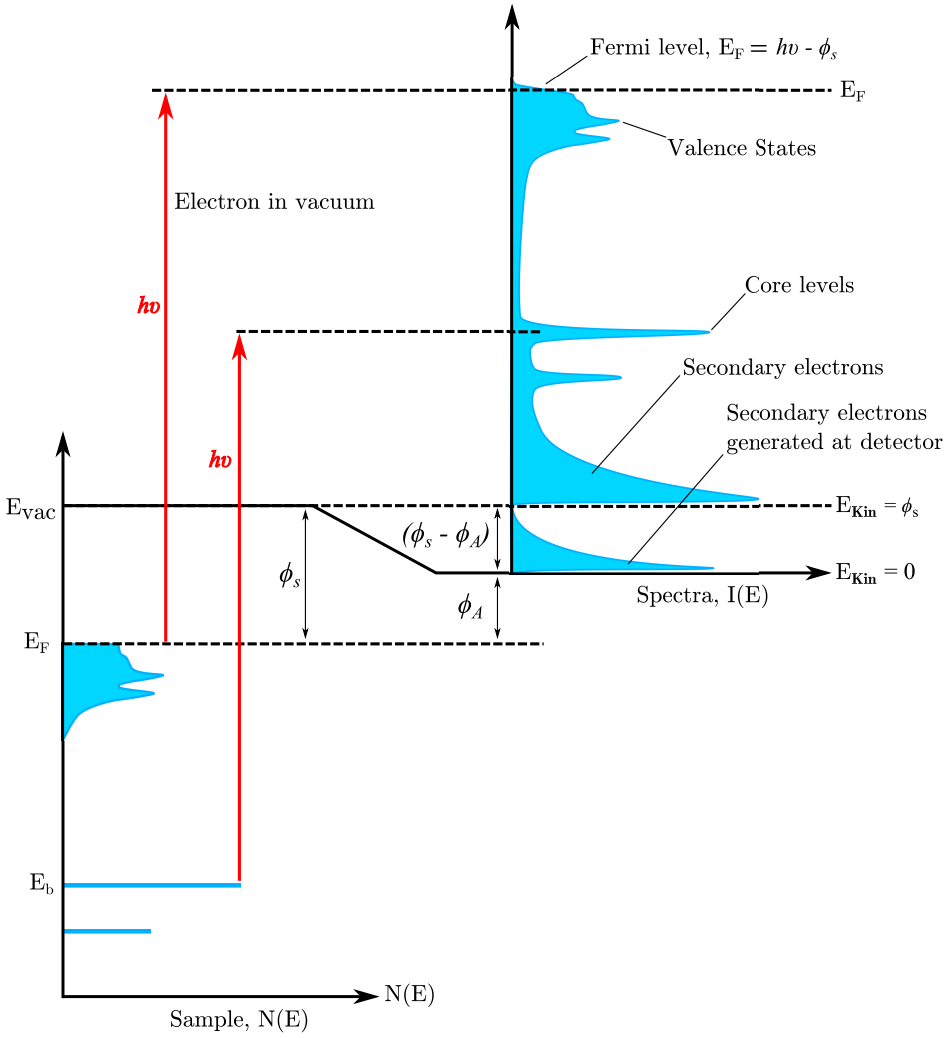

Figure 2.1. Relationship between a sample's density of states N(E) and the photoelectron spectrum I(E) generated by photons of energy $h\upsilon$. The abscissa for photoelectrons is kinetic energy with zero at the vacuum level of the sample. The binding energy for solid samples is measured in reference to the Fermi level. Figure apdapted from S. Hufner [29]

causes an offset in the photoelectron's E_k. This changes equation 2.7 to

$$E_k = hv - E_b - \phi_s + (\phi_s - \phi_A) \tag{2.8}$$

which leaves the final equation required to experimentally measure the binding energies of bound electrons in a sample as

$$E_k = hv - |E_b| - \phi_A \tag{2.9}$$

This mathematical relation is shown schematically in figure 2.1. It is convention among researchers using PES on solid samples to reference E_b to the Fermi level, whereas measurement of free atoms or molecules uses the true vacuum level.

2.2.2 Conservation of Electron Momentum

As well as the kinetic energy of photoelectrons, it is possible to ascertain their momentum in the vacuum $\overrightarrow{K}$ if the emission angle is also recorded. Translational symmetry of the crystal surface potential means the in-plane component of the electron momentum $\overrightarrow{k}$ is conserved across the surface boundary, such that

$$\overrightarrow{K_\parallel} = \overrightarrow{K_x} + \overrightarrow{K_y} = \overrightarrow{k_\parallel} \tag{2.10}$$

$$\overrightarrow{k_\parallel} = \frac{\sqrt{2mE_k}}{\hbar} \cdot \sin\vartheta \tag{2.11}$$

On the other hand, the normal component of the electron momentum $\overrightarrow{K_\perp}$ is not conserved across the surface boundary, such that

$$\overrightarrow{K_\perp} = \overrightarrow{K_z} \neq \overrightarrow{k_\perp} \tag{2.12}$$

If the photoelectron has a large energy compared to the vacuum level, then the normal electron momentum component can be calculated by assuming that the dispersion of the final electron states approximates to the free-electron model. This means that $\overrightarrow{k_\perp}$ can be expressed as

$$\overrightarrow{k_\perp} = \frac{1}{\hbar}\sqrt{2m(E_{kin}\cos^2\vartheta + V_0)} \tag{2.13}$$

where V_0 is the inner potential of the crystal which arises due to a zero-energy difference between the crystal and the vacuum. This value is usually approximated by comparing theoretical modelling to data acquired at different excitation energies [30]. The V_0 term can be ignored for studies of 2d materials where $\overrightarrow{k_\perp} = 0$. The electron's full in-plane momentum vector is determined by measuring the polar ϑ and azimuthal φ angles that photoelectrons leave the sample surface, using a technique known as angle-resolved photoemission spectroscopy (ARPES). This information can be used to construct an image of the density of electronic states in the reduced surface Brillouin zone, i.e. binding energy against momentum (K-) space [29].

2.2.3 Photoionization Cross-section

When interpreting a photoelectron spectra, one may be lead to think that the relative intensities of spectral features in PES directly infer the relative atomic composition. However the reality is not quite as simple. It is vital to remember that not all atoms give up their electrons to the photoionization process so readily. The 'eagerness' of a system, whether it be molecular or condensed matter, to ionize due to absorbing electromagnetic radiation is its photoionization cross-section σ, and it is a necessary parameter to consider when analysing PES data. It is defined as the total probability per unit area, per unit

time that a photon of energy hv will be absorbed by an electron and cause an ionization event from all possible excitation paths of each electron orbital. The transition probability P per unit time between N-electrons in the initial state i with wavefunction Ψ_i, to the final state f with the wavefunction Ψ_f, is dictated by Fermi's Golden Rule which states that

$$P_{i\to f} \propto \frac{2\pi}{\hbar}|M_{fi}|^2\delta(E_f - E_i \pm hv) \tag{2.14}$$

where E_i and E_f are the initial and final energies of the electron respectively, and $\hbar v$ is the incident photon energy. M_{fi} represents the perturbation matrix element, mathematically described as

$$M_{fi} = \langle\Psi_f|\Delta|\Psi_i\rangle = \langle\Psi_f|\boldsymbol{A}\cdot\boldsymbol{p}|\Psi_i\rangle \tag{2.15}$$

where Δ is the perturbation Hamiltonian between Ψ_i and Ψ_f, which is further expressed in terms of the incident photon vector potential $\boldsymbol{A}$, and the electron momentum vector $\boldsymbol{p}$ [31, 32]. This rule holds true when the initial state has not been significantly depleted due to the photoemission process. The photoionization cross-section is a function of excitation energy and differs between atoms and their electron orbitals. For example when $hv = 1253.6\,\text{eV}$, the normalised Scofield cross-section of the Fe $2p$ core level (i.e. when C $1s$ is set to unity) is 15.97 [33, 34]; even a small amount of iron on a predominately carbon-containing sample would herald a spectrum with a significant Fe $2p$ contribution. If a PES experiment has access to a variable energy photon source, such as a synchrotron, then specific excitation energies can be selected to favour a larger photoionization cross-section from an element of interest. The values of photoionization cross-section for most elements have been calculated for a range of excitation energies [35, 36] and are available online at the Virtual Unified

Office of the Elettra synchrotron [37]; the quantitative XPS analysis presented in this work uses these cross-sections.

2.2.4 The Electron Mean-free Path

In section 2.1.1, the mean free path of particles in vacuum was discussed. UHV is utilised to increase the mean free path of ejected photoelectrons to the order of metres, thus allowing the use of photoelectron detectors with large path lengths. However, the photoelectron does not begin its journey at the vacuum-material interface; it must travel through the material to the surface, during which there is a probability that a scattering event will occur and the photoelectron will lose some kinetic energy. The average distance an electron travels in a material before an inelastic scattering event occurs is known as the electron's inelastic mean-free path (IMFP) and is typically on the order of nanometres, as shown by the universal mean-free path curve in figure 2.2. The IMFP means that the intensity of a photoelectron peak becomes a function of the distance from the surface

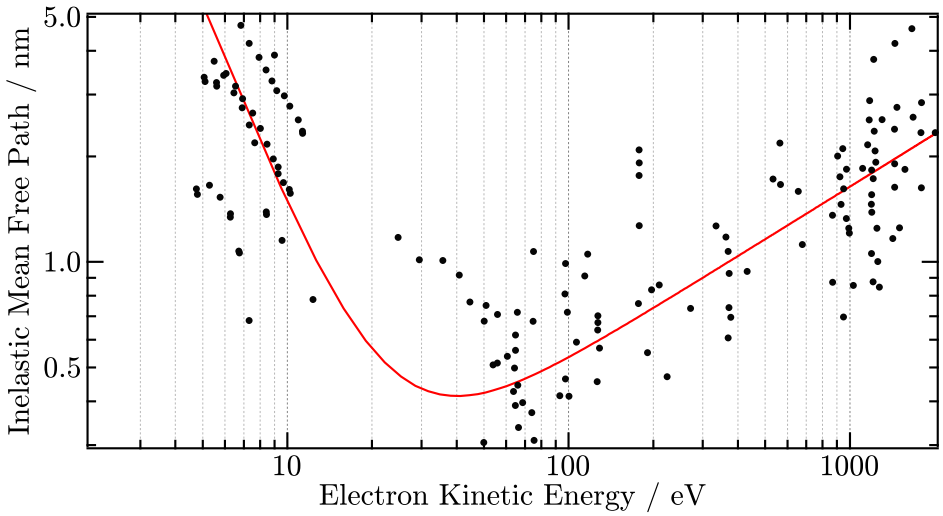

Figure 2.2. The universal curve of electron IMFP as a function of kinetic energy for all elements. Whilst all materials follow this relationship, the actual values of IMFP are scattered around the main curve. Figure adapted using equation (5) and data accumulated from many studies by the work of Seah & Dench [38]

that its photoelectrons were generated; the probability that a photoelectron undergoes scattering decreases by e^{-1} over a distance known as the effective attenuation length (EAL), λ, and is shown mathematically by

$$I = I_0 e^{\left(-\frac{x}{\lambda \cos\theta}\right)} \tag{2.16}$$

where I is the measured core photoelectron intensity, I_0 is the intensity from the clean bulk material, and x is the emission depth. By setting x as multiples of λ, the probability that a photoelectron will reach the surface without inelastic scattering, $P(x)$, can be calculated. At $x = \lambda$, $\approx$37 % of the photoelectrons reach the surface with their initial kinetic energy; at $x = 2\lambda$, $P(x)$ is $\approx$14 %; and at $x = 3\lambda$, only 5 % of the photoelectrons reach the surface without scattering. This means that 95 % of the photoelectron intensity originates less than 3λ from the material's surface [29, 39]. It is worth noting that the IMFP and EAL were once used interchangeably to describe the attenuation of a photoelectron signal through a material (either substrate or overlayer). It is now understood that elastic scattering modifies the trajectories of the principle photoelectrons so that they do not travel directly to the material surface. It is more appropriate to use the EAL to describe photoelectron signal attenuation [40]. As EAL is typically measured on the order of nanometres, it follows that photoelectron techniques have a very high surface sensitivity despite X-ray penetration depths on the order of micrometres. The surface sensitivity can be enhanced by use of variable energy photon sources and off-normal measurements. A lower energy photon source results in a lower kinetic energy for a given core level, thus shifting the IMFP, and the EAL, to a minimum on the universal curve and increasing surface sensitivity. Adjusting the angle of sample relative to the analyser, θ, also yields a more surface sensitive measurement.

2.2.5 Core Level Emission

The first form of PES was developed by Kai Seigbahn in 1957 and was called electron spectroscopy for chemical analysis (ESCA), more commonly known as X-ray photoelectron spectroscopy (XPS) [41]. XPS determines the binding energies of core level electrons which are largely unique for atoms of different elements, and so the technique is used to ascertain the identities of elemental compositions as well as the nature of their local chemical environment. As the name suggests, the technique uses X-rays to generate the photoelectrons from the core levels. Figure 2.3 shows a typical core level photoelectron spectrum of a copper sample measured using X-ray radiation emitted from a non-monochromated Mg anode ($h\nu = 1253.6\,\text{eV}$). A photoelectron peak

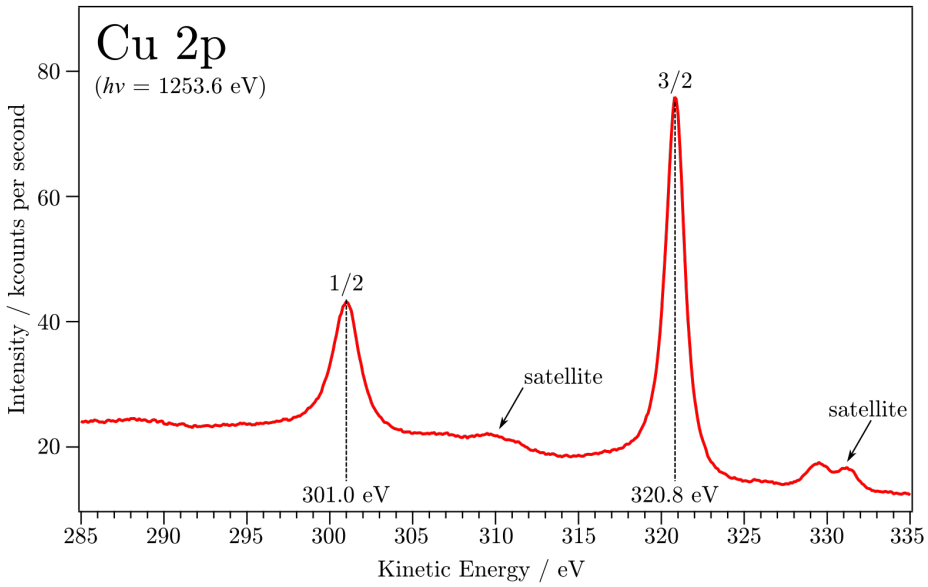

Figure 2.3. A high resolution scan of the Cu 2p core level.

corresponds to specific energy level in the atom's electronic structure and is presented in modified spectroscopic notation, i.e. nl_j, where n is the principle quantum number (period), l is the orbital angular momentum number (i.e. s, p, d, f... for $l = 0, 1, 2, 3...$), and j is the total angular momentum number.

n **(shell)**	l **(sub-shell)**	j	**XPS Notation**	**Auger Notation**	**#orbitals**	**#electrons**
1	s	$1/2$	$1s$	K	1	2
2	s	$1/2$	$2s$	L_1	1	2
	p	$3/2$, $1/2$	$2p_{3/2,1/2}$	$L_{2,3}$	3	6
3	s	$1/2$	$3s$	M_1	1	2
	p	$3/2$, $1/2$	$3p_{3/2,1/2}$	$M_{2,3}$	3	6
	d	$5/2$, $3/2$	$3d_{5/2,3/2}$	$M_{4,5}$	5	10

Table 2.4. Spectroscopic notations for photoelectron core levels up to $n = 3$

Table 2.4 provides spectroscopic notation of photoelectron core levels up to $n = 3$ with corresponding quantum numbers and Auger notation. Core electron energy levels have discrete energies but are broadened by core-hole relaxation lifetimes, thermal Doppler effects, and instrumental contributions (see section 2.2.7: Photoemission Lineshape for more details). Therefore the total intensity of a photoelectron peak is the area under the curve (without the background contribution).

2.2.6 Valence State Emission

After the success of XPS, another form of PES was developed by David Turner between 1962 and 1967. A helium discharge lamp emitting photons with an energy of 21.3 eV was used to generate photoelectrons from gas phase samples. Turner coined the technique as molecular photoelectron spectroscopy, but it is far more well known as ultra-violet photoelectron spectroscopy (UPS) due to the ultra-violet (UV) nature of the photon source [42]. The photoemission process is exactly the same as XPS, but the lower energy of the photon source means that only electrons in the valence states (or low binding energy core levels) can be excited into the vacuum. Whilst higher energy photons could theoretically produce photoelectrons from this regime, the photoionization cross

section of core-level electrons at these energies is much larger than that of the valence electrons, meaning that the core level peaks dominate the spectrum and valence features diminish. UPS probes the valence states of the surface of a material and hence the molecular orbital energies from which a wealth of electronic properties can be quantitatively extracted such as work function, Fermi level energy (for metals and electrically conductive samples), density of states, and electron affinity.

2.2.7 Features of Photoemission Spectra

Photoemission Lineshape

For a given core level, there may be multiple species related to that element. For example, a C 1s peak from adventitious carbon may contain components at different binding energies which relate to different compounds (e.g. C−O, C−OH, C−N, etc.) or different hybridisation states (e.g. C−C sp^3 or C=C sp^2). Each component is a convolution of lineshapes from various sources which must be taken into account during analysis. The excitation source imparts a lineshape depending on how it generates photons. Standard lab sources which use characteristic X-ray emission lines provide a Lorentzian contribution (see section 3.2.1) unless they are monochromated, whereas synchrotron sources are Gaussian in nature (see section 3.2.3). Further lineshape contributions are given by intrinsic processes at the instant the photoelectron is generated. A Lorentzian broadening is imparted by the core-hole lifetime of the sample, whereas atomic vibrations (Doppler Broadening) and varying defect densities in the sample provide a Gaussian contribution. The photoelectron analyser also broadens photoelectron peaks with a significant Gaussian contribution. When fitting photoelectron peaks, a Voigt profile is typically used as it is a convolution of Lorentzian and Gaussian lineshapes. However the true form of the Voigt

is computationally intensive to apply, and so many researchers have proposed their own pseudo-Voigt lineshapes which are Lorentzian-Gaussian convolution functions that simulate the Voigt profile [43]. Much of the modern debate is focused around whether the sum or the product of a Lorentzian-Gaussian profile is the closest approximation of a Voigt [44]. In this work, the sum pseudo-Voigt function proposed by Ida *et al.* has been implemented. The normalised pseudo-Voigt function is given by:

$$f_{pV}(x,\Gamma) = (1-\mu)f_G(x,\Gamma) + \mu f_L(x,\Gamma) \tag{2.17}$$

where f_G and f_L are the normalised Gaussian and Lorentzian functions respectively and μ is a linear mixing parameter ($0 \leq \mu \leq 1$) [45]. The linear pseudo-Voigt approximation for the convolution of f_G and f_L, proposed by Thompson *et al.* is given by:

$$\begin{aligned}\Gamma = (\Gamma_G^5 + 2.69269 \cdot \Gamma_G^4 \cdot \Gamma_L + 2.42843 \cdot \Gamma_G^3 \cdot \Gamma_L^2 \\ + 4.47163 \cdot \Gamma_G^2 \cdot \Gamma_L^3 + 0.07842 \cdot \Gamma_G \cdot \Gamma_L^4 + \Gamma_L^5)^{\frac{1}{5}}\end{aligned} \tag{2.18}$$

where Γ_G and Γ_L are the full-width-at-half-maximum (FWHM) of the Gaussian and Lorentzian functions respectively [46]. This pseudo-Voigt function results in a maximum discrepancy from a true Voigt of $\sim$1 %.

Peak asymmetry is another factor to consider, especially when analysing core levels from electrically conducting samples like metals. When electrons in a metal are excited by an incident photon source, they must travel through the 'Fermi sea', an energy region close to the Fermi level where there is a high density of states. Some of the excited electrons will lose energy to coulombic

interactions with electrons in this 'Fermi sea' and due to the large density of states in this region, a distribution of lower kinetic energy electrons will be ejected into the vacuum. This distribution manifests as a extended tail on the higher binding energy side (lower kinetic energy side) of the photoelectron peak. The Doniach-Sunjic lineshape (DS), a Gaussian-Lorentzian peak with an extended tail on the higher binding energy side, is widely used to fit asymmetric photoelectron peaks [47, 48]. Although the DS lineshape has a strong theoretical backing, its practical use is difficult. The integral of the DS lineshape is infinite when a non-zero asymmetry parameter is used, meaning that an arbitrary cut-off must be defined at some point, hence introducing a degree of subjectivity when determining stoichiometries from peak intensities [49]. For this work, asymmetric peaks have instead been fitted using an asymmetric pseudo-Voigt proposed by Schmid *et al.* that heralds identical peak shapes and area to DS whilst requiring less computational effort and a finite area. The pseudo-Voigt FWHM, Γ, calculated in equation 2.18 is substituted into a sigmoidal expression of the form:

$$f_\sigma(x) = \frac{2\Gamma}{1 + \exp(-a(x-b))} \tag{2.19}$$

where a is the sigmoidal step width and b is shift of the sigmoidal step centre relative to the main peak. The $f_\sigma(x)$ is then substituted into equation 2.17 in order to produce the asymmetric line shape.

Spin-orbit Coupling

Electrons exhibit two kinds of angular momentum: spin s and orbital angular momentum l. These angular momenta also have an associated magnetic moment, μ_s and μ_l, and it is the interaction between these magnetic moments that results in spin-orbit coupling. There are two possible orientations that

μ_s and μ_l have with respect to each other, 'parallel' (lower energy) and 'anti-parallel' (higher energy) meaning that the atomic energy levels split in two, resulting in what is called the fine structure [50]. The total angular momentum j of electrons in these energy levels is given by:

$$j = |l \pm s|\,; \quad s = \frac{1}{2} \tag{2.20}$$

With the exception of the s-subshell ($l = 0$), all the subshells exhibit spin-orbit coupling, resulting in two peaks for a given core level in a photoelectron spectrum. These peaks will have a specific intensity ratio R due to the degeneracy of each spin state, which is given by:

$$R = \frac{2j_+ + 1}{2j_- + 1}, \tag{2.21}$$

where j_+ and j_- are the total angular momenta calculated in equation 2.20 by adding and subtracting the electron spin respectively. The table 2.5 shows the j values and area ratios for subshells s, p, d, and f. The ΔE of the splitting increases with atomic number Z, but decreases for larger quantum numbers n. For example the Si $2p$ splitting is only 0.63 eV, which often means the Si $2p$ looks like a single asymmetric peak when measured at larger analyser pass energies (see section 3.4). On the other hand, Fe $2p$ has a large splitting of 13.1 eV for the same subshell.

Satellites, Plasmons, and Ghosts

Satellite peaks occur when the incident photon source is not monochromatic. Non-preferential X-ray emission lines that reach the sample generate their own photoelectrons and because the measured kinetic energy of a photoelectron is dependant on hv, its corresponding peak appears at a different position in

Subshell	j-values	Area Ratio
s	$^1/_2$	n/a
p	$^1/_2$ $^3/_2$	1:2
d	$^3/_2$ $^5/_2$	2:3
f	$^5/_2$ $^7/_2$	3:4

Table 2.5. Spin-orbit coupling: j-values vs. sub-peak area ratios

the spectrum. The acquisition software calculates binding energy based on the primary X-ray emission line and so the satellite peak seems to have a different binding energy compared to the primary photoelectron peak, when in fact because it originated from the same core level, it also has the same binding energy. The intensity of these satellite peaks is weak compared to their corresponding main peak because the non-preferential X-ray lines that cause them are also weak. Non-monochromatic lab sources also attempt to attenuate these non-preferential X-rays using an aluminium window, however some of them still reach the sample. Thankfully the intensity and energy shifts of these satellites are well documented and so they can be easily subtracted by analysis software. It should be noted that PES systems that use monochromatic sources, such as a synchrotron, do not observe satellites in their spectra.

Plasmon peaks are caused by quantised oscillations in the valence band or by free electrons in conductors. When a positive core-hole is formed due the photoemission process (detailed in section 2.2.1), a coupling may occur with the quantised oscillations of electrons in the valence states, i.e. plasmons [51, 52]. The emitted photoelectron loses energy to these plasmons equal to $n\hbar\omega$ where ω is the oscillation frequency and n is the harmonic order. The oscillation

frequency is different for the bulk and surface plasmons (i.e. $n\hbar\omega_b$ and $n\hbar\omega_s$ respectively) which results in two series of plasmon peaks for a given core level in a spectrum. Plasmon loss events are either: intrinsic, meaning that the loss event happens simultaneously with the photoemission process and is localised to the atom where the photoemission occurred; or extrinsic, where the electric field of the photoelectron couples with plasmons whilst travelling through the material. As an example, diamond has a rich bulk and surface plasmon structure that appears between 26 eV and 40 eV on the lower kinetic energy side of the C $1s$ peak [53].

Ghost peaks occur when a non-monochromated X-ray source has an oxidised anode. As well as producing characteristic X-rays from the main anode material, O Kα X-rays are also produced with a $h\nu = 524.9$ eV. For example, the C $1s$ core level when excited by Mg Kα has a kinetic energy of $\sim$969 eV. However when it is excited by O Kα, is has a kinetic energy of $\sim$241 eV (which corresponds to an incorrect binding energy of 1012.6 eV).

Auger Emission Features

The second most dominant features in photoelectron spectra are Auger peaks which originate from the emission of Auger electrons. The Auger electron process for a carbon atom is demonstrated in figure 2.4a and consists of three distinct steps: (**1**) a primary photoelectron is ejected from a deep core level (e.g. K-shell) and leaves behind a positive core-hole. (**2**) Next, an electron from a higher energy level (e.g. L_1-shell) drops down to recombine with the core-hole and re-equilibrate the electronic structure. In doing this, the electron loses energy by emitting a photon with $h\nu$ equal to the transition energy which is typically in the X-ray region of the electromagnetic spectrum. This photon

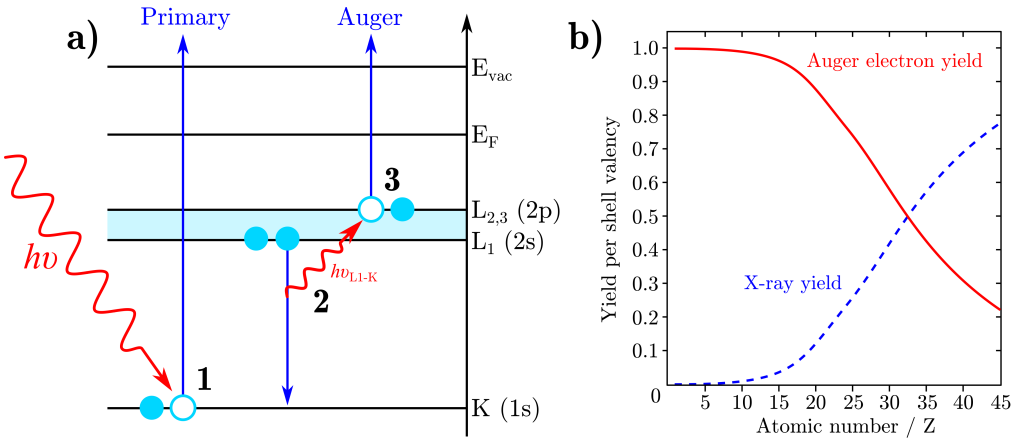

Figure 2.4. **(a)** The C KLL Auger emission process **(b)** The yield of Auger electrons and X-rays with increasing atomic mass number (calculated for a KLL event). Adapted from [54]

can be emitted into the vacuum and detected directly, which is the principle behind X-ray emission spectroscopy (XES). However in the Auger process, this photon is absorbed by another electron in either the same orbital or a higher one (e.g. $L_{2,3}$-shell). (**3**) This electron now has enough energy to be ejected from the atom in the form of an Auger electron. For lighter elements, the ratio of Auger electron yield to X-ray emission yield is much higher, as shown in figure 2.4b, whereas for heavier elements the ratio decreases until X-ray emission is the more favourable process. An advantage of Auger electrons is they are always emitted with the same kinetic energy because their excitation source is based on a fixed transition energy:

$$E_k = E_{Core} - E_B - E_{C'} \tag{2.22}$$

where E_{Core} is the binding energy of the principle photoelectron, E_B is binding energy of the recombination electron, and $E_{C'}$ is the binding energy of the Auger electron. For the process shown in figure 2.4a, the Auger electron is denoted C $K_1L_1L_2$, meaning that the core-hole was generated in the K-shell, the re-

combination electron originated from the L_1-shell, and the Auger electron was emitted from the L_2-shell [50]. There is also a special case for Auger emission called a Coster-Kronig transition where the core-hole is filled by an electron of the same shell (i.e. a higher subshell) [55]. Coster-Kronig transitions tend to occur in heavier atoms where there is a rich core level structure, and so are not considered in this work.

2.2.8 Quantification

Analysis of photoemission spectra provides a plethora of information about the surface of a sample. A survey spectrum reveals the elemental fingerprint of the sample, the intensity ratios of each peak indicates the elemental composition, and loss features such plasmons can even reveal some structural information. A high resolution core level spectra can be deconvolved to further determine the local chemical environment that each element is involved in and determine stoichiometry. However, before this information can be extracted, a number of post-acquisition steps must be taken. It helps to first define the contributions of photoelectron intensity I for a energy level n_l (assuming a homogeneous solid) [39]:

$$I(n_l, E_k) \approx J(hv) \cdot N_i \cdot \sigma(n_l, hv) \cdot T(E_k, K) \cdot \lambda(E_k, \theta) \tag{2.23}$$

$J(hv)$: Incident photon flux which is defined as the number of photons arriving at a unit area per unit time ($\mathrm{cm}^{-2}\,\mathrm{s}^{-1}$). An important parameter to consider when analysing data from a synchrotron where the photon flux may change substantially for differing photon energies hv.

N_i: The number of atoms in the sample belonging to chemical species i.

$\sigma(n_l, hv)$: Photoionization cross-section is the probability per unit area per unit

time ($\mathrm{cm}^{-2}\,\mathrm{s}^{-1}$) that an electron in an energy level n_l will absorb a photon of energy hv and undergo ionization, as discussed in section 2.2.3.

$T(E_k), K$**:** Transmission function of the analyser (see section 3.4) which describes the transmission efficiency of the analyser for photoelectrons at kinetic energy E_k. The factor K accounts for experimental parameters such as entrance slit size, detector voltage, and pass energy to name a few.

$\lambda(E_k, \theta)$**:** Effective attenuation length (see section 2.2.4).

In order to calculate the atomic percentage of elements (or species) in a spectra, a sensitivity factor S that incorporates all of the non-N_i terms must be defined and used to normalise the peak intensities. This leaves a series of peaks whose intensities directly infer the elemental composition $[N_i]$ of a sample. This can be calculated as an atomic percentage using:

$$[N_i]\mathrm{at}\% = \left(\frac{I_i/S_i}{\sum_{n=i}^{n} I_n/S_n} \right) \times 100 \tag{2.24}$$

where I_n and S_n are the intensities and corresponding sensitivity factors for n atoms/species. Once the $[N_i]$ of all the species in an XPS spectrum are known, stoichiometry can be determined. For example, homogeneous aluminium oxide (Al_2O_3) has the molar ratio X_n of 2:3 (Al:O). The expected atomic percentage $[A_i]$ of species i would be:

$$[A_i]\mathrm{at}\% = \left(\sum_{n=i}^{n} \frac{X_n}{X_i} \right)^{-1} \times 100 \tag{2.25}$$

Using equation 2.25, the atomic percentage of oxygen [O] in Al_2O_3 is therefore:

$$[\mathrm{O}]\mathrm{at}\% = \left(\frac{2}{3} + \frac{3}{3}\right)^{-1} \times 100 = 60\mathrm{at}\% \tag{2.26}$$

meaning that oxygen's $[N_i]$ from equation 2.24 should also be 60 at%. It follows then that the values of $[N_i]$ for elements/species in an XPS spectrum can be used to determine stoichiometry and the bonding configurations in the sample.

In section 2.2.4, the intensity contribution at different sample depths is calculated using equation 2.16. This equation is also known as the Beer-Lambert law and is used to calculate signal attenuation due to absorption, meaning that this equation can used to calculate the expected intensity from a substrate with a known overlayer thickness x, or vice versa. Using a single spectrum that contains core levels related to the substrate and the overlayer allows a thickness calculation based on the area ratios to be performed. The intensity of the substrate signal I_{sub} is:

$$I_{sub} = e^{-\frac{x}{\lambda}} \cdot \sigma_{sub} \tag{2.27}$$

where σ_{sub} is the photoionization cross-section of the core level related to the underlying substrate, and λ is the EAL of substrate photoelectrons travelling through the overlayer. For the overlayer, the intensity I_{over} is:

$$I_{over} = 1 - e^{-\frac{x}{\lambda}} \cdot \sigma_{over}. \tag{2.28}$$

For the work herein, the ratio of C $1s$ to Fe $2p$ intensity is used to determine the thickness of a graphitic overlayer on bulk iron. For a single sheet of graphene, the ratio $I_{C1s} : I_{Fe2p} = 1 : 42$ [56].

2.3 Low Energy Electron Diffraction (LEED)

In 1928, Davisson and Germer performed an experiment where low energy electrons incident on a crystalline nickel target backscattered to produce a pattern of intensity with regular angular dependance [57]. This pattern had the same diffraction intensity for X-rays of the same energy, and so the Davisson-Germer experiment provided the first evidence that confirmed de Broglie's theory of wave-particle duality, i.e. that matter exhibits wave-like behaviour such as diffraction [58]. De Broglie's relation between wavelength λ and the kinetic energy E_k of a particle with mass m and elementary charge e is:

$$\lambda = \frac{h}{p} = \frac{h}{\sqrt{2mE_k}} = \frac{h}{\sqrt{2meV}} \tag{2.29}$$

where p is momentum, h is Planck's constant, and V is an acceleration voltage. For acceleration voltages between 20 V and 200 V, the de Broglie wavelength of an electron is of the order of angstroms (i.e. around 1 Å to 3 Å) which is the typical inter-planar distance of most crystalline materials. The EAL of electrons in this kinetic energy regime is also very small (see section 2.2.4), again on the order of angstroms, and so the electrons only interact with the surface region of the sample. This means that low energy electrons see the surface of a crystalline solid as a diffraction grating in 2-dimensions. If we consider two electrons that have been backscattered by two adjacent lattice points on the surface by the same angle θ relative to the surface plane, they will have a path difference D between them such that:

$$D = \alpha \sin(\theta) \tag{2.30}$$

where α is the distance between the lattice points. The two electrons will then interact with each other, destructively interfering when $D = (n + 1/2)\lambda$ and

constructively interfering when $D = n\lambda$. The diffracted intensity varies slowly with θ between destructive and constructive interference, reaching a maximum intensity when the Bragg condition is met at $n\lambda$. The incident electron beam spot size can be anywhere between micrometres and millimetres across, meaning that a large number of surface unit cells contribute toward electron diffraction and the LEED spot intensities. Figure 2.5 shows a simulated LEED pattern and the corresponding real and reciprocal lattice that produced it. The LEED pattern is a direct image of the reciprocal space of the sample surface, and therefore can be used to determine the surface structure. However, electron diffraction requires highly crystalline samples in order to provide a clear sharp pattern. Non-crystalline regions, dislocations, and point defects all increase the likelihood of elastic scattering which can contribute a background like the one represented by the green diffuse green area behind the diffraction spots in figure 2.5 [59]. However this can also be caused by setting incorrect grid and mesh voltages, thus allowing secondary electrons to reach the phosphor screen.

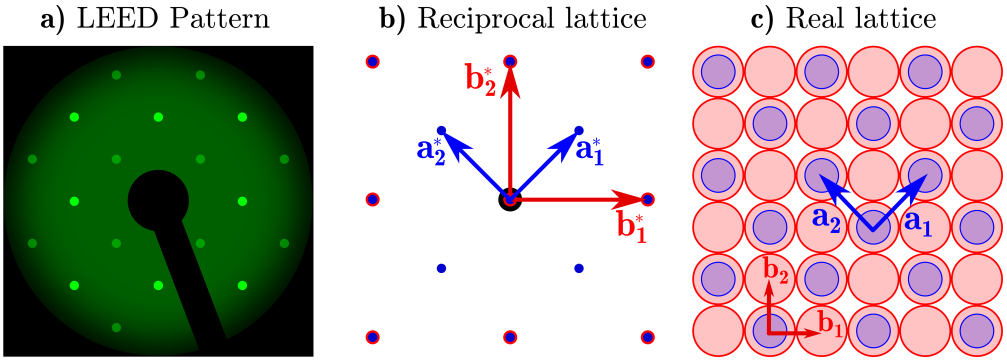

Figure 2.5. **(a)** A simulated LEED pattern showing both diffraction spots, a background (either elastic or inelastic scattering), and the shadow of the electron gun on the zero-order spot. **(b)** The reciprocal space lattice of the sample which directly maps onto the LEED pattern. There are two lattices here with different periodicities, i.e. lattice **a** (a_1^*,a_2^*) has double the periodicity of lattice **b** (b_1^*,b_2^*). **(c)** The corresponding real space lattice of the sample, where it becomes clear that lattice **a** is a (2×2) absorpate on lattice **b**, an fcc $(100)(1 \times 1)$ surface.

LEED as a method of surface analysis did not begin in earnest until the 1960s when better vacuum technology began to emerge [60]. Figure 2.6 shows an experimental LEED setup using a rear-view geometry similar to the one used in the home laboratory. Data is acquired by taking images of the phosphor screen with a camera, with the grid/mesh voltages optimised to reduce the intensity of the background and hence improve the contrast of the principle diffraction spots. With more sophisticated software, the incident electron energy can be altered continuously whilst a series of diffraction pattern images are taken. The intensity of single diffraction spots can be plotted with respect to the incident electron energy to produce LEED I-V (intensity-voltage) curves, which when compared to theoretical LEED I-V curves, can be used to determine the position of atoms on the surface or the number of atomic planes in a layered structure such as graphene.

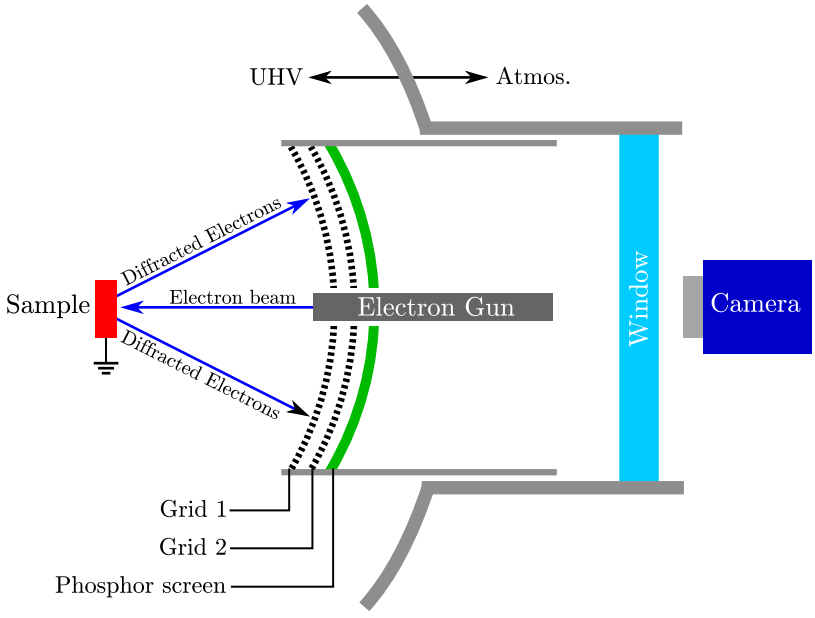

Figure 2.6. A schematic of a rear-view LEED unit similar to the one used in this work.

2.4 Electron Microscopies (XPEEM & LEEM)

Photoemission electron microscopy (PEEM) images the chemical state of the surface. Areas of differing elemental composition, allotropes, and chemical species can be laterally resolved with a resolution of nanometres and an energy resolution of less than 500 meV. In this work, X-ray Photoemission electron microscopy (XPEEM) is utilised in chapter 7 to measure the lateral extent of graphene grown using the iron-mediated graphitisation technique. The first operational photoemission electron microscope was developed and demonstrated by Ernst Brüche in 1933 [61]. This early set-up focused UV light from a mercury lamp onto a zinc plate engraved with holes and letters to generate photoelectrons, which were then subsequently passed through an axially divergent magnetic field in order to enlarge the image of the zinc plate whilst maintaining the energy dispersion of the photoelectrons. Using this method, Brüche was able to image the sample surface with a $\times 10$ magnification [61]. Early PEEM instruments suffered from a poor lateral resolution on the order of tens of micrometres. Work conducted by Henneberg, Recknagel, Langmuir and Artsimovich demonstrated the inherent image aberrations induced by uniform accelerating fields, a limiting factor in the resolution of PEEM [62–65]. It was found that the image resolution d was proportional to the energy of emitted electrons E, and inversely proportional to the accelerating potential U near the surface of the sample, such that

$$d \approx \frac{E}{U}. \tag{2.31}$$

Vast improvements in the lateral and energy resolution of PEEM were made in the years after Brüche's original experiment. Developments included improved electron optics such as multiple electrostatic lenses (triodes) by W. Schaffernicht

[66]; the addition of contrast and field apertures to the back-focal plane to remove diffracted photoelectrons from other emission angles; as well as characterising other sources of imaging errors such as the spherical error on the incident beam and diffraction on the imaging aperture by Boersch [67]. Later, significant improvements in UHV-equipment facilitated the production of more complex PEEM systems with far better resolution limits. Nowadays the technique is approaching the theoretical limit of emission microscopy, i.e. the minimum of the electron mean free path curve [68], thanks to electron optics that can correct for spherical and chromatic aberrations, the theoretical groundwork of which was developed by Gertrude Rempfer in 1990 [69].

Low-energy electron microscopy (LEEM) was developed alongside PEEM and other electron microscopies such as transmission electron microscopy (TEM) and scanning electron microscopy (SEM). This technique involves illuminating the sample surface with a beam of low-energy electrons which are then diffracted (see section 2.3) by the sample surface. The backscattered electrons are then collected by the objective lens and accelerated to high kinetic energies before entering the imaging optics. Accelerating the electrons for the imaging optics has the advantage of producing a diffraction image with a constant energy, thus making LEED-IV curves easier to obtain, as the location of the diffraction spots does not move when changing the incident electron energy. Furthermore because the diffracted beams are bent around a beam splitter, the zero-order diffraction spot (i.e. (00)) is also acquired alongside the n^{th}-order diffraction spots. To produce a LEEM image, a single diffraction spot is selected at the imaging plane on the system (i.e. at the contrast aperture, see figure 2.7). Bright-field imaging selects the zero-order diffraction spot whereas dark-field imaging selects one of second-order diffraction beams, e.g. a surface reconstruction. This selectivity

allows LEEM to discern, via contrast differences, various surface structures and crystallinity, for example terraces, reconstructions, overlayer growth, and phase changes to name a few. The high intensity of the back scattered electrons means that images can be recorded in real-time, therefore time-resolved studies of surface reactions or thin-film growth are possible.

Here, a brief overview of the PEEM/LEEM instrument used in this study will be presented: the SMART instrument (Spectro-Microscopy with Aberration correction for many relevant Techniques) at the BESSY II synchrotron (Berlin), the first PEEM/LEEM instrument to correct for imaging aberrations and achieve a lateral resolution limit of 2.6 nm (LEEM) [70, 71]. A simplified schematic of the SMART instrument is shown in figure 2.7. Information is acquired from the sample surface by two methods: either illuminatation by electromagnetic radiation (lab source or synchrotron radiation) to induce photoemission; or a focused high-energy electron beam is sent through a beam splitter to be directed at a normal to the surface and then decelerated to kinetic energies between 1 eV to 200 eV to diffract on the sample sample. Photoelectrons (PEEM) or diffracted electrons (LEEM) from the sample surface are accelerated toward an objective lens consisting of an electrostatic immersion lens with a superimposed magnetic field, stigmator, and deflection field. The objective lens collects the imaging electrons, forming a virtual image behind the sample. However in the process, it induces chromatic and spherical aberrations which result in blurring of the image formed at the intermediate image planes (after the objective lens but before the beam splitter, and after the beam splitter but before the electron mirror). To resolve this issue, and hence improve the lateral resolution of the image, electrons from the sample are directed through a beam splitter towards a concave-convex tetrode electron mirror where chromatic and

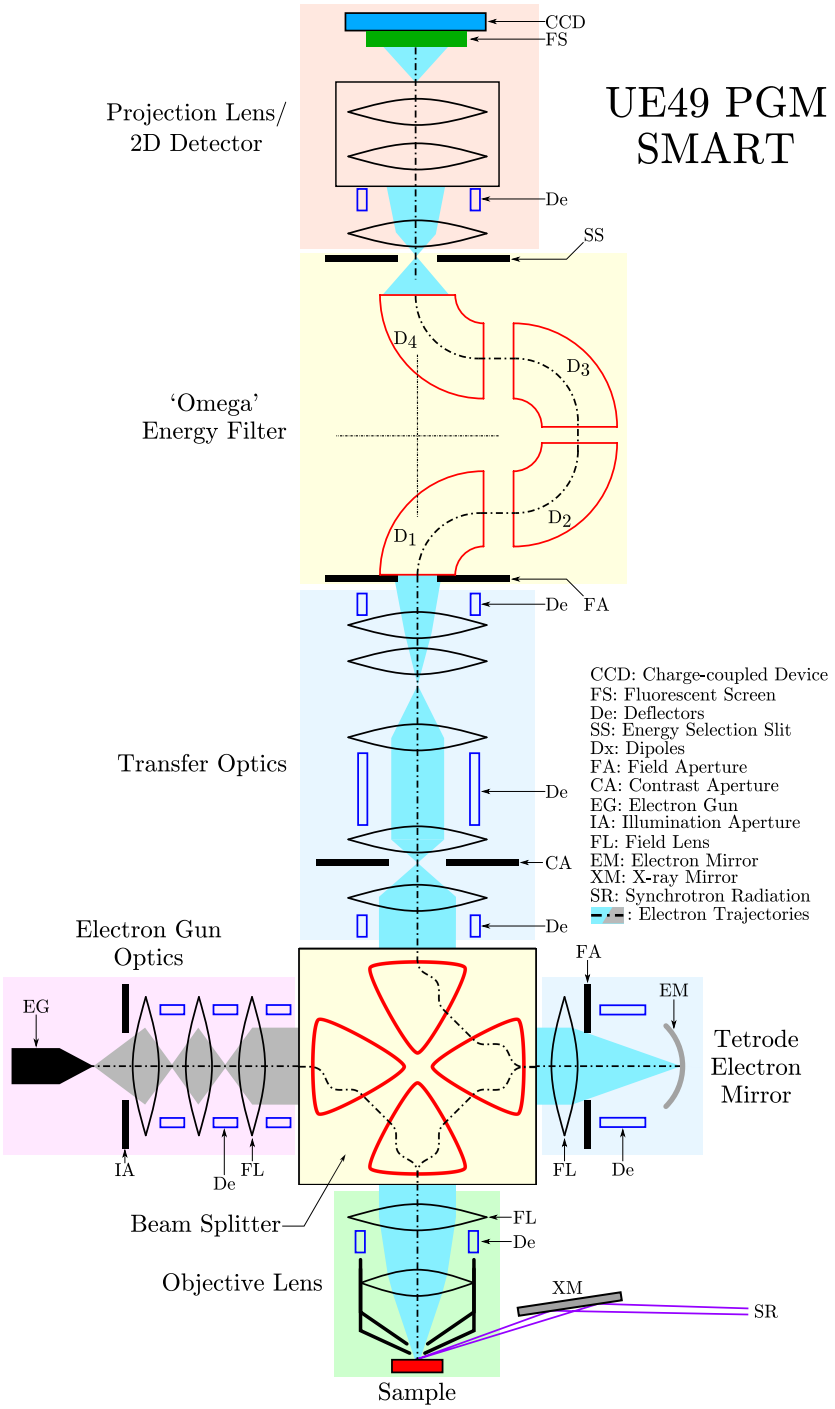

Figure 2.7. A simplified schematic of the UE49 PGM SMART instrument at the BESSYII synchrotron, Berlin. Figure adapted from [72].

spherical aberrations are simultaneously corrected for. The imaging electrons are then passed back into the beam splitter where they are guided toward the transfer optics which form a magnified real-space image of the sample and a de-magnified reciprocal-space image of the diffraction pattern at two separate positions before the energy filtering optics. Several operating modes (i.e. imaging modes such as PEEM, LEEM, and Mirror Electron Microscopy, Dispersive Plane Imaging for XPS, and Diffraction Plane Imaging for LEED) can be selected by use of a field-limiting aperture at the intermediate image plane and a contrast aperture at the intermediate focal plane. The imaging electrons then enter the 'Omega-filter' which is the energy filter for photoelectrons (in PEEM) as well as inelastically scattered and secondary electrons (in LEEM). The Omega filter creates an energy dispersion $\sim$15 eV wide at the detector plane. A slit at the exit plane of the Omega-filter selects the desired photoelectron energy from the energy dispersed image. For XPS, the full dispersive plane energy is used by fully opening this slit. Imaging electrons of a specific energy are then passed onto the projection lens, which form the final image onto a fluorescent screen placed in front of a 2-dimensional CCD camera. A far-more detailed description of the SMART instrument can be found in the following referenced articles [68, 70, 72, 73].

2.5 Raman Spectroscopy

When a photon interacts with matter, it can either be absorbed or scattered. Absorption occurs when the energy of the interacting photon corresponds to the energy between some ground state and an excited state of the matter. The photon is absorbed and the matter now exists in a higher energy state until loss processes occur to allow the matter to return to the ground state, for example

by re-emitting a photon or a series of phonons. In the case of scattering, photons do not have energies which match the energy transitions in the matter. Instead, the matter is excited into short-lived virtual states in the gaps between energy levels. These virtual states are not at all stable, and so the photon is quickly re-emitted. If the energy of scattered photon is equal to the original photon, then the process is known as elastic scattering (or Rayleigh Scattering in the case of molecules, see figure 2.8b). This type of scattering predominantly occurs in the electronic structure of the scattering medium. Electrons are relatively low in mass, and so any photon energy losses due to distortions of the electron distribution are negligible. The scattering process is inelastic when the scattered photon has a different energy to the incident photon; this is known as the Raman

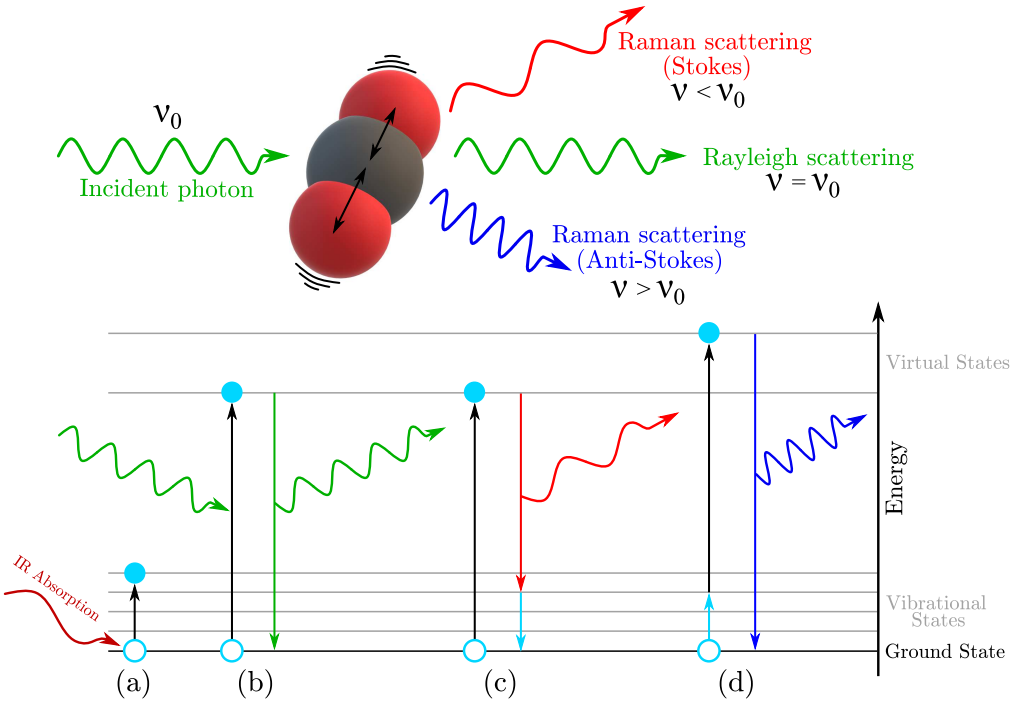

Figure 2.8. Rayleigh and Raman scattering processes. The incident photon λ_0 is scattered by matter, in this case a carbon dioxide molecule, and undergoes elastic (Rayleigh) and inelastic scattering (Raman). **(a)** The incident photon is low enough in energy to be absorbed and promote an electron to a vibrational level. **(b)** Rayleigh Scattering. **(c)** Stokes and **(d)** Anti-Stokes Raman scattering. Adapted from [74]

scattering phenomenon, which was first experimentally demonstrated in 1928 by C. V. Raman (from whom the effect is named after) and his colleague K. S. Krishnan [75]. Figure 2.8 illustrates the Rayleigh and Raman scattering processes. An incident photon excites an atom or molecule in the scattering medium to a virtual state. Some of the photons energy is absorbed by the atom/molecule as vibrational or rotational energy, and hence the scattered photon is emitted with less energy than the original photon. This energy change is known as a Stokes shift. After the scattering event, the atom/molecule will exist in a rovibrational energy level above the ground state (Figure 2.8c). If the atom/molecule is already in a rovibrational level above the ground state, then the incident photon can excite the atom/molecule into a higher virtual state, thus releasing a photon with more energy as the atom/molecules relaxes to the ground state. This is known as an Anti-Stokes shift (Figure 2.8d). The Raman effect is extremely weak with only one in 10^6 to 10^8 photons undergoing a Stokes or Anti-Stokes shift. However with modern laser and microscope systems which can deliver high power densities to micrometer-sized areas, reasonable Raman signals are routinely achievable albeit at the risk of sample damage and background fluorescence [76].

Raman scattering is utilised by Raman spectroscopy, a technique used to determine rovibrational (i.e. rotational and vibrational) modes of molecules and condensed matter. A Raman spectrum is a plot of the scattered light intensity versus the inverse wavelength of the scattered photon, i.e. the wavenumber (cm^{-1}). The wavenumber of a specific vibrational or rotational mode $\bar{\nu}$ is given by:

$$\bar{\nu}[\mathrm{cm}^{-1}] = \frac{1}{\lambda_0} - \frac{1}{\lambda_\nu} \tag{2.32}$$

where λ_0 is the wavelength of the incident light and λ_ν is the wavelength of the Raman scattered light. This wavenumber notation is used because it is independent of the incident light frequency. For example, the diamond first order Raman mode occurs at $\sim$1332 cm^{-1} for all excitation wavelengths. When plotted against Raman wavelength, the diamond main Raman line shifts with excitation energy, e.g. a 572.57 nm Raman shift from a 532 nm excitation, and 691.29 nm shift from a 633 nm excitation. The presence of specific rovibrational modes in a Raman spectrum provides a 'fingerprint' that can be used to identify the chemical composition of sample. The local atomic environment around a Raman scattering centre can drastically alter the photon-phonon coupling, and hence the size, shape, and number of Raman peaks in spectrum. This means that Raman spectroscopy has a wide range of applicability, from chemical species identification, determination of crystal structure, the orientation of molecules, and measuring residual stress in a material. Raman spectroscopy has become an essential technique in the study of graphene and 2-dimensional materials, and in the context of this study, Raman data have provided complimentary evidence of the presence and quality of graphene produced in the iron-mediated graphitsation experiment outlined in chapter 6.

2.6 Scanning Probe Microscopy

Scanning probe microscopy (SPM) refers to a range of analysis techniques which use a cantilever with a near-atomically sharp tip to scan a sample and determine its surface properties. The field of SPM began in earnest with the development of scanning tunnelling microscopy (STM) by Binnig *et al.* in 1982, and later atomic force microscopy (AFM) in 1986. Since then, a plethora of SPM techniques have emerged that probe different surface properties from topography, to friction

coefficients, to charge distributions. SPM's main advantage is that it is not subject to an optical diffraction limit like standard microscopes, but rather the probe-sample interaction volume which is on the order of picometres, meaning that the resolution of SPM techniques is far superior. SPM probes are typically mounted on a silicon chip and consist of a micrometre scale long silicon cantilever with a near-atomically sharp tip (∼50 to 0.1 nm tip radius) perpendicular to the cantilever on one side, and have a thin layer of reflective material on the other. The tip side can also be coated with a conductive material such as platinum for techniques such as electrostatic force microscopy (EFM) and STM. For the purpose of this report, only AFM will be discussed as it is the most pertinent SPM technique to the project in hand. AFM measures the atomic forces that manifest between the sample surface and the tip; this information is typically interpreted as the topography of the sample surface. Binnig *et al.* were able to resolve forces as small as 10^{-18} N with a lateral and vertical resolution of 30 Å and 1 Å respectively using their atomic force microscope. Today's AFMs have far improved lateral resolution, and when operated in low voltage modes, can resolve single atoms on a sample surface. Figure 2.9a illustrates the AFM setup on a sample with a varied topography. The sample is attached to a piezoelectric-controlled xy-stage, and the AFM tip is mounted onto a motor driven z-stage with a piezoelectric element to control the vertical deflection of cantilever to angstrom resolution. As the cantilever approaches within 100 nm of the sample, the tip begins to bend toward the surface due to attractive van-der-Waals forces that are spontaneously formed as the surface atoms polarise in proximity to the AFM tip. At this sample-tip distance, non-contact measurements are taken as shown by figure 2.9d. As the tip is forced closer to the sample, to within a few angstroms, it enters a regime where exchange interactions due to the overlap of atomic orbitals dominate. These interactions manifest as a large repulsive force,

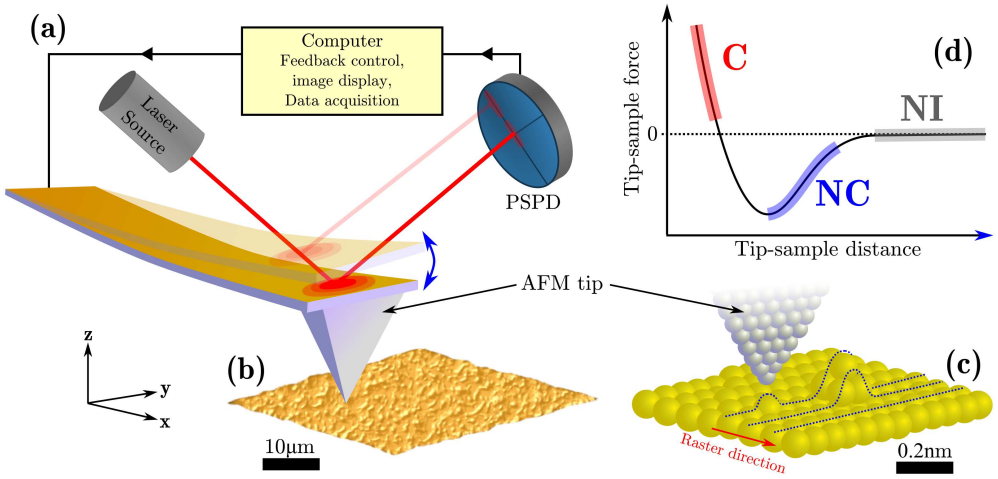

Figure 2.9. The AFM process. (a) The cantilever/PSPD/computer feedback system. (b) A topography over which the AFM tip is being scanned. (c) The tip rasters across the surface and responds to the changes in topography. (d) Different modes of AFM are required for differing set points above the sample.

which bends the cantilever away from the surface. Due to the very small sample-tip distance, contact measurements are taken in this regime. To determine the amount of cantilever bending, a laser is shone on to the end of cantilever and the reflected beam is detected by position-sensitive photo diode (PSPD). Any vertical or horizontal deflection of the cantilever causes the laser spot on the PSPD to move in the corresponding directions. The AFM tip is quickly scanned across the sample in one direction, and at discrete steps the signal from the PSPD is interpreted by a computer to give the sample height at a given point. The tip is also slowly scanned in the perpendicular direction and rasters across the surface, slowly building up an image of the sample topography as it goes. AFMs can be operated in contact and non-contact modes depending on the sample being analysed, for example soft easy-to-damage biological specimens or polymers benefit from non-contact modes to avoid the tip piercing or scratching the sample. In contact mode, the cantilever deflection is kept constant by moving the cantilever up and down as it traverses the sample. Changes in the cantilever

deflection cause a signal change on the PSPD which feeds back to the z-stage piezoelectric element and adjusts the cantilever height accordingly. In non-contact mode, the z-stage piezoelectric element vibrates the cantilever at its resonant frequency. Here it is the cantilever oscillation that is kept constant; any change in the cantilever oscillation due to atomic forces is detected and corrected by altering the cantilever height accordingly. Both modes produce a topography image of the sample surface, as well as some lateral force and error signal data which can be used in other analysis methods (i.e. lateral force is used in lateral force microscopy to measure friction coefficients on the nanometre scale). In this work, contact and non-contact probes have been used to gather surface topographies of diamond substrates and graphene-iron-diamond samples respectively.

Chapter 3

Instrumentation

The research presented in this thesis would not have been possible were it not for the plethora of instrumentation available to apply the techniques discussed in chapter 2; table 3.1 summarises the numerous instruments and facilities used for this work. Some instrumentation for minor techniques has already been addressed in the previous chapter. The home laboratory UHV system and synchrotron beamlines contributed the majority of data, and so this chapter will explore the Aberystwyth UHV system, the variety of photon sources used for photoelectron spectroscopy including synchrotron radiation, and the operation of the hemispherical analyser which is vital to photoelectron techniques.

Instrumentation	**Techniques**	**Institute / Location**
Aberystwyth UHV System*	REES, XPS, UPS, LEED	IMPACS, Aberystwyth, UK
Kratos Axis Ultra DLD*	XPS	NPL, Teddington, UK
SGM3 Beamline†	ARPES	ASTRID2, Aarhus, Denmark
SMART Beamline*	PEEM, LEEM, LEED, XPS	BESSY, Berlin, Germany
Horiba LabRam HR800*	Raman Spectroscopy	IMPACS, Aberystwyth, UK
Park Systems XE-100*	AFM	IMPACS, Aberystwyth, UK

Table 3.1. A list of instrumentation used in this work* and previous relevant studies†

3.1 Aberystwyth UHV System

The majority of the work presented in this thesis was conducted in the home laboratory in Aberystwyth, using a bespoke UHV system built as part of a previous EPSRC project. This system consists of four stainless steel / Mu-metal chambers pumped by turbo-molecular and getter pumps, with each chamber equipped with various surface treatment and analysis apparatus.

The Analysis Chamber ("REES") The Aberystwyth UHV system is primarily a photoelectron spectrometer, and also has the capability of measuring spectra in real-time, parallel to *in-situ* processes such as heating or thin-film deposition. This technique is known in the home laboratory as real-time electron emission spectroscopy (REES). Data acquisition takes place in the analysis chamber or "REES" chamber, named for the aforementioned primary technique of the system. This spherical chamber has a SPECS PHOIBOS 100 hemispherical analyser coupled with a twin-anode X-ray source and a UV source (see sections 3.2.1 and 3.2.2 respectively), allowing both XPS and UPS/ARPES analysis. Samples are positioned manually with a vertically mounted $xyz\theta$ manipulator with a sample stage that includes a Boralectric BN/graphite heater plate (See section 3.3.1). In line with the hemispherical analyser on the opposite side of the chamber is a rear-view LEED unit to determine sample crystallinity. Helium leak testing and identification of outgassing species is achieved by a residual gas analyser (mass spectrometer) mounted above the UV source. The REES chamber also has two home-made Knudsen cells for depositing iron and silver *in-situ* which can be used during REES measurements to determine overlayer thickness. The K-cells are collimated to prevent material depositing on the X-ray source or analyser entrance cone, and they have a shutter assembly for precise deposition times. During normal operation, the REES chamber

is continually pumped by an ion pump and periodically pumped by titanium sublimation pump (TSP), resulting in a base pressure of $\sim 5 \times 10^{-11}$ mbar; such a low base pressure preserves the sample surface condition for days as detailed in section 2.1.2. Figure 3.1 shows a top-down view of the REES chamber with the aforementioned components.

The Preparation Chamber Samples loaded into the Aberystwyth UHV system from the fast load lock are passed into the cylindrical preparation chamber where they can undergo surface treatments before being loaded into the REES chamber. The preparation chamber has an $xyz\theta$ manipulator and sample heating stage similar to the REES chamber as well as an additional sample stage below the heater which has a hole-matrix mask for patterned deposition. Another series of homemade K-cells are mounted in this chamber for depositing iron and gold. The iron K-cell on the preparation chamber, contrary to its analysis chamber counterpart, is mounted on a linear drive mechanism behind a gate valve and has its own pumping port allowing it to be transferred between different chambers and UHV systems (see section 3.3.2). Unlike the analysis chamber, quartz crystal thickness monitors are positioned opposite the K-cells for determination of the deposition rates. For cleaning and sputtering of samples, a PHI model 20-005 ion sputter gun is used in conjunction with a back-filled environment of $\sim 10^{-5}$ mbar argon to produce Ar^+ ions. The preparation chamber has many additional ports for mounting new K-cells, valves, surface treatment apparatus, etc. The main system turbo-molecular pump is attached to the preparation chamber behind a large gate valve. This pump brings the entire system to UHV after venting and pumps away water and contaminants during a bake-out. During normal operation it is valved off from the system, and the preparation chamber's own ion pump / TSP assembly brings the pressure

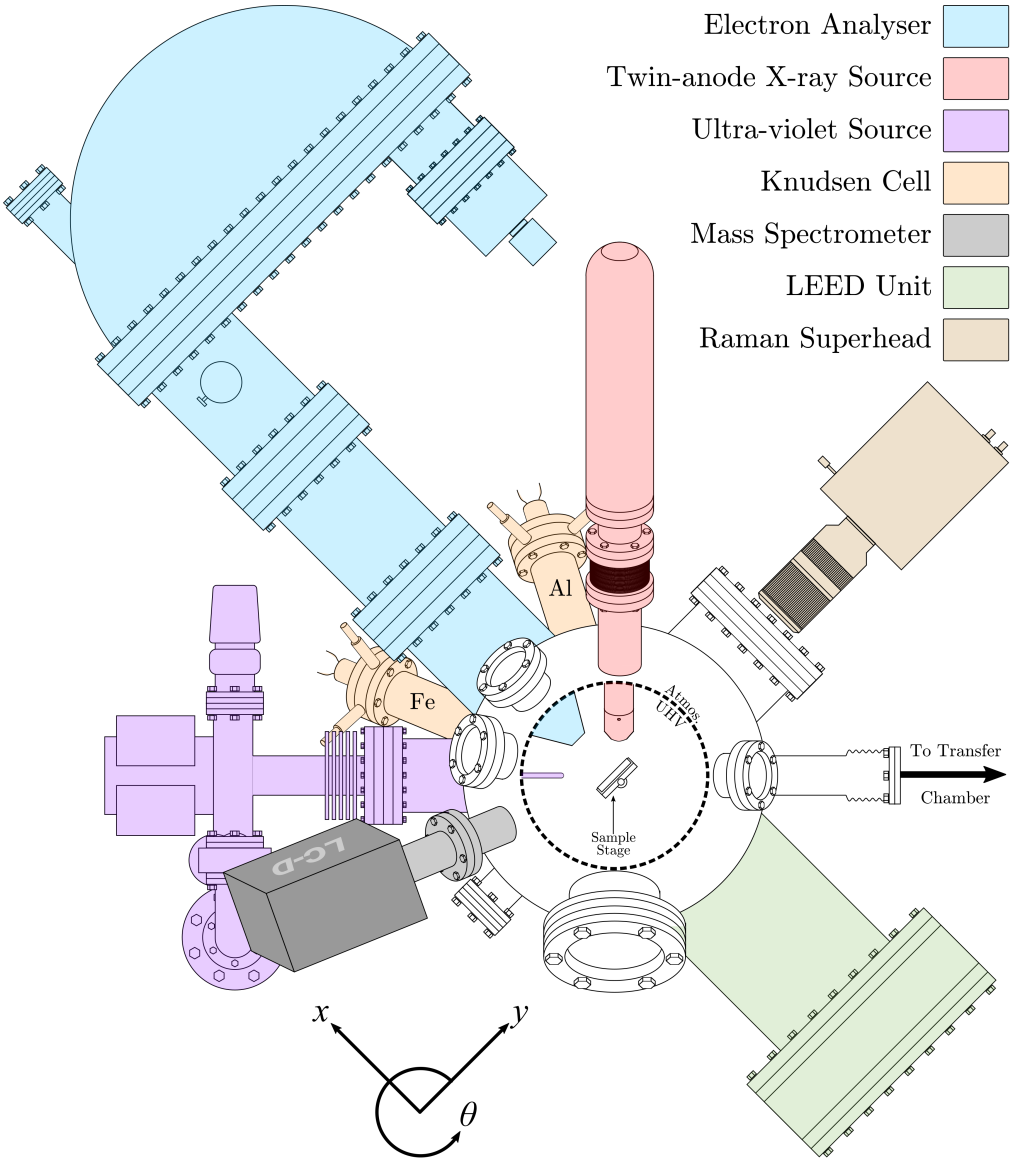

Figure 3.1. A top-down schematic of analysis chamber ("REES") of the Aberystwyth UHV system showing the location of the various photon sources, evaporation cells, and analysis tools available. The manipulator (not shown) is bolted to the top of the chamber with the z-direction into the page. The other manipulator axes are shown at the bottom. This schematic is not to scale.

down to that of the REES chamber. Magnetic arms from the fast load lock and plasma chamber meet in the preparation chamber, and samples are transferred from one arm to the other via the preparation sample stage.

The Plasma Chamber Surface treatments involving the use of plasmas take place in the plasma chamber, of course. This chamber is attached to the transfer chamber and the main magnetic arm of the system, which is used to move samples into the REES chamber. Pumping is achieved by a turbo-molecular pump and pressure is measured using a cold cathode vacuum gauge. Samples can be heated by close proximity to a 50 W tungsten filament which is attached to linear drive electrical feed-through. Process gases are bled into the chamber by use a VG precision leak valve, allowing selection of the optimum partial pressure for plasma generation.

The Load Lock The fast-entry load lock provides access for introducing samples into the UHV system. The load lock is attached to the transfer chamber and separated by a gate valve. The load lock can be vented to atmospheric pressure, either via a screw valve (to laboratory air) or using dry N_2 gas via the plasma chamber gas line. The latter method is preferable as it avoids introducing H_2O into the system which over consequtive vent-purge cycles, would increase the base pressure of the entire system. The load lock is pumped by a turbo-molecular pump and pressure measurement is given by a Penning gauge. Due to the frequency at which the load lock sees atmosphere, the ultimate pressure never exceeds 5×10^{-7} mbar, and transfer of samples is usually performed at pressures less than 1×10^{-6} mbar. Functionally, samples are passed into the transfer chamber and undergo pre-treatments before moving into the REES chamber. The separation of the load lock and the REES chamber means that contaminants from the venting process do not reach the REES chamber.

3.2 Photon Sources

3.2.1 Twin-anode X-ray Source

Production of soft X-rays in the home laboratory is achieved by use of a Thermo VG Scientific twin anode X-ray source, which is shown by the schematic in figure 3.2. In this source, electrons are generated by thermionic emission from a hot thoria-coated tungsten filament. These electrons are then accelerated toward

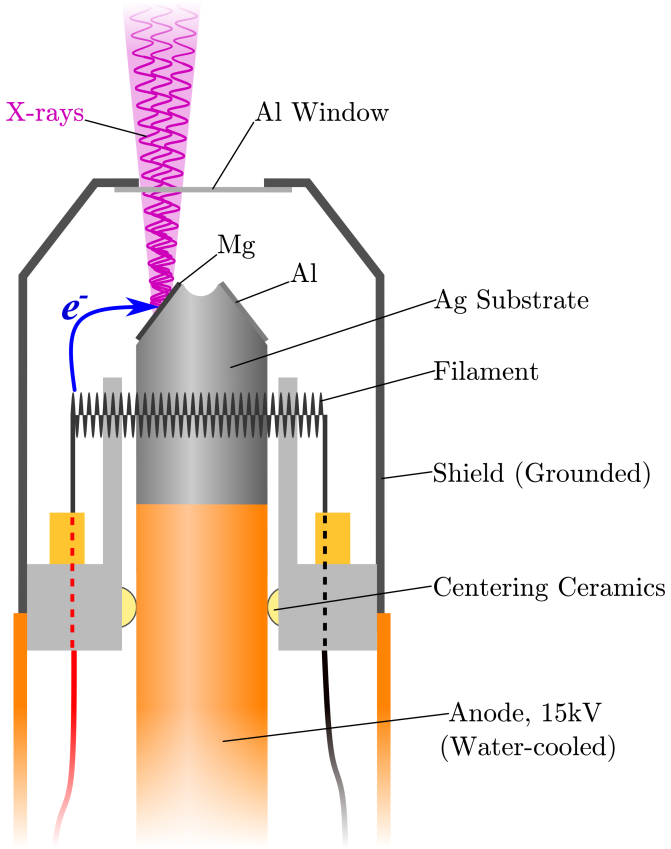

Figure 3.2. A schematic of a typical twin-anode X-ray source. The filament array is consists of two separate filaments with a common ground, and are arranged such that electrons are only thermionically-emitted on the side which has the selected anode target (although some anode cross-talk is expected). The centering ceramics ensure that the high voltage anode is isolated from the grounded components of the gun.

one of two target anodes with a potential of 15 kV relative to the filament and ground. When the electrons strike the anode material, X-rays are generated by either the Bremsstrahlung process or, from allowed electronic transitions giving rise to characteristic emission lines. The laboratory source uses magnesium and aluminium anodes, which are the most common anode metals emitting characteristic $K\alpha_{1-2}$ X-rays at 1253.6 eV and 1486.6 eV respectively; these energies arise from the $2p_{3/2}, 2p_{1/2} \rightarrow 1s$ electronic transitions. Figure 3.3 shows the characteristic emission lines from a non-monochromated Mg anode source, same as the laboratory source. The main $K\alpha_{1-2}$ line, which is Lorentzian in nature, is approximately 0.7 eV for Mg and 0.9 eV for Al as calculated by

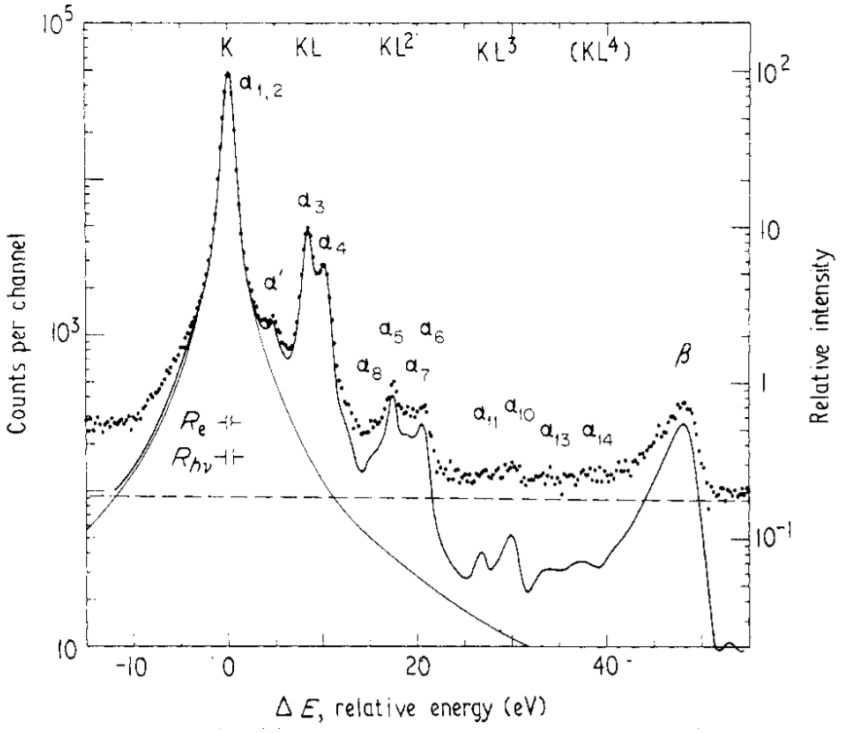

Figure 3.3. The X-ray emission spectrum of a magnesium anode, showing X-rays emitted by electrons transitioning from p-orbitals (i.e. $L1$, $L2$, $L3$, $L4$) to the s-orbital (i.e. K). The dots show the emission spectrum as acquired using a PAX spectrometer, the solid lines show the theoretical emission lineshapes, and the horizontal broken line represents the average background. Figure reproduced from M.Krause & J. Ferreira (1975) [77].

fitting a Voigt-like peak to Ne 1s core levels [77]. Other X-ray energies emitted from the anodes, such as the $K\alpha_{3-4}$ characteristic transitions have intensities of ∼8 % to 4 % of the main $K\alpha_{1-2}$ line after attenuation using an aluminium window [78]. Regardless, use of non-monochromated sources typically requires processing of acquired data to remove satellite and cross-talk features arising from these secondary emission lines.

Monochromated Al $K\alpha$ source

At NPL, a Kratos Axis Ultra with monochromated Al source was used for one XPS experiment in chapter 7. In this set-up, electrons generated using an electron gun are accelerated toward the Al target, generating the characteristic Al $K\alpha_{1-2}$ X-ray emission lines and Bremsstrahlung continuum. The radiation is then diffracted through a curved quartz crystal which allows the X-ray beam to be monochromated and focused on to the sample. The monochromator geometry is adjusted such that the Bragg condition to allow only the $K\alpha_{1-2}$ emission lines to be incident on the sample is satisfied. The curvature of the quartz crystal focuses the beam into a spot size of 300 µm by 700 µm. The advantages of monochromated sources include a decreased background due to Bremsstrahlung, narrower photoelectron peaks (Gaussian broadening becomes dominant), a smaller X-ray spot size, and a lack of satellite peaks, all at the cost of much lower count rates compared to the non-monochromated source.

3.2.2 Ultraviolet Source

For probing the density of states in the valence band, a lower energy source in the UV range is required. In the home laboratory, vacuum ultra-violet (VUV) radiation was provided by a SPECS UVS-300 Helium plasma source which enabled a choice of two photon energies corresponding to the emission

lines of He Iα and He IIα (21.2 eV and 40.8 eV respectively). Figure 3.4 shows a simplified schematic of the UVS-300 source. The UVS-300 source operates by accelerating thermionic electrons from a cathode filament (between 18 A to 22 A) along the lines of a strongly inhomogeneous magnetic field toward an anode (between 1 A to 3 A at 40 V to 150 V), where high purity He gas is leaked into a small discharge region. The electrons collide with the He atoms resulting in core level ionization producing an intense and highly dense plasma which emits very stable and intense VUV radiation. The VUV radiation is extracted on the cathode side by combination of a metal and quartz capillary. The path between the discharge region and the capillary is differentially pumped, and a micro-valve (i.e. the capillary valve) opens the plasma up to the analysis chamber

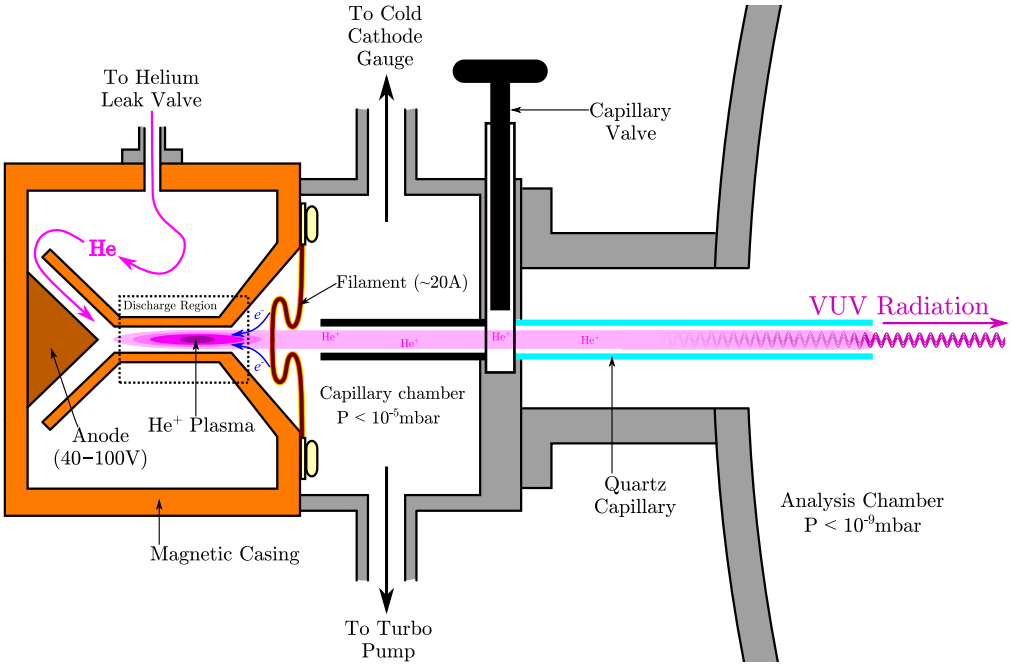

Figure 3.4. A simplified schematic of the UVS-300 source. The plasma opetates at ∼300 W and produces a significant amount of heating which is extracted by a Cu water cooling system. The UVS-300 produces a small spot size on the sample (∼2 mm) and provides a maximum photocurrent of 200 nA (measured on Au). Figure reproduced from SPECS GmbH [79].

allowing the plasma to emit VUV closer to sample stage and thus improve photoelectron intensity. The VUV radiation is emitted with high spectral purity ($>2 \times 10^{16}\,\mathrm{s}^{-1}\,\mathrm{sr}$) with the non-He lines contributing less than 0.2 % of the He I emission line, and the source has an adjustable He I/He II emission ratio depending on the discharge current and gas pressure [80].

3.2.3 Synchrotron Radiation Facilities

Some of the work conducted in this thesis required monochromated and tunable photon sources with high brilliance, or techniques that could not be performed in the home laboratory, for example ARPES studies or photoelectron microscopy. For these experiments, it was necessary to utilise radiation from a synchrotron. In short, synchrotron radiation is emitted when a charged particle travelling at relativistic speeds undergoes a radial acceleration. The theoretical basis for synchrotron radiation was developed soon after the discovery of the electron by various physicists: A. Lienard derived an expression for the radiated power emitted by electrons moving in a circular path, and G. A. Schott studied the emitted radiation for rings of moving electrons in a magnetic field [81, 82]. The first experimental observation of synchrotron radiation was accidentally made in 1947 by Pollock *et al.* when they observed 'an arc in the vacuum tube' of their synchrotron [83]. Although initially the flash of light was thought to be Cerenkov radiation, they later agreed that it was energy loss due to radiating electrons, as detailed in 1944 by Ivanenko and Pomeranchuk [84]. Synchrotron radiation was initially regarded as an unwanted loss of energy in synchrotrons whose purpose was, ironically, to generate X-ray by focusing high kinetic energy electrons onto a suitable target. The first generation of synchrotron facilities were primarily used for high-energy and nuclear physics, and the 'unwanted' synchrotron radiation was used by a few parasitic beamlines. It wasn't until

1981 that users of synchrotron radiation had a dedicated facility in the form of the 2 GeV Synchrotron Radiation Source (SRS) at Daresbury, UK, the first of the second generation synchrotrons [85]. The modern third generation of synchrotron radiation sources are defined by their extremely high brilliance and use of insertion devices to produce radiation along the straight sections the synchrotron storage ring. Figure 3.5 shows a simplified schematic of a modern 3rd generation synchrotron source. A regular source of electrons is generated by thermionic emission from a hot filament in an electron gun, and are then accelerated using a linear accelerator (Linac) to energies on the order of MeV. New free electrons are generated regularly to replenish those lost due to collisions with the walls of the synchrotron and residual gas particles. The linac injects electrons into a booster ring where they are accelerated to the same energy as the storage ring, typically several GeV. The booster ring will then regularly inject electrons into the storage ring in a quasi-continuous manner known as 'top-up mode', therefore maintaining an average stored current. Electrons move around the storage ring near the speed-of-light in 'bunches', confined to a closed path by the 'magnet lattice'. There are three types of magnets used in a synchrotron: dipole or bending magnets which change the direction of the electrons; quadrupole magnets focus the electron beam to account for Coulombic replusion which constantly acts to de-focus the beam; and sextupole magnets which correct for chromatic aberrations induced by the quadrupole magnets. Electrons in the storage ring will gradually lose energy, degrading their orbits and therefore causing them to move toward the inner wall of the storage ring. To prevent this, a regular radio frequency (RF) boost is supplied to the electrons at every pass, providing enough energy to keep their orbit stable. This periodic RF also maintains the distance between the electron bunches therefore preserving the storage ring synchronicity and improving the lifetime of the beam

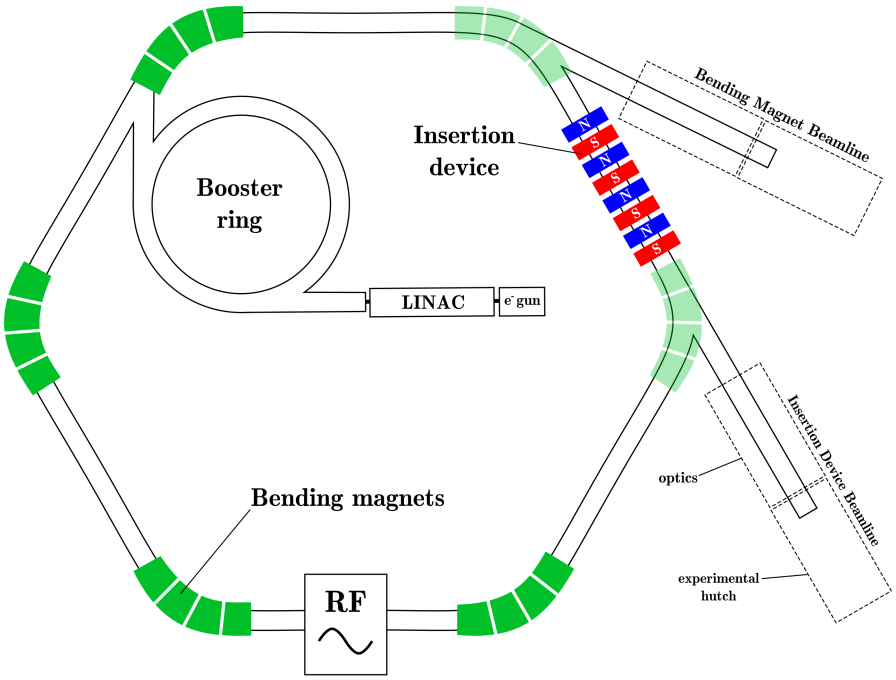

Figure 3.5. A simplified schematic of a modern-day 3rd generation synchrotron source. Figure adapted from Willmott (2011) [85].

current. Finally, the experimental beamlines are positioned around the outside the storage ring, either along the straight-sections after insertion devices, or tangentially at the dipole bending magnets. Of the work presented herein, data from two main synchrotron sources is reported. In chapter 5, ARPES data of diamond surfaces is reported which was obtained from the SGM 3 beamline at the ASTRID synchrotron at the Centre for Storage Ring Facilities, Aarhus (ISA) [86]. An undulator insertion device produces synchrotron radiation which is then guided by vertical and horizontal focusing mirrors through an entrance slit such that it is grazing incident on a spherical gating monochromator. The horizontal mirror can also switch the beam path to other beamline serviced by the same undulator. The spherical monochromator allows a range of energies from 14 eV to 130 eV by switching between three single period crystal gratings.

The radiation then passes through an exit slit, a final toriodal focusing mirror, and through a small 300 µm pinhole slit to generate a 1 mm (horizontal) × 0.5 mm (vertical) spot size at the sample focal point. In chapter 7, LEEM and XPEEM data of catalytically-grown graphene on SiC surfaces is reported which was obtained from the UE49 PGM SMART beamline at the BESSY II synchrotron, Berlin [71]. Synchrotron radiation with a high flux density is produced using an elliptical undulator insertion device which can induce linear or circular polarisation. The light is guided by a series of vertical/horizontal focusing mirrors into a plane grating monochromator (PGM) which allows a range of energies from 100 eV to 700 eV to be selected. After passing through the PGM exit slit, the beam is focused onto the sample by a final X-ray mirror to produce a spot size of 10 µm (horizontal) × 5 µm (vertical). The SMART instrument is capable of a lateral resolution of 2.6 nm (LEEM) and 18 nm (energy filtered XPEEM), as well as an energy resolution of 180 meV in XPEEM mode. More minute details of the two beamline end stations mentioned here can be found in reference [86] for ASTRID's SGM 3 and references [71, 72] for BESSYII's UE49 PGM SMART.

Fundamentals of Synchrotron Radiation

In the first instance, charged particles emit electromagnetic radiation when accelerated, as the electric field manifested by the charge undergoes perturbations which radiate outwards at the speed of light. Radiation emitted from television and radio antennae is produced in this way, as the electrons in the metal are oscillated at a given frequency to generate the carrier wave for the signal. Free electrons in an particle accelerator will also emit radiation and continuous acceleration, like that experienced along a circular orbit, will result in continuous emission of radiation, as shown in figure 3.6. When the electron

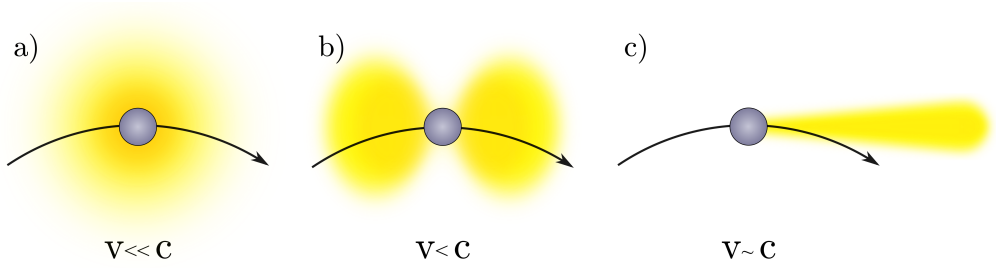

Figure 3.6. Electrons moving in a magnetic field (into the page) emit radiation due to their acceleration. The radiation distribution is **(a)** isotropic when $v << c$, **(b)** a dipole when v is some fraction of c, and **(c)** entirely focused forward when $v \sim c$, i.e. at relativistic speeds. This is known as 'synchrotron radiation'.

velocities are much smaller than the speed of light ($v << c$), this radiation is emitted isotropically. Electrons moving at some small fraction of the speed of light ($v < c$) will emit radiation in a toroidal distribution along the axis of movement, i.e. tangential to the electron orbit. As the electrons begin to move at relativistic speeds ($v \sim c$), the emitted radiation radiates in a narrow cone in front of electron pointing tangentially to the path of motion, like a sweeping spotlight. The angular divergence θ of synchrotron radiation is inversely proportional to the dimensionless Lorentz factor γ such that

$$\theta \sim \gamma^{-1} = \frac{mc^2}{E_k} \tag{3.1}$$

where E_k is the kinetic energy of the electrons in the accelerator and mc^2 is the rest mass-energy of the electron equal to 511 keV. As the electrons turn into the line-of-sight of an observer on the tangent (i.e. the experimental end station), they will see a huge relativistic Doppler shift as the distance between the radiation wavefronts is relativistically compressed. In comparison, an observer at any other position in the electrons orbit will see the relativistic compression quickly reduce as the angle θ between the observers line-of-sight and the electron velocity factor becomes larger than $1/\gamma$.

3.3 *In-situ* Surface Processing

3.3.1 Sample Heating

In the home laboratory, both the analysis and preparation chambers have sample stages for holding samples during *in-situ* processing or measurements. Both sample stages have integrated Boralectric heaters capable of reaching temperatures of 1200 °C. Boralectric ceramic heater stages consist of a pyrolytic graphite filament encased within a pyrolytic boron nitride (pBN) shell, and produce heat by resistive heating up to a maximum current of 8 A. The pBN shell means the heaters are dielectric, chemically inert, and UHV compatible, although at temperatures above 900 °C, the chamber pressure increases rapidly as the pBN begins to significantly outgas hydrogen. The Boralectric heaters have a fast heating rate, and are capable of reaching 1000 °C in less than 15 s. Practically however, sample and heater stage outgassing almost always restricts the heating rate as the chamber pressures should not exceed 10^{-7} mbar. Cooling rates at high temperature are rapid, which is important for quenching catalytic reactions and thermally-driven chemical processes, however cooling rates below 250 °C are very slow, often requiring in excess of 30 min to reach an acceptable measurement temperature.

3.3.2 Knudsen Cell for Metal Deposition

A simple home-made Knudsen cell (K-cell), similar to the one illustrated in figure 3.7, was utilised to deposit pure iron onto samples *in vacuo*. The basic design consists of three components: the electrical feed-through, the cooling jacket, and the Knudsen effusion cell. An extra conflat port allows the cell to be pumped down separately behind a vacuum gate valve, thus allowing the K-cell to be moved between multiple UHV chambers as required. The effusion

cell itself consists of an alumina (Al_2O_3) ceramic crucible which is heated by a tantalum wire filament. The filament array wraps around the crucible in a raster-like pattern with each section of the wire electrically isolated from its neighbour by twin-bore alumina ceramics. Typically one of these ceramics is reserved for a K-type thermocouple, the junction of which is placed in contact with the crucible to provide an internal temperature monitor. The effusion cell is wrapped in a stainless steel or tantalum shroud to hold it together, provide some collimation to the material beam, and function as a radiative heat shield. The cell is supported by a stainless steel threaded rod attached to a CF40 electrical feed-through, and the tantalum filament is spot-welded directly to the feed-through. If carefully constructed, the completed K-cell should register a resistance of $\sim 3\,\Omega$ on the atmosphere side of the feed-through.

Once a K-cell is mounted in UHV, it will typically need conditioning and calibrating before regular use can occur. A brand new or recently vented K-cell

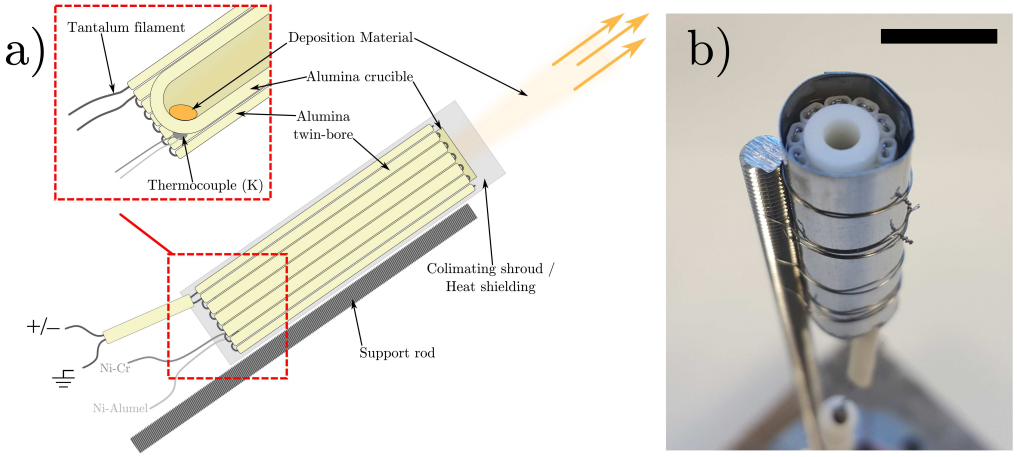

Figure 3.7. A homemade Knudsen cell. **a)** a simplified schematic of a K-cell highlighting the key features. The red outlined inset shows a cutaway of the bottom of the alumina crucible. **b)** a photograph of a completed K-cell. The black scale bar is equal to 10 mm (in-focus).

will require baking at 120 °C whilst the filament is hot to drive off water and other atmospheric containments from the K-cell components and surrounding vacuum port. In the case of iron and other oxide forming metals, several deposition cycles are also required to fully remove atmospheric contaminants before high purity deposition can be achieved. A bakeout is usually sufficient to obtain high purity deposition from a K-cell, but a cooling jacket can also be utilised if the filament is expected to be operated near high-temperature incompatible components, such as Viton gasket seals in a gate valve. During operation of a well-baked metal-depositing K-cell, the chamber pressure should not exceed 10^{-9} mbar.

3.4 Hemispherical Photoelectron Analyser

Electrons have proven to be an outstanding analysis tool due to their strong interaction with matter and, most importantly, they are easy to manipulate and detect experimentally. Energy analysis of charged particles can be achieved by many methods, including resonant collision phenomena, time-of-flight measurements, retardation by a potential gradient, and dispersion in a deflecting electric field [87]. Photoelectron spectroscopy analysers have used the latter two principles in various designs and geometries from toroidal deflection analysers, plane and cylindrical mirror analysers, and hemispherical analysers. For this work, hemispherical analysers (HSAs) were exclusively used; as stated in section 3.1, the Aberystwyth UHV system utilises a SPECS PHOIBOS 100 hemispherical analyser [88] for XPS/UPS studies. Figure 3.8 shows the design of an HSA and the typical path that electrons take through the analyser to the detector. The photoelectrons pass through three key components of the analyser on their way to detection: the lens system, the deflection hemispheres, and the

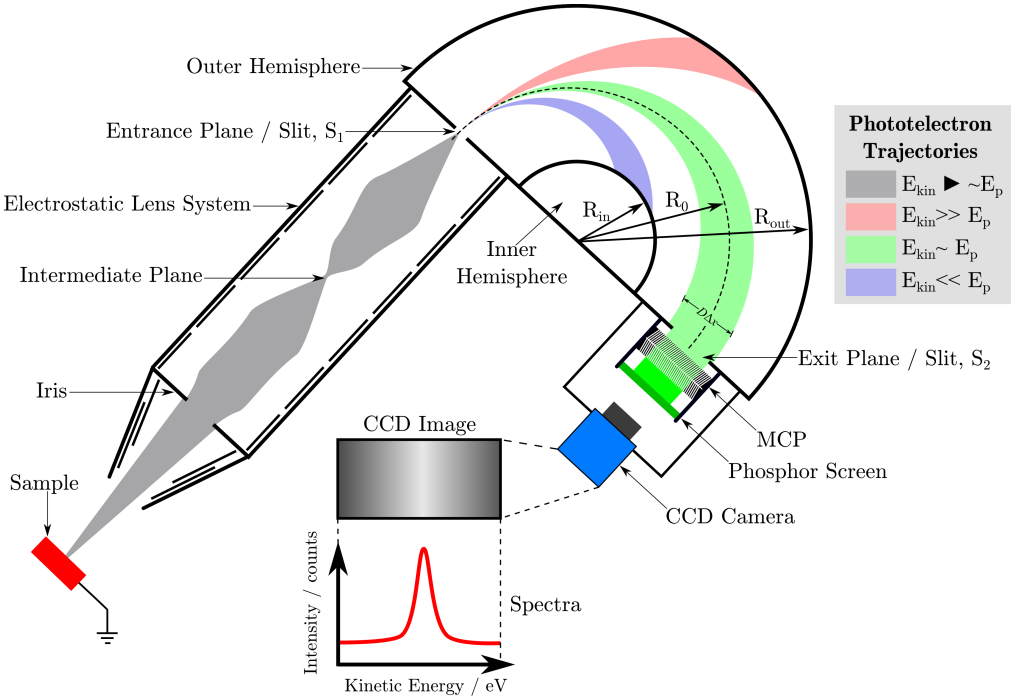

Figure 3.8. A simplified schematic of a HSA with photoelectron trajectories from the sample to the detector array. Photoelectrons with kinetic energies near the pass energy E_p will make it past S_2 into the detector array, whereas photoelectrons with much higher or lower energies approach the outer or inner hemispheres respectively.

detector. The lens system consists of an array of electrostatic lenses which alter the path of photoelectrons travelling toward the deflection hemispheres. These lenses are responsible for: defining the analysis area and solid acceptance angle on the sample; imaging the sample plane on the hemisphere's entrance slit S_1; and most importantly, retarding or accelerating the photoelectrons to the pass energy E_p before they enter the deflection hemispheres. The lens system can be operated in various modes depending on the sample and required analysis. For example when measuring low kinetic energy electrons during UPS, the lens system can be set to an acceleration mode which accelerates the photoelectrons in the first section of the lens system to avoid disturbance by stray magnetic fields and increase overall count rate.

After the lens system, the photoelectrons pass through S_1 into the deflection hemispheres. The SPECS PHOIBOS 100 has a mean radius R_0 of 100 mm on which the entrance slit S_1 and exit window S_2 are centred. The inner R_{in} and outer R_{out} hemispheres have a radius of 75 mm and 125 mm respectively. A fixed electric field gradient is applied between the outer and inner hemispheres which causes the photoelectrons entering through S_1 to disperse as they travel around the hemispheres. Photoelectrons with a lower kinetic energy move toward the inner hemisphere whereas those with a higher kinetic energy move toward the outer hemisphere. Any photoelectrons with kinetic energies equal to the nominal pass energy E_p will travel around the hemispheres in a circular path with radius equal to R_0. The pass energy E_p is calculated using:

$$E_p = -ek\Delta V \tag{3.2}$$

where e is the elementary charge, ΔV is the electric potential across the two hemispheres, and k is the analyser calibration constant where

$$k = \frac{R_{in}R_{out}}{2R_0(R_{out} - R_{in})} = 0.9375. \tag{3.3}$$

The pass energy is an important parameter to consider when acquiring a spectrum as it has a direct effect on the energy resolution and intensity of the photoelectrons measured at S_2. A larger pass energy heralds a greater transmission of photoelectrons but energy resolution suffers; a survey scan benefits from a larger pass energy where peak identification and intensity are required. On the other hand, a smaller pass energy improves energy resolution at the expense of reduced transmission; core level analysis uses smaller pass energies so that multiple components in a core level peak can be resolved. The

ultimate energy resolution $\Delta E_{analyser}$ (or FWHM) of transmitted photoelectron intensity measured at S_2 is given by:

$$\Delta E_{analyser} = E_p \left(\frac{W_1 + W_2}{4R_0} + \frac{\alpha^2}{4} \right) \tag{3.4}$$

where W_1 and W_2 are widths in the energy dispersive direction of S_1 and S_2 respectively, and α is the half-angle dispersion of the photoelectron beam at S_1. The pass energy can either be fixed or variable depending on whether the analyser is being operated in Fixed Analyser Transmission (FAT) mode or Fixed Retard Ratio (FRR) mode. In FAT mode, the pass energy is fixed, which according to equation 3.4 means that the analyser resolution is independent of kinetic energy. Conversely in FRR mode, the pass energy is varied so that all photoelectrons are decelerated by a fixed ratio with respect to their kinetic energies, meaning energy resolution decreases with increasing kinetic energy. The chosen mode also changes the transmission function of the spectrometer, i.e. the efficiency at which the analyser transfers photoelectrons with differing kinetic energies to the detector. For SPECS analysers, the transmission function roughly obeys the following rules (with a $E_k^{-0.7}$ correction factor to account for the energy dependent escape depth of photoelectrons from the sample): in FAT mode, the photoelectron intensity is proportional to ${E_k}^{-1}$ [89] whereas in FRR mode the intensity is directly proportional to E_k [90]. For Auger emission spectroscopy (AES), the FRR mode is preferable because the intensity from lower kinetic energy electrons is approximately equal to the higher kinetic energy electrons. However for this work which predominately used XPS/UPS, it was necessary to maintain the same energy resolution across all measured photoelectron features and therefore FAT mode was exclusively used.

When the photoelectrons arrive at the exit window S_2, they have an energy dispersion ΔE_k in the energy dispersive plane and, depending on the lens mode used, a real-space or angular dispersion in the orthogonal plane. A photoelectron's energy deviation from E_p is determined as a function of lateral position Δx with respect to the S_2 centre such that

$$\Delta E_k = D\Delta x \tag{3.5}$$

where D is the dispersion factor in $\mathrm{eV\,mm^{-1}}$ (or eV per pixel in the case of CCDs). The photoelectrons then pass through the exit window S_2 and enter the detector array. The methods of photoelectron detection have advanced drastically since the first spectrometers thanks to the invention of three key technologies: the position sensitive detector (PSD), the charge-coupled device (CCD) image sensor, and the micro-channel plate (MCP). Before these advancements, photoelectron analysers typically had an exit window with a single electron multiplier tube (or channeltron) mounted behind it. This means that the analyser voltages were scanned such that only photoelectrons of a given energy (i.e. the pass energy E_p) will traverse the deflection hemispheres and reach the channeltron at a given time. It was quickly realised that this method is highly inefficient because photoelectrons that do not have kinetic energies equal to E_p are lost at the exit window, despite the fact their kinetic energies are known according to equation 3.5. Manufacturers began increasing the number of channeltrons either side of the first in order to capture more of the energy dispersion. Some manufacturers still offer this design of detector, for example the SPECS PHOIBOS analyser can be equipped with five or nine channeltrons across the dispersive plane of the analyser [91]. Single channel detectors can only acquire photoelectrons from $\sim$7 % of the available energy window at any

one time, whereas PSDs can sample at least 80 % of the energy dispersion, heralding an order of magnitude improvement [92].

PSDs are able to spatially resolve the electron dispersion at the exit window both in the energy [93] and non-energy dispersive directions [94]; they allow for 2-dimensional detection. PSDs which exclusively measure along the energy dispersion direction typically consist of discrete channels connected to a discriminator and electron counting hardware. In this geometry, greater resolution of the photoelectron dispersion is achieved by increasing the number of channels across the acquisition window. The issues of cross-talk, noise, and hardware geometry have largely been solved by researchers from the Aberystwyth Physics Department and collaborators [95–97]. Whilst 2-dimensional PSDs are possible, a far more simple solution relies on an indirect method of counting electrons. Photoelectrons passing through S_2 can be converted into photons using a phosphorescent screen and recording the light intensity using a CCD camera.

The CCD was invented by Boyle and Smith in 1969 who then published a paper on the concept in 1970 [98]. The CCD was then experimentally verified by Amelio *et al.* shortly after [99]. The subsequent impact that CCDs had to industries and academia that relied on imaging cannot be understated. A CCD consists of an array of Metal-Oxide-Semiconductor (MOS) capacitors which are photosensitive and therefore generate charge (by electron-hole generation) proportional to the number of impinging photons, i.e. the intensity. Once the capacitors have been exposed to a light array, a shift register is used to transfer the charge packets along their respective rows into their neighbouring capacitors. Charge packets at the end of the rows are transferred into a perpendicular capacitor column which then passes the charge packets into an amplifier and

are then converted into a digital signal. This process, often referred to as a 'bucket brigade', is repeated until all the charge packets in the array have been measured, indexed, and converted into an image file. The phosphor screen and CCD configuration is capable of 2-dimensional measurement. The number of channels in the energy dispersive direction (and hence the resolving power) is significantly increased as it is dependent on the number of pixels on the CCD (see equation 3.5). The PixelFly CCD camera on the Aberystwyth PHOIBOS analyser has a window size of 500×500 pixels. Most importantly, it has a large dynamic range which means strong and weak photoelectron signals can be captured in the same acquisition without the weaker signal being lost in the noise.

The number of photoelectrons generated at the sample is usually quite low and so applying some gain to the signal is necessary. Amplification of the CCD output is not possible as this will increase the background noise as well. Using the same process as the channeltron, the number of electrons reaching the phosphor screen can be increased by using a chevron (or V-stack) MCP. An MCP consists of a 2 mm thick plate with a densely-packed array of channel electron multiplier (CEM) tubes which are parallel to each other but angled $\sim 8\,\%$ with respect to the plate. The plate itself is usually made from a highly resistive material which is then treated to produce a surface which can generate a large number of secondary electrons. The microchannel surfaces must also be semiconducting enough that a large voltage ($\sim$1.5 kV to 2 kV) will compensate the lost electrons. As energy dispersed photoelectrons from the deflection hemisphere enter the CEMs, they collide with the walls and generate a cloud of secondary electrons that cause a cascading effect. The gain of a single MCP is limited between 10^3 and 10^4 due to the ion feedback phenomenon where ionised residual gas particles

and adsorbates are accelerated toward the input side of the MCP, therefore causing another cascade event. These secondary electron cascades disturb the measurement and can lead to a permanent glow-discharge effect which destroys the MCP over time. In the chevron configuration, two MCPs are placed back-to-back with their CEM tubes angled in opposite directions, such that the tilt angle is 0°. This configuration acts as an ion trap which considerably reduces the effects of ion feedback and boosts the electron multiplication factor range to between 10^6 and 10^7 per stack, with individual CEM tubes being charge compensated in less than 100 ps [100]. Furthermore, this configuration preserves spatial distribution of photoelectrons (in both the energy dispersive and non-energy dispersive directions) before they collide with the phosphor screen.

The Aberystwyth PHOIBOS 100 analyser is versatile thanks to its sophisticated transfer lens system and MCP-Phosphor-CCD detector which is capable of acquiring photoemission information in the non-energy axis. In a normal transmission lens mode, the non-energy axis is simply a real-space image of the z-axis on the sample, which is useful for alignment of the sample or minimisation of photoelectron contributions from different materials along that axis. In an angular lens mode, the azimuthal angle φ that a photoelectron leaves the sample is preserved. As briefly mentioned in section 2.2.1, this angular information is directly related to the electrons parallel momentum vector whilst bound in the sample and therefore band structures can be directly observed on the CCD image. By altering the samples polar angle ϑ and recording the CCD images (which are a function of $I(E_k, \varphi)$), a 3-dimensional dataset representing the full band structure of the sample can be produced.

Chapter 4

Materials

4.1 Diamond

The metastable crystalline form of carbon at standard pressure and temperature is diamond, which is characterised by its tetrahedral structure formed by sp^3 hybridised bonding. This structure, shown in figure 4.1, forms a face-centred cubic (fcc) lattice with a basis of two atoms at each lattice point: $(0, 0, 0)$ and $(1/4, 1/4, 1/4)$. At room temperature, the diamond lattice constant α_0 is 3.57 Å and from this the C−C bond length of 1.54 Å is exactly a quarter of the diamond unit cell diagonal. Diamond's highly symmetrical structure and strong covalent bonding gives rise to many exceptional properties that have attracted a large research interest from academic institutions and industry alike. Some of these properties have been detailed in table 4.1. Diamond can form naturally through the high pressures and temperatures found in the Earth's lithosphere, or it can be synthesised in the lab using either high-pressure high-temperature (HPHT) or chemical vapour deposition (CVD) techniques. With synthetic techniques, it is possible to selectively dope diamond with other elements such as boron, which is an electron acceptor making boron-doped diamond (BDD) p-type.

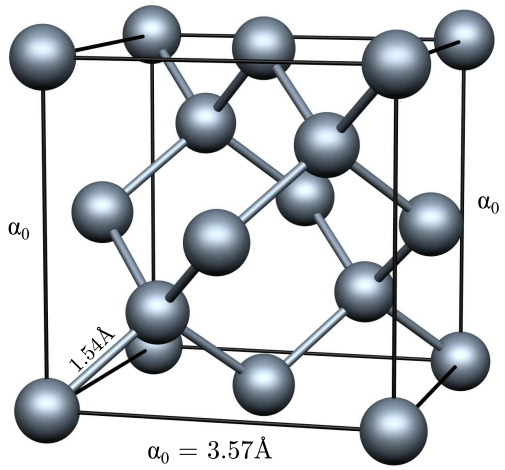

Figure 4.1. The unit cell of bulk diamond.

Highest known mechanical hardness (∼90 GPa)
Highest bulk modulus ($1.2 \times 10^{12}\,\mathrm{N\,m^{-2}}$)
Lowest compressibility ($8.3 \times 10^{-13}\,\mathrm{m^2\,N^{-1}}$)
Highest room temperature thermal conductivity ($2000\,\mathrm{W\,m^{-1}\,K^{-1}}$)
Low linear thermal expansion coefficient at room temperature ($1 \times 10^{-6}\,\mathrm{K^{-1}}$)
Very wide optical transmission window 0.3 µm to 2.5 µm; 7 µm to 100 µm
Very wide band gap (5.48 eV); Excellent electrical insulator ($10^{13}\,\Omega\,\mathrm{m}$)
Biologically inert and compatible; Very resistant to chemical corrosion
Some surfaces exhibit negative electron affinity under hydrogen termination
Metallic conductivity at high boron doping concentrations ($>10^{20}\,\mathrm{cm^{-3}}$)

Table 4.1. A short list of diamond's exceptional properties [102]

Whilst pure diamond is typically an insulator with a band gap of 5.48 eV, at high concentrations of boron doping (i.e. $>10^{20}\,\mathrm{cm^{-3}}$), it can exhibit metallic electrical conductivity [101].

4.1.1 Diamond Synthesis

Natural gemstone diamonds are often described according to the modern Gemological Institute of America grading system, 'The 4Cs' (i.e. clarity, carat, colour, and cut), with other countries and conglomerates using some variation of this system. However the GIA's grading system is purely an

aesthetic one and does not consider impurities at the atomic level in the carbon lattice. Diamonds fall into one of five classifications, which are an indication of the main atomic dopant and in what form it manifests. The first attempts of diamond classification by Robertson *et al.* noted the difference between diamonds that absorbed in the infrared and ultraviolet regions of radiation (Type I; "majority"), and those that did not (Type II; "transparent"). Type I diamonds are characterised by their nitrogen impurities, usually to an upper limit of ∼0.3 at%, whereas Type II diamonds have no measureable nitrogen defects. [103]. Type I and II have been further subdivided based on absorption and phosphorescence spectra respectively. Clark *et al.* showed that Type I diamonds demonstrate distinct infra-red absorption spectra depending on whether nitrogen in the lattice is clustered into large even-numbered aggregates (Type IaA) or nitrogen pairs (Type IaB) [104]. J. F. H. Custers was the first to observe differences in the UV-induced phosphorescence of Type II diamonds. Diamonds with significant boron doping exhibited phosphorescence and high conductivity when illuminated by UV radiation (Type IIb), whereas diamonds with little-to-no defects (Type IIa) did not exhibit this behaviour [105]. Type IIb diamonds are now almost exclusively boron-doped, as boron was identified as the only viable acceptor centre in diamond that imparts semi-conductivity [106]. Table 4.2 summarises the four modern classifications of natural diamond. Excluding diamond formation from meteorite strikes and extraterrestrial sources, the conditions required for natural diamond formation

Type	Description	Natural Occurrence
Ia	Significant nitrogen content, nitrogen pairs (IaA) or clusters (IaB)	Common (95 %)
Ib	Low nitrogen content (ppm), single substitutional defects	Very Rare (0.1 %)
IIa	Undetectable nitrogen, devoid of impurities	Rare (1 % to 2 %)
IIb	Significant boron content; semiconducting	Extremely Rare (<0.1 %)

Table 4.2. A summary of the modern classification of natural diamonds.

only exist deep in the Earth's crust. The minimum conditions of diamond formation occur at depths exceeding 150 km where temperatures above 950 °C and pressures above 4.5 GPa are typical, with large terrestrial diamonds forming in continental geotherms between 38 mW m^{-2} to 42 mW m^{-2} over billions of years [107, 108]. Contrary to popular belief, diamonds do not form from coal. The current consensus agrees that an undefined mobile liquid melt containing oxygen, hydrogen, nitrogen, sulphur, and of course a majority of sp^2-bonded carbon is the precursor material in diamond formation [109]. Molten transition metals such as Cr, Mn, Fe, Co and Ni react with carbon, catalytically converting the basal planes of graphite into numerous nucleation sites for diamond growth [110]. The UHV reverse process of this catalytic reaction is demonstrated later in this work (see chapter 6). In recent history, the demand for diamond in industrial processes has outstripped the natural supply, and underpinned the necessity to produce synthetic diamond. The first synthetic diamonds were produced in the 1950s by General Electric using the high-pressure high-temperature (HPHT) technique that mimics and accelerates the natural formation process. A graphite precursor is placed into a cell with a mixture of transition metal catalysts, and then subjected to extremely high temperatures (∼between 1300 °C to 1500 °C) and pressures (5 GPa to 6 GPa). Figure 4.2 shows the carbon phase diagram of pressure against temperature. The red line is known as the Berman-Simon line and delineates the regions where diamond and graphite are stable or metastable [111, 112]. During HPHT synthesis, the pressure and temperature is selected such that diamond becomes the stable form of carbon at equilibrium, and therefore diamond crystals are formed. As pressure and temperature is reduced post-growth, graphite becomes the stable form again, but the diamond does not re-convert because it is metastable in this regime [113]. The HPHT method has largely been used to produce small grit diamond for use in abrasives, drilling, and

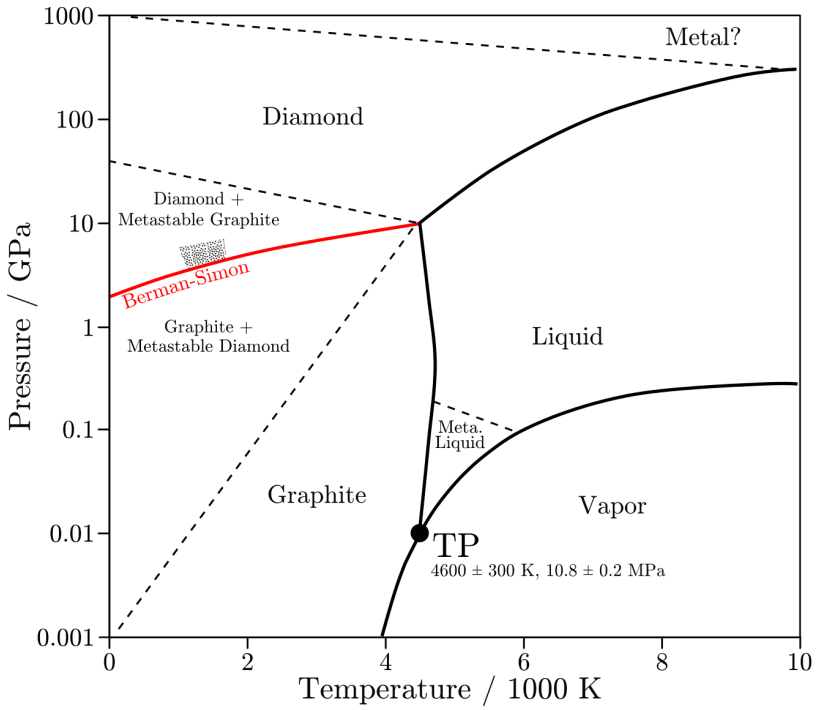

Figure 4.2. Pressure vs. temperature phase diagram for elemental carbon. The region of interest for catalytic HPHT synthesis (dotted region) exists just above the Berman-Simon line between 1300 °C and 1500 °C. Adapted from [113].

polishing as their small size increases their hardness as per the Hall-Petch effect [114, 115]. The modern HPHT technique has more variation, growth conditions, precursors, and catalyst mixtures allowing control over diamond shape (cuboid to octahedral) [116], nitrogen and boron doping level [117], and especially size. As of writing, type IIa diamonds larger than 10 carats have been synthesised using the HPHT technique [118].

Soon after HPHT synthesis was first demonstrated, researchers were also attempting to crystallise diamond from gas phase precursors in a low pressure environment, a process known as chemical vapour deposition (CVD). The first successful CVD deposition of diamond (co-deposited with graphite) was reported in 1962 by W. G. Eversole [119], although it wasn't until the early 1980s that CVD diamond research began in earnest. In 1982, S. Matsumoto and M.

Kamo published their work with a precise growth recipe and apparatus set-up for depositing diamond films on heated silicon substrates (900 °C) using a 30 Torr 1 % CH_4 in H_2 gas precursor [120, 121]. They used the two dominant types of CVD now used in modern diamond synthesis, which are defined by how they activate the gaseous reactants in the precursor: hot filament CVD and microwave plasma-activated CVD (MPCVD). As more groups attempted to grow diamond via CVD, a plethora of growth recipes were reported in the literature. In 1991, Peter Bachmann compiled the results of over 70 diamond growth experiments on carbon-hydrogen-oxygen composition diagram [122, 123], shown in figure 4.3. The Bachmann diagram predicted which precursor gas mixtures would result in diamond growth, and several further studies confirmed its validity and refined the diamond growth region [124, 125]. The main conclusion of the diagram is that the identity of the precursor gases is unimportant but rather the C:H:O ratio of its component elements. Furthermore, oxygen is not essential for diamond growth as evidenced by the diamond growth region extending to C:H edge (see the star symbol in figure 4.3).

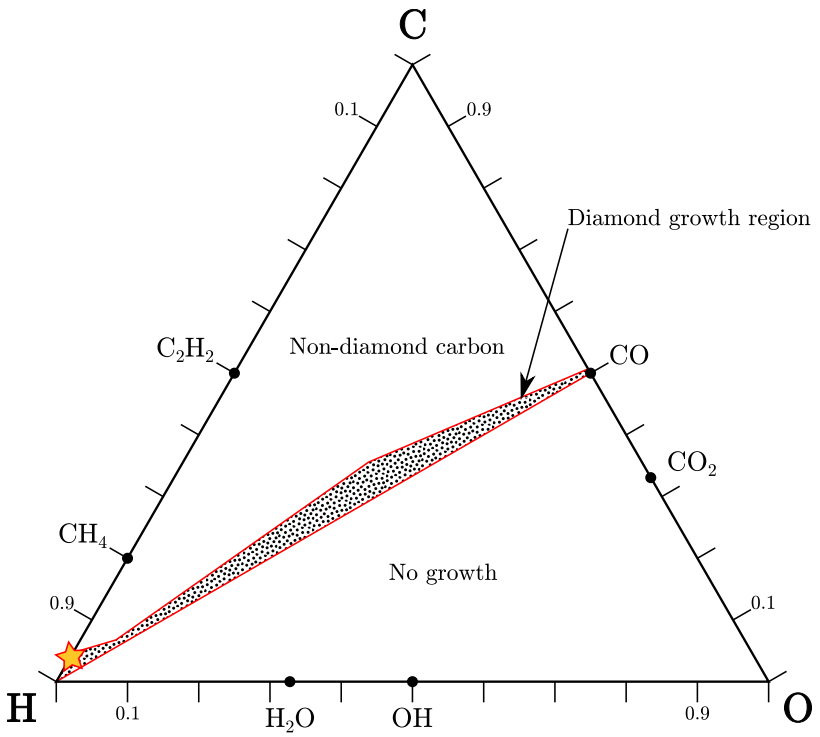

Figure 4.3. The Bachmann diagram (C:H:O ratio plot) of CVD diamond synthesis. The dotted region shows where diamond growth will occur. The star represents the typical CVD diamond growth conditions of 1–3 % CH_4 in H_2. Adapted from [122, 123].

The 'standard model' of diamond CVD growth developed throughout the 1980s and 1990s and now used by academic and industrial research groups is described herein [126, 127]: The diamond surface is stabilised by adsorption of hydrogen to all available bonding sites, preventing the surface from reconstructing or graphitising, although the substrate temperature is typically too low for either of these processes to occur (i.e. <900 °C). A hot filament or microwave source is used to dissociate molecular hydrogen in atoms which in turn reacts with the precursor carbon species (e.g. CH_4) to produce a mixture of hydrocarbon species and reactive carbon-containing radicals (e.g. C_2H_2, $^{\cdot}CH_3$, $^{\cdot}CH_2$, $^{\cdot}C$, etc). The atomic hydrogen also removes hydrogen bonded to the diamond surface, hence producing radical sites. Occasionally and less frequently than hydrogen

re-adsorption, carbon-containing radicals (e.g. $^{\cdot}CH_3$) in the gas phase adsorb onto these surface sites and, due to the substrate temperature, migrate toward step edges or another carbon adsorbate. Further hydrogen abstraction from the adsorbed carbon species allows neighbouring sites to cross-link, converting them from sp^2 to sp^3-bonded carbon, and therefore expanding the carbon lattice. This growth method, where two adsorbed molecules can migrate and react with each other on the surface of a material, is described by the Langmuir-Hinshelwood kinetic theory [128, 129]. Diamond nucleates as small clusters which then expand into isolated islands as migrating CH_3 groups bond to the step-edges of these islands. Eventually, the islands merge to form a continuous perfect diamond layer, assuming of course that a defect does not arise. The $\langle 111 \rangle$ and $\langle 001 \rangle$ surfaces are the principle growth faces during CVD of diamond; they are the slowest growing faces during the CVD and HPHT processes and so remain after the other faces have grown themselves out of existence [130].

4.1.2 Doped Diamond

With a band gap of $\sim$5.48 eV for intrinsic diamond, it is impossible to thermionically promote an electron from the valence band to the conduction band at room temperatures, so diamond is well and truly an electrical insulator. However among the plethora of applications that diamonds have been considered for, the potential for electronic devices is of great interest. Assuming a single crystal CVD growth, diamond's high thermal conductivity, high dielectric breakdown field ($>10\,\mathrm{MV\,cm^{-1}}$), and high electron/hole mobilities at room temperature of any wide band gap material, make it an attractive candidate for high-power high-frequency electronics or where high temperatures and high voltages are required. Dopant atoms which have a higher atomic number than carbon, such as nitrogen, generate donor levels in the band gap (i.e. n-type,

provides negative charge carriers – electrons), whereas atoms with a lower atomic number, such as boron, generate an acceptor level (i.e. p-type, provides positive charge carriers – holes). If the donor/acceptor level is close enough in energy to the conduction/valance band for thermal promotion of a charge carrier, then electron conduction can take place. As mentioned earlier (see section 4.1.1), diamonds are classified based on whether they contain significant amounts of nitrogen or boron. The nitrogen donor level is $\sim$1.7 eV below the conduction band, which is too deep in the band gap for charge carrier promotion to occur and so type I diamonds fail as a potential semiconductor device material [131]. Other dopant atoms have been proposed for n-type doping of diamond (phosphorous [132], sulphur [133], arsenic [134], to name a few), but the larger size of these atoms make incorporation into the diamond lattice during CVD challenging. Unfortunately as of writing, obtaining a viable n-type diamond material still remains a 'holy grail' of diamond electronics research. On the other hand, boron-doped diamond has demonstrated p-type semi-conducting properties with an acceptor state $\sim$369 meV above the valence band maximum [106]. Nowadays, growth of synthetic p-type diamond is routine and well understood. The mechanism of electrical conduction in boron-doped diamond can be explained using the Mott model of hopping conduction [135] until the the boron concentration in the diamond lattice exceeds $\sim 4.5 \times 10^{20}\,\mathrm{cm}^{-3}$ (i.e. the critical Metal-Insulator-Transition (MIT) concentration, n_c). At this point, a boron impurity band is formed in the diamond band gap allowing boron-doped diamond (BDD) to exhibit metallic conductivity [136, 137]. Visually, the diamond will also turn from a deep blue colour to black in appearance. Despite having fewer charge carriers than true metals, BDD is still a sought after material in many applications. For example in the field of electro-chemistry, its wide solvent window, electrochemical reversibility, and reduced fouling make

it a robust electrochemical electrode that can survive in extreme environments (e.g. high temperatures, high pressures, hazardous chemicals, etc) [138, 139]. Above a critical boron-doping level close to the MIT n_c, the diamond can be described as heavily boron-doped diamond (HBDD) and begins to exhibit superconductivity [140] that agrees with the Bardeen-Cooper-Schrieffer (BCS) mechanism [141]. Initial experimental studies demonstrated a superconducting transition temperature T_c of 4 K, with no resistivity measured at 2.3 K. This effect is stable in magnetic fields up to 3.4 T [142], and T_c was also found to increase with higher boron doping concentration depending on the orientation of the diamond film being studied. The T_c of (001) diamond films plateaus out at 4 K, whereas (111) films have demonstrated a continuous increase up to the maximum observed T_c of 10 K [143]. Very heavily boron-doped superconducting diamonds are of particular interest in this work for their potential to produce boron-doped graphene or graphitic structures.

4.2 Diamond Surfaces

A surface is defined as the discontinuity of a condensed phase of matter and the beginning of the surrounding environment, or 'free space', that separates one substance from another. In crystals this deviation from the bulk periodicity at the surface results in new electronic states which bind the crystal's electrons from entering free space without some considerable extrinsic energy input, e.g. an incident photon. The surface atoms of a material will readily interact with external reagents if they possess electrons available for bonding, thus forming surface 'terminating' species or they will reorganise into more favourable positions if the conditions allow; a process called 'reconstruction'. The termination and reconstruction of a material's surface can drastically alter

the properties of the surface with respect to the bulk. In this section, the physics and chemistry of the (111) diamond surface will be explored with respect to its structure (notably the reconstruction) and electronic properties.

4.2.1 The $(111)(1 \times 1)$ Surface

Carbon atoms in the [111]-orientated bulk diamond are terminated by either one bond or three bonds either side of the (111) plane. The natural cleavage plane and most stable (1×1) surface only has one dangling bond [144] as shown in figure 4.4 which is terminated by a single hydrogen or oxygen species. The atomic spacing of the surface atoms with respect to the bulk lattice constant is $\alpha_0/\sqrt{2} = 2.52\,\text{Å}$, which is same for the (100) surface as well. Looking along the [111] direction, the surface atoms form a corrugated hexagonal pattern with alternating surface and sub-surface atoms. The topmost layer of atoms have the surface bond which can accept adsorbates. This surface structure is nearly identical to graphene with only a 2.5 % lattice mismatch between the allotropes, which goes some way to explain why the (111) surface has a higher susceptibility to graphitisation compared to the lower-index surfaces. The band structure of the (111) surface is straight-forward and lacks any occupied surface states in the band gap for both the oxygen and hydrogen terminated surfaces [145]. Theory predicts that surface carbon-hydrogen bonds with a length of 1.12 Å produce occupied bonding states deep in the valence band, $\sim$4 eV below the valence band maximum. Photoemission data equally shows no occupied surface states in the band gap in support of the theoretical data. It would seem that the (111) diamond surface is electronically inactive, however hydrogen-termination does results in a negative electron affinity (NEA) which is unique among organic semiconductors [146]. In solid state physics, NEA occurs when the vacuum energy level is lower in energy than the conduction band minimum by some

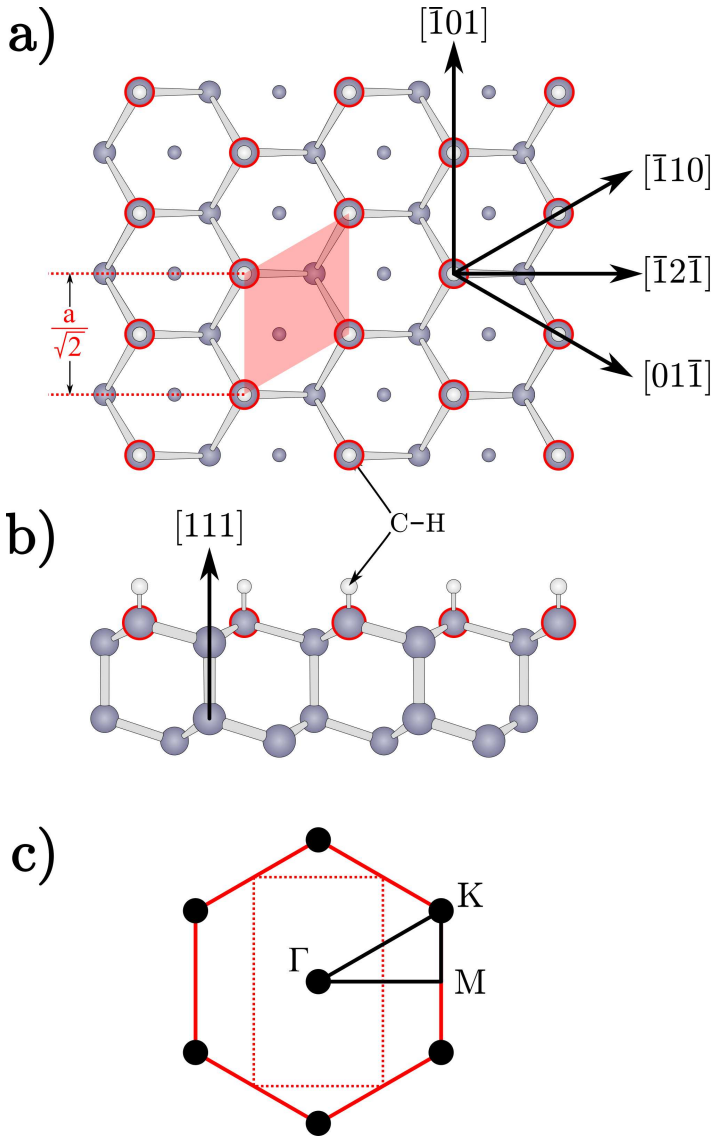

Figure 4.4. The real-space hydrogen-terminated (111)(1×1) diamond surface looking down the **(a)** [111] direction (topdown) and along the **(b)** [$\bar{1}$01] direction (side). Each double layer of atoms forms a corrogated hexagonal sheet seperated by bonds aligned in the [111] direction. The surface atoms are highlighted in red and are bonded to a single hydrogen atom which stabilises the surface and prevents reconstruction. The red-shaped region in **(a)** denotes the surface unit cell. **(c)** shows the reciprocal space (red line) and reduced brillouin zone (black line), along with principle lattice points that have a high degree of symmetry. The red dashed line indicates one domain of the (2×1) reconstruction's brillouin zone (see figure 4.5).

value χ, meaning that electrons in the conduction band encounter no barrier to the vacuum and can be emitted from the material. In contrast to conventional semiconductor elements, carbon is more electronegative than hydrogen which produces an electric dipole at the surface, lowering the barrier to emission. Hydrogen-terminated diamond surfaces have a much lower electron affinity, with NEA manifesting when a high proportion of hydrogenation is achieved. Typically for a hydrogen-terminated $(111)(1 \times 1)$ diamond surface, $\chi = -1.3\,\text{eV}$ [147] whereas for oxygen-terminated surfaces (and reconstructed surfaces), χ can range between 0.35 eV and 3.6 eV [148, 149]. On the other hand adsorbates with a large electronegativity compared to carbon, such as oxygen and fluorine, increase the electron affinity. The NEA of hydrogen-terminated diamond results in an increased electron emission from the conduction band into vacuum, which can be qualitatively observed in UPS as an increase in the secondary electron yield, and quantitatively as a widening of the spectral width.

4.2.2 The $(111)(2 \times 1)$ Reconstruction

In the absence of stabilising terminating species, the $(111)(1\times1)$ diamond surface undergoes a complicated reconstruction, which today is known to be a (2×1) motif. The precise nature of the diamond $(111)(2 \times 1)$ reconstructed surface has been a longstanding topic of controversy dating back over 60 years. Many experimental and theoretical studies have been conducted on this system to date, mainly focusing on its structural and electronic properties. Early LEED studies of the diamond (111) surface were performed by Marsh and Farnsworth [150] and Lander and Morrison [151]. They found that the as-polished surface exhibits the expected (1×1) pattern, and annealing the surface results in half-order spots indicating a doubling of the surface periodicity. However they were unable to determine whether the surface structure was (2×2) or (2×1) from

these patterns [150, 151]; most of following literature quoted the reconstruction as $(2 \times 2)/(2 \times 1)$. Confirmation of the (2×1) surface was later shown using LEED by Derry *et al.* which showed a clear one domain reconstruction. Three (2×1) domains can be rotated by 120° with respect to each other to form an apparent (2×2) reconstruction in the LEED pattern [152]. The actual carbon atom arrangement of this reconstruction was still unknown and several models were submitted over the years based on LEED measurements, e.g. buckled [153], relaxed [151], and graphitic [154]. However, it was known early on that adsorbates played a role in the (111) surface reconstruction, with particular focus on hydrogen. Lander and Morrison were able to recover the (1×1) periodicity by heating the (2×1) surface in a hydrogen atmosphere, showing that hydrogenation of the (1×1) surface can occur [151]. Later, stimulated ion desorption and LEED experiments by Pate *et al.* and Hamza *et al.* showed that H^+ ions desorb at lower temperatures (830 °C) compared to the occurrence of the (2×1) LEED pattern (1000 °C) [155, 156]. Furthermore, whilst the (1×1) surface has a chemisorbed layer of hydrogen, the (2×1) is hydrogen-free which is confirmed by more modern theoretical calculations [157]. K. C. Pandey's seminal paper on the diamond (111) reconstruction was published in 1982 [158], following soon after his work on the (2×1) reconstruction of (111) silicon [159]. In these papers, Pandey introduced a new geometric model for the (2×1) reconstruction of (111) surfaces, first on Silicon, then on diamond. The Pandey-chain model is now the modern accepted structure for the diamond $(111)(2 \times 1)$ reconstruction, and is shown in figure 4.5. Upon the removal of terminating adsorbates, the (111) diamond surface reconstructs into chains of π-bonded dimers along the $[\bar{1}01]$ direction both in the topmost and second atomic layer (according to Pandey's original calculation). Reconstruction can occur in three main directions in real space rotated by 120° with respect to each other,

conforming to the mirror planes of the (111) surface: $[\bar{1}01]$, $[\bar{1}10]$, and $[01\bar{1}]$. The atomic spacing between carbon atoms along these chains is 1.43 Å which is near identical to that of graphite (1.425 Å). Out-of-plane dangling bonds of p-character are perpendicular to the surface and strongly interact to form π-bonds along the surface chains. The distance between parallel π-bonded chains (i.e. along the $[\bar{1}2\bar{1}]$) direction) is 4.37 Å, minimising the electron interaction between them and as a result, electron interaction is confined within the chains. Pandey's model superseded the previous proposed models largely because valence band calculations on the chain model matched the most recent ARPES data presented by Himpsel *et al.* [160]. In Himpsel's paper, he observed an energy band dispersion which shifted by approximately 1 eV toward the Fermi level in the ΓK direction in reciprocal space. Polarisation dependent photoemission showed that this surface state was fully symmetric [160]. Pandey's calculations showed that for a dimerised chain structure, no states are observed within 0.5 eV of the Fermi energy [159]. Several authors have reported experimental evidence for dimerised Pandey chains. Namba *et al.* [161] used combined UPS and electron energy loss spectroscopy (EELS) to show a 2 eV bandgap opening up along the JK direction in reciprocal space, a result which reproduced Pepper *et al.*'s previous EELS observation [162].

The first density functional theory (DFT) calculations on the $(111)(2 \times 1)$ diamond surface were first performed by Vanderbilt and Louie [163], which sought to determine the most energetically reconstructed surface. Several reconstructions were studied including competing chain models [164, 165], but Pandey's relaxed π-chain yielded the lowest surface energy, approximately 0.3 eV lower than the relaxed (1×1) surface, as well as conforming to the experimental ARUPS data. Furthermore, Vanderbilt and Louie's results suggested that the

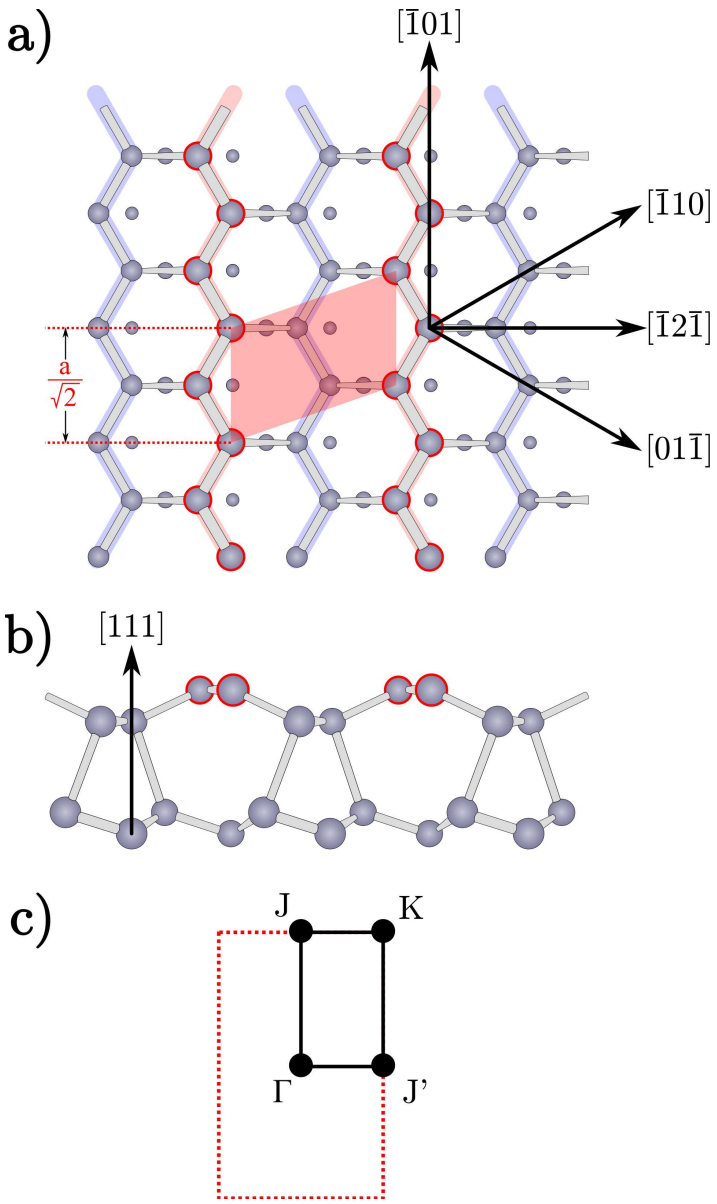

Figure 4.5. The real-space (111)(2 × 1) diamond surface looking down the **(a)** [111] direction (topdown) and along the **(b)** [$\bar{1}$01] direction (side). The first and second layers of atoms on the (111) surface reconstruct to form two parallel chains (highlighted in red and blue) offset in both the [111] (z) and [$\bar{1}2\bar{1}$] (y) directions. The bonds between these chains and the third layer of atoms are no longer parallel, and are angled with respect to the [111] direction. The clean reconstructed surface is stable and therefore has no stabilising adsorbates. The red-shaped region in **(a)** denotes the surface unit cell. **(c)** shows the reciprocal space (red dashed line) and reduced brillouin zone (black line), along with principle lattice points that have a high degree of symmetry.

(2×1) reconstruction was undimerised in contradiction to Pandey's original calculations; in fact dimerisation of the π-chain model resulted in higher surface energies. Agreement between experimental data and the theoretical calculations of the band structure of the (2×1) surface is currently mixed, and it is this disagreement that this work will seek to address with new theoretical and experimental data in chapter 5.

For ΓK, theoretical calculations using both the DFT formalism and first-order quasiparticle effects, predict a strong dispersion relation for both occupied and unoccupied bands. These studies all predict a (semi-)metallic surface with the occupied band rising above the Fermi level at K [166–169]. In contrast, experimental ARPES data from Graupner *et al.* demonstrates that the occupied surface states remains 0.5 eV below the Fermi level, meaning that a semi-conducting band gap of at least 0.5 eV is experimentally verified. In Graupner's report and in other results, photoemission intensity is observed right up to the Fermi level but because the intensity is weak and non-dispersing, it has not been attributed to the diamond surface but rather due to localised areas of graphitisation as a result of annealing [170].

4.3 Graphene

The stable crystalline allotrope of carbon is graphite, a material that consists of stacked sheets of sp^2-bonded carbon. Three valence electrons from each carbon atom are involved in covalent σ-bonding to three other carbon atoms, forming a two-dimensional hexagonal structure. The forth valence electron is de-localised and is thus free to migrate in the plane, giving rise to graphite's electrical conductivity. The σ-bond length is $\sim$1.42 Å, and the interplanar distance is

Extreme room temperature electron mobility ($2.5 \times 10^5\,\mathrm{cm^2\,V^{-1}\,s^{-1}}$)
Massless Dirac fermions + Ambipolar electric field effect
Ability to sustain extremely high densities of electric current ($10^6\times$ that of copper)
Extremely large Young's Modulus (1 TPa)
Highest known mechanical strength (130 GPa)
Extremely light ($\approx$0.77 mg m^{-2})
Highest theoretical thermal conductivity ($>$3000 W mK^{-1})
Significant absorbtion of white light ($\pi\alpha \approx 2.3\,\%$)
Reduced light absorption at saturation fluence
Impermeability to any gases
Can be readily chemically functionalised

Table 4.3. A short list of graphene's exceptional properties [2, 173]

3.35 Å as a result of weak van der Waals bonding. Single atomic layers of graphite have been explored as early as 1947 [171], but were largely thought to be unstable as they only appeared experimentally in derivative forms such as carbon nanotubes, buckminsterfullerenes, and of course graphite [172]. However in 2004, Novoselov *et al.* successfully isolated a single atomic layer of graphite, heralding the world's first two-dimensional material [1]. This material, known as graphene, has since received a considerable amount of attention from the wider scientific community due to its strange and extraordinary properties. Graphene has a distinct band structure with two conical points (K and K') where the conduction and valence bands overlap in the Brillouin zone (BZ); these points are referred to as Dirac points, and electron energies near to these Dirac points follow a linear dependence on the electron wave vector. This band structure arises from the interaction of graphene's two equivalent carbon sub-lattices, shown clearly in figure 4.6, whose own band structures overlap at the BZ edge to establish the conical energy dispersion. Electrons moving around graphene's honeycomb lattice and interacting with the periodic potential are modelled as low-energy quasiparticles by a Dirac-like Hamiltonian, which describes them as massless relativistic particles with energy dispersion $E = \hbar k \nu_F$ and momentum k

as they approach the Dirac points. This means the quasiparticles effectively act as photons where the speed of light is the Fermi velocity $\nu_F = 10^6\,\mathrm{m\,s^{-1}}$ [174, 175]. Figure 4.7 shows graphene's unique band structure, and the positions in reciprocal space where the Dirac points exist. Graphene's band structure results in some electronic properties which have made it a potential candidate for a new generation of electronic devices. In an undoped graphene sheet, the electron density of states only reach the Fermi level, where massless Dirac fermions are expected. However, graphene has also been reported to exhibit an ambipolar electric field effect (i.e. the Fermi level can be shifted into the conduction or valence bands by an external electric field, demonstrated in figure 4.7b) that allows charge carrier concentration tuning between electrons and holes of up to $10^{13}\,\mathrm{cm^{-2}}$ with mobilities greater than $15\,000\,\mathrm{cm^2\,V^{-1}\,s}$ and ballistic

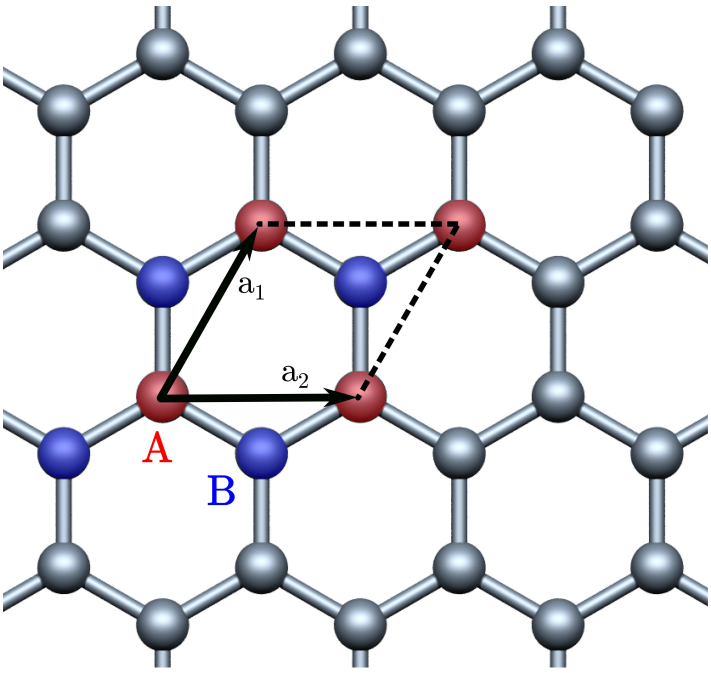

Figure 4.6. A topdown view of a graphene crystal, which consists of two equivilent carbon sublattices A and B. One possible unit cell of graphene is encapsulated by the real space vectors a_1 and a_2; the unit cell of graphene contains two atoms.

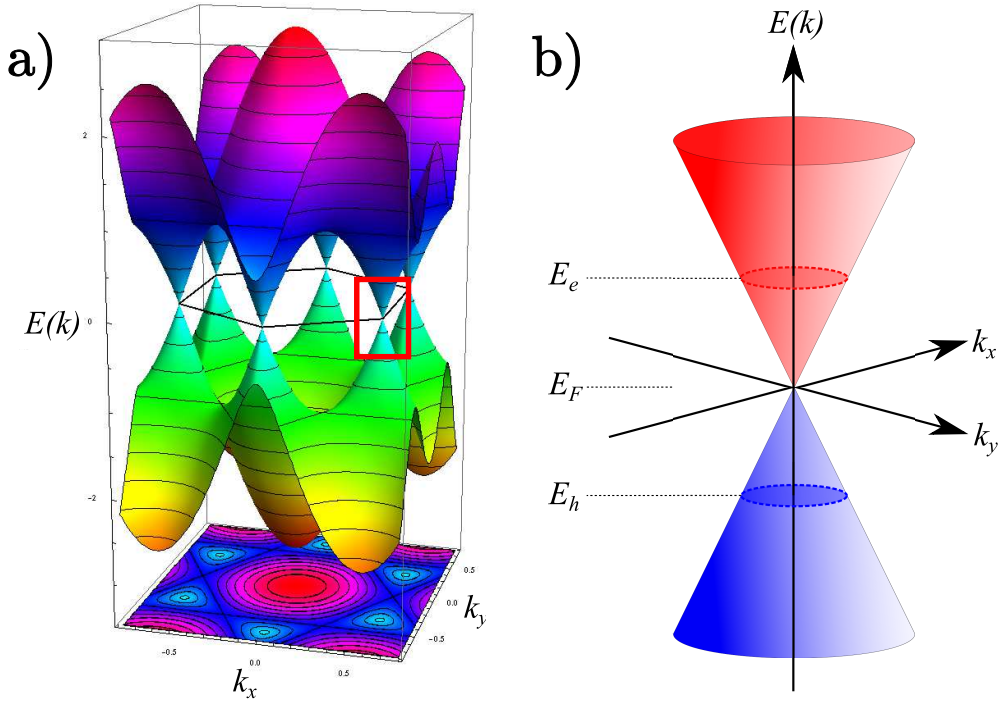

Figure 4.7. **(a)** The band structure of graphene in the first BZ. The Dirac cones are centred on the K points of the BZ (Adapted from [176]). The red region has been expanded in **(b)**, and shows a Dirac cone in more detail with the ambipolar electric field effect shifting the Fermi level with respect to an external electric field.

transport up to sub-micrometer distances [1, 177]. Graphene nano-ribbons (GNR) are quasi one-dimensional structures that have been predicted to be semi-conducting (by introduction of a width-dependent band gap) or metallic depending on their in-axis orientation, and thus have been considered for use in field effect transistors in integrated circuits. With high carrier mobilities, this heralds devices with rapid switching speeds in the GHz to THz range. The use of graphene in flexible electronics has caught the interest of many research groups; its in-plane conductance, low optical absorption (∼2.3 %) [178], and high resistance to fracture strain [179] make it a potential replacement for indium tin oxide (ITO) in touch screen devices and rollable e-paper [180]. As well as integrated electronic devices, graphene (and graphene oxide) has shown promise

as a medium for drug delivery [181], electrochemical sensing [182], energy storage and generation [5], water filtration and contaminant removal [183], and a variety of other applications.

4.3.1 Graphene Synthesis

Mechanical Exfoliation

In their original 2004 paper, Novoselov *et al.* used mechanical exfoliation, or repeated peeling, of small highly ordered pyrolytic graphite (HOPG) mesas to produce the world's first free standing sheets of graphene [1]. The weak interlayer van der Waals interaction of HOPG ($2\,\mathrm{eV\,nm^{-2}}$) and small force required the cleave individual layers ($300\,\mathrm{nN\,\mu m^{-2}}$) means that the crystal can be repeatedly cleaved to its limit by adhesive tape, and then transferred to an appropriate oxidised silicon substrate. This "Scotch tape" method, or micromechanical cleavage, although seemingly straightforward in nature is rather time consuming and labour intensive. The technique has predominantly remained a laboratory-based method with no clear manner with which to scale up for mass-production. Some groups have proposed variations on the micromechanical cleavage route which are more efficient and require less effort on the part of the experimenter. For example, Chen *et al.* proposed a system of continuous exfoliation via a three-roll mill machine with a polymer adhesive (Polyvinyl chloride (PVC) dissolved in dioctylphthalate (DOP)) in their 2012 paper [184]. Another technique proposed by Jayasena *et al.* in 2011, uses a lathe system consisting of a ultra-sharp diamond wedge precisely cleaving nanometre thick graphite flakes from an HOPG-loaded mount [185]. Liquid-phase-assisted exfoliation of graphene, an alternative method for providing the necessary normal/shear force has also been developed in recent years via the techniques of sonication and pressure-driven fluid dynamics. The former

typically disperses graphite powder into specific organic solvents, followed by sonication and centrifugation. The sonication process utilises the cavitation of bubbles that form on the basal and edge planes of the graphite flakes. The compressive stress waves released by the collapsing bubbles propagate through the graphite flakes until they reach the free graphite interface, upon which they are reflected back into the graphite, inducing a tensile stress wave providing the normal force required for exfoliation. Stress waves originating from the edge plane also provide a wedge effect inducing shear forces in adjacent graphite planes, hence separating them [186].

Chemical Vapour Deposited Graphene

Controllable segregation of graphene using carbonaceous gas sources was first reported by Yu *et al.* in 2008 [187]. High purity (99.99 %) polycrystalline foils of nickel were placed into a high temperature chamber with an inert gas. The foils were annealed under a H_2/Ar gas flow for 1 h to remove impurities at the Ni surface before a CH_4 precursor gas is then introduced. The hydrocarbon molecules decompose at the Ni surface and then, due to carbon's high solubility in Ni, the carbon atoms diffuse into the metal with the carbon concentration decreasingly exponentially from the surface into the bulk. In the subsequent cooling period, the carbon solubility of Ni decreases causing the carbon atoms to segregate at the surface. The cooling rate determines the amount and quality of the carbon at the Ni surface, with high quality graphene forming in the $\sim 10\,^{\circ}\mathrm{C\,s^{-1}}$ regime. Fast cooling ($\sim 20\,^{\circ}\mathrm{C\,s^{-1}}$) quenches the segregation resulting in poor state of crystallinity, whilst slow cooling ($\sim 20\,^{\circ}\mathrm{C\,s^{-1}}$) allows the carbon enough time to diffuse further into the bulk, resulting in an insufficient concentration of solute atoms near the surface for segregation. The size and quality of the resulting graphene is highly dependant on the Ni crystallinity

at the growth interface, with polycrystalline Ni resulting in largely multilayer graphene growth due to carbon aggregating at Ni grain boundaries [187].

Following Yu *et al.*'s initial success at using CVD to produce graphene, other groups reported similar results on other metallic substrates demonstrating varying levels of carbon solubility and catalytic effect. In 2009, Ruoff *et al.* demonstrated the CVD growth of graphene on copper substrates [188]. Graphene grown on Cu demonstrates many advantages over Ni and other metallic substrates used in the CVD process; Cu exhibits an ultra-low carbon solubility meaning that a large CH_4 concentration or extended growth period will still result in a small concentration of dissolved carbon in the Cu. The predominant growth mechanism for graphene on Cu arises from catalytic decomposition of the hydrocarbon gas at the Cu surface. Once a monolayer of graphene has been deposited, the Cu surface required for this catalytic reaction is fully covered, and the growth process stops immediately. This means that graphene CVD on Cu is a self-limiting surface-driven process, and thus is highly controllable. Cu foils, typically about 25 µm in thickness, are cheap and graphene grown on them can easily transferred to insulating substrates such as silicon oxide. Parameters such as cooling rate and thickness of the Cu have no effect on the graphene growth rate. Controlling the quality and coverage of graphene-on-Cu is largely influenced by the hydrocarbon gas flow rates, the substrate temperature, and the pre-treatment of the Cu foils. The annealing of Cu foils in a H_2/Ar gas flow prior to the introduction of hydrocarbon precursor gases serves two main functions: it removes the native copper oxide layer which reduces its catalytic ability; and it rearranges the surface morphology, removing structural defects and increasing the Cu grain sizes [189].

The density of graphene nucleation sites is highly dependent on the Cu surface morphology, with carbon adatoms aggregating predominately at surface defects, Cu domain boundaries, and step edges. Techniques such as Cu electro-polishing [190], substrate melting [191], and altering the CH_4/H_2 gas ratio to favour the hydrogen component [192], have reported to reduce the nucleation density allowing graphene domains more space to grow before meeting other graphene domains and coalescing. With respect to the precursor gas, a larger CH_4/H_2 ratio gives rise to a highly polycrystalline graphene sheets with significant multilayer coverage [193].

The mechanism of the surface-driven catalysis on Cu, and the carbon segregation in Ni, have been confirmed experimentally by Ruoff *et al.* through sequential flowing of carbon-12 and carbon-13 precursor gases into the growth chamber. The resulting distribution of carbon isotopes in the graphene were determined using the position of the Raman G peak. Graphene grown on Ni substrates heralds a uniform distribution of carbon isotopes because the diffused carbon mixes before the segregation step. Graphene-on-Cu instead exhibits alternating sections of carbon-12 and carbon-13 congruent to a process involving carbon adsorption and aggregation [194].

Sublimation from Silicon Carbide

Thermal decomposition of silicon carbide (SiC) provides a method of producing large-area homogeneous graphene of extremely high quality. Compared to other growth techniques, it has the advantage of producing graphene-based electronic devices on a commercially available semiconducting substrate without the need for transfer. The mechanism of SiC decomposition has been well studied since it was first demonstrated by Badami in 1965 [195]. When a SiC substrate is

heated to temperatures exceeding 1000 °C in UHV, the negliable vapour pressure of carbon compared to silicon means that the silicon is able to sublimate from the surface. This leaves carbon atoms behind which then optimise into graphene and graphitic layers [196]. Improvements to this technique involve inhibiting the sublimated silicon flux from the SiC surface by introducing 1 bar of Ar gas [197] or disilane gas (at increased temperature, i.e. 1650 °C) [198] into the growth chamber. Graphene grown on SiC using the sublimation method is epitaxial and, as first shown by De Heer *et al.* in 2004, contains Dirac-like charge carriers exhibiting mobilites exceeding $1100\,\mathrm{cm^2\,V^{-1}\,s^{-1}}$ [199, 200] or $2000\,\mathrm{cm^2\,V^{-1}\,s^{-1}}$ using the Ar-pressurization technique [197]. Epitaxial graphene can be grown on either of the polar faces of SiC (i.e. the Si–terminated and C–terminated sides), but the growth conditions and the electronic properties of the subsequent graphene are highly dependent on the chosen growth face as first reported by Bommel *et al.* [201]. There are many examples of large-area single-layer graphene growth on the SiC(0001) surface with excellent reproducibility. It has been reported by many groups using LEED and STM, that before graphitisation the SiC(0001) surface reconstructs into a $(6\sqrt{3} \times 6\sqrt{3})\mathrm{R30°}$ non-conducting carbon-rich 'buffer' layer as silicon atoms begin to sublimate [202, 203]. This buffer layer is partially bonded to the SiC surface and does not exhibit any of the electronic properties of graphene. As temperature continues to rise beyond 1250 °C and more silicon is sublimated, the top most carbon layer detaches and forms a graphene layer, with the next layer of carbon forming the buffer layer. The graphene demonstrates the expected electronic properties as free-standing graphene with a linearly dispersing band structure near the K point in reciprocal space [202]. With a sustained temperature increase, more layers of graphitic carbon are formed with Bernal stacking in either an AA' or AB stacking sequence [204]. On the other hand, graphene growth characteristics of the SiC$(000\overline{1})$

surface are vastly different beyond the expected sublimation of silicon. First the on-set of graphitisation occurs at 1100 °C, and proceeds more rapidly compared to the SiC(0001) surface for any given temperature, leading to rapid multilayer growth [205]. However, growth on this surface involves additional complex surface reconstructions before graphene is produced and typically results in polycrystalline growth with many rotational domains and defects, as well as rotationally disordered stacking in multilayer films [206–208]. For this reason, only the SiC(0001) surface is considered in this work. Production of graphene via the SiC sublimation process is highly energy intensive requiring extremely high temperatures and a UHV environment. Despite the extremely high-quality of the graphene, the proximity to the buffer layer also results in a K-point energy shift of 0.4 eV below the Fermi energy resulting in significant n-type doping. This presented a major issue for future SiC-graphene-based electronic devices as the charge transfer induced n-doping in the graphene becomes a source of electronic scattering, reducing the overal mobility of the graphene [209]. However this effect can removed by intercalating hydrogen between the buffer layer and the SiC surface [210].

Chapter 5

Graphitising the (111) Diamond Surface

In this chapter, the results of a study on the (111) diamond surface are presented. The (111) surface of diamond is altered by heating in UHV up to 1100 °C. Four main surface conditions are identified and chracterised: the oxygen-terminated (1×1) surface, the hydrogen-terminated (1×1) surface, the Pandey-chain (2×1) reconstruction, and the graphitised surface. The key result of this chapter is revealed after heating beyond 1000 °C in UHV; the co-existence of the diamond (111)(2×1) Pandey-chain reconstruction and graphene. This is shown by combined angle-resolved photoelectron spectroscopy data and density functional theory modelling of the surface, of which is in contrary to previous studies conducted on this system.

5.1 The $(111)(1 \times 1)$ Diamond Surface

5.1.1 Oxygen-terminated Diamond

A moderately boron-doped (i.e. [B] = $10^{16}\,\mathrm{cm}^{-3}$) (111)-orientated diamond was delivered to Element 6 Ltd (Didcot, UK) where it was polished on an iron scaife until an near-atomically flat surface was achieved. The nature of the polishing method is not known beyond basic details. The diamond was cleaned by sonication in acetone for 15 minutes in a plastic beaker (to avoid silicon contamination), rinsed with isopropanol, and blow dried with nitrogen gas. Contact atomic force microscopy (C-AFM) was used to confirm the (111) surface roughness and determine whether the polishing had induced any damage to the surface. Figure 5.1 shows the results of the C-AFM study.

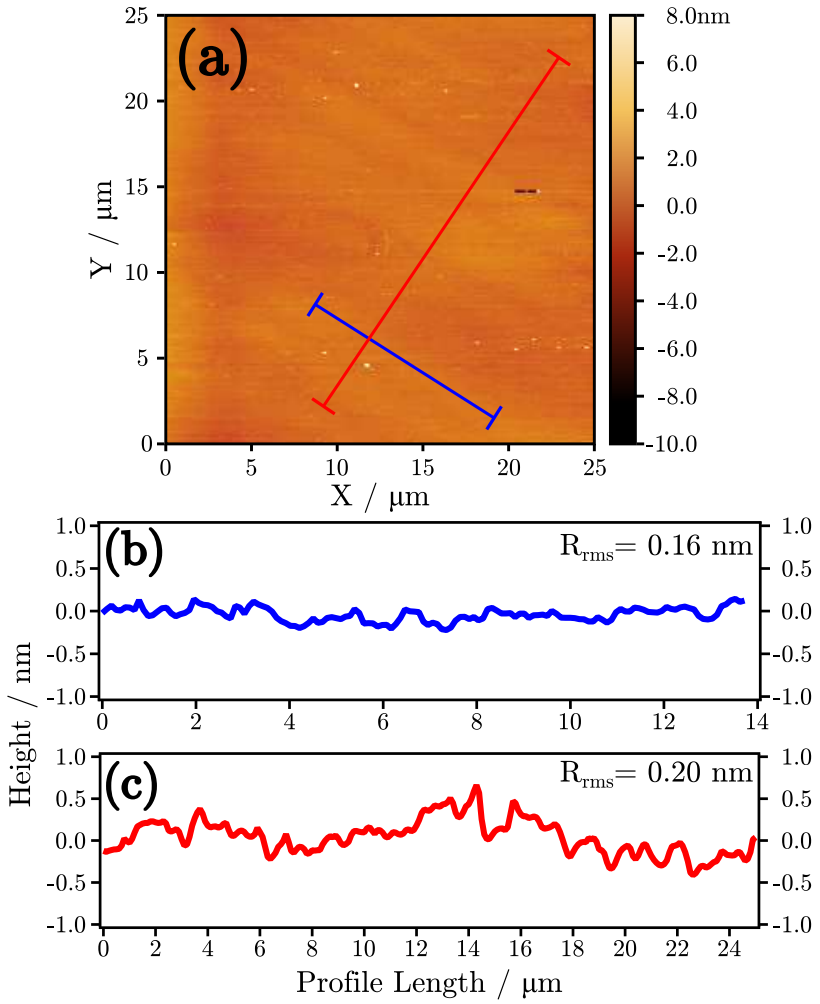

Figure 5.1. C-AFM Images taken from the surface of the moderately boron-doped (111) diamond after an E6 polish. **(a)** A 25×25 µm C-AFM scan. Line profiles have been extracted from the **(b)** blue path and the **(c)** red path in subfigure **(a)**, which are parallel and perpendicular to the polishing direction respectively. The r.m.s. roughness values have been extracted and quoted for each path.

The r.m.s. roughness was calculated to be 0.16 nm in the polishing direction and 0.20 nm in scaife's radial direction, both of which are less than the interlayer spacing of the (111) plane of diamond, therefore confirming atomic flatness of the diamond surface (N.B. true atomic resolution was not achieved on this microprobe, so these values represent an average). The diamond was introduced into the REES system and heated to 300 °C to drive off any adventitious

carbon and oxygen groups from the (111) surface. The pressure in the preparation chamber exceeded 1×10^{-8} mbar during the heating ramp, therefore the sample was held at 300 °C overnight whilst the chamber pressure recovered to $\sim 3 \times 10^{-10}$ mbar to prevent re-adsorption of contaminants. The sample was then cooled to less than 80 °C and moved into the analysis chamber for XPS analysis. Figure 5.2 shows the XPS spectra collected from this clean surface.

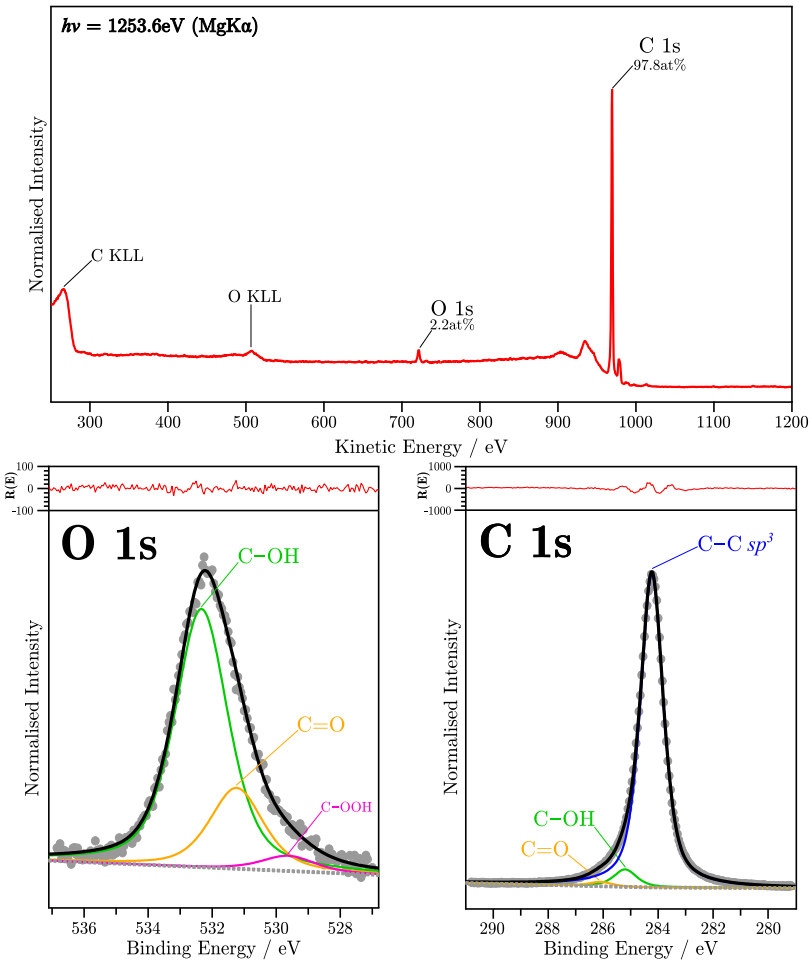

Figure 5.2. XPS spectra of the moderately-doped (111) diamond surface after E6 polish and heating to 300 °C. **Top:** A survey scan showing the C 1*s* peak from the diamond, and O 1*s* from surface oxygen-terminating species. The corresponding C KLL and O KLL Auger features are also present. **Bottom Left:** A high resolution scan of the O 1*s* core level. **Bottom Right:** A high resolution scan of the C 1*s* core level. The red inset traces show the residuals $R(E)$ from the fitting procedures. Table 5.1 shows the fitting results for these spectra.

Component	Position / eV	FWHM / eV	∑GL ratio	At%
C 1s				
C−Csp^3	284.2	1.0	0.60	93.2
C−OH	285.2	1.0	0.60	5.4
C=O	286.1	1.0	0.60	1.4
O 1s				
C−OH	532.3	2.0	0.50	72.9
C=O	531.2	2.0	0.50	22.8
O=C−OH	529.6	2.0	0.50	4.3

Table 5.1. Fitting results for the spectra in Figure 5.2

Post-heating, the survey spectrum shows that the diamond surface is free from contamination with only the carbon and oxygen 1s peaks observable. The O 1s peak accounts for 2.2 at% of the analysis volume, which corresponds to an oxygen surface coverage of ∼90 % on the (111) face [211]. The high resolution scans of the O 1s and C 1s reveal the nature of the surface oxide. The O 1s has been fitted with three components positioned at 532.3 eV, 531.2 eV, and 529.6 eV binding energy. These O 1s components are wholly down to carbon-oxygen bonds at the diamond (111) surface and have been assigned as alcohols (C−OH), ketones (C=O), and carboxyl (O=C−OH) groups respectively. The percentage ratio of these carbon-oxygen groups is 72.9 %:22.8 %:4.3 %. The C 1s consists of a main C−C sp^3 component at 284.2 eV with the surface oxide states at higher binding energy; the C−OH and C=O components are +1.0 eV and +1.9 eV higher in binding energy compared to the main C−C sp^3 component. The O=C−OH component could not be fitted confidently, but is nevertheless present in the O 1s peak. The ratios of at% values between different components in the C 1s and O 1s may not be exactly the same due to inherent inaccuracies arising from the selection of the background algorithm and the effective attenuation lengths.

5.1.2 Hydrogen-terminated Diamond

Above 300 °C, surface oxygen groups slowly desorb from the diamond surface and are replaced by hydrogen which is outgassed from the Boralectric heater plate in the UHV chamber. As shown later in section 5.2, single dangling bonds at the surface must be hydrogen terminated immediately after oxygen desorption, otherwise reconstruction will occur. To achieve a fully H-terminated surface, the (111) diamond was slowly heated to 900 °C whilst ensuring the pressure did not exceed 1×10^{-7} mbar. The diamond was held at 900 °C for ~5 min before cooling rapidly to 800 °C. The diamond sample was held at high temperature until the UHV chamber pressure dropped below 5×10^{-9} mbar before cooling. This heating procedure was repeated three times to reduce the chamber pressure at high temperature and therefore reduce the re-adsorption of oxygen onto the diamond surface. Once the diamond was cooled below 80 °C, XPS measurements were taken. Figure 5.3 shows the XPS measurements after heating to 900 °C. Immediately it is apparent in the survey scan that there is no measurable O 1*s* peak, in contrast to figure 5.2. The complete lack of an O 1*s* peak, which is more convincingly illustrated by the high resolution scan, indicates that the surface oxygen must be less than 0.1 at% of the analysis volume and thus below the detection limit for this system [212]. However, there is a very small O KLL contribution around 490 eV which is more apparent when the intensity is plotted on a logarithmic scale. The lower kinetic energy of the O KLL photoelectrons means that they have increased surface sensitivity, and therefore indicate that the signal is originating from the very surface of the

Component	Position / eV	FWHM / eV	∑GL ratio	At%
C–C sp^3 / C–H	284.7	1.0	0.75	100

Table 5.2. Fitting results for the spectra in Figure 5.3.

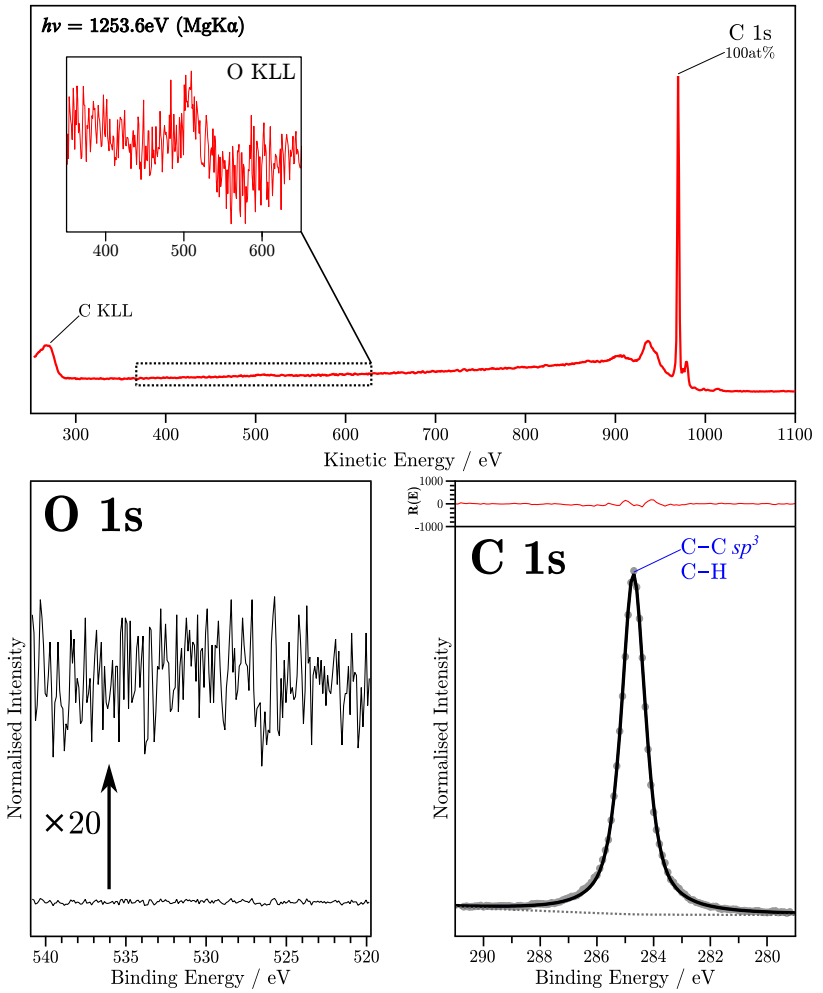

Figure 5.3. XPS spectra of the moderately-doped (111) diamond surface after heating to 900 °C. **Top:** A survey scan showing only the C 1*s* peak and C KLL Auger feature from the diamond, with no other contaminating elements. **Bottom Left:** A high resolution scan of the O 1*s* region showing a lack of oxygen. **Bottom Right:** A high resolution scan of the C 1*s* core level. The red C 1*s* inset trace show the residual $R(E)$ from the fitting procedure. Table 5.2 shows the fitting results for this spectrum.

diamond, suggesting that some trace oxygen is still present on the surface (i.e. <0.1 at%). The most likely explanation for this trace oxygen is re-absorption of C−O during the cooling stage, despite improving the UHV chamber pressure with repeated heating cycles. The high resolution scan of C 1*s* consists of a single component which has been attributed to the 'bulk' sp^3 carbon and surface

hydrocarbon. The lack of higher binding energy components indicates that there are no surface oxides, and the lack of lower binding energy components means that the surface has not reconstructed or graphitised (see section 5.2). The (111)(1×1) diamond surface will reconstruct without a stabilising termination species such as oxygen or hydrogen. At 900 °C, the temperature is too high for oxygen to remain bonded to the surface, freeing up bonding sites to be replaced by outgassed hydrogen from the Boralectric heater (see section 3.3.1). The immediate replacement of oxygen with hydrogen keeps the (111)(1×1) surface stable and therefore prevents the surface from reconstructing. Section 4.2.1 explains that the surface layer of a (111)(1 × 1) diamond has carbon bonded to either three satisfied bonds (surface), or four other carbons (sub-surface), and this staggered (111) plane is repeated into the bulk. The (1 × 1) surface lattice was confirmed by LEED measurements, shown in figure 5.4. The maxima of the two sets of symmetry-equivilent first order beams characteristic of the hydrogen-terminated diamond (111)(1 × 1) surface are observed with increasing incident energy from 87 eV to 102 eV, as observed in previous literature [17, 56].

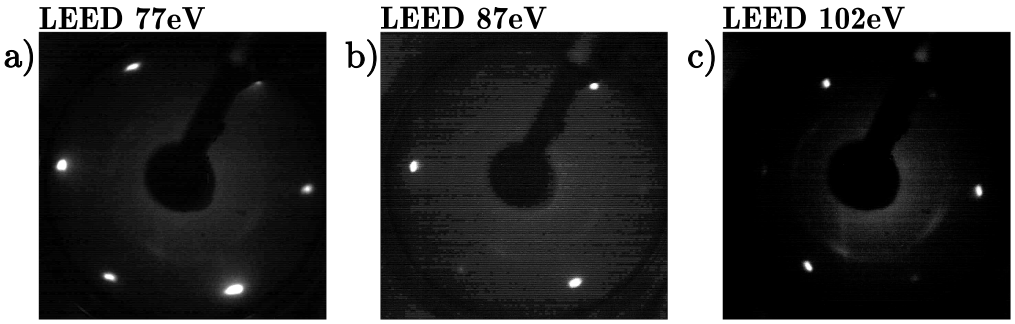

Figure 5.4. LEED study of the hydrogen-terminated (111)(1×1) diamond surface at **(a)** 77 eV, **(b)** 87 eV, and **(c)** 102 eV incident electron kinetic energy.

5.2 The $(111)(2 \times 1)$ Reconstruction)

5.2.1 The Clean (2×1) Reconstruction

To demonstrate the (2×1) reconstruction of the diamond (111) surface, an insulating HPHT diamond was used. The HPHT diamond was heated to temperatures between 930 °C and 1000 °C whilst ensuring the chamber pressure did not exceed 1×10^{-7} mbar. During this heating ramp, the oxygen-terminating species are thermally desorbed leaving behind a hydrogen-terminated (1×1) before reconstruction occurs above 930 °C. The diamond was then cooled to 800 °C and the pressure in the UHV chamber was allowed to recover to 5×10^{-9} mbar before cooling to acquire XPS measurements. As before, this procedure is repeated three times. Figure 5.5 shows the XPS survey scan and C 1*s* peak of the insulating HPHT diamond surface post-reconstruction. Due to the available analysis area of the HPHT sample (circular Ta mask with ∼1.5 mm diameter), a significant amount of tantalum from the sample plate is visible in the survey scan. However after heating

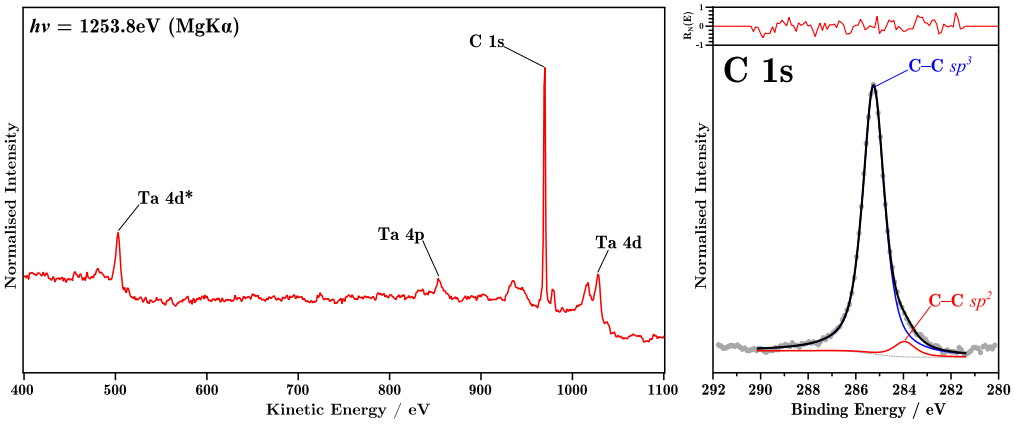

Figure 5.5. XPS spectra of the insulating (111) diamond surface after heating to 1000 °C. **Left:** A survey scan showing the C 1*s* peak from the diamond, and the Ta peaks from the sample holder. **Right:** A high resolution scan of the C 1*s* core level. The red inset trace show the normalised residual $R_N(E)$. Table 5.3 shows the fitting results for this spectrum.

Component	Position /eV	FWHM / eV	∑GL ratio	At%
C−C sp^3	285.1	1.1	0.60	94.6
C=C sp^2	283.8	1.1	0.60	5.4

Table 5.3. Fitting results for the spectra in Figure 5.5

to 1000 °C, no evidence of carbide was observed in the C 1*s* high resolution spectra which would convolute the photoelectron intensity from the diamond sample. The high resolution C 1*s* scans for both diamond surfaces show the 'bulk' C−C component as well as a smaller component on the higher kinetic energy side. The larger C−C component is naturally attributed to the sp^3-bonded carbon of the diamond structure, but the smaller component, which has a binding energy consistent with a C=C sp^2 species (i.e. ∼284 eV), only emerges when the samples are subjected to temperatures greater than 930 °C. It should be noted that the oxygen and hydrogen-terminated HPHT diamond surface is insulating and therefore the surface undergoes charging. The diamond surface does not charge indefinitely as low kinetic energy secondary electrons generated at the Al window of the twin-anode X-ray source are able to fill the electronic vacancies. The equilibrium binding energy of the insulating (111) diamond is measured at 287.0 eV in the home laboratory. For the insulating HPHT diamond, the emergence of this C=C sp^2 component coincides with a total C 1*s* peak position shift of −1.9 eV, to a new equilibrium binding energy of 285.1 eV. This means that the new sp^2 carbon in the surface region is providing a 'shorting path' where free electrons from the tantalum metal are able to reach the positive charges in the diamond surface and negate them. The crystallographic nature of the new surface carbon was revealed using LEED, and figure 5.6 shows a LEED pattern acquired from the moderately-doped diamond (111) surface after heating to 950 °C. The (2 × 1) LEED pattern only shows a

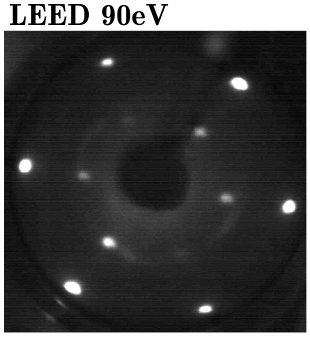

Figure 5.6. LEED pattern of the (111)(2×1) diamond surface after 950 °C.

doubling of the surface periodicity in two predominant directions, as opposed to the three directions expected from a (2×1) reconstruction from a non-atomically flat diamond (111) surface. Clearly, reconstruction in the third real-space direction is inhibited on the newly polished surface, an effect not observed on other (111) diamond surfaces measured in this study. Derry *et al.* are the only authors of publications that have reported a single-domain $(111)(2 \times 1)$ reconstructed surface on diamond, produced using mechanical polishing [152, 213]. They suggested that a departure from the true (111) plane during the polishing step produces terraces of varying widths. Terraces with even integer numbers of atomic rows preferentially reconstruct because an exact number of doubled periods can fit onto the basal plane of the terrace. On the moderately-boron doped diamond, the direction of polishing lines is likely the cause of the two-domain reconstruction for the following reason. The height variation extracted from figure 5.1c in the non-polishing direction suggests that there are more atomic terraces. These terraces potentially have a reconstruction breaking effect preventing any long-range order chains from forming. Whereas the atomic flatness in the polishing direction facilitates the conditions for long unbroken Pandey-chains to form, and therefore real-space lattice directions that are near in angle to the polishing direction will readily reconstruct.

In a previous study conducted by Dr Simon Cooil and colleauges, ARPES data was also obtained at the SGM 3 beamline of ASTRID at ISA (Aarhus, Denmark) from the moderately boron-doped diamond (111) surface. These measurements were taken along the $K\Gamma K$ direction of the (111)(2×1) BZ; full details of the experimental procedure can be found in references [56]. To affirm this previously obtained ARPES data, Kohn-Sham density functional theory (KS-DFT) calculations of the graphene-on-diamond electronic structure were obtained using the *ab initio* modelling program, Aimpro, a quantum-mechanical modelling package capable of predicting meaningful physical properties from a system of atomic positions and species [214]. The core electron potentials are replaced by Hartwigsen-Goedecker-Hutter (HGH) pseudopotentials and the valence electron orbitals are produced by d-character Gaussian basis functions with four exponents centred on atomic sites. A graphene-on-(111)(2×1) diamond system was constructed from a primitive orthorhombic unit cell containing 64 sp^3-bonded carbon atoms (diamond) and 8 sp^2-bonded carbon atoms (graphene). The relevance of the graphene sheet will become clear in the next section (see section 5.2.2). This unit cell was repeated *ad infinitum* in the xy-plane to produce a diamond slab, and both (111) surfaces are terminated by the (2×1) reconstruction and graphene sheets to prevent electric field effects which could arise from structural asymmetry in the graphene-on-diamond unit cell. A vacuum layer $\sim$30 Å thick was introduced above the diamond surface to separate the slabs that repeat in the surface normal direction, thus forming alternating layers of diamond and vacuum. Optimisation calculations of this structure allowed the atoms to adjust their positions until the maximum force on any atom was less than $1 \times 10^{-3}\mathrm{Ha}/a_0$. Optimisation causes the graphene sheets to move to a stable distance of $\sim$6.46 a.u. (3.42 Å) away from the diamond surface to avoid buckling. This distance is only slightly larger than

the graphite interlayer distance of 3.35 Å. The bond lengths in first (1×1) diamond layer, immediately under the (2×1) reconstructed surface, deviate from the typical C−C bond length of 1.54 Å by approximately 0.1 Å, as the optimisation allows the structure to relax. The band structure calculation is sampled from the surface reciprocal space by an 8×4 Monkhorst-Pack grid. As mentioned in section 4.2.2, the $(111)(2 \times 1)$ diamond surface can have up to three rotational domains of the (2×1) reconstruction (rotated by 120° with respect to each other) statistically distributed over the diamond surface. These other reconstruction domains were essential for modelling the diamond-graphene interface, as the ARPES sampling spot size was 500 µm×500 µm and so certainly recorded photoemission data from all three domains. No significant difference in the band structure were found between the three rotational domains. In Aimpro, the electronic states are represented by lines indicating the average energy-momentum dispersion without spectral broadening effects. In order to directly compare the DFT modelling of the density of states, the bare bands must be broadened in energy to account for the inherent photoemission process and experimental effects; the theoretical description of band broadening in ARPES, implemented by Dr Simon Cooil is as follows: the spectral weight, i.e. the relative intensity of the energy level relative to total intensity of the spectrum, in terms of binding energy E_b and electron momentum k is mathematically described as

$$I(E,k) = I_0 \cdot A(E,k) \cdot f_{FD}(E) \tag{5.1}$$

where I_0 is the incident photon energy and experimental geometry-dependent matrix element, $f_{FD}(E)$ is the Fermi-Dirac distribution, and $A(E,k)$ is the single-particle spectral function that describes the energy-momentum relation of an electron in a solid. The $A(E,k)$ term was used to apply the band

broadening correction to the bare bands of Aimpro's DFT calculation, and is mathematically described as

$$A(E,k) = -\frac{1}{\pi}\frac{\Sigma}{(E-\varepsilon_0)^2 + \Sigma^2} \tag{5.2}$$

where ε_0 is the bare band energy dispersion and Σ is a variable representing the complex self-energy parameter that describes all the electron-electron interactions that take place in a solid according to Landau's Fermi liquid theory [29, 215]. Not shown in the equation is a Gaussian distribution convolution to $A(E,k)$ to account for thermal broadening due to the experiment being run at 291 K. For this work, $\Sigma = 0.2$ eV and the FWHM of the Gaussian convolution was 0.5 eV. Finally as alluded to in equation 5.1, ARPES is only capable of measuring the occupied density of states below the Fermi level, therefore the spectral function broadened bands are passed into the Fermi-Dirac function in order to account for the lack of photoemission intensity above the Fermi level. The Fermi-Dirac function is given by

$$f_{FD}(E,T) = \frac{1}{e^{(E-\mu)/k_B T} + 1} \tag{5.3}$$

where μ is the chemical potential (i.e. the Fermi level energy), k_B is Boltzmann's constant, and T is the temperature of the sample (i.e. 291 K) [56]. Figure 5.7 shows a composite of experimental ARPES data and theoretical DFT modelling of the diamond (111)(2×1) surface in the $K\Gamma K$ direction in reciprocal space. The coloured lines overlaid on the figure represent the bare bands as calculated by Aimpro, and are included in order to guide the eye toward the important features in the data, notably the bulk and surface states. The grey scale images show the K-space corrected photoemission intensity from the previous ARPES study at the SGM 3 beamline, and the spectral function broadened DFT-

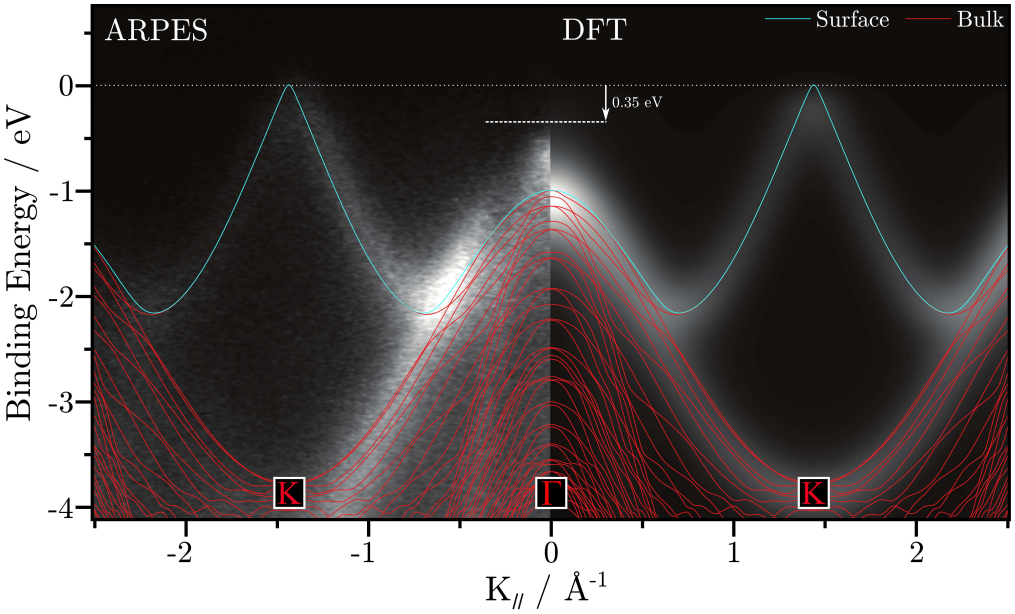

Figure 5.7. The band structure of the $K\Gamma K$ reciprocal space direction from the (111)(2×1) diamond surface, as obtained by (**Left**) ARPES data ($h\nu = 125\,\text{eV}$) [56] and (**Right**) a spectral function broadened modern DFT calculation. The bare bands of the DFT calculation are shown (red = bulk, blue = surface state).

calculated electronic states from this work (see equation 5.2). Immediately it is obvious that there is good agreement between the experimental and theoretical data in terms of the band dispersions. In the centre of the image at $K_{||} = 0\,\text{Å}^{-1}$, the σ-band from bulk diamond is observed, rising up to $\sim$0.35 eV binding energy below the Fermi edge, in both the ARPES and broadened DFT-calculated bands. Moving away from the BZ centre, the σ-band decreases in energy to a minimum at $K_{||} = 1.44\,\text{Å}^{-1}$. On the other hand, the π-band from the (111)(2×1) surface state, whilst initially following the same dispersion as the highest occupied bulk bands, diverges and begin to increase in energy. When the σ-band reach a minimum, the surface π-band reaches an energy maxima and intersects the Fermi level at the K high-symmetry point in the diamond (111)(2×1) BZ. The photoemission intensity (both real and simulated) drops to zero beyond the Fermi level, but the un-broadened π-band can be seen to

increase above the Fermi level by 15 meV. With broadening, this shows that the diamond (111)(2 × 1) surface is in fact metallic, and the experimental ARPES data appears to support this conclusion. The modelling using the modern Aimpro code agrees with earlier modelling attempts on the (111)(2 × 1) surface by multiple groups such as Kern *et al.* and most recently, Marsili *et al.* [166–169], which also predict a metallic surface. ARPES data obtained from the diamond (111)(2 × 1) surface by Graupner *et al.* instead show that a band gap of at least 0.5 eV between occupied and unoccupied π-states remains at the K point [170]. Conversely the ARPES results obtained by Cooil *et al.* at the ASTRID SGM 3 beam line agree with the DFT modelling in the literature and the Aimpro calculation conducted for this work. Such a strong reconciliation between the experimental and theoretical density of states of the diamond (111)(2 × 1) surface has not been demonstrated previously in the literature by a single research group.

5.2.2 High Temperature Graphitisation of Diamond

The high temperature catalyst-free graphitisation of the diamond (111) surface was attempted on the insulating HPHT diamond. The XPS data presented here was obtained in the home laboratory. Following the procedure to reconstruct the (111) surface described in section 5.2.1, the insulating HPHT diamond was rapidly heated to 1000 °C. The REES/Transfer valve was opened and the main system turbo pump was used for additional pumping as the chamber walls and Boralectric heater outgas significantly above 1000 °C. The sample was then 'flashed' to 1100 °C three times before cooling to 800 °C where the pressure allowed to recover below 5×10^{-9} mbar. The sample was then cooled below 80 °C for XPS analysis. Figure 5.8 shows the XPS survey scan and C 1s high resolution scan of the insulating HPHT diamond surface post-graphitisation.

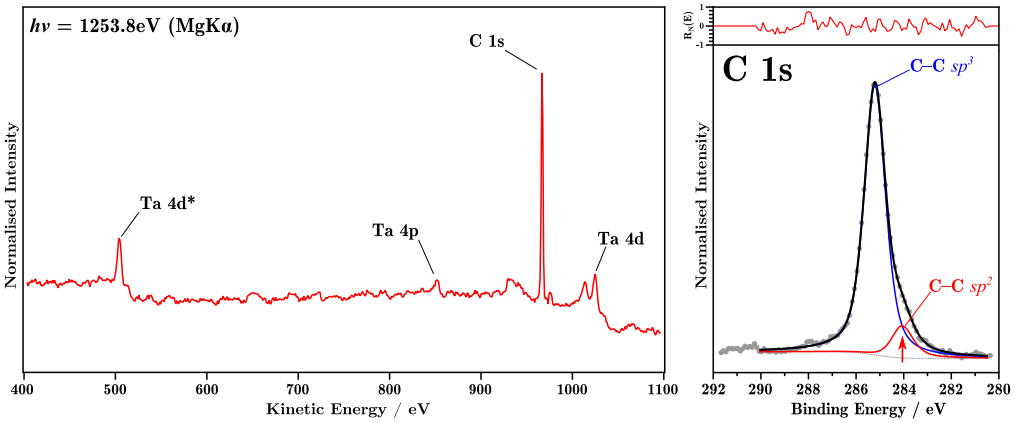

Figure 5.8. XPS spectra of the insulating (111) diamond surface after heating to 1100 °C. **Left:** A survey scan showing the C 1*s* peak from the diamond, and the Ta peaks from the sample holder. **Right:** A high resolution scan of the C 1*s* core level. The red inset trace show the normalised residual $R_N(E)$. Table 5.4 shows the fitting results for this spectrum.

Component	Position /eV	FWHM / eV	∑GL ratio	At%
C–C sp^3	285.1	1.1	0.47	89.4
C=C sp^2	284.1	1.1	0.47(*0.14)	10.6

Table 5.4. Fitting results for the spectra in Figure 5.8 (*Asymmetry parameter)

The survey scan of the graphitised (111) surface shows no noticeable difference from the reconstructed surface shown in figure 5.5. The high resolution scan of the C 1*s* core level shows the same components of carbon: the C−C sp^3 peak at 285.1 eV and the C=C sp^2 peak at 284.1 eV. The C=C sp^2 component has a small degree of asymmetry (∼0.14) meaning that metallic conductivity, characteristic of graphene, has been achieved. This component doubled in area after the sample is heated to 1100 °C, from 5.4 % to 10.6 % of the total C 1*s* area. The difference between sp^2 carbon in the surface reconstruction and the graphene sheet cannot be determined by peak position as the chemical shift between these states is less than the resolution of the HSA at this pass energy (∼0.2 eV). This means that this component must account for two structures

of sp^2 carbon: the buckled (111)(2 × 1) reconstruction, and the flat graphene sheet. If the area of the sp^2 peak in figure 5.5 represents a single layer of sp^2 carbon due to the reconstruction, then it follows that a doubling of this area must be the graphene sheet, as two layers of reconstruction is not possible and sub-surface reordering has not been demonstrated within the literature.

The co-existence of the graphene and (2 × 1) reconstruction on the diamond (111) surface was also previously demonstrated by Cooil *et al.* with ARPES measurements on the SMG 3 beamline; again, full details of the experimental procedure can be found in reference [56]. The ARPES measurements clearly show a Dirac cone along the K_gMK_g direction in reciprocal space. In this work, the band structure for the K_gMK_g direction for the graphene-on-(111)(2 × 1) diamond surface was calculated using Aimpro in order to provide theoretical support. As previously shown in section 5.2.1, band broadening with the spectral function was also applied to the K_gMK_g modelling. Figure 5.9 shows a composite of experimental ARPES data and theoretical DFT modelling of the diamond (111)(2 × 1) surface in the K_gMK_g direction in reciprocal space. At $K_{||} = 0\,\text{Å}^{-1}$, the bulk bands of the (111) diamond are seen in the DFT modelling as the M point in the graphene sits atop an equivalent Γ point in the bulk diamond. Spectral broadening has only been applied to the surface state, which in this case is the graphene π-band. Similar to data shown in figure 5.7, there is remarkable agreement between the ARPES data and the DFT modelling when one considers the band dispersions. The graphene Dirac cones are clearly observed, centred at the K_g points in the graphene BZ. K_g is observed at $K_{||} = 0.805\,\text{Å}^{-1}$ with a $K_g \rightarrow K_g$ distance of $1.61\,\text{Å}^{-1}$, which is typical of graphene. The Dirac cones are clearly seen intersecting the Fermi level both in the DFT simulation and, as can be seen by the high contrast inset, the ARPES

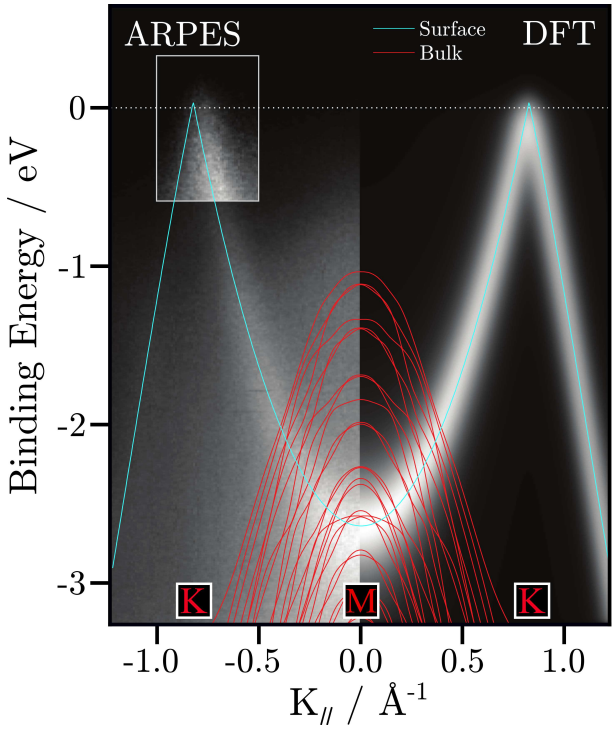

Figure 5.9. The band structure of the K_gMK_g reciprocal space direction from the graphene on (111)(2 × 1) diamond surface, as obtained by (**Left**) ARPES data ($h\nu$ = 45 eV) [56] and (**Right**) a spectral function broadened modern DFT calculation. The bare bands of the DFT calculation are shown (red = bulk, blue = surface state). **Inset:** the tip of the Dirac cone in ARPES scaled in intensity for clarity.

data. This agreement provides strong evidence, in conjunction with the XPS data from the home laboratory, that high quality epitaxial graphene is formed on the diamond (111) surface in coexistance with the (2 × 1) reconstruction with high temperature graphitisation. In pristine, undoped, and unbuckled graphene, the binding energy of the graphene π-band at the M-point should equal ∼3 eV. However, in both the ARPES and DFT modelling of graphene on the diamond (111)(2 × 1) surface, the graphene π-band only reaches a binding energy of ∼2.4 eV, with no corresponding shift in the Dirac cones. This up-shift in binding energy is not observed at the K_g points, meaning that the dispersion around Dirac cones has been altered. This up-shift of the π-band at the M-

point (and by extension, a flattening of the K_gMK_g dispersion) can potentially be attributed to an increased third-nearest atomic neighbour coupling due to either uniaxial pressure, shear, or strain forces, doping, or more likely in this situation, an increased graphene-substrate interaction [216, 217].

5.3 Chapter Conclusion

In this chapter, the high temperature catalyst-free UHV graphitisation of the diamond (111) surface has been investigated, as well as intermediate stages during a heating cycle to 1000 °C. Two diamonds, a Type IIb natural diamond, and a Type Ia HPHT diamond were polished to within 1° of the (111) crystallographic plane, to a near-atomically flat finish. After polishing and heating to 300 °C in UHV, the (111) surface is covered by a monolayer of oxygen and hydrogen containing species. High resolution XPS scans of the C 1s and O 1s reveal a surface covered in alcohols (C−OH), ketones (C=O), and carboxyls (O=C−OH) in a ∼73:23:4 ratio. Heating the diamond beyond 300 °C slowly desorbs oxygen from the surface which is rapidly replaced by hydrogen in the UHV chamber or from the Boralectric heater plate. Above 900 °C, no oxygen groups remain chemisorbed to the diamond surface, and a hydrogen terminated surface is formed. This is confirmed by a complete lack of an O 1s peak (although a small O KLL remains), and by a single C−C/C−H component in the C 1s peak. LEED images, taken of the diamond surface after heating to 900 °C, demonstrate that a reconstruction has not occurred by exhibiting a single corrugated hexagon pattern indicative of a (111)(1 × 1) surface.

In order to study the Pandey-chain (2 × 1)-reconstruction of the diamond (111) surface, temperatures exceeding 930 °C in UHV are required. Above

this temperature, hydrogen can no longer remain bound to the surface and desorbs. The surface, unable to be stabilised by hydrogen adsorption, undergoes reconstruction into a (2×1) crystallographic motif. High resolution scans of the C 1*s* show a small C=C sp^2 component on the lower binding energy side of the main C−C sp^3 component and, in the case of an insulating type Ia HPHT diamond, surface charging is compensated by the increased conductivity of the surface due to the reconstruction. LEED images taken on the type IIb diamond after 950 °C provide more striking evidence, as a doubling of the surface periodicity is observed in only two directions on the (111) surface. The third reconstruction domain is inhibited by the surface topography created by the polishing process which, whilst atomically flat in the polishing direction, likely formed an increased number of atomic terraces in the perpendicular direction which have a reconstruction breaking effect. The band structure of $(111)(2 \times 1)$ diamond surface has also been investigated with DFT modelling using the Aimpro code. Band structure modelling has been compared to previously acquired ARPES data from ASTRID's SGM 3 beamline by Cooil *et al.* Further broadening of the DFT bare bands using the spectral function and convolution with the Fermi-Dirac function allowed a simulated ARPES data set to be produced. Along the $K\Gamma K$ direction in the diamond $(111)(2 \times 1)$ BZ, there is good agreement between the experimental and theoretical data. The high symmetry K points have been shown to extend past the Fermi level meaning that the $(111)(2 \times 1)$ surface is metallic, in contrary to the most recent published ARPES data by Graupner *et al.* which showed a bandgap at least 0.5 eV wide. This work is the first modern evidence reconciling both experimental ARPES and theoretical calculations of the band structure for the $(111)(2 \times 1)$ surface of diamond.

Experiments conducted on a type Ia HPHT diamond in the home laboratory have demonstrated UHV catalyst-free graphitisation of the (111) surface after reconstruction. The HPHT diamond was heated to 1100 °C in UHV to induce graphitisation. XPS analysis of the C 1*s* peak shows that the surface C=C sp^2 component doubles in intensity after the heating cycle, which has been interpreted as two separate components overlapping each other due to their similar binding energies: one corresponding to the surface reconstruction, and another from a graphene monolayer. This implies that the graphene coexists on top the reconstructed diamond surface. Once again, ARPES results from Cooil *et al.* and DFT calculations from this work provide the strongest evidence for the graphene-reconstruction co-existence. The ARPES data acquired on the graphitised type IIb natural diamond revealed a Dirac cone extending up to the Fermi level along the K_gMK_g direction in the graphene BZ. In this work, the band structure for the same direction was simulated using DFT and resulted in a superb agreement in the dispersion of the π-band. The Dirac cones extend up to and beyond the Fermi level both in the experimental dataset and the DFT modelling at $K_{||} = 0.805\,\text{Å}^{-1}$. An upshift in the M-point energy at $K_{||} = 0\,\text{Å}^{-1}$ has been attributed to an increased third-nearest neighbour coupling in the graphene, inferring a strong graphene-substrate interaction. The graphene-reconstruction co-existance has not been shown previously in the published literature, until Cooil *et al.* performed up-to-date ARPES measurements on the graphitised (111) diamond surface. Increasingly so in the literature, the importance of modelling to complement experimental measurements in materials and condensed matter physics, is being realised. The DFT modelling conducted in this work re-affirms the validity and conclusions of the ARPES dataset, providing a strong case for publication.

Chapter 6

Iron-mediated Graphitisation

6.1 Iron-on-Diamond

Deposition of Fe overlayers on diamond (111) and SiC surfaces was achieved using a Knudsen evaporation cell, built to the specification outlined in section 3.3.2. The precise controllability of deposition rate exhibited by the home-made K-cells allowed Fe films from tens of nanometres thick to single monolayers of Fe atoms to be fabricated. During depositions, REES was utilised to monitor a core level originating from the substrate in order to ascertain the Fe growth mode and attenuation of the photoelectron intensity from the substrate. The technique can also reveal changes in the surface charging of insulating materials, which in turn can be used to qualitatively infer the conductivity of an overlayer.

6.1.1 Deposition

For the study detailed in section 6.2.1, an Fe film was required that was thick enough to completely attenuate the diamond C 1s peak. Using the NIST EAL database [218], it was calculated that to reduce the C 1s to $<0.1\,\%$ of its initial intensity, an Fe overlayer of at least 8.1 nm was required. Figure

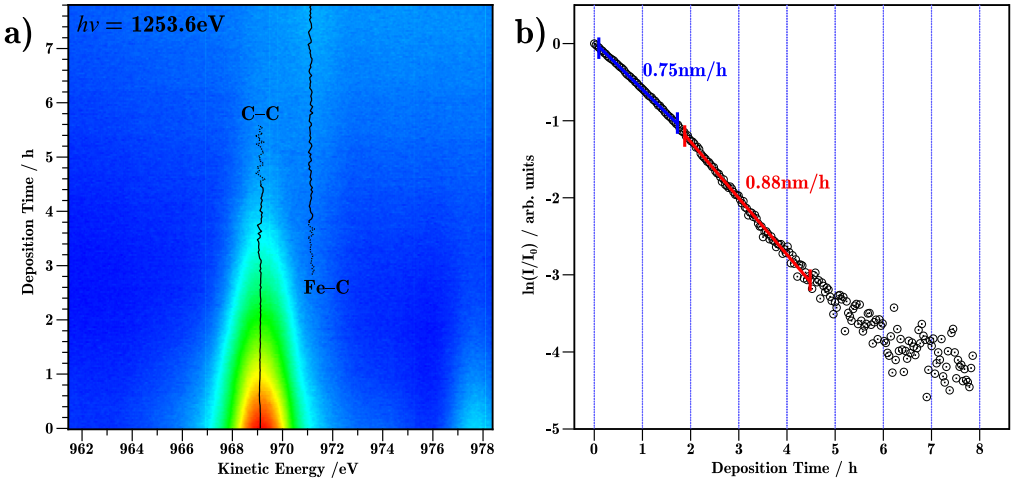

Figure 6.1. REES data acquired during deposition of a 12 nm thick film of Fe. **a)** Raw snapsot spectra of the C 1*s* core level with respect to deposition time. The kinetic energy for the C–C and Fe–C components during deposition are shown by the annotated black lines. **b)** A semi-logarithmic plot showing the exponential attenuation of C 1*s* photoelectron intensity during Fe deposition.

6.1a shows 2d plot of C 1*s* snapshot spectra acquired during deposition of a 12 nm-thick overlayer of Fe on moderately boron-doped diamond. The main C−C sp^2 component is significantly attenuated during the deposition and no peak shift is observed. As the substrate is buried, the small Fe-C component eventually becomes the dominant peak at ∼6 h. Figure 6.1b is a normalised semi-logarithmic plot of the C 1*s* peak intensity with deposition time. This attenuation has been fitted with two linear slopes. The need for two linear fits is due to an increase in the K-cell deposition rate brought about by a small increase in power around the 2 h mark. The gradients of these fits, i.e. the attenuation rate α, are $-0.62\,\mathrm{h}^{-1}$ (**blue line**) and $-0.73\,\mathrm{h}^{-1}$ (**red line**). According to the NIST EAL database [218] the averaged EAL, λ, of C 1*s* photoelectrons in an Fe overlayer is 1.20 nm. The deposition rate, D, of the K-cell is described by

$$D = -\alpha\lambda. \tag{6.1}$$

Using equation 6.1, the deposition rates in Figure 6.1b are $0.75\,\mathrm{nm\,h^{-1}}$ and $0.88\,\mathrm{nm\,h^{-1}}$ respectively. After 5 h of deposition, the C 1s intensity is so low, that the accuracy of the fit begins to fail, hence the increased spread of data points in this region. Figure 6.2 shows the XPS survey scan and Fe 2p peak of the 12 nm Fe overlayer. The survey scan shows the primary and Auger photoelectron peaks of Fe with no other contaminating species. The C 1s peak from the substrate has been fully attenuated. The high resolution Fe 2p scan

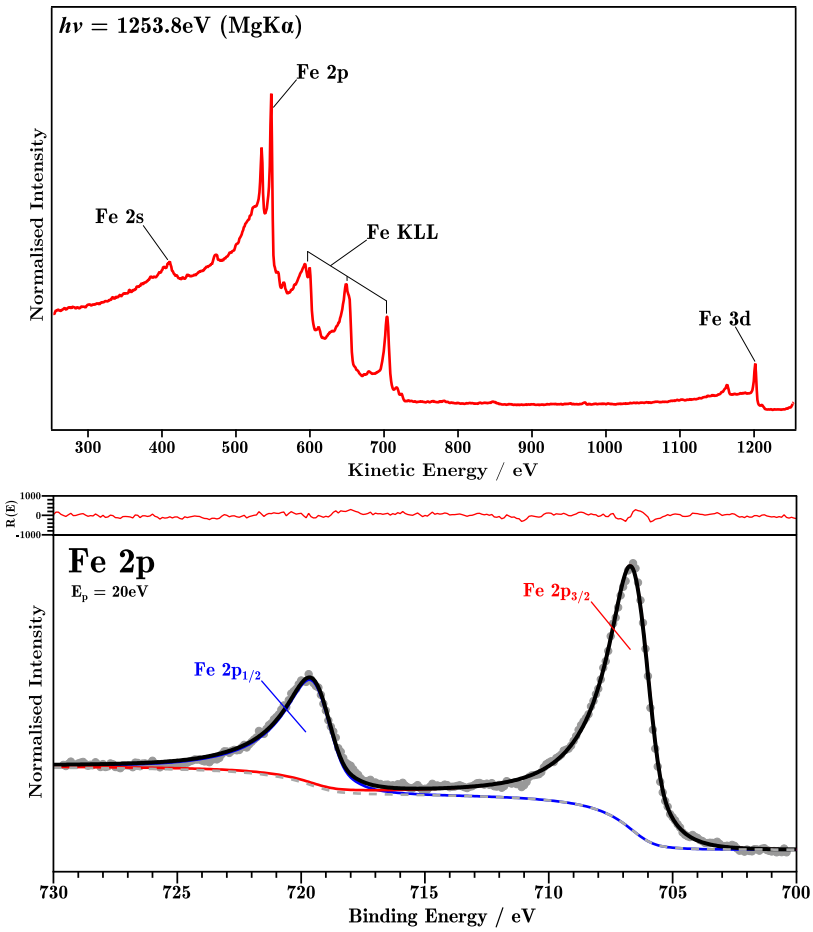

Figure 6.2. XPS spectra of a 12 nm-thick film of Fe. **Top:** A survey scan showing the principal Fe photoelectron peaks. **Bottom:** A high resolution scan of the Fe 2p core level. The red inset shows the residual $R(N)$. Table 6.1 shows the fitting results for this spectrum.

Component	Position /eV	FWHM / eV	∑GL ratio	Doublet Ratio
Fe $2p_{3/2}$	706.7	2.2	0.75(*0.57)	1
Fe $2p_{1/2}$	719.7	2.6	0.75(*0.57)	0.45

Table 6.1. Fitting results for the spectra in Figure 6.2

shows the two spin-orbit coupled components ($j = 1/2, 3/2$) with an area ratio of 0.45 : 1, which is near the expected area ratio of 0.5 : 1. The two components are due to bulk Fe (i.e. Fe–Fe), with no evidence of any other Fe-containing species. The initial stages of depositing a thin 1.25 nm Fe overlayer has also been reported. Figure 6.3 shows an XPS survey scan and C 1s peak of a 1.25 nm Fe overlayer on moderately boron-doped diamond. The key difference in the survey scans between a thick and thin overlayer of Fe is the presence of the C 1s from the underlying diamond (111) surface. The high resolution C 1s

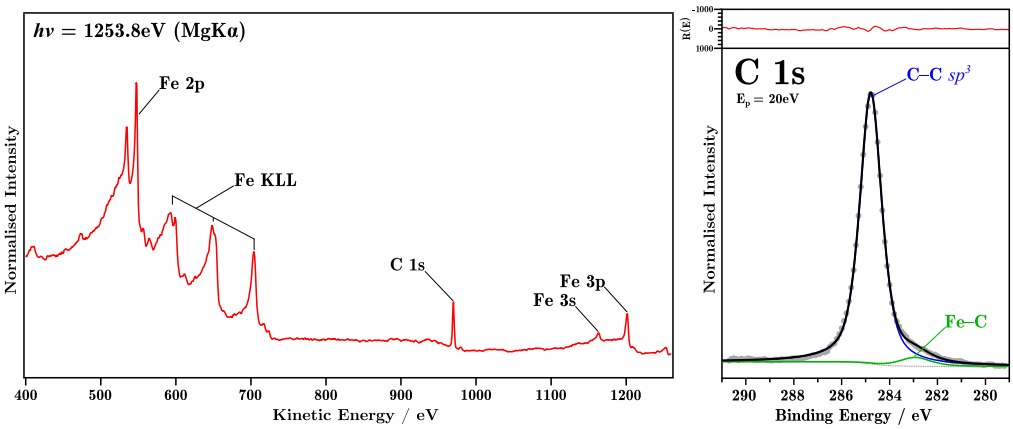

Figure 6.3. XPS spectra of a 1.25 nm-thick film of Fe. **Top:** A survey scan showing the principal Fe photoelectron peaks and C 1s from the diamond substrate. **Bottom:** A high resolution scan of the C 1s core level revealing a Fe-C component. The red inset shows the residual $R(N)$. Table 6.2 shows the fitting results for this spectrum.

Component	Position /eV	FWHM / eV	∑GL ratio	At%
C–C sp^3	284.8	1.1	0.69	95.6
Fe–C	282.9	1.6	0.69	4.4

Table 6.2. Fitting results for the spectra in Figure 6.3

scan reveals a component on the low binding energy side of the main C−C sp^3 component ($\Delta = -1.9\,\text{eV}$) which is attributed to the iron carbide (FeC) interface between the Fe and the diamond surface.

6.1.2 Structural and Electronic Transition

As reported in section 5.2.1, an insulating diamond surface will undergo a charging effect at the surface which reduces the kinetic energy of photoelectrons ejected from the surface. This charging effect is inhibited by creating a 'shorting' path on the surface with a conducting structure, which a (2×1)-reconstruction will provide. A metallically-conducting overlayer will also have the same effect. Figure 6.4a shows a 2d plot of C 1s snapshot spectra acquired during deposition of a 1.75 nm-thick overlayer of Fe on an insulating HPHT diamond surface. Before deposition the C 1s peak resides at 966.3 eV, which is ~ -2 eV compared to (1×1) moderately boron-doped diamond (111) surface, indicating a significant amount of surface charging. During the first 20 min of Fe deposition, the intensity of the C 1s peak first increases before the expected attenuation begins, and the peak shifts toward higher kinetic energy. Significant surface charging reduces the overall photoemission intensity from a given core level (and the inelastic background). So it follows that as surface charge is compensated and given a path to ground via the iron overlayer, the C 1s intensity would actually increase before the attenuating effects of the overlayer begin to manifest. Therefore, the maximum C 1s intensity actually occurs at $\sim$0.5 nm. In figure 6.4b, the peak shift with respect to the overlayer thickness has been plotted. As well as the overlayer thickness calculated from the K-cell calibration, the number of complete monolayers of Fe (according to the pseudo-morphic fcc growth mode) is shown at the top of the plot by the blue numbers and dashed lines. The C 1s does not reach its 'true' binding energy until at least three

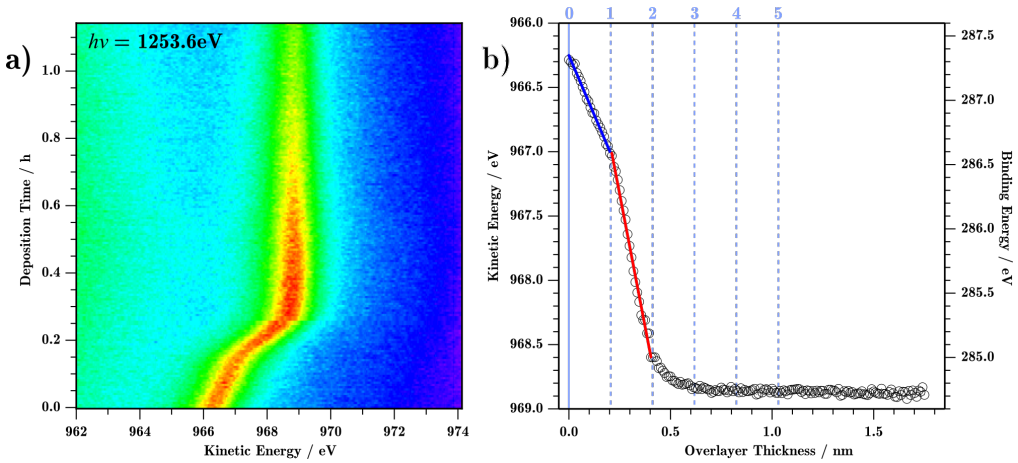

Figure 6.4. REES data acquired during deposition of a 1.75 nm thick film of Fe on an insulating HPHT diamond. **a)** Raw snapshot spectra of the C 1*s* core level with respect to deposition time. **b)** The C 1*s* peak position with respect to Fe overlayer thickness (and Fe layer number, shown by the blue numbers at the top). The blue and red lines represent two linear fits with differing gradients.

layers of iron have been deposited. The rate of kinetic energy shift appears to be different during the first three layers of Fe. The growth of layers one and two results in a linear shift of kinetic energy shown by the red and blue lines in figure 6.4b. At this stage, the Fe overlayer is unable to fully compensate for the diamond surface charging, even when a full layer of iron coverage has been achieved. This may be due to the conductivity characteristics of metals at ultra-thin thicknesses, that is, metal sheet resistivity increases with decreasing thickness. The reduced conductivity (hence increased resistivity) of the complete Fe monolayer and ultra-thin Fe film can likely be attributed to the Fuchs and Sondheimer model of electron scattering near metal surfaces [219, 220]. Layer three sees a reduction in the kinetic energy shift as the true value of the C 1*s* is approached. Above three layers, the Fe overlayer is fully compensating for the surface charging, which indicates that the Fe has a sufficient number of charge carriers and a direct path to ground in order to replace the electrons lost in the photoemission process. However, this does not necessarily mean that the

iron is exhibiting bulk conductivity – this would require surface conductivity measurements which have not been conducted at this time. Figure 6.5 shows the result of a LEED measurement taken from a 12 nm-thick Fe overlayer on a (111)(2 × 1) diamond surface after heating to 450 °C. The temperature was selected in order to anneal the Fe overlayer without inducing graphitisation. It has been shown previously that the Fe initially deposits in a disordered pseudo-morphic (111) motif, but heating the Fe film above 300 °C (as shown later in section 6.2) provides enough thermal energy for dislocations, point defects, and stacking faults to be annealed out of the film. Furthermore, the most stable polymorph of Fe below the Curie temperature is *bcc* [221], so annealing allows the Fe to undergo a phase transition from the metastable pseudo-morphic *fcc* to stable *bcc*. The LEED pattern observed in figure 6.5 is the result of the Fe (110) *bcc* lattice being constrained by the *fcc* diamond lattice. As shown in previous studies by Cooil *et al.* [20, 56], the Fe is able to lattice match in two dimensions, such that the *bcc* [$\bar{1}$10] and *fcc* [$\bar{2}$11] directions are parallel as well as their orthogonal counterparts in the surface plane. The surface unit

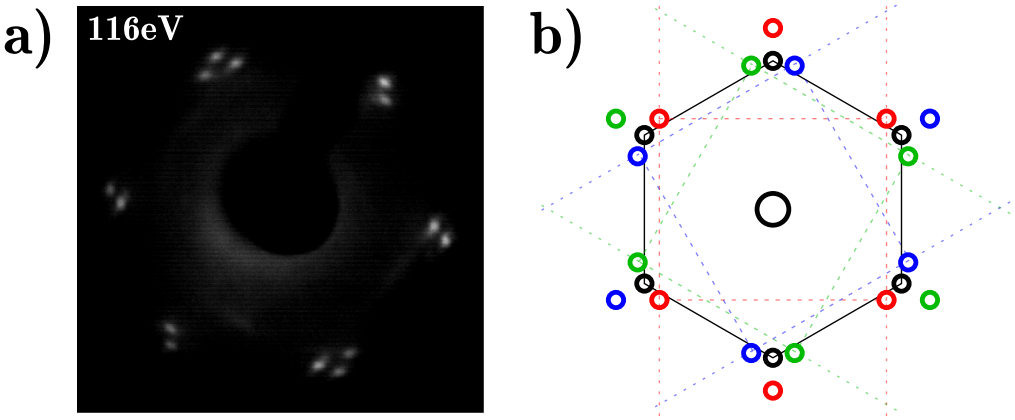

Figure 6.5. a) LEED pattern of an Fe overlayer on a (111)(2×1) diamond surface after heating above 440 °C, exhibiting at least two-rotational domains of a *bcc* (110) structure. Electron energy shown in top left. **b)** A simulated LEED pattern demonstrating a Nishiyama–Wassermann orientated *bcc* iron (110) reciprocal lattice on a *fcc* diamond (111)(1 × 1) reciprocal lattice. Subfigure **(b)** is adapted from [56]

cell for the *bcc* (110) plane is a rhombus where $|\overrightarrow{a}| \neq |\overrightarrow{b}|$, meaning that the reciprocal space LEED pattern will appear as stretched hexagon. This pattern is able to map on to the fcc (111) diamond surface three times where each domain is rotated 60° with respect to each other. This $bcc-fcc$ interface, which was first proposed by Nishiyama [222] and Wassermann [223] (NW), results in the simulated LEED pattern shown in figure 6.5b [20, 56]. However, the experimental LEED pattern shown in figure 6.5a is missing some of the expected spots. As this is a thick iron film, the (1×1) and (2×1) spots from the underlying diamond are not visible. As seen in section 5.2.1, the LEED pattern from the (2×1) is missing spots from one particular rotational domain, meaning that the diamond surface has only reconstructed in two directions. For Fe deposited on a (1×1) surface, the three rotational *bcc* domains would be expected to occur roughly an equal number of times, meaning that the NW LEED pattern would have the same intensity across all the spots. The missing spots in figure 6.5a correspond to the *bcc* domain that would be aligned with the missing reconstruction domain on the diamond surface. This alludes to an important step in the iron-mediated graphitisation process, as the iron overlayer is capable of transferring the crystallographic register of the diamond surface, in this case a $(111)(2 \times 1)$ diamond reconstruction with two predominant reconstruction domains.

6.2 Catalytic Graphitisation of Diamond

6.2.1 Intrinsic Graphene Growth

The results in this section follow on from the Fe deposition data presented in figures 6.1 and 6.2 on a semiconducting $(111)(2\times1)$ diamond surface. Figure 6.6 shows a REES acquisition taken during a heating and cooling cycle from ∼20 °C

to ∼685 °C of a 12 nm Fe overlayer deposited on a semiconducting (111)(2 × 1) diamond surface. Snapshot spectra of the C 1*s* and Fe $2p_{3/2}$ peaks have been fitted and the area intensities have been plotted against the temperature at which the spectra were recorded at. The spectra were recorded every 15 seconds using an analyser pass energy of 100 eV to maximise count rate. The four regions (A, B, C, and D) in figure 6.6 signify temperature ranges where the behaviour of the C 1*s* and Fe $2p_{3/2}$ intensities changes, therefore highlighting a growth stage in the graphitisation process. Region A extends from 30 °C to 510 °C. In this

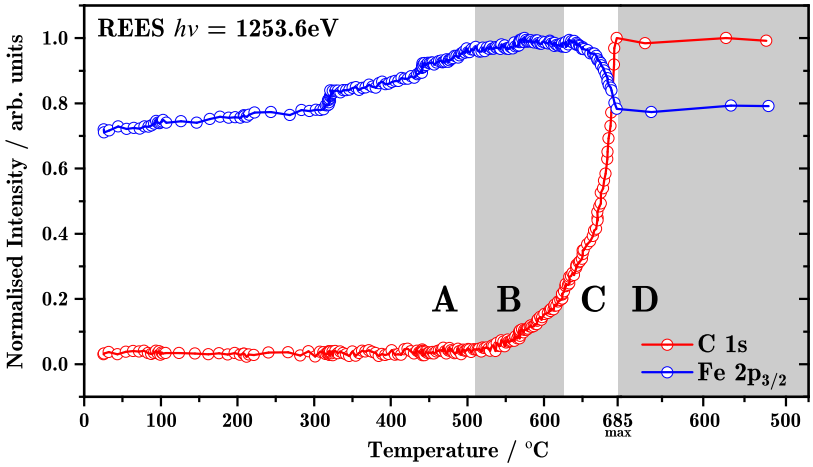

Figure 6.6. Normalised intensities of the C 1*s* and Fe 2*p* core level acquired from a 12 nm thick overlayer of Fe on diamond during a heating-cooling cycle. The maximum temperature reached during the heating cycle was 685 °C. Four regions (A, B, C, and D) are identified, corresponding to different key stages during the graphitisation process.

temperature regime, the C 1*s* peak intensity does not change at all, whereas the Fe $2p_{3/2}$ peak steadily increases from ∼70 % to ∼95 % of its maximum intensity. At 320 °C and 440 °C, the temperature ramp was briefly halted as evidenced by the large density of data points at these temperatures. The increase in Fe $2p_{3/2}$ photoelectron yield is attributed to an improvement of the Fe film crystallinity with annealing (i.e. channelling, imrovement in EAL, etc.), as it transitions from a disordered pseudomorphic (111) *fcc* structure to a highly-

ordered single crystal (110) *bcc* structure, supported by LEED data in section 6.1.2 and previous studies of iron phase transitions [20, 56]. The increase in the photoelectron yield at 320 °C and 440 °C when the temperature is constant confirms that temperature-related effects to photoemission yield can be ruled out (although core level broadening / lineshape changes due to temperature is not observed for metal samples [29, 224]). Region B represents a smaller range of temperatures between 510 °C and 625 °C where the C 1*s* intensity begins to increase rapidly. In this temperature regime, the hot iron layer catalytically breaks the sp^3 carbon bonds at the diamond surface and accepts interstitial carbon atoms into its lattice due to its increased carbon solubility. As more carbon is accepted into the iron overlayer from the iron-diamond interface, the interstitial carbon is transported toward the iron-vacuum interface. It follows then, that the increase in the C 1*s* intensity in region B is due to interstitial carbon moving into the XPS analysis volume from the deepest analysis depth around 3λ. The Fe $2p_{3/2}$ intensity reaches its maximum in this regime, indicating that the phase transition from *fcc* to *bcc* is complete at ∼550 °C. Region C starts at 625 °C and stops at the maximum temperature of 685 °C (although the lowest reported onset temperature for this regime is as low as 500 °C [20]). The C 1*s* intensity begins to increase rapidly as more and more carbon is transported into the analysis volume and toward the surface. In this region, the Fe $2p_{3/2}$ peak begins to decrease in intensity as carbon reaches the surface and recrystallises into graphene. The attenuation of the Fe $2p_{3/2}$ peak can be used as a rough estimate to determine when a full layer of sp^2 carbon covers the iron surface. Using the NIST EAL database [218] and an average $\lambda = 1.51$ nm, the Fe $2p_{3/2}$ peak is expected to attenuate by (20 ± 10) % for a 0.335 nm overlayer of carbon. The large uncertainty is due to the inherent inaccuracy of the calculated EAL. In region D, the temperature ramp is quickly reversed to quench the graphitisation

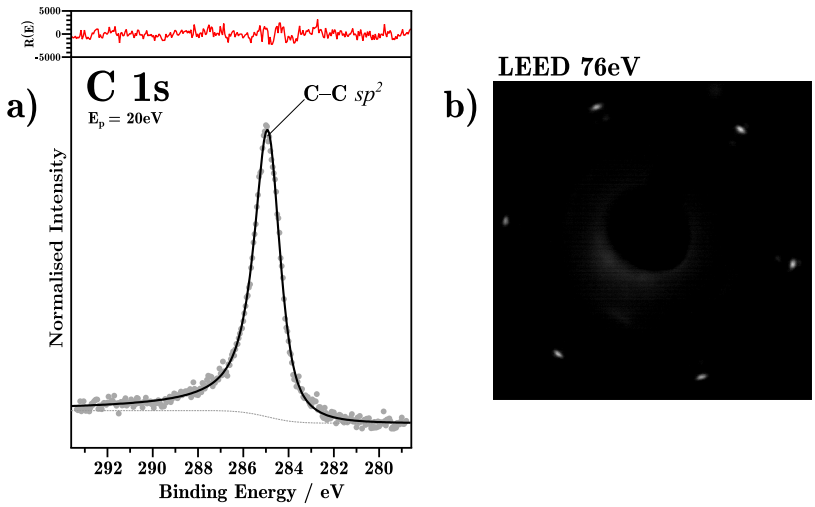

Figure 6.7. a) A high resolution scan of the C 1*s* core level from graphene on a 12 nm Fe overlayer on diamond after graphitisation. The red inset shows the residual $R(N)$. Table 6.3 shows the fitting results for this spectrum. **b)** A LEED pattern acquired after graphitisation on the same surface.

reaction and prevent a multilayer graphene structure from forming. Following the heating and cooling cycle, XPS and LEED was conducted below 50 °C, shown in figure 6.7, to determine whether graphene had been produced. A high resolution spectrum of the C 1*s* core level post-graphitisation can only be fitted with a single asymmetric C=C sp^2 component, with no additional components at higher or lower binding energies which would correspond to oxide and carbide species respectively. The lack of a strong $\pi - \pi*$ transition at ~290 eV (which arises from interaction of the π-bonds between multiple graphene sheets [225, 226]) rules out multilayer growth. The C=C sp^2 component is centred at 284.9 eV which is significantly higher in binding energy compared to the typical value of sp^2 carbon of ~284 eV [225, 226]. This increase in the C 1*s*

Component	Position / eV	FWHM / eV	∑GL ratio	At%
C=C sp^2	284.9	1.4	0.71(*-0.23)	100

Table 6.3. Fitting results for the spectra in Figure 6.7a. (*Asymmetry)

binding energy indicates a strong interaction between the graphene layer and the underlying iron which induces n-type doping in graphene, an effect which has been observed in previous studies on this surface [20]. Metal-induced doping has also been observed experimentally, for example in ARPES measurements taken from CVD graphene on a Fe (110) substrate [227] and DFT modelling of graphene-metal contacts [228]. A LEED pattern was also acquired post-graphitisation and reveals a (1×1) hexagonal pattern typical of graphene. The diffraction spots have the same intensity indicating a flat 2-dimensional structure (in constrast to the corrugated layers of the (111) diamond plane) and only a single rotational domain is present that is in registry with the underlying diamond surface (see figures 5.4 and 5.6 for LEED patterns on diamond surface). As the incident electron beam spot is on the order of millimetres, a similar-sized area is also sampled during LEED analysis, meaning that the graphene produced here has excellent crystallinity over a large area.

6.2.2 Boron-doped Graphene Growth

For the work conducted in sections 6.2.1 and previous diamond-related work conducted by the Aberystwyth materials research group, a moderately-doped (111)-orientated diamond was used [17, 20, 56]. The boron-doping level for this natural diamond is estimated to be $\sim 10^{16}\,\mathrm{cm}^{-3}$, which is enough to make the diamond semi-conducting evidenced by a lack of significant charging on the sample surface during XPS analysis. In atomic composition percentage, the amount of boron in the carbon matrix is $\sim 0.000\,01\,\%$ which is far below the detection limit of the analyser (and the XPS technique in general). Using MgKα x-rays, the detection limit for boron in a carbon matrix is 1 at% calibrated to a maximum intensity of 10^5 counts/s of the Ag3$d_{5/2}$ peak from clean Ag [212]; this corresponds to a boron concentration greater than $1.8 \times 10^{21}\,\mathrm{cm}^{-3}$.

A heavily boron-doped diamond grown using microwave plasma-assisted CVD (MPCVD) by the Kawarada group at Waseda University (Japan) [229] was provided for a catalytic graphitisation experiment. The sample consisted of a 3×3 mm insulating type IIa diamond with a 300–400 nm heavily boron-doped diamond (HBDD) layer grown by MPCVD onto the (111) surface. The diamond was shipped from Japan immediately after growth, so the surface was expected to be H-terminated. Upon arrival, the HBDD surface was first cleaned by sonication in acetone for 10 min, then rinsed with IPA, and blow-dried with nitrogen gas. The HBDD surface was studied using C-AFM and Raman spectroscopy to determine the r.m.s. roughness and the boron doping concentration [B] respectively. Figure 6.8 shows the C-AFM results from the HBDD. The r.m.s. roughness was ∼3.67 nm, calculated by Gwyddion SPM software [230] using the full area of the scan. Raman spectra were acquired using a 532 nm laser source, operated at 10 mW at an objective lens with ×100 magnification. A gate time of 60 s over 10 accumulations was required to achieve an acceptable signal-to-noise. Figure 6.9 shows a *ex-situ* Raman spectra taken before graphitisation from the HBDD surface between 100 and 3000 cm^{-1}. The main Raman line for diamond does not appear as a single peak at 1332 cm^{-1}, but rather as a broad shoulder on the higher wavenumber side of the broad peak at 1166.7 cm^{-1}, labelled $L2$. The precise diamond Raman line position cannot be determined, however the downshift and asymmetric broadening is due to two reasons. The high concentration of boron in the diamond lattice would result in semiconductor degeneracy of valence states near the Fermi level, and the diamond would begin to act like metal in terms of conductivity. Electronic scattering from this continuum of states near the Fermi level interacts with the discrete diamond Raman line resulting in a phenomenon known as Fano

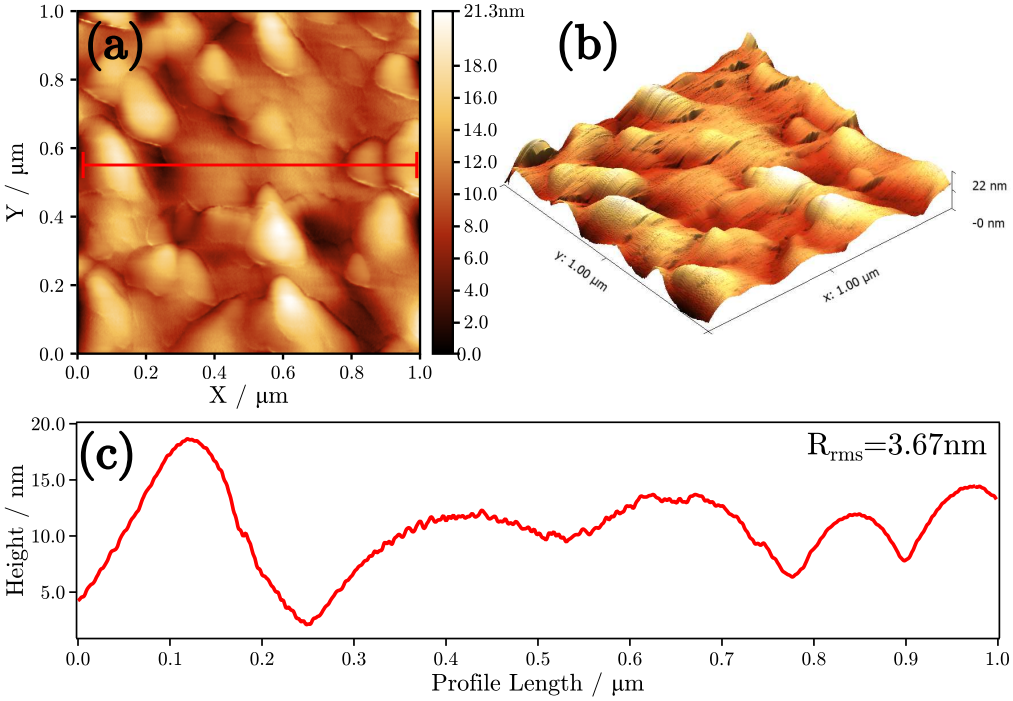

Figure 6.8. C-AFM images taken from the surface of the Waseda (111) HBDD. **(a)** A 1×1 µm C-AFM scan and **(b)** a 3d representation of the HBDD surface. Note that the vertical scales have been exaggerated. **(c)** A line profile extracted from the red path in **(a)**. The surface height varies up to ∼20 nm but the r.m.s. roughness as calculated by Gwyddion is 3.67 nm.

resonance, which broadens the diamond Raman line and imparts significant asymmetry. The downshift of the diamond Raman line is likely due to a deformation of the lattice as boron is preferentially incorporated along (111) direction [231, 232]. Another large broad peak at 431.2 cm^{-1} $L1$ dominates the spectrum at lower wavenumbers, and there also appears to be several smaller features between $L1$ and $L2$. $L1$ has been attributed as a boron-related feature and $L2$ is a C−C vibration mode; both features are characteristic of HBDD [233]. The position of the $L1$ feature, ν_{L1}, as determined by a Lorentzian peak fit can used to calculate the boron concentration [B] (cm^{-3}) of the diamond by

using the equation [234]:

$$[B] = 8.44 \times 10^{30} \exp -0.048\nu_{L1} \tag{6.2}$$

Using equation 6.2, the boron concentration of the Waseda diamond was calculated to be $(8.66 \pm 3.32) \times 10^{21}$ atoms/cm^3. Above 1300 cm^{-1}, characteristic Raman modes of non-diamond carbon are observed, namely the D (1358.5 cm^{-1}), G (1584.8 cm^{-1}), and $2D$ ($\sim$2710 cm^{-1}) peaks. This non-diamond carbon is likely a result of the MPCVD growth process, as high concentrations of boron have been known to increase the likelihood of grain boundaries and growth defects in diamond films. For example, in micro- and nanocrytalline diamond films, boron has been observed to accumulate in grain boundaries [235]. The HBDD sample was then loaded into the REES system and heated to 340 °C to drive off any adventitious carbon and oxygen

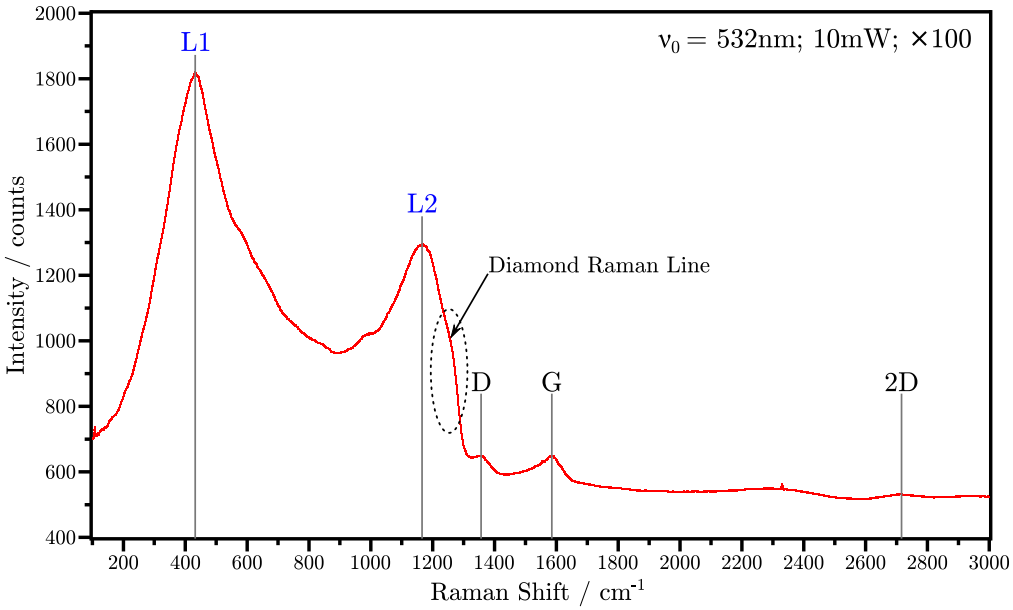

Figure 6.9. Raman spectrum between 100 cm^{-1} and 3000 cm^{-1} for the HBDD before it was introduced to the UHV system. The positions of the graphite-related features, D, G, and $2D$ as well as the boron-related features $L1$ and $L2$ have been labelled.

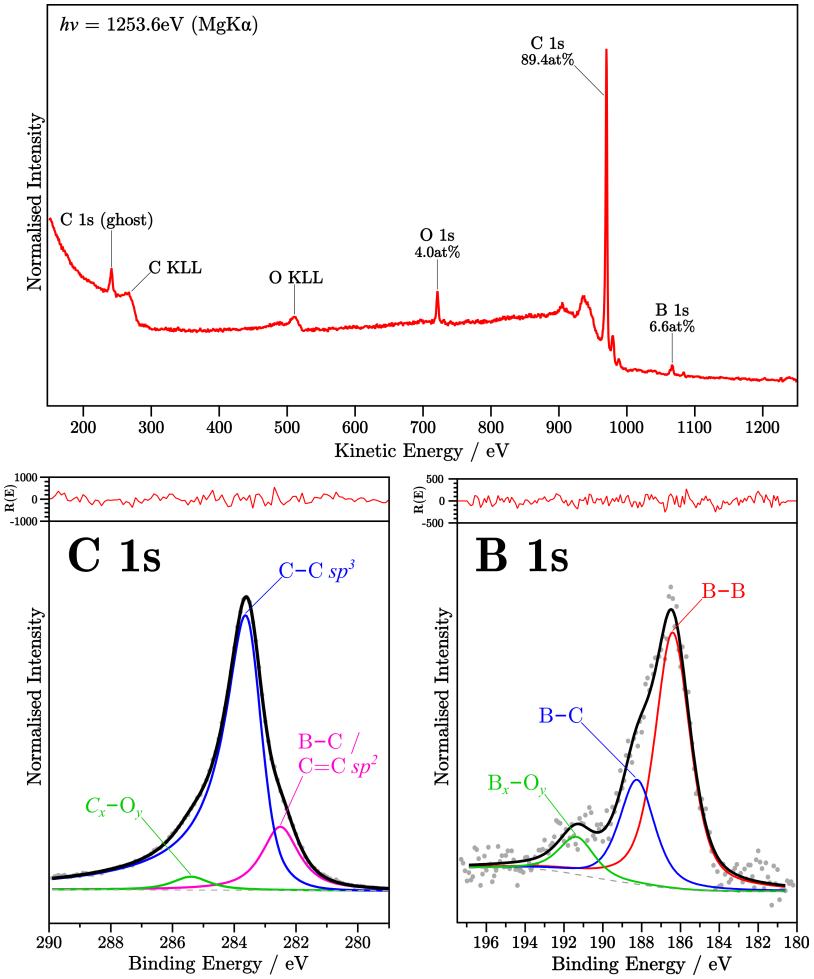

Figure 6.10. XPS spectra of the HBDD surface after heating to 340 °C. **Top:** A survey scan showing the C 1*s* peak from the diamond, O 1*s* from the surface oxides, and the B 1*s* peak from the boron-dopant. **Bottom:** High resolution scans of the C 1*s* (left) and B 1*s* (right) core levels. The red inset traces show the residual $R(E)$. Table 6.4 shows the fitting results for these spectra.

groups. Figure 6.10 shows the XPS survey scan, C 1*s*, and B 1*s* core level scans after heating to 340 °C. The expected C 1*s*, C *KLL*, and C 1*s* ghost features from the predominate carbon matrix are observed in the survey spectra. Diamond surfaces that emerge from a CVD reactor are typically H-terminated, however there appears to be a significant oxygen contribution, evident from the O 1*s* and O *KLL* peaks which account for 4.0 at%. The peak at ∼1066 eV

Component	Position /eV	FWHM / eV	∑GL ratio	Area / kcpseV
C 1s				
C–B / C=C sp^2	282.5	1.4	0.70	18.2
C–C sp^3	283.7	1.4	0.70(*-0.59)	86.3
C_xO_y	285.4	1.4	0.70	3.9
B 1s				
B–B	186.4	2.2	0.30	5.1
B–C	188.2	2.2	0.30	2.1
B_xO_y (x/y <1.5)	191.3	2.2	0.30	0.74

Table 6.4. Fitting results for the spectra in Figure 6.10 (*Asymmetry).

KE is the B1s core level and accounts for 6.6 at% of the analysis volume. High resolution scans of the C 1s reveal a highly asymmetric C−C sp^3 peak at 283.7 eV, which is ∼0.2 eV below the flat-band binding energy for semi-conducting diamond (i.e. 283.9 eV) [236]. This means that the Fermi level resides within the valance band, as expected of metallic conductors. The C−C sp^3 component was fitted using a floating asymmetric factor which converged on a value near to that of pure Fe (see table 6.1) further confirming the metallic conductivity of the diamond. Compared to the oxygen-terminated moderately boron-doped diamond in section 5.1.1 (see figure 5.2), the C−C sp^3 binding energy is shifted by −0.5 eV in the HBDD. This C 1s energy shift has been shown to be closely related to the boron concentration in the diamond lattice. For a similar single-crystal (111) HBDD with $[B]$ =∼2×10^{21} atoms/cm^3, Yokoya *et al.* demonstrated using ARPES that the Γ-point in the diamond reciprocal space shifted (0.4 ± 0.2) eV above the Fermi level [140]. This energy shift between the diamond Γ-point and Fermi level is roughly the same energy shift seen in the C 1s core level using XPS, both in hard X-ray photoelectron spectroscopy (HaXPES) experiments (which has a greater photoelectron yield from the 'bulk' crystal) conducted by Yokoya *et al.* [237], and in this work. The larger chemical shift seen in this work is a result of the larger dopant density in the Waseda HBDD.

On the higher binding energy side of the C 1s core level, the component at 285.4 eV has been attributed to C−O/C−OH species on the HBDD diamond, and comparing the intensity to the corresponding component in the O 1s peak, reveals a stoichiometry of 1 : 1. The peak position and stoichiometry suggests that the surface oxygen could be in the form of C−O or, if the sample was previously hydrogen terminated after growth, C−OH. The component at 282.5 eV has been attributed to both C=C sp^2 and substitutional boron in the diamond lattice in the general form C_x−B. In sputtered or CVD-grown boron carbide films, typically of the B_4C stoichiometry, the carbide component of the C 1s peak appears between 281.6 eV to 283.5 eV [237–242].

The high resolution scan of the B 1s can be resolved into three components. The component at 186.4 eV corresponds to B−B, either in the form of dimer centres in the carbon matrix or bulk boron metalloid. In the literature, elemental boron bonding is typically assigned a binding energy of 187.2(9) eV when charge referenced either to boron oxide (B_2O_3) at 192.4 eV or adventitious hydrocarbons at 284.8 eV [78, 238]. In this sample, the B−B peak resides near the lower bound of the accepted range of binding energies likely due to the high conductivity of the carbon matrix. The position of the component at 188.2 eV BE corresponds to boron carbide species (B−C) expected of substitutional boron in a carbon matrix. The corresponding C−B component in the C 1s peak overlaps the C=C sp^2 component, so precise stoichiometry cannot be determined. The final component in the B 1s peak at 191.3 eV corresponds to a boron oxide species (B_x−O_y) with an approximate stoichiometry of $x/y = 0.43$ when compared to same component in the O 1s. When accounting for uncertainty in the pseudo-Voigt peak fitting, this stoichiometry could suggest

Component	Position /eV	FWHM / eV	∑GL ratio	Area / kcpseV
C 1*s*				
C–B / C=C sp^2	282.3	1.4	0.61	11.3
C–C sp^3	283.6	1.4	0.61(*-0.50)	64.7
π–π*	290.0	4.0	0.61	3.8
B 1s				
B–B	186.4	2.3	0.30	3.3
B–C$_x$	188.2	2.3	0.30	2.8
B–C$_y$	190.2	2.3	0.30	1.5
B$_x$**O**$_y$ **(x/y = 1.5)**	192.9	2.3	0.30	0.81

Table 6.5. Fitting results for the spectra in Figure 6.11 (*Asymmetry).

that boron oxide is in the form of boron trioxide (B_2O_3, $x/y = 0.4$) or boron dioxide/oxycarbide (BO_2/BCO_2, $x/y = 0.5$). The relative shift of -1.1 eV compared to the accepted boron trioxide binding energy infers that the $B_x{-}O_y$ component actually corresponds to a boron dioxide/oxycarbide species [239].

Continuing with the standard catalytic-graphitisation procedure, the HBDD sample was heated to 1000 °C whilst ensuring that the chamber pressure did not exceed 1×10^{-7} mbar. The sample was then cooled using the same procedure outlined in section 5.2.1 before repeating the XPS measurements. Figure 6.11 shows the XPS survey scan as well as the C 1*s* and B 1*s* high resolution spectra after heating to 1000 °C. The survey spectra shows that nearly all the oxygen has been removed from the surface. The O *KLL* Auger peak suggests that a trace amount (∼0.6 %) of oxygen remains on the surface of the HBDD. There was also a relative increase in the B 1*s* peak compared to the C 1*s* peak, with boron now accounting for 9.4 % of the same analysis region. With the photoemission signal from the subsurface no longer being attenuated by the surface oxygen, this boron:carbon ratio of the core levels can be used to calculate a more accurate [B] in the surface region. The high resolution C 1*s* spectrum reveals that all C−O

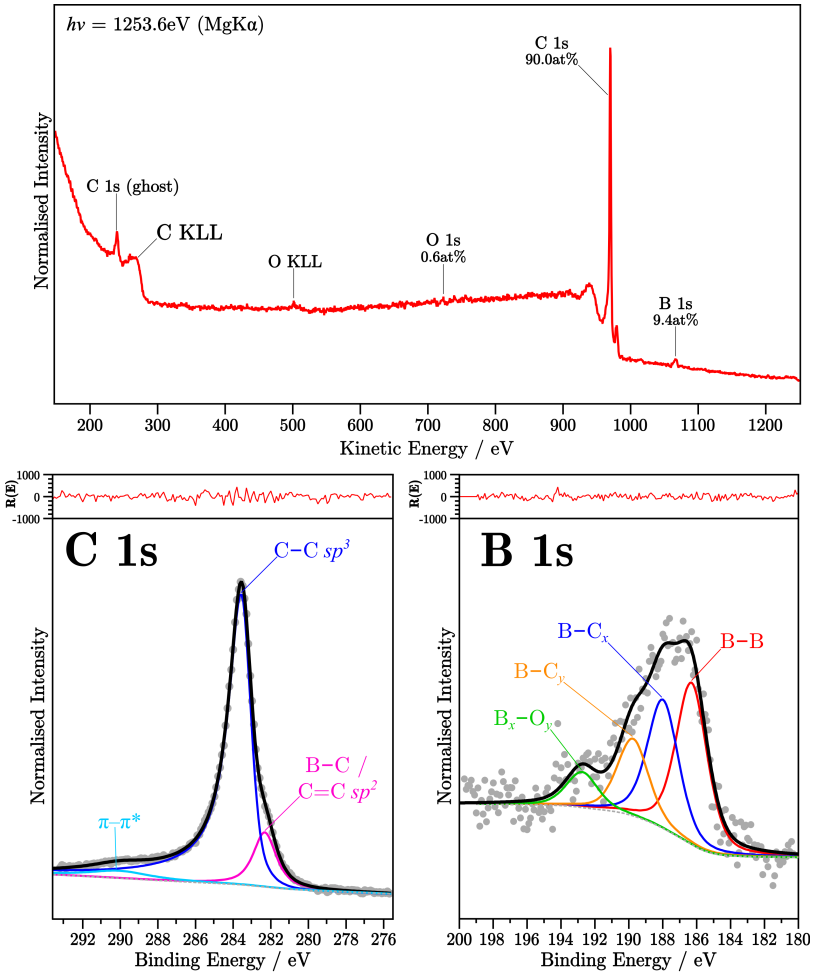

Figure 6.11. XPS spectra of the HBDD surface after heating to 1000 °C. **Top:** A survey scan showing the C1*s* peak from the diamond and the B1*s* peak from the boron-dopant. **Bottom:** High resolution scans of the C1*s* (left) and B1*s* (right) core levels. The red inset traces show the residual $R(E)$. Table 6.5 shows the fitting results for these spectra.

species have been removed, and the $\pi \rightarrow \pi*$ transition has appeared at 290.0 eV, indicating that an oxygen-free graphitic structure has emerged in the analysis volume. This means that the trace oxygen seen in the survey scan is likely due to boron oxide components only. Whilst carbon oxygen bonds are readily broken at 1000 °C, boron oxygen bonds are more resistant to temperature. Boron oxides on the surface of boron carbide often require temperatures in excess of 1500 °C

to be removed fully [243]. The B 1s peak has broadened post-1000 °C which has been interpreted as a new component. The B−B component resides in the same position at 186.4 eV, as well as the B−C component at 188.2 eV, which is now annotated as $B-C_x$, to indicate a specific (but unknown) boron carbide phase. The B_x-O_y component has shifted to a higher binding energy (192.9 eV) and the stoichiometry, when compared to the O 1s intensity, has changed to $x/y = 1.5$. This stoichiometry indicates that a boron suboxide has formed in the analysis region, but the binding energy shift of this component predicts a higher oxidation state (more electronegative oxygen atoms), and corresponds closely to the more stable boron trioxide species (B_2O_3). It should be noted that the decreased signal-to-noise level of the both the O 1s core level and the oxide component in the B 1s core level imparts a large uncertainty in the stoichiometry calculation. The region between the B_x-O_y and $B-C_x$ components has been fitted with a new component at 190.2 eV. This new component is believed to be a new boron carbide phase and hence has been annotated as $B-C_y$.

A 10 nm overlayer of Fe was then deposited onto the HBDD sample to completely attenuate the diamond C 1s signal. The sample was quickly heated to 640 °C whilst the C 1s core level was monitored using snapshot XPS spectra (N.B. the formal REES technique was not used here). The sample was held at 640 °C until the C 1s signal began rapidly increasing, at which point the sample was rapidly cooled to the quench the catalytic conversion. Figure 6.12 shows the XPS survey scan and high resolution scans of C 1s and B 1s post-graphitisation. The survey spectrum shows features related to the Fe-overlayer, of which the Fe $2p_{3/2}$ peak was used in quantification. Using the Fe $2p_{3/2}$ intensity before and after the 640 °C heating step, and the Beer-Lambert's law (see equation 2.16) with $\lambda = (1.49 \pm 0.15)$ nm (NIST EAL Database [218]), the carbon overlayer is

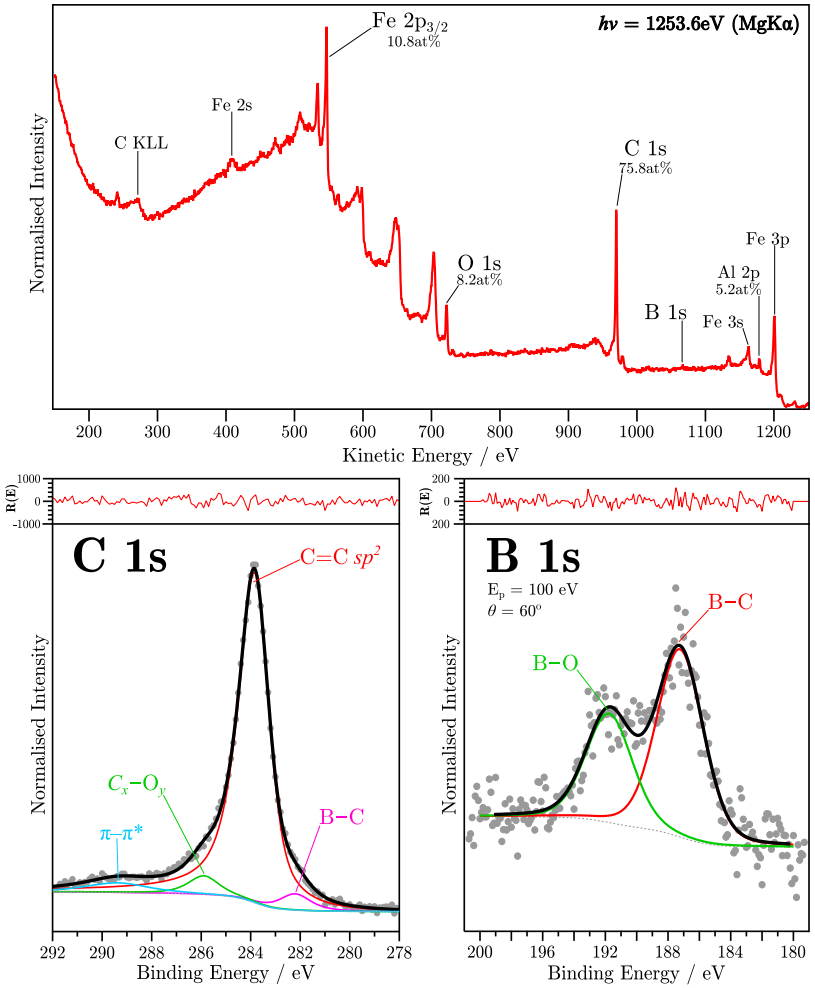

Figure 6.12. XPS spectra of the HBDD surface after depositing 10 nm of Fe and heating to 640 °C. **Top:** A survey scan showing Fe-related features and an intense C 1*s* peak related to surface graphite. Contaminant Al peaks are also detected. **Bottom:** High resolution scans of the C 1*s* (left) and B 1*s* (right) core levels. The red inset traces show the residual $R(E)$. Table 6.6 shows the fitting results for these spectra.

calculated to be (1.37 ± 0.23) nm thick, which converts to $\sim 3.5 - 5$ layers of graphene. Due to the initial roughness of the diamond, single layer ordered graphene growth was not possible. The specific K-cell that was used in this deposition was contaminated with Al_2O_3 and so Al 2*p*, Al 2*s*, and O 1*s* peaks are observed in the spectrum, with Al comprising of 5.2 at% of the sample surface. Nevertheless, the contamination was not enough to completely inhibit

Component	Position /eV	FWHM / eV	∑GL ratio	Area† / kcpseV
C 1s				
C–B	282.2	1.5	0.75	1.8
C=C sp^2	283.9	1.5	0.75(*-0.23)	35.1
C_xO_y	285.9	1.5	0.75	2.0
$\pi-\pi*$	289.4	3.0	0.75	2.1
B 1s				
B–C	187.2	3.5	0.30	0.36
B–O	191.8	3.5	0.30	0.21

Table 6.6. Fitting results for the spectra in Figure 6.12 (*Asymmetry, †E_p-corrected to 30 eV).

the catalysis, and so layers of graphene were produced, as shown by the intense C 1s peak post-heating. Like the Fe, the Al does not incorporate into the resulting graphene sheets, and remains either as interstitial atoms, or results in localised alloying at high temperature. The decrease in the Al $2p/2s$ relative intensities supports this idea, as the Al signal is attenuated with the growth of the carbon overlayer. On the other hand, the relative increase in the O 1s means that oxygen has probably been incorporated into the graphitic overlayer. The high resolution C 1s scan is fitted with four components. The main asymmetric C=C sp^2 is positioned at a binding energy of 283.9 eV and has the same lineshape and asymmetry as the graphene produced in section 6.2.1 (see figure 6.7, table 6.3). The small downshift in binding energy compared to undoped graphene grown on diamond (284.9 eV, see table 6.3), is observed in boron-doped graphene due to a shift in the Fermi level caused by boron-carbon bonds, similar to the HBDD [244]. The C−B component is a small shoulder on the lower binding side of the main C=C sp^2, positioned at 282.2 eV, and the C−O component is positioned at 285.9 eV. These two peaks have similar peak areas compared to the C=C sp^2 component, which indicates that there is a similar concentration of boron and oxygen in the graphene layers. By taking the ratio of the intensities of the

C=C sp^2 and C−B component (i.e. B:C), the [B](at%) of the graphitic carbon was calculated to be ∼5 %. The $\pi \rightarrow \pi*$ transition reappears with the C 1s indicating the ordered graphitic nature of the surface carbon. Due to the low intensity of the B 1s peak, the core level scan pass energy was increased from 30 eV to 100 eV. The B 1s spectrum was also acquired at 60° off-normal with the sample surface facing toward the X-ray source. This had the effect increasing the B 1s count rate and the surface sensitivity of the measurement (N.B. avoid any possible B 1s contribution from the underlying substrate). Due to pass energy broadening, the B 1s could only be fitted with two components confidently, one at 187.2 eV representing the B−C species, and another at 191.8 eV from the B−O species. Despite a lack of clarity regarding chemical species of boron present in the analysis volume beyond C−B, the mere observation of boron post-graphitisation whilst using a more surface sensitive emission angle, clearly demonstrates that boron is transported through the iron layer with the carbon, and forms some boron-carbon structure on the iron surface.

After XPS analysis, the HBDD sample was removed from UHV and measured again with Raman spectroscopy *ex-situ* using the same the parameters that were used to acquire the spectra in figure 6.9. Figure 6.13 shows the Raman spectrum of the HBDD sample between 100 cm^{-1} and 3000 cm^{-1} after catalytic graphitisation. As before, the main diamond Raman line is not resolvable. The boron-related $L1$ and $L2$ features have been attenuated but the initial D, G, and $2D$ peaks have not attenuated by the same degree. The $L1$ and $L2$ peaks are positioned at 432.1 cm^{-1} and 1173.1 cm^{-1} respectively. The graphitic carbon related peaks, D, G, and $2D$, are positioned at 1353.2 cm^{-1}, 1584.8 cm^{-1}, and 2696.5 cm^{-1} respectively. The first important observation is that the D, G, and $2D$ peaks all have increased in intensity when compared to the spectra

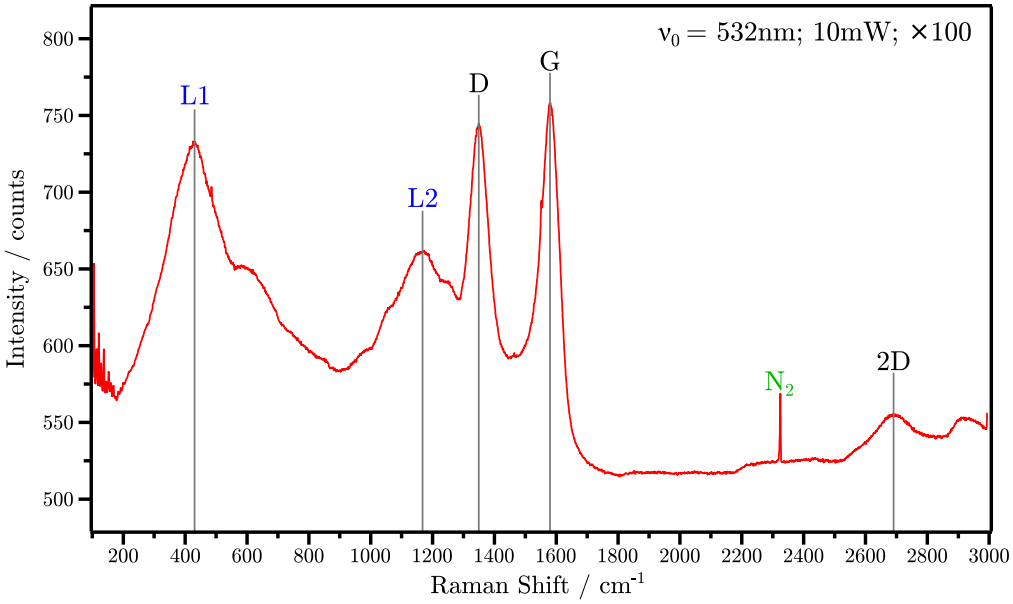

Figure 6.13. Raman spectrum between 100 cm^{-1} and 3000 cm^{-1} for the HBDD after catalytic-graphitisation. The positions of the graphite-related features, D, G, and $2D$ as well as the boron-related features $L1$ and $L2$ have been labelled. Gaseous N_2 between the sample and objective gives the feature at 2330 cm^{-1}.

acquired in figure 6.9. The presence of graphite related Raman peaks in the boron-doped diamond before graphitisation makes the the interpretation of figure 6.13 difficult. However, the presence of an iron overlayer would attenuate the 'bulk' graphite signal, so it follows that an increase in the graphite Raman bands can be attributed to surface graphite produced by iron-mediated graphitisation. The D and G peak lineshape also changes after graphitisation. The lineshape of the D and G peaks before graphitisation may suffer from a Fano-type interference from the carbon-boron matrix, making them appear slightly asymmetric, but this effect can also be attributed to amorphous carbon or disordered graphite[245]. After graphitisation, the lineshape of the D and G peaks becomes more symmetric and is more prominent with respect to the boron-related features ($L1$ and $L2$). The D peak in a graphene Raman spectrum is usually attributed to the breathing mode of the individual carbon rings, which

can only occur when there is a nearby defect (i.e. a missing carbon, or sp^3 structure) [246]. It is also observed in boron-doped graphene/graphite, as the substitution of boron into the graphene lattice causes local structural distortions and defects to occur, hence activating the graphene breathing mode [247, 248]. It has been shown in the literature, that as the boron concentration of doped graphene increases, there is significant increase in the D/G ratio. For a boron concentration of 0.22 at% in graphene, a D/G ratio of ~ 7 has been reported [249]. For graphite however, the D/G ratio is estimated to be ~ 0.5 for a boron concentration of 2.2 at% [247]. In the case of graphene, the large D/G ratio also corresponds to a shift in the G peak position; for carbon-only point defects, the G exhibits an up-shift of $\sim$10 cm^{-1} for $D/G > 3$, whereas substitutional boron-related defects cause a slight down-shift [249]. However, the D/G ratio in figure 6.13 is less than one, so any peak shifts due to boron or carbon related defects are firmly within the uncertainty range. Compared to graphite or graphene, the FWHMs of the D and G peaks (90 cm^{-1} and 85 cm^{-1} respectively) are much larger than expected, which suggests that there may also be considerable amount of disordered carbon that does not correspond to a layered graphite structure. With these qualitative considerations, it is clear that the Raman spectrum is figure 6.13 is suggesting that a multilayer graphene or graphite structure has been grown on the surface, but that there are also regions of disordered perhaps amorphous carbon. Deconvolving the D peak contribution of carbon-only defects from boron-related distortions is not trivial and cannot be explicitly determined here.

6.3 Chapter Conclusion

In this chapter, the graphitisation of the diamond (111) surface using an iron-catalyst has been investigated. REES measurements have allowed precise monitoring of the deposition rate of a K-cell for both thick and thin Fe overlayers. The well-calibrated and extremely clean K-cell has been shown to deposit pure films of Fe as evidenced by the lack of other contaminating species (such as carbon or oxygen) in the survey spectrum and the high resolution Fe $2p$ spectrum in figure 6.2. Depositing a thin 1.75 nm Fe overlayer on an insulating HPHT diamond compensates the surface charging induced by the X-ray source similar to the (2×1) reconstruction on the (111) diamond surface. As the Fe overlayer was deposited, REES measurements allowed continuous monitoring of the C $1s$ peak position. The shift of the peak position, back to the 'true' C $1s$ binding energy proceeds in two distinct linear relationships to the thickness of the Fe overlayer until three complete layers of fcc (111) Fe are deposited. The reduced conductivity of the Fe overlayer at extremely thin thicknesses is attributed to the Fe sub-monolayer coverage and then the Fuchs–Sondheimer model of electron scattering near metal surfaces for multiple layers. Evaporated Fe initially deposits in a disordered pseudomorphic fcc structure, but undergoes a phase transition into the bcc polymorph of Fe after annealing to at least 320 °C. This is evidenced by LEED patterns post-annealing that support the Nishiyama-Wassermann model of $bcc - fcc$ interfaces with a missing rotational domain, showing that registry from the underlying $(111)(2 \times 1)$ reconstructed diamond substrate (which is also missing one of the rotational domains) is preserved.

Iron-mediated graphitisation was studied for a 12 nm thick Fe overlayer on a semiconducting (111) diamond surface. REES measurements allowed second-

by-second monitoring of the C $1s$ and Fe $2p_{3/2}$ peak intensities as the sample was heated to maximum temperature of 685 °C. Four distinct regimes pertaining to the Fe film and the carbon were identified during the heating process: as previously discussed, the iron undergoes a phase transition and an improvement in crystallinity; the carbon is detached from the diamond surface and begins to migrate through the Fe overlayer as interstitial carbon; carbon reaches the surface of the Fe and precipitates into ordered graphene sheets hence attenuating the Fe signal; the reaction is rapidly quenched by dropping the sample temperature and transport of carbon to the surface of the Fe ceases immediately. After the heating cycle, XPS and LEED characterisation confirm the chemical and structural purity of the resulting graphene respectively. The single graphene domain and lack of the characteristic $\pi - \pi*$ transition in the C $1s$ peak confirm that a single layer of graphene was produced. This graphene sheet exhibits a C $1s$ peak that has higher binding energy compared to the reference value for graphitic carbon ($\sim$284 eV). This indicates that there is a strong graphene-substrate interaction which, in agreement with previous studies on this surface, suggests significant charge transfer induced n-doping in the graphene.

The growth process of iron-mediated graphitisation described in section 6.2 only takes into account the carbon content of the diamond substrate. The fate of the boron atoms in the lattice is not considered due to their low concentration, which is far less than the detection limit of the XPS technique. If boron is similarly transported through the iron overlayer during heating, then the question was whether it could also be incorporated into the graphitic carbon on the surface of the iron. The iron-mediated graphitisation experiment was therefore repeated, using a (111)-orientated HBDD with a boron concentration

of $(8.66 \pm 3.32) \times 10^{21}$ atoms/cm^3 (as determined by Raman spectroscopy). This allowed the boron to be detected and monitored at each stage during the iron-mediated graphitisation process using XPS. Post-graphitisation, a measurable and significant boron contribution is detected in XPS at a more surface sensitive 60° emission angle, indicating that the boron has successfully been transported through the Fe overlayer during heating. High resolution core level spectra of the C 1s and B 1s reveal boron-carbon components whose at% ratio suggests a [B] of $\sim$5 at%. The downshift in the main C=C sp^2 component in the C 1s is also indicative of p-type doping expected of boron-doped graphene/graphite. However, as shown in post-graphitisation Raman spectroscopy, due to the initial roughness of the HBDD substrate, the structural quality of the boron-carbon structure is heavily defected and may contain regions of disordered carbon. Going forward, this experiment would benefit from repeated attempts with HBDD polished to achieve a surface roughness comparable to the semiconducting natural diamond used in earlier experiments. Based on the extensive study of this method of producing graphene both in previous work and in this investigation, it is possible that boron-doped single-layer graphene can be fabricated under optimal growth conditions. In general, this experiment has shown that multi-element materials can be converted into their congruent 2-dimensional allotrope using the iron-mediated graphitisation technique.

Chapter 7

Toward Architectures of Catalytically-grown Graphene

The focus of this chapter is the patterning of catalytically-grown graphene into simple architectures, which can be measured *in-situ* using XPEEM/LEEM, and subsequent transfer to SiO_2/Si for in-depth characterisation with Raman spectroscopy, AFM, and XPS. The key advantage to iron-mediated graphitisation is the reduction of the transition temperature required to convert the sp^3-bonded carbon in the solid source, to ordered sp^2 carbon in the form of graphene and graphite. Naturally, this means that during a temperature ramp up to 1000 °C on a diamond or silicon carbide substrate, graphene will be produced in the regions where iron has been deposited, long before catalyst-free graphitisation occurs. It follows that if the iron catalyst can be deposited in specific regions on the substrate, then patterned graphene (which is required for the fabrication of useful devices) can be produced. In this work, patterned graphitisation was attempted on SiC substrates with the aim to fabricate simple architectures of graphene, namely dots of varying sizes. To further characterise the catalytically-grown graphene, a systematic graphene transfer study was performed. Reference

samples of CVD graphene were transferred to 90 nm SiO_2/Si using 'wet' and 'dry' techniques in order to compare the quality of the post-transferred graphene. The results from the CVD graphene transfer informed the subsequent transfer of catalytically-grown graphene to SiO_2 and provide a quality comparison for future studies; for this experiment, graphene grown on the diamond (111) surface was transferred.

7.1 Patterning of Catalytically-grown Graphene

7.1.1 Graphene dots on SiC (Aberystwyth)

A 9×9 mm square of silicon carbide (6H-SiC orientated to the (0001) silicon face) was subjected to an 'RCA clean' of hydrofluoric acid (HF) to remove any organic contaminants and strip away the native silicon oxide (SiO_2) layer. The SiC was then heated in UHV to 950 °C to remove any remaining oxide and adventitious carbon that adsorbed on the surface prior to loading in the REES system. The SiC was then moved to the transfer chamber and placed behind a shadow mask consisting of an array of 1 mm diameter holes with a 2 mm pitch, as shown in figure 7.1a. A 2 nm thick iron layer was then deposited onto the SiC to form iron dots with the same motif as the mask, as shown in figure 7.1b. The graphitisation step involved a heating cycle to 700 °C which was then held for 30 minutes before rapidly cooling. For an iron overlayer thickness between 0.75 nm and 2 nm, the catalytic reaction on SiC is self-terminating and therefore will only grow one layer of graphene [17, 56]. Post-graphitisation, the SiC was transferred to the REES chamber for XPS and ARXPS analysis. The photoelectron analyser was set to a lens mode which allowed spectra to be recorded from sub-millimetre areas on the sample surface. In this case, measurements were obtained from a spot on the sample 300 µm wide in the energy dispersive plane and 2 mm in

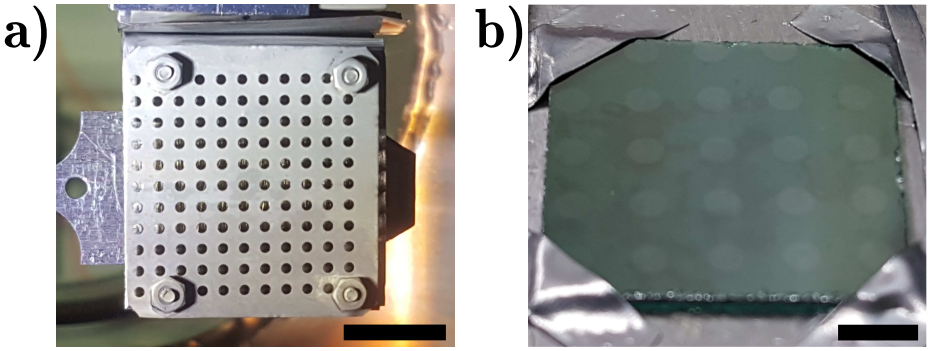

Figure 7.1. a) The shadow mask in the transfer chamber, located at the bottom of the sample stage. The inset scale bar is 10 mm long. **b)** The resulting deposited pattern of iron on SiC, post-graphitisation, and outside UHV. The inset scale bar is 2 mm long.

the non-energy dispersive plane. The small analysis area allowed XPS spectra to be measured directly on a single graphene spot or in the non-metallised SiC gaps. Figure 7.2 shows XPS survey scans of the SiC sample for regions on the graphene dots and on the bare SiC between in the masked regions. The SiC gap spectra (Figure 7.2a) shows the characteristic silicon and carbon peaks of the 'bulk'. SiC has a structure with alternating planes of carbon and silicon atoms in the [0001] direction. Similar to high temperature sublimation growth method described in section 4.3.1, the silicon-terminated face of the crystal is preferable for this experiment to ensure the formation of the FeSi layer without defects. The higher Si $2p$ to C $1s$ ratio indicates that the Si-terminated side of the sample has been mounted upwards correctly, as the additional silicon layer at the surface attenuates the carbon signal. The Si $2p$ and $2s$ peaks are repeated again at lower kinetic energy (424.5 eV and 373 eV) due to photoelectrons excited by O Kα radiation emitted from the partially oxidised Mg anode. There is also some calcium oxide contamination on the SiC, indicated by the Ca $2s$ and O $1s$ peaks. This contaminant is likely from the cutting tools used to divide the SiC into squares. In contrast, a spectrum acquired from a graphene spot (Figure 7.2b), where the Fe $2p$ / Fe $2s$ core levels and Fe KLL Auger structure

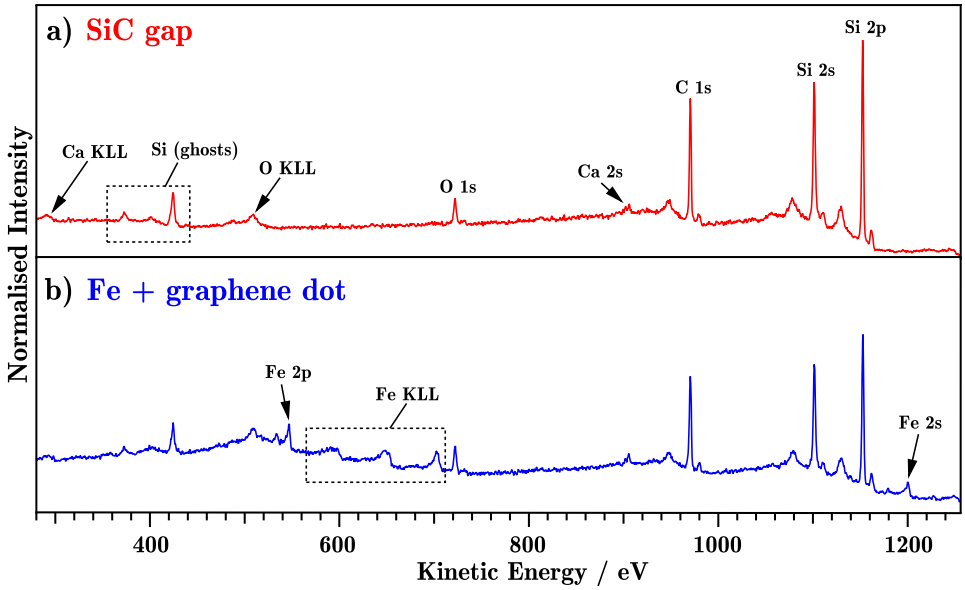

Figure 7.2. XPS survey scans (hv =1253.6 eV, E_p =100 eV) of catalytically graphitised SiC in **a)** the bare SiC gaps and **b)** on a dot from graphitised pattern.

originating from the iron catalyst is present. Once focused on a graphene dot, high resolution core level spectra were acquired both at normal emission and at 60° off-normal, shown in figures 7.3a and 7.3b respectively. The C 1s consists of

Angle	Component	Position/eV	FWHM/eV	∑GL ratio	At%
Norm	Si−C	283.0	1.3	0.55	83
	C=C sp^2	284.6	1.3	0.55(*0.33)	17
60°	Si−C	283.0	1.3	0.66	69
	C=C sp^2	284.5	1.3	0.66(*0.29)	31

Table 7.1. Fitting results for the spectra in Figure 7.3 (*Asymmetry factor).

two components post-graphitisation: the Si−C peak from the growth substrate at ∼283 eV, and the asymmetric C=C sp^2 peak from the graphene overlayer at ∼284.5 eV. Due the metallic conductivity of graphene, the C=C sp^2 component has been fitted with a floating asymmetric factor to compensate for conduction band shake-up events [50, 250]. The spectra taken at 60° off-normal shows the C=C component significantly increasing with respect to the Si−C component.

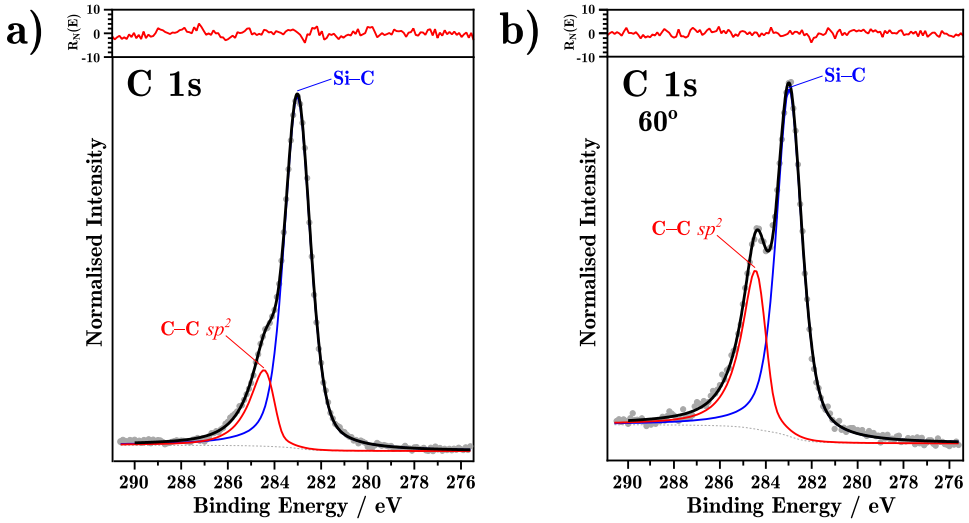

Figure 7.3. High resolution XPS spectra (hv = 1253.6 eV, E_p = 30 eV) of **a)** C 1s at normal emission and **b)** C 1s at 60° emission from a graphene dot on SiC. The red inset traces show the normalised residuals $R_N(E)$. Table 7.1 shows the fitting results for these spectra.

This suggests, in line with the work performed on the diamond (111) surface, that the C=C component originates from the surface region as opposed to the Si−C bulk.

To confirm the presence of graphene on the iron dots post-heating, *ex-situ* Raman spectroscopy was employed. Static scans, shown in figure 7.4, were taken between 1200 cm^{-1} and 3000 cm^{-1} to check the characteristic D, G, and $2D$ peaks of graphene, both on and off the patterned regions. The region containing the D and G peaks is dominated by second order SiC Raman scattering [251] and coupled with a lack of surface-enhancement of the graphene signal, identification of the G peak was particularly difficult. Conversely, the $2D$ peak is not convoluted with other features and can therefore be identified easily. The $2D$ peak appears to be much wider ($\sim$75 cm^{-1}) than expected for pristine graphene (between $\sim$35 cm^{-1} and 50 cm^{-1}) [252]. Along with the intensity increase around the D-peak region, the Raman data in figure 7.4 appears to suggest that

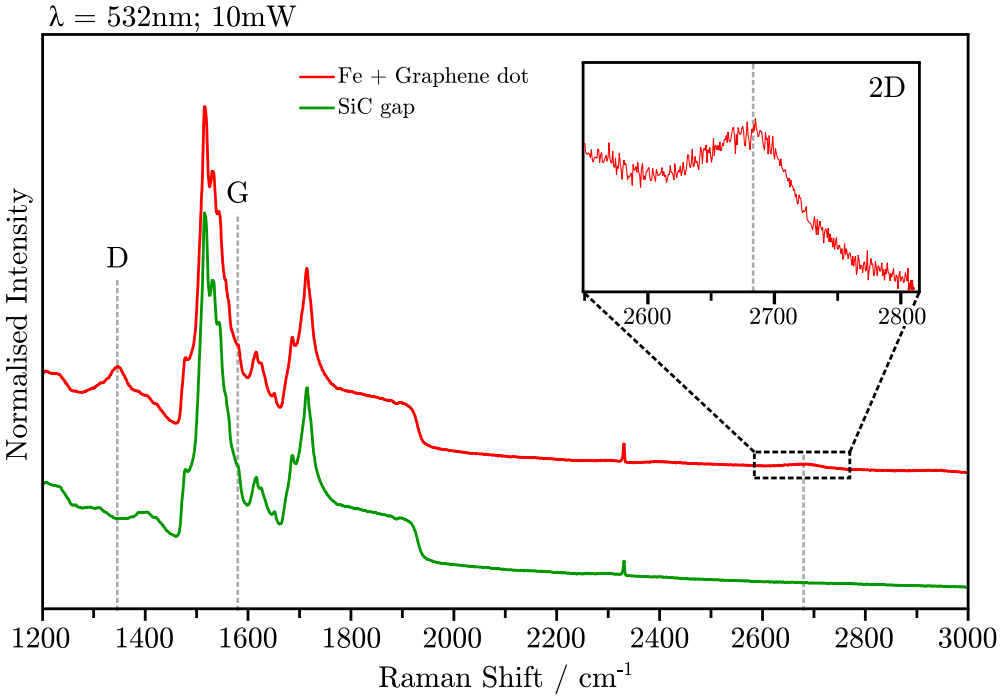

Figure 7.4. Raman spectra between 1200 cm^{-1} and 3000 cm^{-1} for the SiC substrate (**green**) and patterned graphene regions (**red**). The positions of the D, G, and $2D$ peaks of graphene have been labelled. The feature at 2330 cm^{-1} is due to gaseous N_2 between the sample and the objective. **Inset:** A zoomed-in graphene $2D$ peak from the patterned regions.

a defected graphene sheet has been grown. The Raman spectrometer was then switched to mapping mode, allowing spatial Raman mode information of the graphene to be measured. The characteristic graphene Raman modes were used to measure the spatial extent of the graphitisation, and determine whether the deposited catalyst pattern has successfully reproduced the matching graphene pattern. The gate time for full static spectra was 120 s over 10 accumulations to achieve a reasonable signal-to-noise. The long acquisition times meant that full spectra Raman mapping was not feasible, even with the Raman optics optimised for maximum transmission of scattered light. Therefore only the $2D$ region was measured to reduce the experimental time. Figure 7.5a shows a $2D$ band Raman map of catalytically-grown graphene on patterned Fe deposited on SiC. The

dark regions in the map correspond to areas where no graphene is present (see figure 7.5b), as confirmed by the absence of a $2D$ peak, whereas the brighter regions indicate some $2D$ band intensity and therefore graphene growth (see figure 7.5c). The Raman map clearly demonstrates that the edge of the graphene growth region corresponds to the edge of the Fe-deposition region, i.e. conforms to a circular pattern. It also shows that there are extensive areas ($\sim$10 µm to 30 µm in at least one dimension) in the graphene growth region where a $2D$ peak cannot detected or has a significantly lower intensity than the majority of the data points. These areas are either devoid of graphene or have defected graphene. The reason for the emergence of these defects can be attributed to contaminants on the surface which inhibit the graphitisation process (e.g. the residual calcium oxygen species from cutting tools).

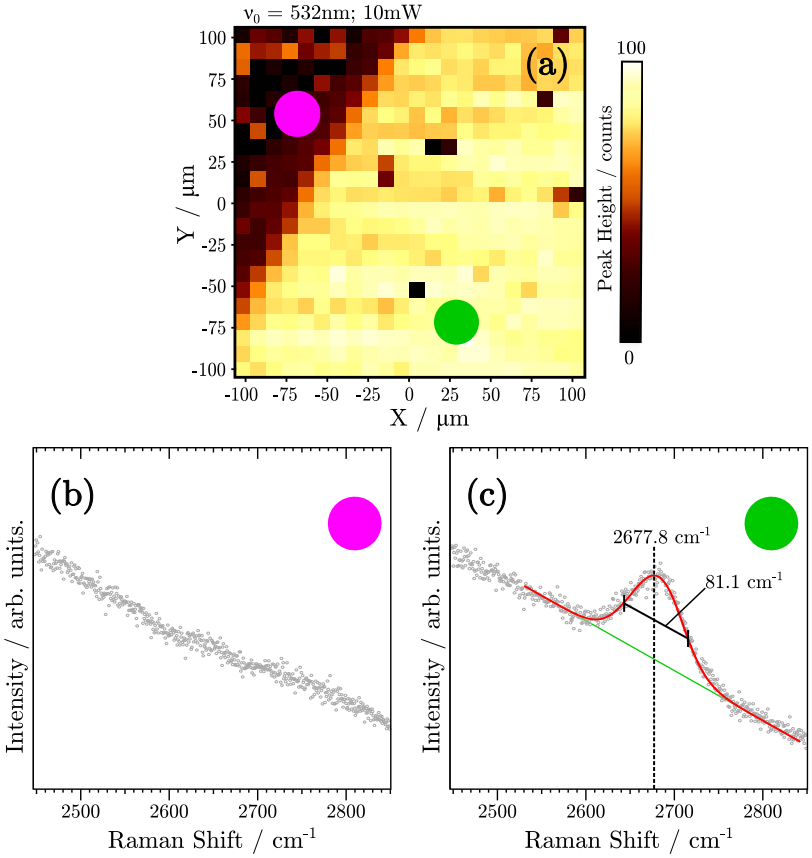

Figure 7.5. a) A 200×200 µm Raman map taken at the edge of a graphene dot between 2450 cm^{-1} and 2850 cm^{-1}. The brighter regions indicate the presence and intensity of the graphitic $2D$ peak. The Raman spectra for the dark (**pink**) and bright (**green**) regions have been extracted in **b)** and **c)** respectively.

7.1.2 Graphene dots on SiC (BESSY II)

Another 9×9 mm square of SiC, subjected to an RCA clean, was taken to the UE49 SMART beamline at the BESSY II synchrotron (Berlin). A tantalum shadow-mask with five 500 µm diameter holes was mounted on top of the sample prior to loading into the UHV system. The SiC sample was heated to 900 °C to drive off any adventitious carbon and oxygen species on the surface. A thin-film of Fe was deposited onto the SiC surface and then the sample was heated to 750 °C to induce catalytic graphitisation. Figure 7.6 shows a low-energy

diffraction study (LEEM/LEED) of the SiC at each stage of the experiment. After heating the SiC to 880 °C, the LEEM image shows two distinct phases arranged in a striped pattern, which is probably a result of polishing. The LEED pattern taken at this position reveals a $(\sqrt{3} \times \sqrt{3})$R30° reconstruction on the SiC surface [253]. After a thin film of Fe is deposited, LEEM imaging shows a smoothing of the surface as the polishing lines are filled in. The Fe film appears homogeneous, but XPS reveals a significant amount of oxygen has also been incorporated into the film. The Fe film appears to have been deposited in a pseudomorphic (111) orientation as the LEED pattern shows broad spots over the (1×1) SiC structure. These Fe-related features appear to rotationally broaden, which is due to slightly rotationally misaligned Fe layers, and radially broaden which implies a deviation from the (1×1) periodicity brought about from the Fe attempting to adhere to the $(\sqrt{3} \times \sqrt{3})$R30° SiC reconstruction at room temperature. Finally, the Fe on SiC is heated to 620 °C for 30 min to catalytically graphitise the surface. In the LEEM image, there is a clear structural difference between regions on the Fe film. It appears that the lighter regions represent a coalescence of ordered carbon like single and multi-layered graphene, whereas the darker regions appear to exhibit disordered or amorphous carbon growth. The corresponding LEED pattern for this area shows multiple rotational domains producing many diffraction spots that are close together, giving the appearance of a smeared out diffraction pattern. This pattern may be indicative of graphene diffraction spots characteristic of multilayer graphene sheets that are rotationally misaligned [200, 254]. Figures 7.7a and 7.7b show a series of XPEEM images taken at the edge of a patterned region after heating to 750 °C. The photon energy was set to 385 eV and a series of images were taken between 94 eV KE and 102 eV KE at 0.2 eV intervals, in order to measure the C $1s$ intensity. The gradual decrease in signal from the centre to the top-left corner

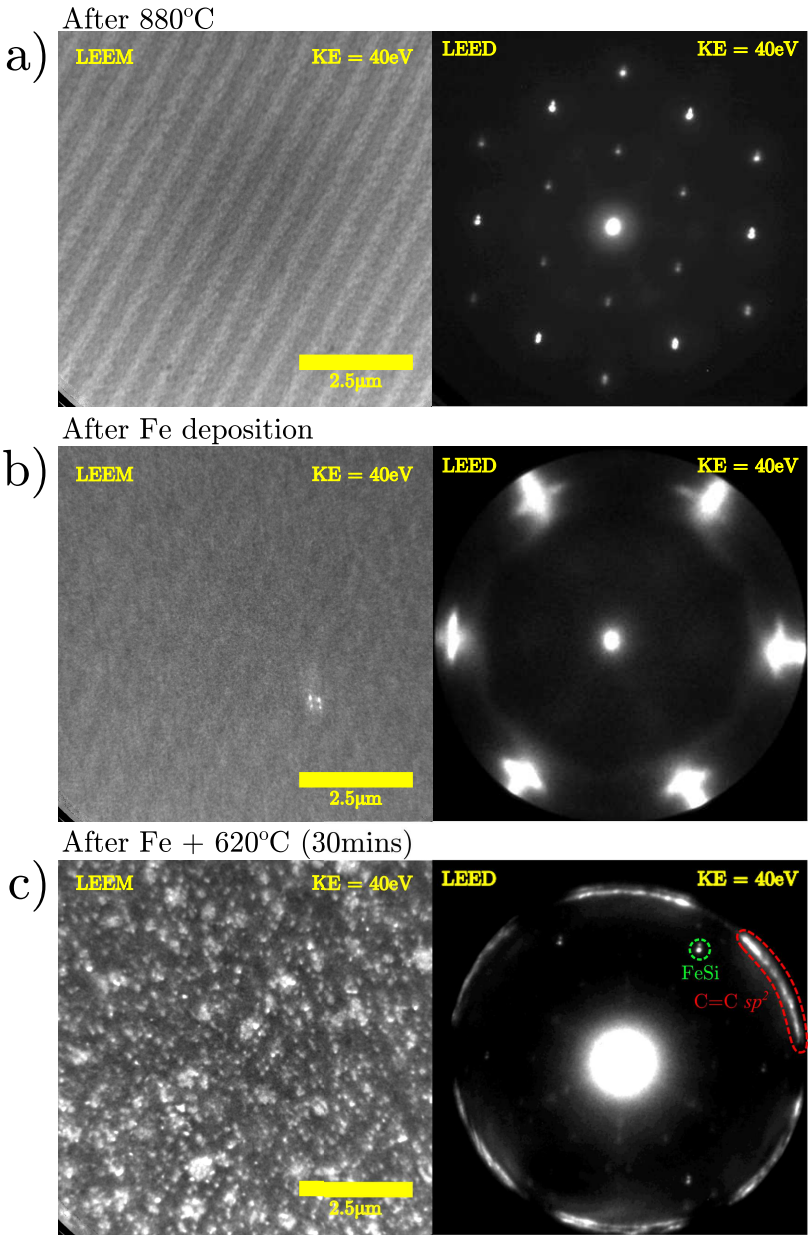

Figure 7.6. LEEM images and LEED patterns acquired on the SMART beamline at the BESSY II synchrotron during three stages of the graphitisation experiment on SiC 6H-(0001): **(a)** after 880 °C to remove adventitious carbon and oxygen-terminating species; **(b)** after 2 h of Fe deposition; **(c)** After heating to 620 °C to induce catalytic graphitsation. All data were acquired using an incident electron kinetic energy of 40 eV.

is likely due to the profile of the X-ray beam. At 98.1 eV kinetic energy, the C 1s yield increases in the region where the Fe has been deposited, whereas at 99.2 eV kinetic energy, the C 1s yield originates in the region without iron. Figure 7.7c shows the photoelectron yield against kinetic energy for the red and blue areas in figures 7.7a and 7.7b respectively. Here the chemical composition of the C 1s peak is revealed for the Fe dot and bare SiC regions. The red region has a large asymmetric peak that has been attributed to sp^2-bonded C=C, characteristic of graphitic carbon, whereas the blue region has a smaller and less asymmetric peak from the SiC substrate.

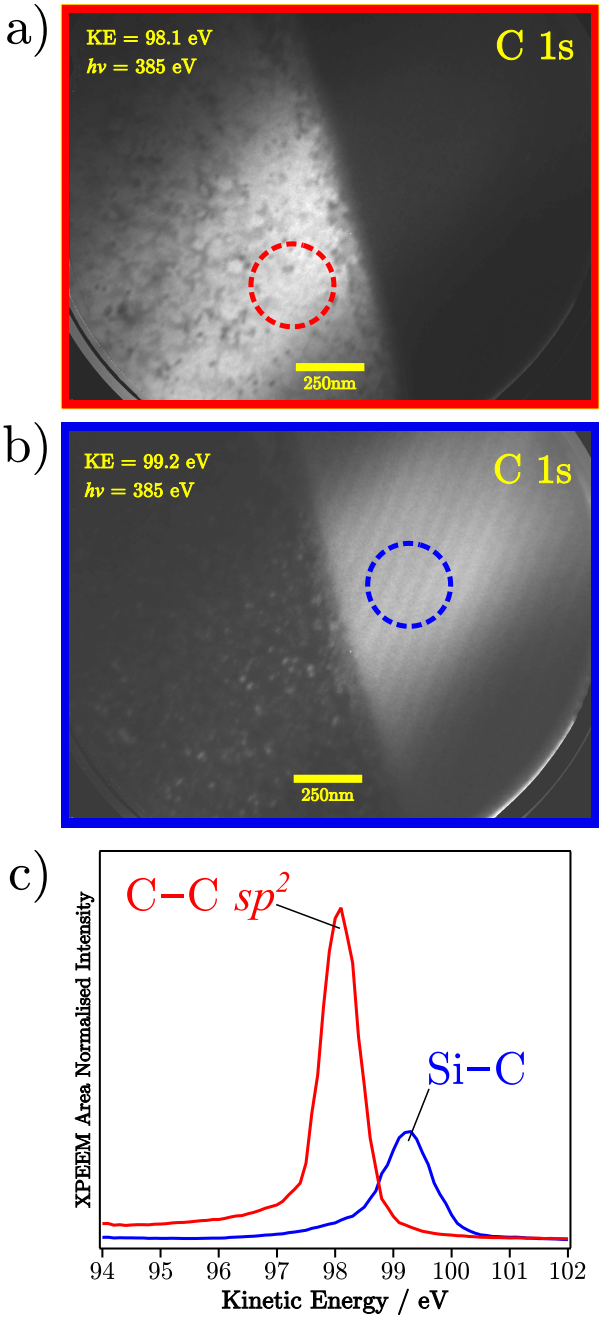

Figure 7.7. C 1*s* XPEEM images acquired at the edge of an Fe region on SiC after heating to 750 °C at kinetic energies of **(a)** 98.1 eV KE corresponding to C=Csp^2 and **(b)** 99.2 eV KE corresponding to Si−C. The normalised photoemission yield from the areas denoted by the red and blue dashed circles have been extracted in **(c)**. By scanning the KE of the XPEEM images, the C 1*s* core level can be acquired.

Post-graphitisation, the sample was removed from the beam line and taken back to the home laboratory for Raman spectroscopy analysis. Spectra were acquired using a 10 mW 532 nm laser source focused through a long-working distance objective lens with ×50 magnification. Figure 7.8 shows a representative static Raman spectra between 1100 cm^{-1} and 2900 cm^{-1} taken from a graphitised Fe-dot on SiC and bare SiC. Both spectra were normalised to the SiC feature at ~1510 cm^{-1} before a difference spectra was calculated. The residual background

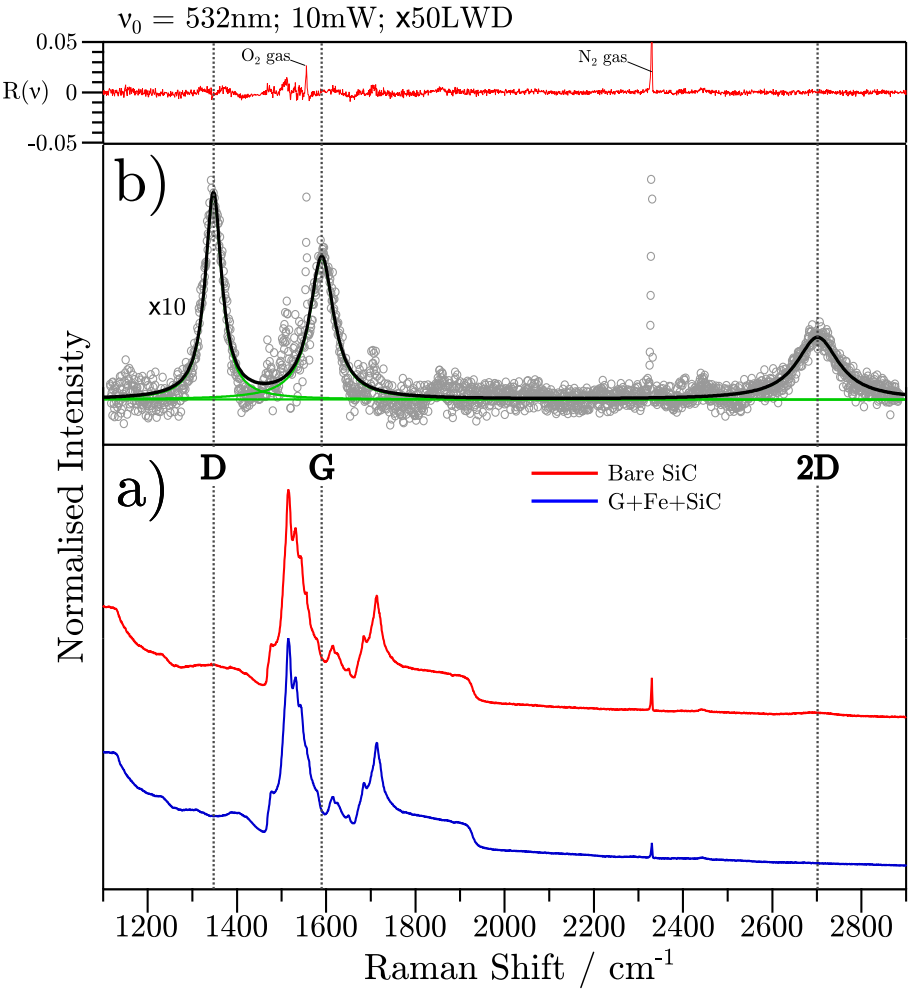

Figure 7.8. **(a)** Raman spectra between 1150 cm^{-1} to 2850 cm^{-1} for a catalytically-grown graphene dot on the surface of a Fe-SiC dot (**blue**) and bare SiC (**red**). **(b)** The difference spectra with background correction. The D, G, and $2D$ bands have been fitted using Lorentzian peaks.

was then fitted with a spline and subtracted to achieve a flat background. The resulting D, G, and $2D$ bands were fitted with Lorentzian peaks; due to the low count rate, the residual count is comparable to the signal (between 5 % and 52 % of the D peak maximum), but is otherwise flat indicating a suitable fit. The $2D/G$ ratio is ∼0.42 and the D/G ratio is ∼1.46 indicating a high density of defects. Figure 7.9 shows a $2D$ band Raman mapping study of the BESSYII graphene. Figure 7.9a shows the intensity of the $2D$ band across the red region shown in the microscopy image in figure 7.9b. The microscope image

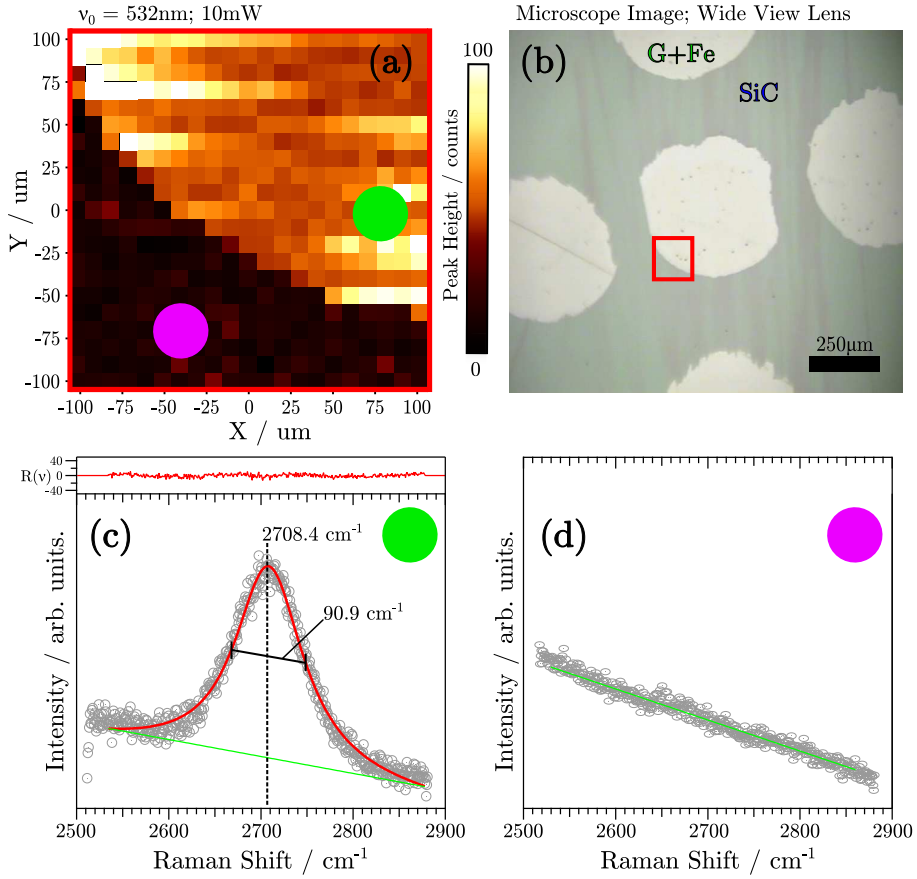

Figure 7.9. **(a)** A 200×200 µm Raman map taken between 2500 cm^{-1} and 2900 cm^{-1} at the edge of a graphene dot denoted in by the red region in the optical microscopy image in **(b)**. The brighter regions indicate the presence and intensity of the graphitic $2D$ peak. The Raman spectra for the dark (**pink**) and bright (**green**) regions have been extracted in **(c)** and **(d)** respectively.

shows the number five 'die' pattern of graphene-on-Fe clearly, and demonstrates that shadow mask produces a sharp edge to the patterned regions. The $2D$ band only appears in the graphene/Fe region, as shown by the spectra collected at the blue and green regions on the map (see figures 7.9c and d respectively), further demonstrating the feasibility of patterning graphene with this method. The $2D$ peak is significantly upshifted to $\sim$2708 cm^{-1}, and the FWHM is $\sim$91 cm^{-1} which is much wider than the typical CVD graphene values of $\sim$35 cm^{-1} to 50 cm^{-1} [246, 252, 255]. The $2D$ band was fitted with a single Lorentzian peak, which indicates a single layer of graphene has been produced in this particular area, and the FWHM suggests that the sheet may be heavily defected. However, many other areas contained multi-component $2D$ peaks typical of multi-layer graphene / graphite which was expected based on the LEED pattern shown in figure 7.6c .

7.2 Transfer of CVD Graphene

7.2.1 Wet Transfer Technique (Acid Etch)

For as long as graphene has been grown on metal substrates, acid etching has been used to remove the growth substrate and isolate the graphene so that it is ready to be transferred to an arbitrary substrate. A typical wet-transfer technique for CVD graphene grown on Cu [256, 257] is described as follows and is shown in figure 7.10. The growth substrate was first carefully flattened between a pair of clean and dust-free microscope slides with care taken to not introduce any wrinkles, creases, or bends in the Cu foil. Care was also taken to not impart any shear force between the microscope slides whilst the graphene-coated Cu was between them (figure 7.10a). A clean pipette was used to deposit a few drops of 4 %w/w poly(methyl methacrylate) (PMMA, MW 950k) in chlorobenzene

onto the top side of the graphene-Cu foil whilst it rested on the chuck of a spin-coater. Care was taken to ensure that no bubbles of PMMA formed on the graphene surface during deposition. The spin-coater was operated for 1 minute at 2000 rpm to achieve an even coverage of PMMA, and then the foil was baked in a drying oven for 1 minute at 80 °C (figure 7.10b). The Cu foil was then placed into an O-plasma etcher with the uncoated back side facing toward the highest plasma density. The foil was exposed to an O-plasma for ∼2–3 minutes to remove the graphene on the uncoated side of the Cu so that it did not inhibit

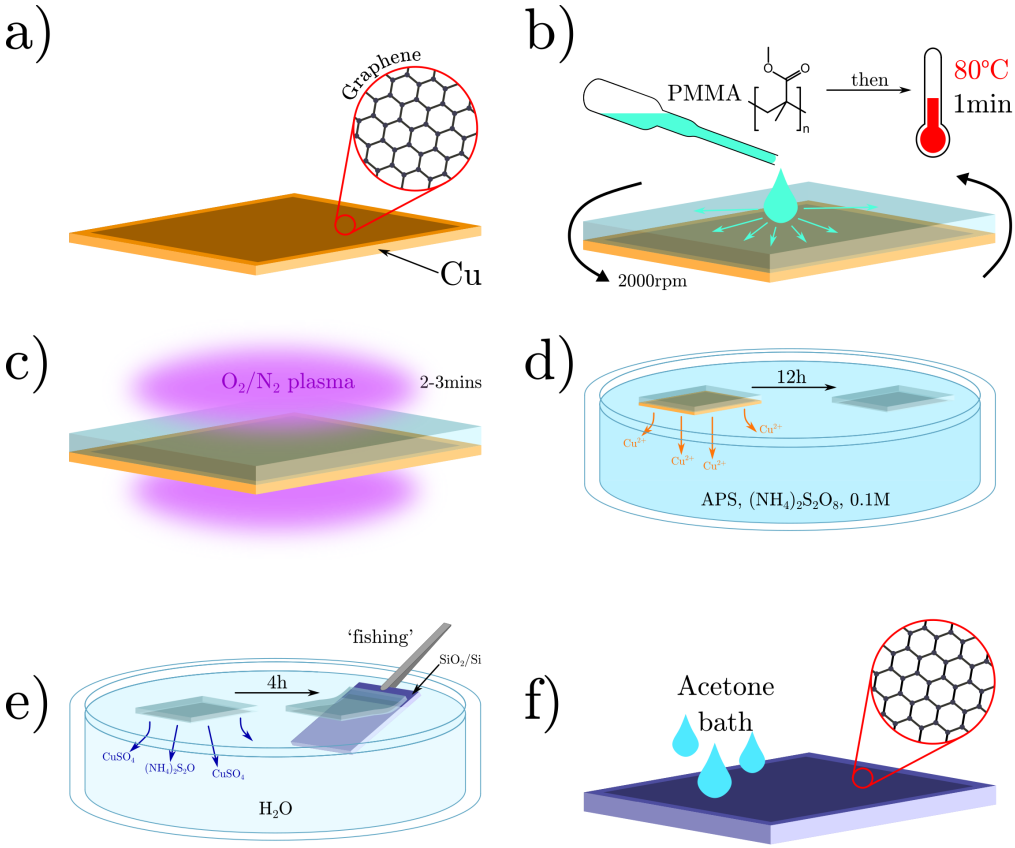

Figure 7.10. The wet-transfer technique used in this work. **(a)** CVD graphene grown on Cu foil; **(b)** Spin-coating of PMMA onto the graphene; **(c)** Backside graphene is removed using an O-plasma; **(d)** Cu removed by an APS acid etch until only PMMA/Graphene is left; **(e)** The graphene is transferred to water for additional cleaning before transfer to the target substrate; **(f)** The PMMA support layer is removed with an acetone bath, to leave graphene on the target substrate, usually a SiO_2/Si wafer.

the acid etching of the growth substrate (figure 7.10c). The growth substrate was placed, Cu side down, onto a solution of 0.1M Ammonium persulphate ($(NH_4)_2S_2O_8$, $\geq$98 % assay) (APS) and left for 12 h until the Cu had completely etched away (figure 7.10d). Using a large watch glass, the PMMA-graphene stack was scooped up along with some of the APS to keep the graphene floating on liquid, and then transferred to a bath of deionized water. The PMMA-graphene stack was left in the deionized water for 4 h to remove any leftover particles of Cu and APS residue. The target substrate, in this case 90 nm SiO_2/Si, was then used to 'fish' the PMMA-graphene stack from the deionized water, taking care not to produce wrinkles or folds in the graphene sheet or trap bubbles between the target substrate and graphene (figure 7.10e). The PMMA-graphene-SiO_2/Si stack was allowed to air dry until all visible water had evaporated, and then it was placed in a vacuum desiccator for 1 h to remove any residual moisture. To remove the PMMA and complete the transfer, the PMMA-graphene-SiO_2/Si stack was placed in a bath of acetone for 1 h at 30 °C, rinsed with iso(propanol) alcohol, and blow dried with nitrogen gas (figure 7.10f).

7.2.2 Dry Transfer Technique (PVA-assisted)

Whilst the standard wet-transfer technique is well understood in the literature and is widely used, it cannot be used to transfer graphene grown by iron-mediated graphitisation. This transfer method relies on the etchant having a large contact area with the metal foil so that it removes material homogeneously, as well as a large reservoir of fresh etchant in order to encourage a strong diffusion gradient. In the iron-mediated graphitisation method, the growth substrate (diamond or SiC) cannot be etched away, and the interface between the iron catalyst and the etchant is small enough that removal of the iron is strongly inhibited (likely due to capillary forces and a weak diffusion gradient).

This results in etching times of several days, even with the frequent addition of fresh etchant. With acid etching ruled out, dry mechanical de-lamination – although currently not scalable – provided a method whereby Aberystwyth-grown graphene could be transferred to SiO_2/Si oxide substrates for Raman analysis. After considering and practising several transfer techniques [258, 259], the method proposed by Yang *et al.* had consistently more success. This technique uses a polyvinyl alcohol (PVA) as an adhesion layer that aids in de-laminating graphene from its growth substrate. Figure 7.11 illustrates the transfer technique which has been adapted for transferring catalytically-grown graphene from the diamond (111) surface, and CVD graphene from Cu foil. Quoted temperatures were measured with either a K-type thermocouple for solid substrates, and a glass thermometer for solutions. A solution of PVA (0.2 g in 20 ml) was prepared using PVA powder (MW 9000–10000, 80 % hydrolyzed) which was slowly dissolved in deionized water whilst heating to 80 °C and continually mixing with a magnetic stirrer. In the pre-treatment step, the growth substrate was submersed in this PVA solution at 50 °C for approximately 18 h. In this pre-treatment step, the PVA hydrocarbons are strongly adsorbed onto the hydrophobic graphene sheet and increase the adhesion between the graphene and the PVA carrier layer. This ensures that when the PVA carrier layer is retracted later, the graphene sheet also detaches from the growth substrate with minimal tearing or leaving graphene left on the growth substrate (figure 7.11b). The graphene growth substrate was removed from the PVA solution and thoroughly rinsed with deionized water and dried with nitrogen gas. Following this pre-treatment, a carrier layer of PVA (0.2 g in 20 ml, MW 9000–10000, 80 % hydrolyzed) was deposited onto the growth substrate using a micro-pipette, and then dried in an oven at 80 °C for at least 10 min (figure 7.11c). A strip of Kapton tape was then firmly pressed onto the carrier layer to

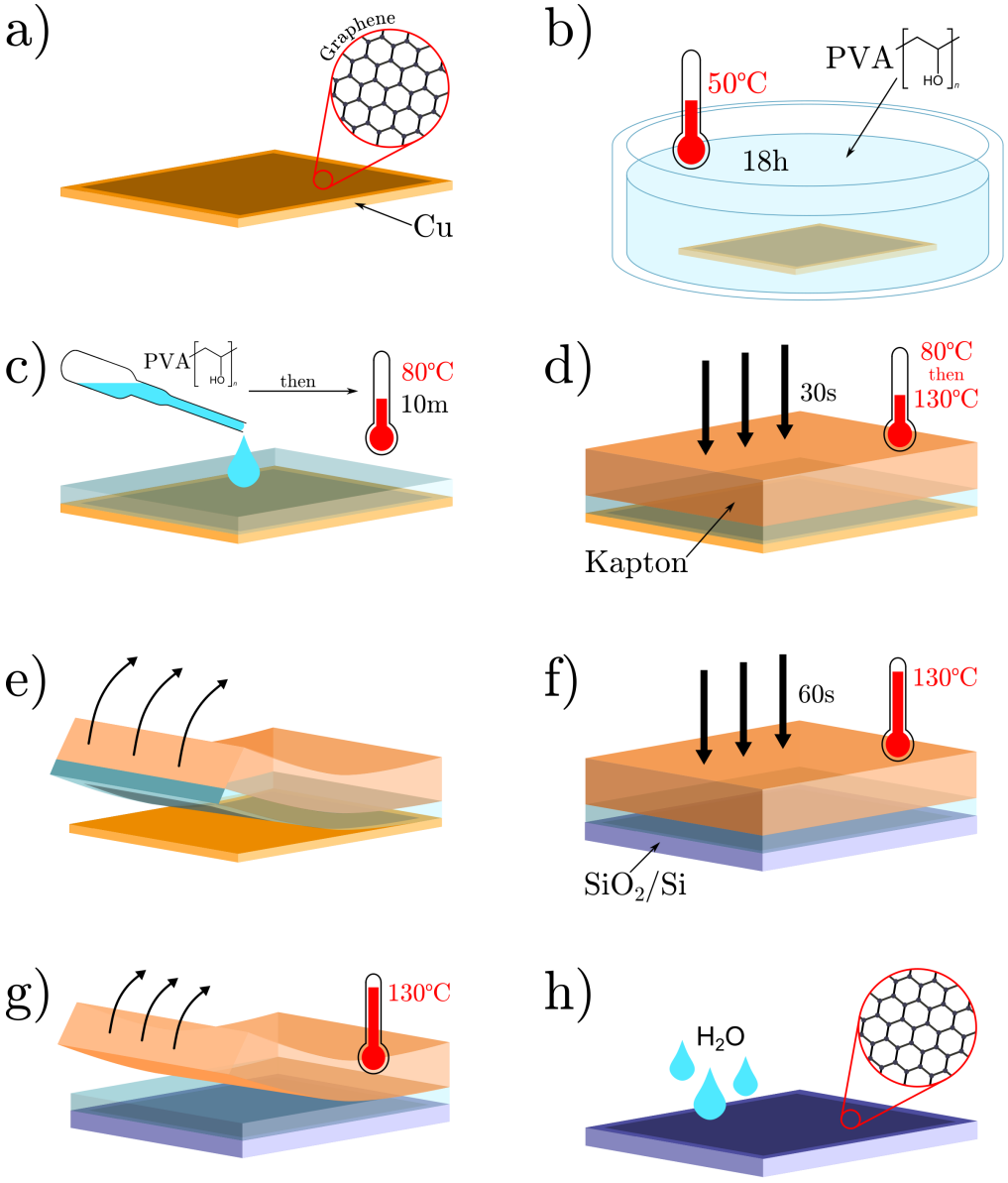

Figure 7.11. The dry-transfer technique used in this work. **(a)** Graphene grown on Cu (or iron-on-diamond); **(b)** The graphene and growth substrate is submersed in a PVA solution for 18 h at 50 °C; **(c)** After rinsing in DIW, more PVA is deposited onto the graphene and cured at 80 °C for 10 min; **(d)** Kapton tape is pressed onto the PVA and force is applied at different temperatures to ensure conformal contact; **(e)** Kapton is rapidly retracted to peel PVA/Graphene away from growth substrate; **(f)** PVA/Graphene is pressed onto the target substrate for 1 min at 130 °C before **(g)** the Kapton is slowly peeled away; **(h)** PVA support layer is removed with a water bath to leave graphene on target substrate, usually a SiO_2/Si wafer.

establish conformal contact before returning to the oven for a further 10 minutes at 80 °C. As the sample is removed from the oven, further conformal pressure is applied until the sample is cool. The sample was then placed on a hot plate at 130 °C and conformal pressure applied a third time for at least 30 s. The sample is then allowed to cool to room temperature (figure 7.11d). To remove the PVA-graphene stack from the growth substrate, the Kapton tape was retracted at high speed to maximise the adhesion force between the Kapton and the carrier layer, and hence de-laminate the graphene from the growth substrate (figure 7.11e). The carrier-graphene stack was then pressed against a 90 nm SiO_2/Si substrate at 130 °C for 1 min to release the Kapton from the carrier layer (figure 7.11f). The Kapton tape was slowly peeled off during heating to transfer the graphene to the SiO_2/Si substrate (figure 7.11g). Finally, the PVA carrier layer was removed by submersing the graphene-SiO_2/Si in deionized water at 35 °C for three hours. To remove any other residues from the Kapton tape, the sample was then placed in a bath of acetone for 1 h at 30 °C, rinsed with isopropanol alcohol, and blow dried with nitrogen gas (figure 7.11h).

7.2.3 CVD Graphene on SiO_2

As explored in section 4.3.1, high-quality large-area graphene can be produced via CVD, using copper as a growth substrate and a mixture of CH_4 and H_2 as a process gas. CVD graphene was used in this work as a benchmark of quality to compare the transfer techniques and establish a figure-of-merit comparison for the catalytically-grown graphene from the diamond (111) surface. Samples of 2×2 cm CVD graphene on Cu were produced by Dr Neil Wilson (Department of Physics, University of Warwick, UK) and shipped to the home laboratory in Aberystwyth. Raman spectroscopy confirmed the presence of high-quality graphene on the Cu substrates, which lacked a D peak at all measured areas.

CVD graphene was transferred to varying thicknesses of silicon oxide using both the APS acid etch technique (Wet-transfer, section 7.2.1) and the PVA-assisted delamination technique (Dry-transfer, section 7.2.2). The quality and continuity of the transferred CVD graphene was investigated using Raman spectroscopy and AFM over several areas. Raman spectra were acquired using a 532 nm laser source, operated at 10 mW at an objective lens with $\times 100$ magnification. For graphene transferred to 13 nm SiO_2/Si substrates, an extended gate time of 60 s over 10 sweeps was required to obtain a signal-to-noise better than 10:1. In the DG region (1250 cm^{-1} to 1750 cm^{-1}), third-order Raman modes from the underlying silicon substrate convoluted the spectra, making the determination of the D/G ratio difficult. To recover graphene only spectra, the region greater than 1650 cm^{-1} was background subtracted and the mode at 1450 cm^{-1}, which is attributed to the third-order silicon TO phonon, was used for normalisation. The same process was used on a spectrum taken from the SiO_2/Si area only, which was then subtracted from the graphene spectra to remove the silicon contribution. For graphene transferred to 90 nm SiO_2/Si, there is no Raman contribution from the underlying silicon crystal and the surface enhancement effect from the oxide thickness means that gate times of >0.1 s herald acceptable signal-to-noise. The reduced gate time for measurements on graphene transferred to 90 nm SiO_2/Si meant that Raman mapping could be used to ascertain graphene quality over a large area on the sample. Figure 7.12 shows a series of Raman maps of a 500×500 µm area of CVD graphene transferred to 90 nm SiO_2/Si using the wet-transfer technique. The D, G, and $2D$ maps (a – c respectively) provide the raw count rate of the fitted Raman peaks. The G and $2D$ in conjunction display the extent of transferred graphene, and show clear regions where there is no graphene due to large tears in the sheet. The D peak intensity map is a spatial indication

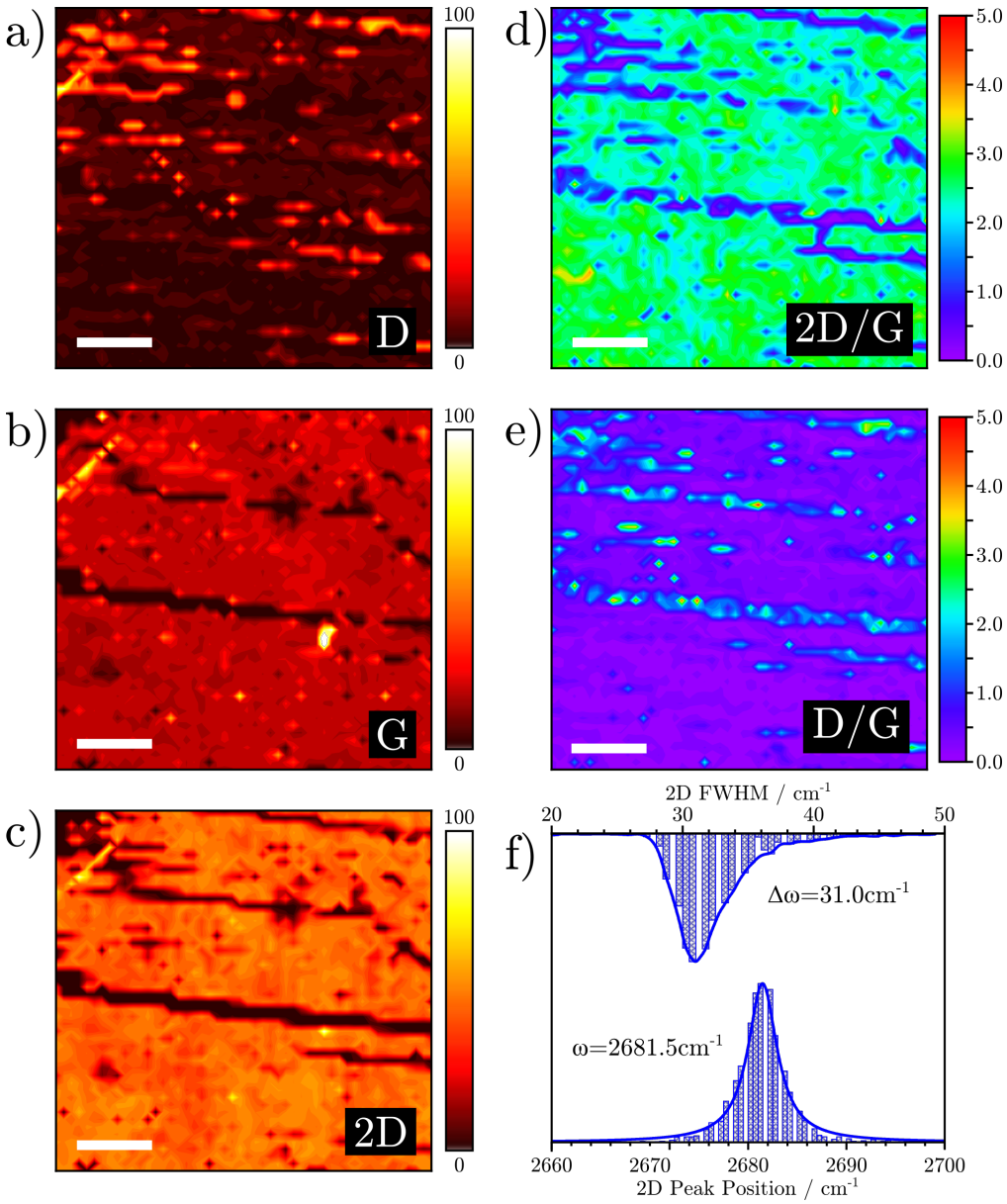

Figure 7.12. Raman mapping of CVD graphene transferred to SiO_2 using the wet-transfer technique. The white scale bars are 100 µm in length. The peak intensities of the **(a)** D band, **(b)** G band, and **(c)** $2D$ band have been used to generate the **(d)** $2D/G$ and **(e)** D/G peak height ratios. The histograms in **(f)** show the number of occurrences for different positions and FWHMs of the $2D$ peak across the mapped area.

of defects in the graphene sheet. The $2D/G$ and D/G ratio maps provide a clearer picture – the majority of the measured areas show a $2D/G$ ratio greater than two, confirming that a single layer of graphene has been transferred. The D/G ratio appears to be consistent across the graphene sheet and below 0.5, but increases above 1 in the regions where single layer graphene is not present, both in the tear regions and on the sheet. This could either be disordered adventitious carbon or a result of the fitting program dividing the noise-related intensity when there is no significant carbon-related Raman signal. In figure 7.12f, histograms showing the peak position and FWHM of the $2D$ peak for all the collected spectra are shown. The modal value of FWHM was $31.0\,\mathrm{cm}^{-1}$ and the mean peak position was $2681.5\,\mathrm{cm}^{-1}$, both very typical values for CVD graphene transferred to SiO_2/Si substrates [246, 255].

There were several successful dry-transfers of CVD graphene to silicon substrates with varying thicknesses of silicon dioxide overlayer. Figure 7.13 shows a representative Raman spectrum of CVD graphene transferred using the PVA-carrier technique after background subtraction. The G and $2D$ peaks are clear at $1586\,\mathrm{cm}^{-1}$ and $2681\,\mathrm{cm}^{-1}$ respectively, and the $2D/G$ ratio is $\sim$2.24. Both the G and $2D$ peaks have been fitted using a Voigt profile for which the $2D$ peak gives a FWHM of $\sim 35\,\mathrm{cm}^{-1}$. There was little-to-no D peak observed in most of the spectra ($D/G < 0.1$), however there is a feature at $\sim 2450\,\mathrm{cm}^{-1}$ which is attributed to the $D + D$" intra-valley process. The large sharp deviation at $1550\,\mathrm{cm}^{-1}$ is attributed to atmospheric molecular oxygen O_2 between the sample and the detector. The Raman maps for dry-transferred CVD graphene are shown in figure 7.14. Compared to the wet-transferred graphene in 7.12, the most immediate difference seen in the dry-transferred graphene is the low density of defects shown by the D peak map in figure 7.14a. Across the analysed area,

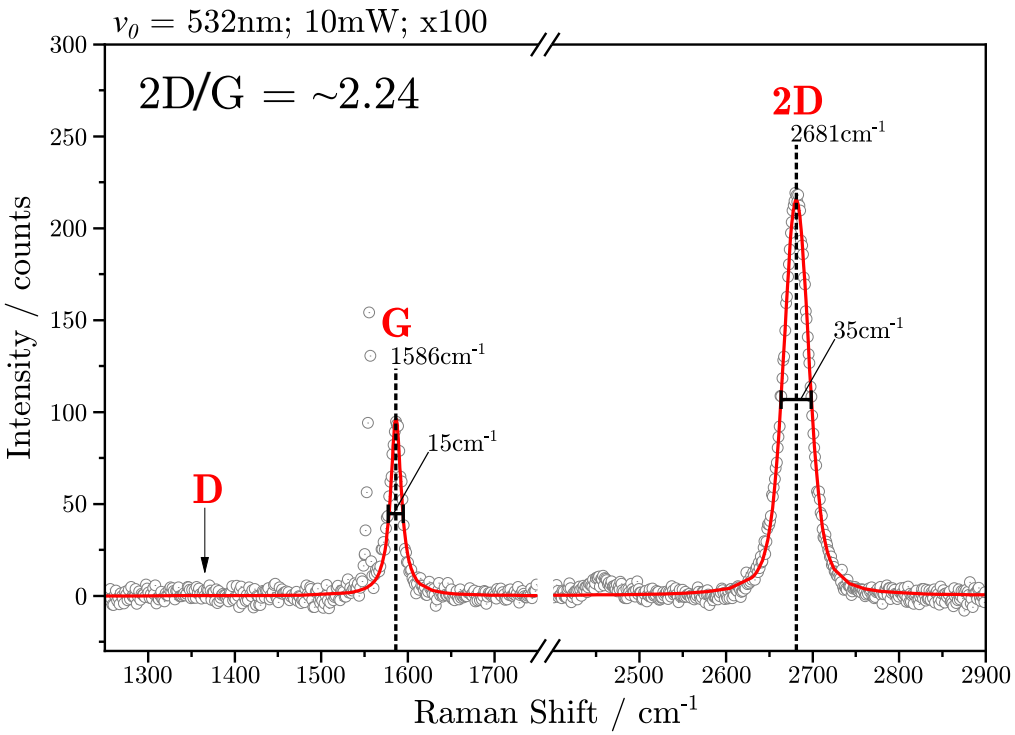

Figure 7.13. Raman spectrum between 1250 cm^{-1} to 2900 cm^{-1} for CVD graphene transferred to SiO_2/Si using the PVA-transfer technique. The positions and FWHMs of the D, G and $2D$ peaks of graphene have been stated. The lack of a D peak and the large $2D/G$ ratio indicate high quality single layer graphene.

the D peak intensity is nearly negligible with only a few small localised points exhibiting an increased D peak intensity. The G and $2D$ peak intensities reveal that there are no tears or rips in the transferred graphene, but there are localised regions where no graphene is present. However, closer inspection on many of these regions reveals that the G and $2D$ peaks are present, but at significantly lower intensity. Again, the ratio maps provide a clearer picture – the $2D/G$ map confirms that a majority of the analysed graphene exhibits a $2D/G$ ratio between 1.5 and 2.5 (see figure 7.14d). Inspection of the spectra with $2D/G$ less than 2 was undertaken, and in most cases the $2D$ peak could be fitted with a single component and had a narrow FWHM (i.e. less than 40 cm^{-1}). The D/G ratio map of dry-transferred graphene (see figure 7.14e) reveals many localised

defects with a D/G ratio of ~ 1, of which many correspond to the areas in the G and $2D$ maps which are either devoid of graphene or have reduced intensities. The rest of the graphene sheet appears to be homogeneous with D/G values less than 0.1. In figure 7.14f, histograms showing the FWHM and peak position of the $2D$ peak result in a modal FWHM value of $33.1\,\mathrm{cm}^{-1}$ and an average peak position value of $2681.5\,\mathrm{cm}^{-1}$. Raman mapping has the advantage of collecting lots of spectra in a short amount of time. As already seen for the $2D$ peak position and FWHM in figures 7.12 and 7.14, the large number of data points (e.g. 2500 spectra in this case) allows a statistical determination of the $2D/G$ and D/G ratios for the dry and wet transferred CVD graphene. Figure 7.15 shows the distribution of $2D/G$ and D/G ratio values of the mapped areas in figures 7.12 and 7.14. Immediately it is clear in 7.15a that the wet-transferred CVD graphene has a larger $2D/G$ ratio of 2.44, compared to the dry-transfer ratio of 1.83. The distribution of $2D/G$ ratios have been fitted with Lorentzian peaks and both have similar widths for both wet and dry transferred graphene, although the wet-transfer technique does have more occurrences below 1 that are not described by the Lorentzian fit. The wet-transferred graphene also has a narrower $2D$ FWHM of $31.0\,\mathrm{cm}^{-1}$ compared to $33.1\,\mathrm{cm}^{-1}$ for the dry-transferred graphene. Figure 7.15b reveals that the dry-transfer technique results in a D/G ratio that is predominately less than 0.1, with modal number of measured spectra in the 0.01 bin. The wet-transfer technique produced a wider spread of D/G ratios ranging from 0.01 to 0.6 (ignoring bins with less than 10 occurrences) with a maxima at 0.14. Both subfigures 7.15a and 7.15b have occurrences above the maximum x-limit, but the bin values are random and have less than 10 occurrences. These anomalous bins are likely due to the Raman instrument's software attempting to fit non-existent peaks in the noise where there may have been a lack of graphene. The D/G ratio has often been used as a

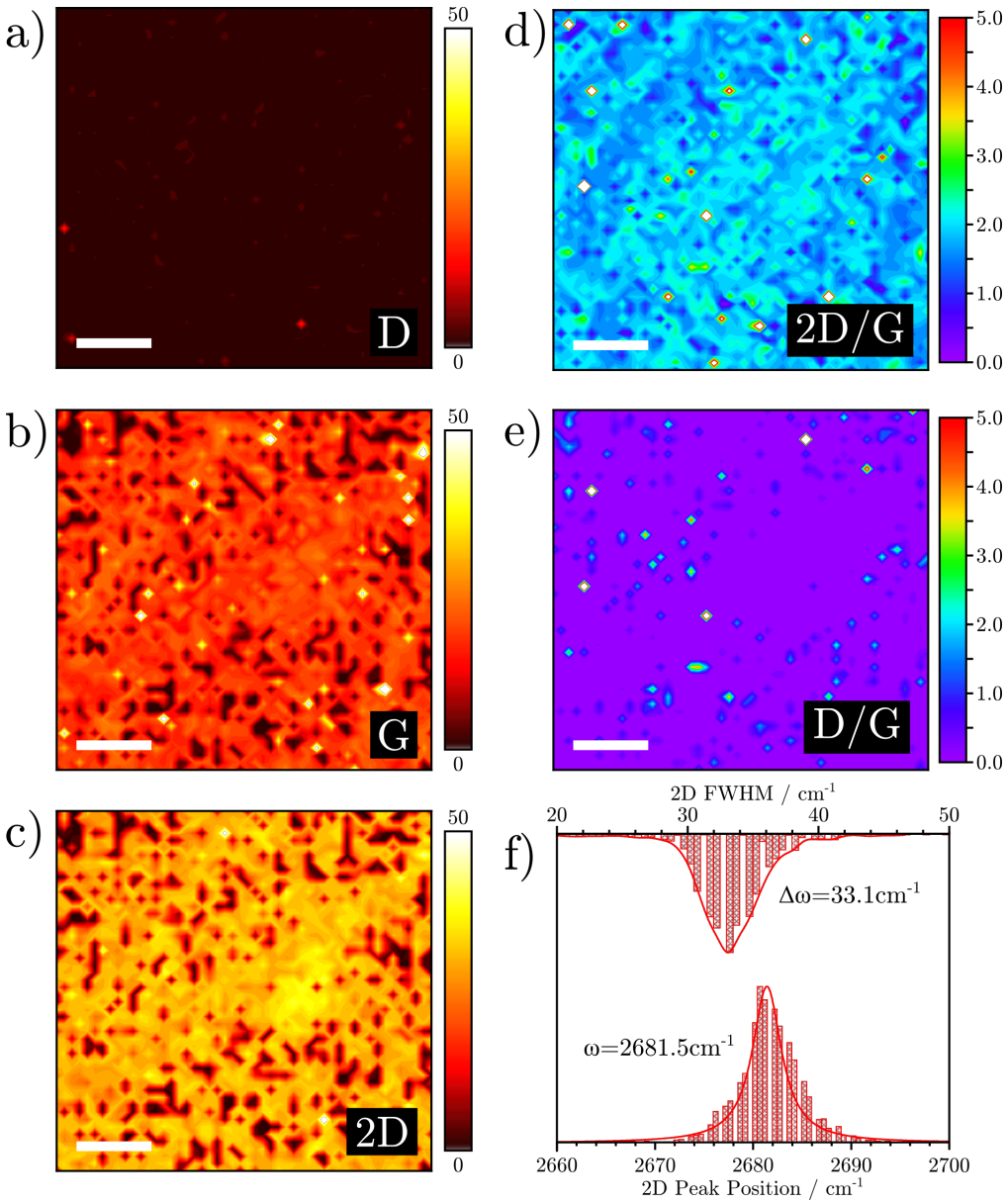

Figure 7.14. Raman mapping of CVD graphene transferred to SiO_2 using the dry-transfer technqiue. The white scale bars are 100 µm in length. The peak intensities of the **(a)** D band, **(b)** G band, and **(c)** $2D$ band have been used to generate the **(d)** $2D/G$ and **(e)** D/G peak height ratios. The histograms in **(f)** show the number of occurrences for different positions and FWHMs of the $2D$ peak across the mapped area.

qualitative measure of defective graphene, and considerable effort by the Raman spectroscopy community has been spent to find quantitative methods of analysis that use this ratio. One particular approach involves producing a known number of point defects using highly-controllable doses of Ar^+ bombardment and then measuring the D/G ratio. A relationship between the D/G ratio and the areal defect density n_D was proposed by Lucchese *et al.* and Cancado *et al.* [260, 261], then systemically confirmed by Pollard *et al.* [262]. For an average inter-defect distance greater than 10 nm, the relation (see equation 1 in ref [261]) can be simplified to:

$$n_D(\mathrm{cm}^{-2}) = (7.3 \pm 2.2) \times 10^9 E_L^4 \left(\frac{I_D}{I_G}\right) \tag{7.1}$$

where E_L^4 is the incident photon energy in electron volts, and I_D/I_G is the area ratio of intensities of the D and G peaks. This relation is used here to provide a tangible figure-of-merit for comparing the aforementioned transfer techniques. Using the average D/G ratios extracted from the histograms in figure 7.15 and the photon power for a 532 nm green laser (i.e. 2.33 eV), the defect density of the wet and dry-transferred graphene is $(3.01 \pm 0.90) \times 10^{10}\,\mathrm{cm}^{-2}$ and $(2.15 \pm 0.65) \times 10^9\,\mathrm{cm}^{-2}$ respectively. Despite these equations relying on experimental Raman data from ion-bombarded graphene, they remain valid for other types of point defects such as substitutional atoms and resonant scatters because the D/G ratio is largely unaffected by the nature of the defect. There are however certain graphene defects which do not contribute to the D peak intensity, such as uniaxial/biaxial strain, intercalates, and perfect zigzag edges. The near-zero D/G ratio for dry-transferred CVD graphene implies a high-quality graphene sheet, but the D peak map does show localised damage on the order of the laser spot size ($\sim$10 µm). The dry-transferred graphene was

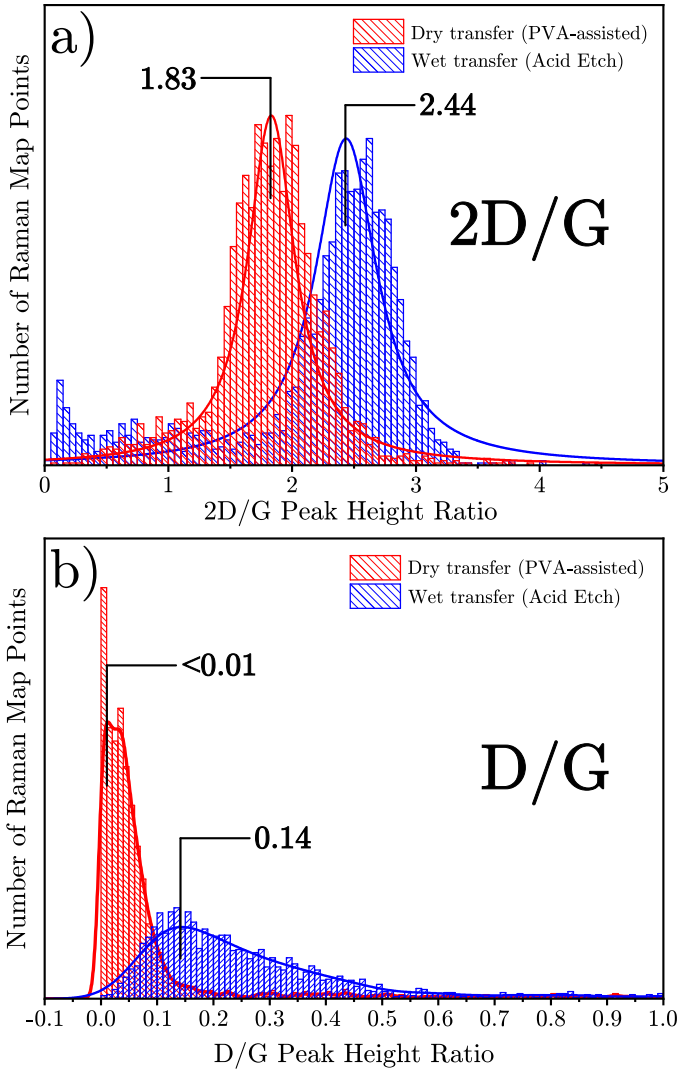

Figure 7.15. Histograms showing the occurrence of **(a)** $2D/G$ and **(b)** D/G ratios for CVD graphene transferred using the wet and dry transfer techniques. The most common ratios have been annotated.

therefore studied further with AFM over several areas to determine coverage and damage on the microscale, beyond the resolution of the Raman spectrometer. AFM images were acquired in non-contact mode to avoid damaging the graphene or picking up surface contaminants which would blunt the probe tip. The microscope was operated in high-voltage mode using a NSG03 Pt-coated silicon cantilever at a set point of 0.04 µm and a Z-servo gain of 1. Widescan images

were taken over areas of 40 µm^2 and narrow images over 10 µm^2. Figures 7.16a and 7.16b show a representative AFM images of CVD graphene transferred using the PVA-carrier technique. In the 40 µm^2 image, there appears to be a majority of graphene coverage demonstrating that the PVA-carrier is capable of lifting a continuous sheet of graphene away from the growth substrate. There are some highly-localised areas that exceed the upper z-range of the image, which are likely to be residual polymer contaminants. The 10 µm^2 image, which was acquired from the blue dashed region in figure 7.16a, shows evidence of some tearing, wrinkling, and folding in the graphene sheet. Figure 7.16d illustrates an interpretation of the damage highlighted by the white dashed box in figure 7.16b. During peel off from the growth substrate, a section of graphene became simultaneously detached from both the PVA-carrier and the growth substrate. This 'free-standing' graphene was then unintentionally folded either before or during the stamping of the graphene sheet onto the SiO_2. This results in a region where turbostratic single, bi- and tri-layer graphene exists.

A common issue with transferring graphene from its growth substrate is the polymer scaffold residues that are left post-transfer which affect the electronic properties and the structure of the graphene. In the literature, a considerable amount of effort has been invested into removing these polymer residues, with methods ranging from annealing in reactive gases (e.g. H_2 [263], CO_2, NO_2 [264], etc), chemical washes (e.g. acetic acid and acetone [265]), and UV-radiation induced breakdown [266]. XPS is an apt technique for ascertaining the level of contamination from polymer residues, as well as any other chemicals used in transfer techniques, such as acid residues. Both the wet and dry-transfer graphene samples were rinsed in isopropanol and dried with N_2 gas, before being loaded into UHV. For this XPS experiment, a Kratos Axis Ultra DLD

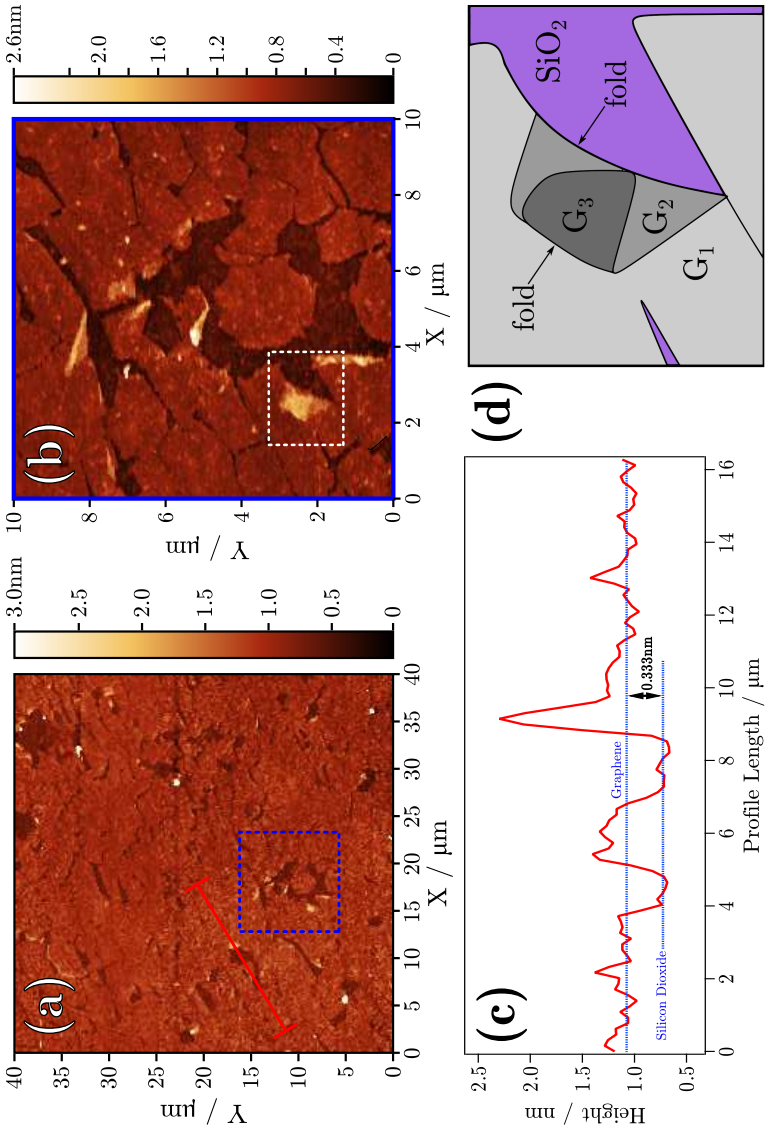

Figure 7.16. AFM conducted on CVD-grown graphene transferred to 5 nm SiO_2. **(a)** 40×40 µm widescan. The blue dashed line denotes the border of the 10×10 µm area studied in **(b)**. A height profile was extracted from the solid red line to give **(c)**. The white dashed line in **(b)** is the subject of the interpretation presented in **(d)**. The graphene has been successfully transferred with a high degree of coverage, although evidence of tears, folds, and wrinkles is present. The height profile obtained in **(c)** confirms the graphene is approximately 0.333 nm above the SiO_2 substrate surface.

at the National Physical Laboratory (NPL) was used. This instrument used a monochromated Al Kα X-ray source with an analyser defined spot size of 300×700 µm. Unlike the twin-anode source used for rest of this work, the monochromated source does not generate a source of secondary electrons which compensate sample surface charging. Therefore, a low-energy electron source was used to compensate the surface charging. Figure 7.17 shows the results of the XPS analysis on the transferred graphene on SiO_2/Si. The survey

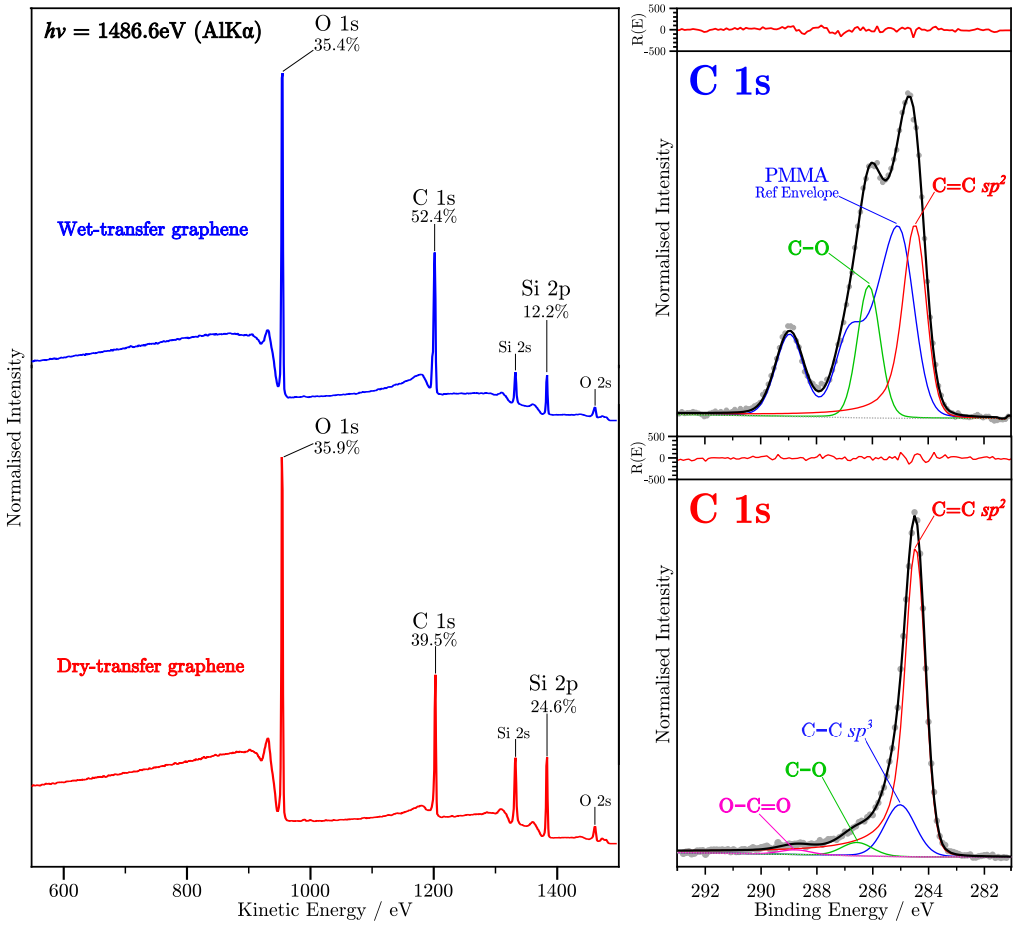

Figure 7.17. XPS spectra of CVD graphene transferred to SiO_2/Si. **Left:** Survey scans for the wet (blue) and dry (red) transferred graphene containing the O 1*s*, C 1*s*, and Si 2*p* core level quantification. **Right:** High resolution scans of the C 1*s* core level for wet-transferred (top) and dry-transferred (bottom) graphene. The red inset traces show the residual $R(E)$. Tables 7.2 and 7.3 shows the fitting results for these spectra.

Component	Position / eV	FWHM / eV	∑GL ratio	At%
Graphene				
C=C sp^2	284.4	1.0	0.45(*0.31)	27.3
C–O / C–OH	286.1	1.0	0.10	15.2
PMMA Reference [267, 268]				
CH_2 / CH_3	285.0	1.2	0.10	23.0
C–C	285.8	1.2	0.10	11.5
C–O	286.8	1.2	0.10	11.5
O–C=O	289.0	1.2	0.10	11.5

Table 7.2. Fitting results for the PMMA-transferred graphene spectra in Figure 7.17 (*Asymmetry factor).

Component	Position / eV	FWHM / eV	∑GL ratio	At%
C=C sp^2	284.4	0.9	0.46(*0.52)	78.7
C–C sp^3	285	1.3	0.10	15.8
C–O	286.5	1.3	0.10	4.1
O–C=O	288.8	1.3	0.10	1.4

Table 7.3. Fitting results for the PVA-transferred graphene spectra in Figure 7.17 (*Asymmetry factor).

scans for both wet (blue) and dry (red) transferred graphene show Si 2p and 2s peaks originating from the underlying silicon oxide substrate, C 1s from the transferred graphene and polymer residues, and the O 1s peak from the silicon oxide underlayer and polymer residues. There are no other elements present in the survey spectra, even at higher binding energies. The dry-transfer technique does not use any aggressive chemicals to detach the CVD graphene from the copper growth substrate, so for the exception for copper, only adventitous carbon and PVA residue is expected. However the wet-transfer technique uses APS to remove the copper substrate, and so nitrogen, copper, and sulphate species which may have been found adsorbed to the graphene. However, the lack of principle and Auger photoelectron peaks from any of these contaminants seems to confirm the high-quality of the transfer techniques used in this study. In terms of atomic composition, the wet-transferred graphene has

a much higher carbon contribution (52.4 at%) compared to the dry-transferred graphene (39.5 at%). The wet-transferred graphene also has a smaller Si $2p$ contribution (12.2 at%) compared to the dry-transferred graphene (24.6 at%). An accurate determination of the carbon overlayer is difficult due to the inherent uncertainty of the EAL for complex systems containing multiple sources of carbon photoelectrons, i.e. graphene and the polymer in this case. It should also be noted, that the extracted quantitative atomic compositions are only valid for homogeneous systems, which these spectra do not represent. Qualitatively, the increase of the carbon-silicon ratio in the wet-transferred graphene implies a thicker carbon overlayer which is unlikely to be multi-layer graphene due to the self-limiting nature of CVD graphene growth on copper. The background shape also provides qualitative information supporting a thicker carbon overlayer on wet-transferred graphene. The inelastic background region between 640 eV and 940 eV kinetic energy has a different shape for the two graphene samples. The maximum of the inelastic background generated by O $1s$ photoelectrons for wet-transferred graphene is shifted to lower kinetic energy by $\sim$50 eV. This is analogous to regime D (bulk substrate photoelectrons travelling through an overlayer) described by S. Tougaard [269], where a larger proportion of the O $1s$ photoelectrons are inelastically scattered whilst travelling through the thicker carbon overlayer, compared to a single sheet of graphene. This causes a shift in the average kinetic energy of the inelastically scattered electrons. The core level spectra shed more light on the structure of the carbon overlayer for both samples. The top C $1s$ spectrum in figure 7.17 was acquired from the wet-transferred graphene, and the fitting envelope is rather complex. Following from the evidence presented by the survey spectrum, it was deduced that a significant amount of PMMA residue was still bonded to the wet-transferred graphene. As such, a C $1s$ PMMA envelope was constructed using reference data from

Beamson and Briggs [267] as well as Girardeaux and Pireaux [268]. The fitting parameters used for each component of the PMMA envelope (i.e. CH_2/CH_3, C−C, C−O, and O−C=O) are shown in table 7.2. The PMMA envelope was fitted to the normalised C 1*s* spectra, and the residual revealed two components that were not compensated for. These two components were subsequently fitted and assigned as C=C sp^2 (284.4 eV) and C−O/C−OH (286.1 eV) [225, 226]. The C=C sp^2 is of course due to the graphene sheet, and whilst it is possible that some intensity the C−O/C−OH component corresponds to aromatic ether or hydroxyl bonded to the sheet, the lack of a characteristic graphene oxide Raman spectrum means that it is more likely that this component belongs to adventitious carbon species. The bottom C 1*s* spectrum in figure 7.17 was acquired from the dry-transferred graphene. Similar to the C 1*s* spectrum from wet-transferred graphene, the PVA support polymer reference spectrum (again from Beamson & Briggs) was constructed and fitted to the raw data along with the predominant C=C sp^2 component [270, 271]. However the PVA reference spectrum did not result in a satisfactory fit, as the C−C:C−O ratio is $\sim$ 1 in PVA, and a larger ratio was required to reduce the residual. Therefore, the fitting parameter constraints were relaxed in order to improve the fit. The results of that fit are shown in table 7.3. Again, the C=C sp^2 component (284.4 eV) is present but in the case of dry-transferred graphene, it dominates the C 1*s* intensity. The positions of the C−O (286.5 eV) and O−C=O (288.8 eV) components are consistent with oxygen bonded to aliphatic carbon when compared to the charge-referenced C−C sp^3 component, i.e. adventitious carbon [225, 226]. Whilst some of this adventitious carbon is likely to be PVA, even assuming that the maximum proportion of the C−C sp^3 to match the C−O component, the PVA residue only accounts for an upper bound of 8.2 % of the total C 1*s* intensity.

7.3 Catalytically-grown Graphene on SiO_2

The results from section 7.2 demonstrate that the dry-transfer technique, which uses a PVA as an adhesion layer to mechanically de-laminate the graphene from the growth substrate, is far superior to the wet-transfer technique in maintaining both the structural and chemical purity of graphene. The method is highly controllable, can be applied to a multitude of target substrates, and can used on catalytically-grown graphene on diamond or SiC without extended acid-etch times. In section 6.2.1, a moderately boron-doped (111)-orientated diamond was graphitised using the iron-mediated graphitisation technique. The graphene grown in this experiment was transferred to an unpolished 90 nm SiO_2/Si substrate using the dry transfer technique described in section 7.2.2. It should be noted, that the transfer to the unpolished side of the silicon wafer was unintentional. The catalytically-grown graphene on silicon sample was immediately analysed with Raman spectroscopy. A representative Raman spectrum from this experiment is shown in figure 7.18. Similar to the CVD-transferred graphene, G and $2D$ peaks are clear at $1591\,\mathrm{cm}^{-1}$ and $2683\,\mathrm{cm}^{-1}$ respectively, with a $2D/G$ ratio of $\sim$1.22. Once again, the G and $2D$ peaks have been fitted using a Voigt profiles which result in FWHMs of $\sim 16\,\mathrm{cm}^{-1}$ and $\sim 36\,\mathrm{cm}^{-1}$ for the G and $2D$ peaks respectively; both values exhibited by CVD graphene. The $2D$ peak is very clearly resolved and can be fitted with a single component. It follows then that figure 7.18 confirms the presence of single layer graphene produced using the iron-mediated graphitisation method. However, the dominant peak in this spectrum is the defect-related D peak at $1345\,\mathrm{cm}^{-1}$. The D/G ratio is $\sim$2.09 which indicates that the transferred graphene is heavily defected, with a defect density of $(4.50 \pm 1.35) \times 10^{11}\,\mathrm{cm}^{-2}$ which is an order of magnitude higher than the CVD graphene transferred in section 7.2.3. Also

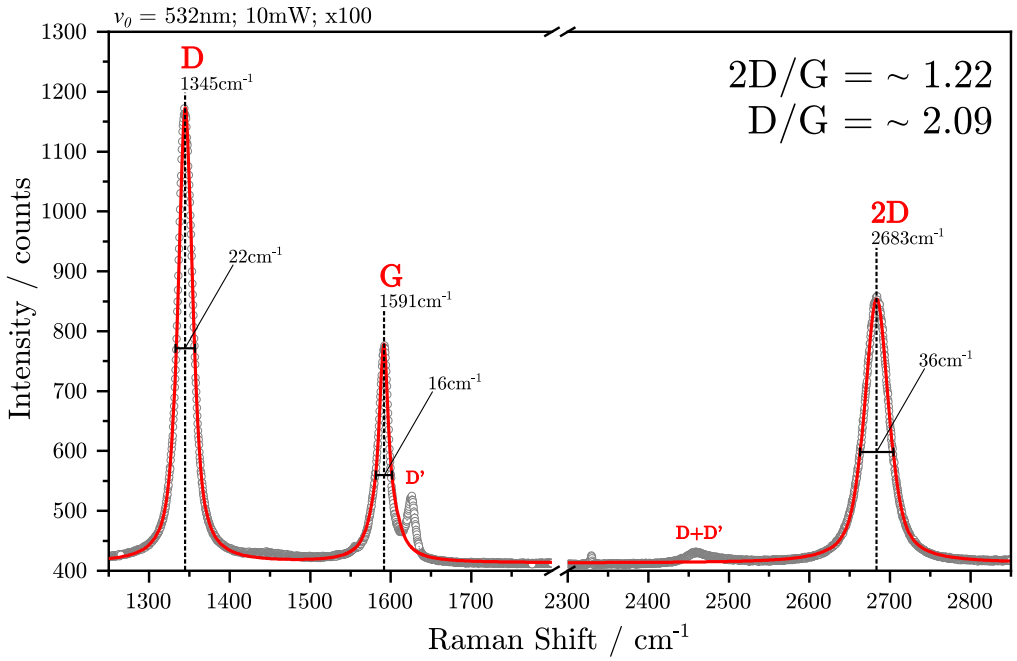

Figure 7.18. Raman spectrum between 1250 cm^{-1} to 2850 cm^{-1} for catalytically-grown graphene from a diamond (111) surface transferred to 90 nm unpolished SiO_2/Si using the PVA-transfer technique. The positions and FWHMs of the D, G, and $2D$ peaks of graphene have been stated. The red line represents a multiple Lorentzian peak fit of the D, G, and $2D$ peaks.

visible in figure 7.18 is the D' peak which arises from defect-induced intra-valley scattering [246]. The D' peak is not often considered as it is usually small enough to only contribute a small shoulder to the G peak, or is completely absent in the case of pristine graphene. However in this experiment, D' is clearly resolvable with a D'/G ratio of ~0.32. With this information, a confident assessment of the defect type is possible. The D peak is very narrow with a FWHM of ~22 cm^{-1} and highly symmetrical, unlike the D peak profiles of other types of disorder carbon such as sp^3 amorphous carbon, which are very broad and tend to overlap with the G peak. A more quantitative approach involves extracting the ratio between the D and D' peaks which can distinguish between sp^3-related defects (i.e. chemical defects from functionalised and oxidised graphene) and vacancy related defects (i.e. structural gaps, missing atoms, etc) due to the

differing linear dependencies of $I(D)$ and $I(D')$ for different types of defect [272]. The D'/D ratio for the transferred graphene in figure 7.18 is ∼6.53, which means that vacancy type defects are most prevalent in the catalytically-grown graphene [272]. It is most likely that these defects were caused by transfer onto a rough unpolished SiO_2 surface. Referring back to figure 6.7 in chapter 6, the LEED pattern recorded immediately after graphitisation exhibited very sharp diffraction spots and a single rotational domain of graphene as well as almost no secondary electron contribution on the rest of the phosphor screen. If the catalytically-grown graphene was as defected as implied by the Raman spectrum in figure 7.18 before removal from the UHV system, then the LEED pattern would not have shown such a high degree of crystallinity [273] or a lack of secondary electrons. Needless to say, this experiment must be repeated and a successful transfer to polished 90 nm SiO_2/Si completed to definitely know the Raman-extracted figures of merit, which can be extracted statistically using large-area Raman mapping.

7.4 Chapter Conclusion

In the first half of this chapter, the patterning of catalytically-grown graphene into simple architectures on SiC was demonstrated in both the home laboratory and at a synchrotron end station. In both cases, the quality of the graphene / graphite produced was not of the same quality of previous work on this system as evidenced by a large D/G ratio and $2D$ FWHM. In both cases, the experiments could not be conducted under the ideal conditions required for extremely high quality graphene growth. In both the home laboratory and the beamline, the annealing step to remove oxygen and reclaim a (1×1) SiC-(0001) surface was unsuccessful, meaning that the ideal registry transfer from the substrate to

the catalytically-grown graphene was not achieved. Another factor was the cleanliness of the iron evaporation source at the SMART beamline at BESSYII which was unable to maintain a constant deposition rate, and evidence of oxygen contamination was detected in the iron film by XPS. Despite these issues, the use of spatially resolved spectroscopic techniques such as Raman mapping and XPEEM, as well LEED and LEEM have overwhelmingly demonstrated that the graphitised regions adhere perfectly to the deposited iron pattern. In the home laboratory, small area XPS on a graphitised region reveals a characteristic asymmetric C=C sp^2 peak of graphene coinciding with the SiC at lower binding energy, and ARXPS data taken at 60° from normal emission confirms that this sp^2 carbon is at the surface of the iron. The ability to grow graphene directly into a specific pattern is a significant advantage which avoids the potentially damaging effect of post-growth lithography techniques. Iron-mediated graphitisation holds another advantage over CVD graphene, in that the substrates used for the method, i.e. diamond and SiC, have equally favourable properties for the fabrication of electronic devices. In the case of SiC, the iron catalyst is converted to a FeSi interfacial layer during the graphitisation process which strongly interacts with the graphene. A proposed route to producing a graphene field-effect transistor (GFET) based radiation sensor is as follows: by introducing this interfacial layer to an oxygen-rich environment, the silicon will oxidise to form a insulating SiO_2 layer that does not strongly interact with the graphene. This results in the GFET architecture where a radiation-induced ionisation event in the semiconducting SiC substrate would generate an electric-field which could be detected by the highly sensitive graphene as a resistivity change [274]. Direct growth of high-quality graphene into the desired architecture for the fabrication of devices is highly favourable.

Regardless, transferring graphene to arbitrary substrates is also required, both for device fabrication and for characterisation efforts. To enable further characterisation of catalytically-grown graphene using Raman spectroscopy, a comparative study was undertaken to assess two different methods for transferring graphene. The first 'wet' method is a standard transfer technique used for CVD graphene grown on transition metal foils such as copper. However, this technique is not suitable for the iron-mediated graphitisation method, because the nano-scale thickness of the metal interface inhibits the diffusion of the etchant from the edges of the graphene sheet into the middle, vastly increasing the transfer time and introducing more opportunity for tears, cracks, and folds to form. The increased contact time with aggressive chemicals may also have an effect on the electronic and structural properties of the graphene, as contaminants from the etchant may remain on the graphene even after cleaning in de-ionised water. To avoid the common issues with the wet-transfer technique, a second acid-free 'dry' transfer technique was developed which uses water-soluble PVA as a polymer scaffold to aid in mechanical delamination of graphene from its growth substrate. The two transfer techniques were used to transfer CVD graphene from copper foil to 90 nm SiO_2 on Si wafers, and then Raman spectroscopy, Raman mapping, AFM, and XPS were all used to compare the quality of the post-transferred graphene. Whilst both techniques successfully transferred the CVD graphene, the dry-transfer technique performed overwhelmingly better than the wet-transfer technique in all areas, from graphene quality, coverage, and amount of polymer residues. Using the D/G statistical information from Raman maps acquired post-transfer, the defect density for dry-transferred graphene ($(2.15 \pm 0.65) \times 10^9\,\mathrm{cm}^{-2}$) was an order of magnitude smaller than the wet-transferred graphene ($(3.01 \pm 0.90) \times 10^{10}\,\mathrm{cm}^{-2}$). Raman mapping and non-

contact AFM confirms that continuous sheets of graphene have been successfully transferred by both techniques, although the dry-transfer method results in far fewer long-range defects such as tears, with most large defects measuring less than 10 µm in any one dimension. Chemical purity and the amount of polymer residue was measured using XPS. The C 1*s* scan of the dry-transferred graphene reveals a dominant C=C sp^2 component with additional components consistent with adventitious carbon contamination indicating a maximum possible atomic concentration of PVA-related species at ∼8 %. On the other hand, the C 1*s* scan of the wet-transferred graphene is dominated by PMMA-related components which account for ∼58 % of the total carbon contribution. Qualitative assessment of the inelastic background on the higher binding energy side of the O 1*s* indicates that there is a thicker carbon overlayer on the wet-transferred graphene which in conjunction with the core level scans and survey quantification, suggests a significant amount of PMMA residue.

To conclude this chapter, the superior dry-transfer technique was used to transfer a sheet of catalytically-grown graphene from diamond to an unpolished 90 nm SiO_2/Si wafer. Raman spectroscopy conducted on the graphene post-transfer revealed the characteristic D, G, and $2D$ peaks of ordered sp^2 carbon. The G and $2D$ peak exhibited positions and FWHMs similar to that of CVD graphene on 90 nm SiO_2/Si substrates. Although the $2D/G$ intensity ratio was less than the literature accepted figure-of-merit for single-layer graphene (i.e. greater than 2), the $2D$ peak contains a single component that has a FWHM of 36 cm^{-1} indicative of single layer graphene. The $2D/G$ ratio can be deminished by other factors like disorder and doping, and therefore should not be used in isolation as a measure of the number of graphene layers [275]. The presence of a large D and D' peak intensity means that the transferred graphene is heavily

defected, with a calculated defect density of $(4.50 \pm 1.35) \times 10^{11}\,\mathrm{cm}^{-2}$; an order of magnitude higher than the CVD graphene on SiO_2 analysed in this work. By analysis of the D/D' ratio, the origin of the defect Raman peaks can be attributed to structural type defects such as vacancies in the graphene sheet. Previous LEED measurements, taken immediately after graphitisation whilst the graphene was still on the diamond growth substrate and in UHV conditions, indicate a high degree of crystallinity with no evidence of a significant defect density. Furthermore, the dry-transfer technique has been shown to preserve the high structural and chemical purity of CVD graphene, with minimal levels of polymer residue. Therefore, it is highly probable that the damage induced in the catalytically-grown graphene was due to the roughness of the unpolished SiO_2 layer. However in order to confirm this, the experiment must be repeated with a successful transfer to a polished 90 nm SiO_2/Si and a subsequent statistical application of Raman mapping over a large area of transferred catalytically-grown graphene.

Chapter 8

Thesis Summary

The focus of this thesis was to advance the understanding of diamond-graphene interfaces and develop new techniques for the production of catalytically-grown graphene from diamond/SiC and its fabrication into useful devices in the future. This work consisted of three main research avenues: catalyst-free UHV graphitisation of diamond (111) surfaces; iron-mediated graphitisation to produce doped graphene; and the patterning and transfer of catalytically-grown graphene from diamond and SiC.

In chapter 5, the high temperature catalyst-free UHV graphitisation of near-atomically flat diamond (111) surfaces was presented, as well as the intermediate surface conditions during a heating cycle to 1000 °C. Post-polishing, the (111) surface is covered by a monolayer of alcohol, ketone, and carboxyls in a ∼73:23:4 ratio. After heating above 900 °C in UHV, a hydrogen terminated surface is formed, exhibiting a single corrugated hexagon pattern in LEED indicative of a (111)(1 × 1) surface. Above 930 °C, the surface undergoes reconstruction into a (2 × 1) crystallographic motif. Doubling of the surface periodicity was observed in only two directions on the (111) surface. Topography created by the

polishing process is likely to have formed an increased number of atomic terraces perpendicular to the polishing direction which have a reconstruction breaking effect. ARPES and DFT modelling conducted along the $K\Gamma K$ direction in the diamond (111)(2 × 1) BZ shows good agreement, and confirms that the reconstructed surface is metallic, in contrary to the most recent ARPES data by Graupner *et al.*. This work is the first modern evidence reconciling both experimental ARPES and theoretical calculations of the band structure for the (111)(2 × 1) surface of diamond. UHV catalyst-free graphitisation of the (111) surface occurs after the reconstruction beyond temperatures of 1000 °C, such that graphene coexists on top the reconstructed diamond surface. Once again, ARPES and DFT calculations provide the strongest evidence for the graphene-reconstruction coexistence. ARPES and DFT modelling was conducted along the K_gMK_g direction in the graphene BZ in order to fully sample the π-band, and resulted in a superb agreement in both energy and dispersion. The Dirac cones extend up to and beyond the Fermi level both in the experimental dataset and the DFT modelling, and an upshift in the M-point energy at $K_{||} = 0\,\text{Å}^{-1}$ has been attributed to an increased third-nearest neighbour coupling in the graphene, inferring a strong graphene-substrate interaction.

High temperature UHV graphitisation of the diamond surface is an energy intensive and largely uncontrollable method of producing graphene. The graphitisation of the diamond (111) surface using an iron-catalyst has been shown to reduce the required temperature by up to half. The deposition of Fe on diamond has been monitored using the REES technique revealing a reduced conductivity at extremely thin thicknesses. This was attributed to sub-monolayer Fe coverage and then the Fuchs–Sondheimer model of electron scattering near metal surfaces for multiple layers. Evaporated Fe has been shown

to initially deposit in a disordered pseudomorphic fcc structure, but undergoes a phase transition into the Nishiyama-Wassermann bcc polymorph of Fe after annealing to at least 320 °C. The iron exhibits two rotational domains showing that registry from the underlying $(111)(2 \times 1)$ diamond surface, which had only reconstructed in two directions, is preserved. The true growth mode of iron-mediated graphitisation was studied on a semiconducting (111) diamond surface using REES up to maximum temperature of 685 °C. Four distinct regimes pertaining to the Fe film and the diamond surface were identified during the heating process: *i)* iron undergoes a phase transition; *ii)* the carbon is detached from the diamond surface and migrates through the Fe overlayer as interstitial carbon; *iii)* carbon precipitates on the surface of the Fe into ordered graphene sheets, hence attenuating the Fe signal; *iv)* the reaction is rapidly quenched by dropping the sample temperature and transport of carbon to the surface of the Fe ceases immediately. XPS and LEED have confirmed the chemical and structural purity of the resulting graphene and suggest that there is a strong graphene-substrate interaction which, in agreement with previous studies on this surface, suggests significant charge transfer induced n-doping in the graphene. The iron-mediated graphitisation experiment was repeated using a (111)-oriented HBDD with a boron concentration of $(8.66 \pm 3.32) \times 10^{21}$ atoms/cm^3. Boron was successfully transported through the Fe overlayer during the catalysis, creating a boron-doped carbon overlayer with a $[B]$ of $\sim$5 at% and p-type doping expected of boron-doped graphene/graphite. Based on the extensive study of this method of producing graphene, it is possible that boron-doped single-layer graphene with superior chemical and structural purity can be fabricated, as well as other materials with 2D allotropes.

The patterning of catalytically-grown graphene into simple architectures on

SiC was demonstrated in both the home laboratory and at a synchrotron end station. The use of spatially resolved spectroscopic techniques such as Raman mapping and XPEEM, as well as diffraction techniques such as LEED, LEEM, and spatially-resolved ARXPS have overwhelmingly demonstrated that the graphitised regions adhere perfectly to the deposited iron pattern. The ability to grow graphene directly into a specific pattern is a significant advantage which avoids the potentially damaging effect of post-growth lithography techniques. Iron-mediated graphitisation holds another advantage over CVD graphene, in that the substrates used for the method, i.e. diamond and SiC, have equally favourable properties for the fabrication of electronic devices, such as graphene field-effect transistor (GFET) based radiation sensors. Direct growth of high-quality graphene into the desired architecture for the fabrication of devices is entirely possible using this growth technique.

The importance of transferring graphene to arbitrary substrates was also addressed in the context of device fabrication and for metrology efforts. To avoid the common issues with the standard acid-etch technique of transferring graphene, a second acid-free 'dry' technique was developed which used water-soluble PVA as a polymer scaffold to aid in mechanical delamination of graphene from its growth substrate. The dry-transfer technique performed overwhelmingly better than the wet-transfer technique in all areas, from graphene quality, coverage, and amount of polymer residues, as well as achieving a defect density that is an order of magnitude smaller. Continuous sheets of graphene have been successfully transferred by both techniques, although the dry-transfer method results in far fewer long-range defects such as tears and folds. Chemical purity and the amount of polymer residue was measured using XPS, and demonstrates that the wet-transfer technique leaves a significant

amount of PMMA residue, compared to the dry-transfer technique which does impart some PVA residue, but only accounts for up to 8.2 % of the total carbon content. To conclude this work, the superior dry-transfer technique was used to transfer a sheet of catalytically-grown graphene from diamond to an unpolished 90 nm SiO_2/Si wafer. The transferred graphene is heavily defected, which can be attributed to damage caused by the roughness of the unpolished SiO_2 layer. Future work should aim to repeat this transfer experiment, and obtain a statistical report of the defects in catalytically-grown graphene using Raman mapping.

References

[1] K. S. Novoselov, A. K. Geim, S. V. Morozov, D. Jiang, Y. Zhang, S. V. Dubonos, I. V. Grigorieva, and A. A. Firsov. "Electric field effect in atomically thin carbon films", *Science* **306**, 5696 (2004), pp. 666–669.

[2] K. S. Novoselov, V. I. Fal'ko, L. Colombo, P. R. Gellert, M. G. Schwab, and K. Kim. "A roadmap for graphene", *Nature* **490**, 7419 (2012), p. 192.

[3] P. Avouris and F. Xia. "Graphene applications in electronics and photonics", *MRS Bulletin* **37**, 12 (2012), pp. 1225–1234.

[4] H. Jang, Y. J. Park, X. Chen, T. Das, M-S. Kim, and J-H. Ahn. "Graphene-based flexible and stretchable electronics", *Advanced Materials* **28**, 22 (2016), pp. 4184–4202.

[5] M. D. Stoller, S. Park, Y. Zhu, J. An, and R. S. Ruoff. "Graphene-Based Ultracapacitors", *Nano Letters* **8**, 10 (2008), 3498–3502.

[6] X. Li and L. Zhi. "Graphene hybridization for energy storage applications", *Chemical Society Reviews* **47**, 9 (2018), pp. 3189–3216.

[7] H. Xu, L. Ma, and Z. Jin. "Nitrogen-doped graphene: Synthesis, characterizations and energy applications", *Journal of Energy Chemistry* **27**, 1 (2018), pp. 146–160.

[8] E. K. Wujcik and C. N. Monty. "Nanotechnology for implantable sensors: carbon nanotubes and graphene in medicine", *Wiley Interdisciplinary Reviews: Nanomedicine and Nanobiotechnology* **5**, 3 (2013), pp. 233–249.

[9] A. E. Jakus, E. B. Secor, A. L. Rutz, S. W. Jordan, M. C. Hersam, and R. N. Shah. "Three-dimensional printing of high-content graphene scaffolds for electronic and biomedical applications", *ACS nano* **9**, 4 (2015), pp. 4636–4648.

[10] L. Feng and Z. Liu. "Graphene in biomedicine: opportunities and challenges", *Nanomedicine* **6**, 2 (2011), pp. 317–324.

[11] F. Bonaccorso, Z. Sun, T. Hasan, and A. C. Ferrari. "Graphene photonics and optoelectronics", *Nature Photonics* **4**, 9 (2010), p. 611.

[12] X. Wan, Y. Huang, and Y. Chen. "Focusing on energy and optoelectronic applications: a journey for graphene and graphene oxide at large scale", *Accounts of Chemical Research* **45**, 4 (2012), pp. 598–607.

[13] A. Sedaghat, M. K. Ram, A. Zayed, R. Kamal, and N. Shanahan. "Investigation of physical properties of graphene-cement composite for structural applications", *Open Journal of Composite Materials* **4**, 01 (2014), p. 12.

[14] Z. Yan, D. L. Nika, and A. A. Balandin. "Thermal properties of graphene and few-layer graphene: applications in electronics", *IET Circuits, Devices & Systems* **9**, 1 (2015), pp. 4–12.

[15] Zion Market Research. *Graphene Market (Mono-Layer and Bi-Layer Graphene, Few Layer Graphene, Graphene Oxide and Graphene Nano Platelets) for Composites, Energy Storage, Electronics and Others Applications: Global Industry Perspective, Comprehensive Analysis, and Forecast, 2016-2022*. `https://www.zionmarketresearch.com/report/graphene-market`. pdf. 2017.

[16] Graphene Flagship. *European Roadmap for Graphene Science and Technology*. `https://graphene-flagship.eu/project/roadmap/Pages/Roadmap.aspx`. 2019.

[17] S. P. Cooil, F. Song, G. T. Williams, O. R. Roberts, D. P. Langstaff, B. Jørgensen, K. Høydalsvik, D. W. Breiby, E. Wahlström, D. A. Evans, et al. "Iron-mediated growth of epitaxial graphene on SiC and diamond", *Carbon* **50**, 14 (2012), pp. 5099–5105.

[18] F. S. Phinney. "Graphitization of diamond", *Science* **120**, 3114 (1954), pp. 393–394.

[19] J. Sung. "Graphite → diamond transition under high pressure: A kinetics approach", *Journal of Materials Science* **35**, 23 (2000), pp. 6041–6054.

[20] S. P. Cooil, J. W. Wells, D. Hu, Y. R. Niu, A. A. Zakharov, M. Bianchi, and D. A. Evans. "Controlling the growth of epitaxial graphene on metalized diamond (111) surface", *Applied Physics Letters* **107**, 18 (2015), p. 181603.

[21] Y. Y. Wang, Z. H. Ni, Z. X. Shen, H. M. Wang, and Y. H. Wu. "Interference enhancement of Raman signal of graphene", *Applied Physics Letters* **92**, 4 (2008), p. 043121.

[22] D. Yoon, H. Moon, Y-W. Son, J. S. Choi, B. H. Park, Y. H. Cha, Y. D. Kim, and H. Cheong. "Interference effect on Raman spectrum of graphene on SiO_2/Si", *Physical Review B* **80**, 12 (2009), p. 125422.

[23] J. F. O'Hanlon. *A User's Guide to Vacuum Technology*. 3rd ed. John Wiley & Sons, Inc, 2003.

[24] P. Atkins and J. de Paula. *Atkins' Physical Chemistry*. 8th ed. Oxford University Press, 2006.

[25] J. W. Jewett and R. A. Serway. *Physics for Scientists and Engineers with Modern Physics*. 8th ed. Cengage Learning, 2010.

[26] G. T. Barnes and I. R. Gentle. *Interfacial Science: An Introduction.* 2nd ed. Oxford University Press, 2011.

[27] H. Hertz. "Ueber einen Einfluss des ultravioletten Lichtes auf die electrische Entladung", *Annalen der Physik* **267**, 8 (1887), pp. 983–1000.

[28] A. Einstein. "The photoelectric effect", *Annalen der Physik* **17**, 132 (1905), p. 4.

[29] S. Hüfner. *Photoelectron spectroscopy: principles and applications.* Springer Science & Business Media, 2013.

[30] A. K. Schenk, A. C. Pakpour-Tabrizi, A. J. U. Holt, S. K. Mahatha, F. Arnold, M. Bianchi, R. B. Jackman, J. A. Miwa, Ph. Hofmann, S. P. Cooil, et al. "The occupied electronic structure of ultrathin boron doped diamond", *arXiv preprint arXiv:1907.00673* (2019).

[31] "The quantum theory of the emission and absorption of radiation", *Proceedings of the Royal Society of London A: Mathematical, Physical and Engineering Sciences* **114**, 767 (1927), pp. 243–265.

[32] E. Fermi. *Nuclear physics: a course given by Enrico Fermi at the University of Chicago.* University of Chicago Press, 1950.

[33] J. H. Scofield. *Theoretical photoionization cross sections from 1 to 1500 keV.* Tech. rep. California University, Livermore, Lawrence Livermore Lab, 1973.

[34] J. H. Scofield. "Hartree-Slater subshell photoionization cross-sections at 1254 and 1487 eV", *Journal of Electron Spectroscopy and Related Phenomena* **8**, 2 (1976), pp. 129–137.

[35] J. J. Yeh and I. Lindau. "Atomic subshell photoionization cross sections and asymmetry parameters: $1 \leq Z \leq 103$", *Atomic Data and Nuclear Data Tables* **32**, 1 (1985), pp. 1–155.

[36] J. J. Yeh. *Atomic calculation of photoionization cross-sections and asymmetry parameters.* Gordon & Breach Science Publ.; AT&T Bell Laboratories, 1993.

[37] *Atomic Calculation of Photoionization Cross-Sections and Asymmetry Parameters.* `https://vuo.elettra.eu/services/elements/WebElements.html`. Date Accessed: 2015-2018.

[38] M. P. Seah and W. A. Dench. "Quantitative electron spectroscopy of surfaces: A standard data base for electron inelastic mean free paths in solids", *Surface and interface analysis* **1**, 1 (1979), pp. 2–11.

[39] J. F. Watts and J. Wolstenholme. *An introduction to surface analysis by XPS and AES.* Wiley Online Library, 2003.

[40] A. Jablonski and C. J. Powell. "The electron attenuation length revisited", *Surface Science Reports* **47**, 2-3 (2002), pp. 33–91.

[41] K. Siegbahn and K. Edvarson. "β-Ray spectroscopy in the precision range of 1:10^5", *Nuclear Physics* **1** (8 1956), pp. 137–159.

[42] D. W. Turner and M. I. Al Jobory. "Determination of Ionization Potentials by Photoelectron Energy Measurement", *Journal of Chemical Physics* **37** (12 1962), p. 3007.

[43] J. J. Olivero and R. L. Longbothum. "Empirical fits to the Voigt line width: A brief review", *Journal of Quantitative Spectroscopy and Radiative Transfer* **17**, 2 (1977), pp. 233–236.

[44] R. Hesse, P. Streubel, and R. Szargan. "Product or sum: comparative tests of Voigt, and product or sum of Gaussian and Lorentzian functions in the fitting of synthetic Voigt-based X-ray photoelectron spectra", *Surface and Interface Analysis* **39**, 5 (2007), pp. 381–391.

[45] T. Ida, M. Ando, and H. Toraya. "Extended pseudo-Voigt function for approximating the Voigt profile", *Journal of Applied Crystallography* **33** (2000), pp. 1311–1316.

[46] P. Thompson, D. E. Cox, and Hastings J. B. "Rietveld Refinement of Debye-Scherrer Synchrotron X-ray Data from Al_2O_3", *Journal of Applied Crystallography* **20** (1987), pp. 79–83.

[47] G. D. Mahan. "Excitons in Metals: Infinite Hole Mass", *Physical Review* **163**, 3 (1967), pp. 612–617.

[48] S. Doniach and M. Sunjic. "Many-electron singularity in X-ray photoemission and X-ray line spectra from metals", *Journal of Physics C: Solid State Physics* **3**, 2 (1970), pp. 285–291.

[49] S. Evans. "Curve synthesis and optimization procedures for X-ray photoelectron spectroscopy", *Surface and Interface Analysis* **17**, 2 (1991), pp. 85–93.

[50] D. Briggs. *XPS: basic principles, spectral features and qualitative analysis*. 2003.

[51] P. Steiner, H. Höchst, and S. Hüfner. "Analysis of the plasmon structure in XPS experiments of simple metals", *Physics Letters A* **61**, 6 (1977), pp. 410–412.

[52] R. A. Pollak, L. Ley, F. R. McFeely, S. P. Kowalczyk, and D. A. Shirley. "Characteristic energy loss structure of solids from x-ray photoemission spectra", *Journal of Electron Spectroscopy and Related Phenomena* **3**, 5 (1974), pp. 381–398.

[53] R. F. Egerton and M. J. Whelan. "The electron energy loss spectrum and band structure of diamond", *Philosophical Magazine* **30**, 4 (1974), pp. 739–749.

[54] W. Bambynek, B. Crasemann, R. W. Fink, H-U. Freund, H. Mark, C. D. Swift, R. E. Price, and P. V. Rao. "X-Ray Fluorescence Yields, Auger, and Coster-Kronig Transition Probabilities", *Reviews of Modern Physics* **44**, 4 (1972), pp. 716–813.

[55] D. Coster, L. Kronig, and R. De. "New type of auger effect and its influence on the x-ray spectrum", *Physica* **2**, 1-12 (1935), pp. 13–24.

[56] S. P. Cooil. "Controlling the Epitaxial Growth of Graphene on Diamond Surfaces". Ph.D. thesis. Aberystwyth, 2014.

[57] C. J. Davisson and L. H. Germer. "Reflection of Electrons by a Crystal of Nickel", *Proceedings of the National Academy of Sciences of the United States of America* **14**, 4 (1928), pp. 317–22.

[58] L. de Broglie. "Recherches sur la theorie des Quanta". Paris, 1925.

[59] G. Held. "Low-energy electron diffraction crystallography of surfaces and interfaces", *Bunsen-Magazin*, 12 (2010), pp. 124–131.

[60] L. H. Germer and C. D. Hartman. "Improved Low Energy Electron Diffraction Apparatus", *Review of Scientific Instruments* **31**, 7 (1960), pp. 784–784.

[61] E. Brüche. "Elektronenmikroskopische abbildung mit lichtelektrischen elektronen", *Zeitschrift für Physik A Hadrons and Nuclei* **86**, 7 (1933), pp. 448–450.

[62] W. Henneberg and A. Recknagel. "Der chromatische Fehler bei elektronenoptischen Anwendungen, insbesondere beim Bildwandler", *Zeitschrift für Physik* **16** (1935), pp. 230–235.

[63] A. Recknagel. "Theorie des elektrischen Elektronenmikroskops für Selbststrahler", *Zeitschrift für Physik* **117**, 11-12 (1941), pp. 689–708.

[64] D. B. Langmuir. "Theoretical limitations of cathode-ray tubes", *Proceedings of the Institute of Radio Engineers* **25**, 8 (1937), pp. 977–991.

[65] L. A. Artsimovich. "Electron-optical properties of electron emission systems", *Reports of the USSR Academy of Sciences* **8** (1944), N6.

[66] E. Bauer. "A brief history of PEEM", *Journal of Electron Spectroscopy and Related Phenomena* **185**, 10 (2012), pp. 314–322.

[67] H. Boersch. "Erhöhung der Auflösung im Emissions-Elektronenmikroskop", *Naturwissenschaften* **30**, 8 (1942), pp. 120–120.

[68] T. Schmidt, U. Groh, R. Fink, E. Umbach, O. Schaff, W. Engel, B. Richter, H. Kuhlenbeck, R. Schlögl, H-J. Freund, et al. "XPEEM with energy-filtering: advantages and first results from the SMART project", *Surface Review and Letters* **9**, 01 (2002), pp. 223–232.

[69] G. F. Rempfer. "A theoretical study of the hyperbolic electron mirror as a correcting element for spherical and chromatic aberration in electron optics", *Journal of Applied Physics* **67**, 10 (1990), pp. 6027–6040.

[70] T. Schmidt, A. Sala, H. Marchetto, E. Umbach, and H-J. Freund. "First experimental proof for aberration correction in XPEEM: Resolution, transmission enhancement, and limitation by space charge effects", *Ultramicroscopy* **126** (2013), pp. 23–32.

[71] HZB Helmholtz Zentrum Berlin. *SMART: Spectro-Microscopy with aberration correction for relevant techniques.* `https://www.helmholtz-berlin.de/pubbin/igama_output?modus=einzel&sprache=en&gid=1687&typoid=37587`. Date Accessed: 29/06/2019.

[72] R. Fink, M. R. Weiss, E. Umbach, D. Preikszas, H. Rose, R. Spehr, P. Hartel, W. Engel, R. Degenhardt, R. Wichtendahl, et al. "SMART: a planned ultrahigh-resolution spectromicroscope for BESSY II", *Journal of Electron Spectroscopy and Related Phenomena* **84**, 1-3 (1997), pp. 231–250.

[73] T. Schmidt, H. Marchetto, P. L. Lévesque, U. Groh, F. Maier, D. Preikszas, P. Hartel, R. Spehr, G. Lilienkamp, W. Engel, et al. "Double aberration correction in a low-energy electron microscope", *Ultramicroscopy* **110**, 11 (2010), pp. 1358–1361.

[74] Nanophoton. *What is Raman Spectroscopy?* `https://www.nanophoton.net/raman/raman-spectroscopy.html`. Date Accessed: 11/11/2018.

[75] C. Venkata Raman and K. S. Krishnan. "A new type of secondary radiation", *Nature* **121**, 3048 (1928), p. 501.

[76] E. Smith and G. Dent. *Modern Raman spectroscopy: a practical approach.* John Wiley & Sons, 2013.

[77] M. O. Krause and J. G. Ferreira. "Kα X-ray emission spectra of Mg and Al", *Journal of Physics B: Atomic and Molecular Physics* **8**, 12 (1975), pp. 2007–2014.

[78] J. F. Moulder. "Handbook of X-ray Photoelectron Spectroscopy", *Physical Electronics* (1995), pp. 230–232.

[79] SPECS GmbH. *Ultraviolet Source UVS 300.* `http://www.specs.de/cms/front_content.php?idcat=121`.

[80] SPECS GmbH. *Ultraviolet Source UVS-300 Manual.* 2007.

[81] A. Liénard. *Champ électrique et magnétique produit par une charge électrique concentrée en un point et animée d'un mouvement quelconque.* 1898.

[82] G. A. Schott. "XI. On the electron theory of matter and on radiation", *The London, Edinburgh, and Dublin Philosophical Magazine and Journal of Science* **13**, 74 (1907), pp. 189–213.

[83] F. R. Elder, R. V. Langmuir, and H. C. Pollock. "Radiation from electrons accelerated in a synchrotron", *Physical Review* **74**, 1 (1948), p. 52.

[84] D. Iwanenko and I. Pomeranchuk. "On the maximal energy attainable in a betatron", *Physical Review* **65**, 11-12 (1944), p. 343.

[85] P. Willmott. *An introduction to synchrotron radiation: techniques and applications*. John Wiley & Sons, 2011.

[86] ISA. *The SGM 3 beamline at ASTRID*. `http://www.isa.au.dk/facilities/astrid/beamlines/sgm3/sgm3.asp`. Date Accessed: 29/06/2019.

[87] D. Roy and D. Tremblay. "Design of electron spectrometers", *Reports on Progress in Physics* **53** (1990), pp. 1621–1674.

[88] SPECS Surface Nano Analysis GmbH. *PHOIBOS 100/150 Hemispherical Energy Analyzer*. pdf. Berlin, Germany, 2012.

[89] S. Evans, R. G. Pritchard, and J. M. Thomas. "Relative differential subshell photoionisation cross-sections (Mg Kα) from lithium to uranium", *Journal of Electron Spectroscopy and Related Phenomena* **14**, 5 (1978), pp. 341–358.

[90] Y. M. Cross and J. E. Castle. "The relationship between transmission efficiencies in the FRR and fat modes of an electron spectrometer", *Journal of Electron Spectroscopy and Related Phenomena* **22**, 1 (1981), pp. 53–60.

[91] SPECS Surface Nano Analysis GmbH. *Extended Range Channel Electron Multiplier (CEM)*. `http://www.specs.de/cms/front_content.php?idart=124`.

[92] P. P. Manning, N. J. Clague, I. W. Kirkman, F. M. Quinn, and P. J. Hicks. "A fast and flexible multichannel electron detector with parallel readout for photoelectron spectroscopy", *Nuclear Instruments and Methods in Physics Research Section A: Accelerators, Spectrometers, Detectors and Associated Equipment* **392**, 1-3 (1997), pp. 345–348.

[93] "Position-sensitive detector performance and relevance to time-resolved electron energy loss spectroscopy", *Review of Scientific Instruments* **57**, 8 (1986), pp. 1469–1482.

[94] H. A. van Hoof and M. J. van der Wiel. "Position-sensitive detector system for angle-resolved electron spectroscopy with a cylindrical mirror analyser", *Journal of Physics E: Scientific Instruments* **13**, 4 (1980), pp. 409–414.

[95] D. P. Langstaff, A. Bushell, T. Chase, and D. A. Evans. "A fully integrated multi-channel detector for electron spectroscopy", *Nuclear Instruments and Methods in Physics Research Section B: Beam Interactions with Materials and Atoms* **238**, 1-4 (2005), pp. 219–223.

[96] D. P. Langstaff and T. Chase. "A multichannel detector array with 768 pixels developed for electron spectroscopy", *Nuclear Instruments and Methods in Physics Research Section A: Accelerators, Spectrometers, Detectors and Associated Equipment* **573**, 1-2 (2007), pp. 169–171.

[97] X. Zhu and D.P. Langstaff. "Reduction of multiple triggering in counting detectors", *Nuclear Instruments and Methods in Physics Research Section A: Accelerators, Spectrometers, Detectors and Associated Equipment* **604**, 1-2 (2009), pp. 400–403.

[98] W. S. Boyle and G. E. Smith. "Charge Coupled Semiconductor Devices", *Bell System Technical Journal* **49**, 4 (1970), pp. 587–593.

[99] G. F. Amelio, M. F. Tompsett, and G. E. Smith. "Experimental Verification of the Charge Coupled Device Concept", *Bell System Technical Journal* **49**, 4 (1970), pp. 593–600.

[100] J. Ladislas Wiza. "Microchannel plate detectors", *Nuclear Instruments and Methods* **162**, 1-3 (1979), pp. 587–601.

[101] A. N. Ndao, F. Zenia, A. Deneuville, M. Bernard, and C. Levy-Clement. "Effect of boron concentration on the electrochemical reduction of nitrates on polycrystalline diamond electrodes", *Diamond and Related Materials* **9**, 3-6 (2000), pp. 1175–1180.

[102] J. E. Field et al. *The properties of natural and synthetic diamond*. Academic Press London, 1992.

[103] R. Robertson, J. Jacob Fox, and A. E. Martin. "Two types of diamond", *Philosophical Transactions of the Royal Society of London. Series A, Containing Papers of a Mathematical or Physical Character* **232**, 707-720 (1933), pp. 463–535.

[104] C. D. Clark, R. W. Ditchburn, and H. B. Dyer. "The absorption spectra of natural and irradiated diamonds", *Proceedings of the Royal Society of London. Series A. Mathematical and Physical Sciences* **234**, 1198 (1956), pp. 363–381.

[105] J. F. H. Custers. "Unusual phosphorescence of a diamond", *Physica* **18**, 8-9 (1952), pp. 489–496.

[106] A. T. Collins and A. W. S. Williams. "The nature of the acceptor centre in semiconducting diamond", *Journal of Physics C: Solid State Physics* **4**, 13 (1971), p. 1789.

[107] H. N. Pollack and D. S. Chapman. "On the regional variation of heat flow, geotherms, and the thickness of lithosphere", *Tectonophysics* **38** (1977), pp. 279–296.

[108] S. Creighton, T. Stachel, S. Matveev, H. Höfer, C. McCammon, and R. W. Luth. "Oxidation of the Kaapvaal lithospheric mantle driven by metasomatism", *Contributions to Mineralogy and Petrology* **157**, 4 (2009), p. 491.

[109] P. Cartigny, M. Palot, E. Thomassot, and J. W. Harris. "Diamond formation: a stable isotope perspective", *Annual Review of Earth and Planetary Sciences* **42** (2014), pp. 699–732.

[110] C-M. Sung and M-F. Tai. "Reactivities of transition metals with carbon: Implications to the mechanism of diamond synthesis under high pressure", *International Journal of Refractory Metals and Hard Materials* **15**, 4 (1997), pp. 237–256.

[111] R. Berman and F. Simon. "Z. f. Elektrochem", *Berichte der Bunsengesellschaft für physikalische Chemie* **59** (1955), p. 333.

[112] F. P. Bundy, H. P. Bovenkerk, H. M. Strong, and R. H. Wentorf Jr. "Diamond-graphite equilibrium line from growth and graphitization of diamond", *The Journal of Chemical Physics* **35**, 2 (1961), pp. 383–391.

[113] J. M. Zazula. *On graphite transformations at high temperature and pressure induced by absorption of the LHC beam.* Tech. rep. CERN-LHC-Project-Note-78, 1997.

[114] E. O. Hall. "The deformation and ageing of mild steel: III discussion of results", *Proceedings of the Physical Society. Section B* **64**, 9 (1951), p. 747.

[115] N. J. Petch. "The Cleavage Strength of Polycrystals", *Journal of the Iron and Steel Institute* **174** (1953), pp. 25–28.

[116] S. Yamaoka, H. Komatsu, H. Kanda, and N. Setaka. "Growth of diamond with rhombic dodecahedral faces", *Journal of Crystal Growth* **37**, 3 (1977), pp. 349–352.

[117] R.C. Burns, J. O. Hansen, R. A. Spits, M. Sibanda, C. M. Welbourn, and D. L. Welch. "Growth of high purity large synthetic diamond crystals", *Diamond and Related Materials* **8**, 8-9 (1999), pp. 1433–1437.

[118] U. F. S. D'Haenens-Johansson, A. Katrusha, P. Johnson, W. Wang, et al. "Large colorless HPHT-grown synthetic gem diamond from New Diamond Technology, Russia", *Gems & Gemology* **51**, 3 (2015).

[119] W. G. Eversole. "US Patents 3,030,187 and 3,030,188", *Synthesis of diamond* (1962).

[120] S. Matsumoto, Y. Sato, M. Kamo, and N. Setaka. "Vapor deposition of diamond particles from methane", *Japanese Journal of Applied Physics* **21**, 4A (1982), p. L183.

[121] M. Kamo, Y. Sato, S. Matsumoto, and N. Setaka. "Diamond synthesis from gas phase in microwave plasma", *Journal of Crystal Growth* **62**, 3 (1983), pp. 642–644.

[122] P. K. Bachmann, D. Leers, and H. Lydtin. "Towards a general concept of diamond chemical vapour deposition", *Diamond and Related Materials* **1**, 1 (1991), pp. 1–12.

[123] J. R. Petherbridge, P. W. May, and M. N. R. Ashfold. "Modeling of the gas-phase chemistry in C–H–O gas mixtures for diamond chemical vapor deposition", *Journal of Applied Physics* **89**, 9 (2001), pp. 5219–5223.

[124] M. Marinelli, E. Milani, M. Montuori, A. Paoletti, A. Tebano, G. Balestrino, and P. Paroli. "Compositional and spectroscopic study of the growth of diamond films from several gaseous mixtures", *Journal of Applied Physics* **76**, 10 (1994), pp. 5702–5705.

[125] R. Beckmann, B. Sobisch, and W. Kulisch. "On the gas-phase mechanisms in MWCVD and HFCVD diamond deposition", *Diamond and Related Materials* **4**, 4 (1995), pp. 256–260.

[126] J. E. Butler and R. L. Woodin. "Thin film diamond growth mechanisms", *Philosophical Transactions of the Royal Society of London. Series A: Physical and Engineering Sciences* **342**, 1664 (1993), pp. 209–224.

[127] J. E. Butler, Y. A. Mankelevich, A. Cheesman, J. Ma, and M. N. R. Ashfold. "Understanding the chemical vapor deposition of diamond: recent progress", *Journal of Physics: Condensed Matter* **21**, 36 (2009), p. 364201.

[128] I. Langmuir. "The adsorption of gases on plane surfaces of glass, mica and platinum", *Journal of the American Chemical Society* **40**, 9 (1918), pp. 1361–1403.

[129] C. N. Hinshelwood et al. "Kinetics of chemical change", (1940).

[130] C. J. Chu, M. P. d'Evelyn, R. H. Hauge, and J. L. Margrave. "Mechanism of diamond growth by chemical vapor deposition on diamond (100), (111), and (110) surfaces: Carbon-13 studies", *Journal of Applied Physics* **70**, 3 (1991), pp. 1695–1705.

[131] R. G. Farrer. "On the substitutional nitrogen donor in diamond", *Solid State Communications* **7**, 9 (1969), pp. 685–688.

[132] S. Koizumi, M. Kamo, Y. Sato, H. Ozaki, and T. Inuzuka. "Growth and characterization of phosphorous doped {111} homoepitaxial diamond thin films", *Applied Physics Letters* **71**, 8 (1997), pp. 1065–1067.

[133] I. Sakaguchi, N. Mikka, Y. Kikuchi, E. Yasu, H. Haneda, T. Suzuki, T. Ando, et al. "Sulfur: A donor dopant for n-type diamond semiconductors", *Physical Review B* **60**, 4 (1999), R2139.

[134] G. Frangieh, M-A. Pinault, J. Barjon, F. Jomard, and J. Chevallier. "Incorporation of arsenic in diamond grown by chemical vapor deposition", *physica status solidi (a)* **205**, 9 (2008), pp. 2207–2210.

[135] N. F. Mott. "Conduction in non-crystalline systems IX. the minimum metallic conductivity", *Philosophical Magazine* **26**, 4 (1972), pp. 1015–1026.

[136] T. Klein, P. Achatz, J. Kacmarcik, C. Marcenat, F. Gustafsson, J. Marcus, E. Bustarret, J. Pernot, F. Omnès, B. E. Sernelius, et al. "Metal-insulator transition and superconductivity in boron-doped diamond", *Physical Review B* **75**, 16 (2007), p. 165313.

[137] A. Deneuville, C. Baron, S. Ghodbane, and C. Agnès. "Highly and heavily boron doped diamond films", *Diamond and Related Materials* **16**, 4-7 (2007), pp. 915–920.

[138] N. Vinokur, B. Miller, Y. Avyigal, and R. Kalish. "Electrochemical Behavior of Boron-Doped Diamond Electrodes", *Journal of the Electrochemical Society* **143**, 10 (1996), pp. L238–L240.

[139] Z. J. Ayres, A. J. Borrill, J. C. Newland, M. E. Newton, and J. V. Macpherson. "Controlled sp^2 functionalization of boron doped diamond as a route for the fabrication of robust and Nernstian pH electrodes", *Analytical Chemistry* **88**, 1 (2015), pp. 974–980.

[140] T. Yokoya, T. Nakamura, T. Matsushita, T. Muro, Y. Takano, M. Nagao, T. Takenouchi, H. Kawarada, and T. Oguchi. "Origin of the metallic properties of heavily boron-doped superconducting diamond", *Nature* **438**, 7068 (2005), p. 647.

[141] E. A. Ekimov, V. A. Sidorov, A. V. Zoteev, J. B. Lebed, J. D. Thompson, and Sergey M. Stishov. "Structure and superconductivity of isotope-enriched boron-doped diamond", *Science and Technology of Advanced Materials* **9**, 4 (2009), p. 044210.

[142] E. A. Ekimov, V. A. Sidorov, E. D. Bauer, N. N. Mel'Nik, N. J. Curro, J. D. Thompson, and S. M. Stishov. "Superconductivity in diamond", *Nature* **428**, 6982 (2004), p. 542.

[143] H. Okazaki, T. Wakita, T. Muro, T. Nakamura, Y. Muraoka, T. Yokoya, S. Kurihara, H. Kawarada, T. Oguchi, and Y. Takano. "Signature of high T c above 25 K in high quality superconducting diamond", *Applied Physics Letters* **106**, 5 (2015), p. 052601.

[144] J. Ristein. "Surface science of diamond: familiar and amazing", *Surface Science* **600**, 18 (2006), pp. 3677–3689.

[145] S. J. Sque, R. Jones, and P. R. Briddon. "Structure, electronics, and interaction of hydrogen and oxygen on diamond surfaces", *Physical Review B* **73** (8 2006), p. 085313.

[146] C. Bandis and B. B. Pate. "Photoelectric emission from negative-electron-affinity diamond (111) surfaces: Exciton breakup versus conduction-band emission", *Physical Review B* **52**, 16 (1995), p. 12056.

[147] J. B. Cui, J. Ristein, and L. Ley. "Low-threshold electron emission from diamond", *Physical Review B* **60**, 23 (1999), p. 16135.

[148] M. J. Rutter and J. Robertson. "Ab initio calculation of electron affinities of diamond surfaces", *Physical Review B* **57**, 15 (1998), p. 9241.

[149] J. B. Cui, J. Ristein, and L. Ley. "Dehydrogenation and the surface phase transition on diamond (111): Kinetics and electronic structure", *Physical Review B* **59**, 8 (1999), p. 5847.

[150] J. B. Marsh and H. E. Farnsworth. "Low-energy electron diffraction studies of (100) and (111) surfaces of semiconducting diamond", *Surface Science* **1**, 1 (1964), pp. 3–21.

[151] J. J. Lander and J. Morrison. "Low energy electron diffraction study of the (111) diamond surface", *Surface Science* **4**, 3 (1966), pp. 241–246.

[152] T. E. Derry, L. Smit, and J. F. Van Der Veen. "Ion scattering determination of the atomic arrangement at polished diamond (111) surfaces before and after reconstruction", *Surface Science* **167**, 2-3 (1986), pp. 502–518.

[153] D. Haneman. "Surface Structures and Properties of Diamond-Structure Semiconductors", *Physical Review* **121**, 4 (1961), pp. 1093–1100.

[154] P. G. Lurie and J. M. Wilson. "The diamond surface: I. The structure of the clean surface and the interaction with gases and metals", *Surface Science* **65**, 2 (1977), pp. 453–475.

[155] B. B. Pate, M. H. Hecht, C. Binns, I. Lindau, and W. E. Spicer. "Photoemission and photon-stimulated ion desorption studies of diamond(111): Hydrogen", *Journal of Vacuum Science and Technology* **21**, 55 (1982), pp. 152103–1391.

[156] A. V. Hamza, G. D. Kubiak, and R. H. Stulen. "The role of hydrogen on the diamond C(111) $-$ (2×1) reconstruction", *Surface Science* **206**, 1-2 (1988), pp. L833–L844.

[157] S. J. Sque, R. Jones, and P. R. Briddon. "Structure, electronics, and interaction of hydrogen and oxygen on diamond surfaces", *Physical Review B* **73** (8), p. 085313.

[158] K. C. Pandey. "New dimerized-chain model for the reconstruction of the diamond (111) $-$ (2×1) surface", *Physical Review B* **25** (6 1982), pp. 4338–4341.

[159] K. C. Pandey. "New π-Bonded Chain Model for Si(111)$-(2\times1)$ Surface", *Physical Review Letters* **47** (26 1981), pp. 1913–1917.

[160] F. J. Himpsel, D. E. Eastman, P. Heimann, and J. F. van der Veen. "Surface states on reconstructed diamond (111)", *Physical Review B* **24** (12 1981), pp. 7270–7274.

[161] H. Namba, M. Masuda, and H. Kuroda. "Electronic states of 2×1 reconstructed surfaces of diamond (111) studied by UPS and EELS", *Applied Surface Science* **33-34** (1988), pp. 187–192.

[162] S. V. Pepper. "Diamond (111) studied by electron energy loss spectroscopy in the characteristic loss region", *Surface Science* **123**, 1 (1982), pp. 47–60.

[163] D. Vanderbilt and S. G. Louie. "Total energies of diamond (111) surface reconstructions by a linear combination of atomic orbitals method", *Physical Review B* **30** (10), p. 6118.

[164] R. Seiwatz. "Possible structures for clean, annealed surfaces of germanium and silicon", *Surface Science* **2** (1964), pp. 473–483.

[165] D. J. Chadi. "π -bonded molecular and chain models for the Si(111) surface", *Physical Review B* **26**, 8 (1982), pp. 4762–4765.

[166] G. Kern, J. Hafner, and G. Kresse. "Atomic and electronic structure of diamond (111) surfaces I. Reconstruction and hydrogen-induced dereconstruction of the one dangling-bond surface", *Surface Science* **366**, 3 (1996), pp. 445–463.

[167] M. Saito, Y. Miyamoto, and A. Oshiyama. "Stability and lattice vibrations of the clean diamond (111) surface", *Surface Science* **427** (1999), pp. 53–57.

[168] W. G. Schmidt, A. Scholze, and F. Bechstedt. "Dimerized, buckled, or ideal chains on the diamond (111) $2\times$ 1 surface?", *Surface Science* **351**, 1-3 (1996), pp. 183–188.

[169] M. Marsili, O. Pulci, F. Bechstedt, and R. Del Sole. "Electronic structure of the C (111) surface: solution by self-consistent many-body calculations", *Physical Review B* **72**, 11 (2005), p. 115415.

[170] R. Graupner, M. Hollering, A. Ziegler, J. Ristein, L. Ley, and A. Stampfl. "Dispersions of surface states on diamond (100) and (111)", *Physical Review B* **55**, 16 (1997), pp. 10841–10847.

[171] P. R. Wallace. "The Band Theory of Graphite", *Physical Review* **71** (9 1947), pp. 622–634.

[172] A. Clauss, G. O. Fischer, U. Hofmann, et al. "Dünnste kohlenstoff-folien", *Zeitschrift Für Naturforschung B* **17**, 3 (1962), pp. 150–153.

[173] J. de La Fuente. *Properties of Graphene*. `https://www.graphenea.com/pages/graphene-properties`. Date Accessed: 28/04/2019.

[174] M. I. Katsnelson, K. S. Novoselov, and A. K. Geim. "Chiral tunnelling and the Klein paradox in graphene", *Nature Phys.* **2**, 9 (2006), pp. 620–625.

[175] A. H. C. Neto, F. Guinea, N. M. R. Peres, K. S. Novoselov, and A. K. Geim. "The electronic properties of graphene", *Reviews of Modern Physics* **81**, 1 (2009), p. 109.

[176] P. Wenk. *GrapheneE2.png*. `https://commons.wikimedia.org/wiki/File:GrapheneE2.png`. Date Accessed: 22/02/2019.

[177] S. Lee and Z. Zhong. "Nanoelectronic circuits based on two-dimensional atomic layer crystals", *Nanoscale* **6**, 22 (2014), pp. 13283–13300.

[178] R. R. Nair, P. Blake, A. N. Grigorenko, K. S. Novoselov, T. J. Booth, T. Stauber, N. M. R. Peres, and A. K. Geim. "Fine structure constant defines visual transparency of graphene", *Science* **320**, 5881 (2008), pp. 1308–1308.

[179] C. Lee, X. Wei, J. W. Kysar, and J. Hone. "Measurement of the elastic properties and intrinsic strength of monolayer graphene", *Science* **321**, 5887 (2008), pp. 385–388.

[180] S. Bae, H. Kim, Y. Lee, X. Xu, J-S. Park, Y. Zheng, J. Balakrishnan, T. Lei, H. R. Kim, Y. I. Song, et al. "Roll-to-roll production of 30-inch graphene films for transparent electrodes", *Nature Nanotechnology* **5**, 8 (2010), pp. 574–578.

[181] X. Sun, Z. Liu, K. Welsher, J. T. Robinson, A. Goodwin, S. Zaric, and H. Dai. "Nano-graphene oxide for cellular imaging and drug delivery", *Nano Research* **1**, 3 (2008), pp. 203–212.

[182] Y. Shao, J. Wang, H. Wu, J. Liu, I. A. Aksay, and Y. Lin. "Graphene Based Electrochemical Sensors and Biosensors: A Review", *Electroanalysis* **22**, 10 (2010), 1027–1036.

[183] S. Lin and M. J. Buehler. "Mechanics and molecular filtration performance of graphene nanoweb membranes for selective water purification", *Nanoscale* **5**, 23 (2013), 11801–11807.

[184] J. Chen, M. Duan, and G. Chen. "Continuous mechanical exfoliation of graphene sheets via three-roll mill", *Journal of Materials Chemistry* **22**, 37 (2012), pp. 19625–19628.

[185] B. Jayasena and S. Subbiah. "A novel mechanical cleavage method for synthesizing few-layer graphenes", *Nanoscale Research Letters* **6**, 1 (2011), p. 95.

[186] A. Ciesielski and P. Samorì. "Graphene via sonication assisted liquid-phase exfoliation", *Chemical Society Reviews* **43**, 1 (2014), pp. 381–398.

[187] Q. Yu, J. Lian, S. Siriponglert, H. Li, Y. P. Chen, and Pei S-S. "Graphene segregated in Ni surfaces and transferred to insulators", *Applied Physics Letters* **93** (2008).

[188] X. Li, W. Cai, J. An, S. Kim, J. Nah, D. Yang, R. Piner, A. Velamakanni, I. Jung, E. Tutuc, et al. "Large-area synthesis of high-quality and uniform graphene films on copper foils", *Science* **324**, 5932 (2009), pp. 1312–1314.

[189] Y. N. Trehan. "The Reduction of Copper Oxides by Molecular Hydrogen", *Zeitschrift für anorganische und allgemeine Chemie* **318**, 1-2 (1962), pp. 107–112.

[190] B. Zhang, W. H. Lee, R. Piner, I. Kholmanov, Y. Wu, H. Li, H. Ji, and R. S. Ruoff. "Low-temperature chemical vapor deposition growth of graphene from toluene on electropolished copper foils.", *ACS Nano* **6**, 3 (2012), pp. 2471–6.

[191] Y. A. Wu, Y. Fan, S. Speller, G. L. Creeth, J. T. Sadowski, K. He, A. W. Robertson, C. S. Allen, and J. H. Warner. "Large single crystals of graphene on melted copper using chemical vapor deposition.", *ACS Nano* **6**, 6 (2012), pp. 5010–7.

[192] X. Li, C. W. Magnuson, A. Venugopal, J. An, J. W. Suk, B. Han, M. Borysiak, W. Cai, A. Velamakanni, Y. Zhu, et al. "Graphene films with large domain size by a two-step chemical vapor deposition process", *Nano Letters* **10**, 11 (2010), pp. 4328–4334.

[193] P. R. Kidambi, C. Ducati, B. Dlubak, D. Gardiner, R. S. Weatherup, M-B. Martin, P. Seneor, H. Coles, and S. Hofmann. "The parameter space of graphene chemical vapor deposition on polycrystalline Cu", *The Journal of Physical Chemistry C* **116**, 42 (2012), pp. 22492–22501.

[194] X. Li, W. Cai, L. Colombo, and R. S. Ruoff. "Evolution of graphene growth on Ni and Cu by carbon isotope labeling", *Nano Letters* **9**, 12 (2009), pp. 4268–4272.

[195] D. V. Badami. "X-ray studies of graphite formed by decomposing silicon carbide", *Carbon* **3**, 1 (1965), pp. 53–57.

[196] Mikael S. and Rositza Y. *Quality comparison: epitaxial graphene vs graphene by CVD.* `cordis.europa.eu/docs/projects/cnect/9/257829/080/deliverables/001-ConceptGrapheneD12ReportupdateM36.pdf`. Date Accessed: 28/05/2019.

[197] K. V. Emtsev, A. Bostwick, K. Horn, J. Jobst, G. L. Kellogg, L. Ley, J. L. McChesney, T. Ohta, S. A. Reshanov, J. Röhrl, et al. "Towards wafer-size graphene layers by atmospheric pressure graphitization of silicon carbide", *Nature Materials* **8**, 3 (2009), p. 203.

[198] R. M. Tromp and J. B. Hannon. "Thermodynamics and kinetics of graphene growth on SiC (0001)", *Physical Review Letters* **102**, 10 (2009), p. 106104.

[199] C. Berger, Z. Song, T. Li, X. Li, A. Y. Ogbazghi, R. Feng, Z. Dai, A. N. Marchenkov, E. H. Conrad, P. N. First, et al. "Ultrathin epitaxial graphite: 2D electron gas properties and a route toward graphene-based nanoelectronics", *The Journal of Physical Chemistry B* **108**, 52 (2004), pp. 19912–19916.

[200] W. A. De Heer, C. Berger, M. Ruan, M. Sprinkle, X. Li, Y. Hu, B. Zhang, J. Hankinson, and E. Conrad. "Large area and structured epitaxial graphene produced by confinement controlled sublimation of silicon carbide", *Proceedings of the National Academy of Sciences* **108**, 41 (2011), pp. 16900–16905.

[201] A. J. Van Bommel, J. E. Crombeen, and A. Van Tooren. "LEED and Auger electron observations of the SiC (0001) surface", *Surface Science* **48**, 2 (1975), pp. 463–472.

[202] M. Ruan, Y. Hu, Z. Guo, R. Dong, J. Palmer, J. Hankinson, C. Berger, and W. A. De Heer. "Epitaxial graphene on silicon carbide: Introduction to structured graphene", *MRS bulletin* **37**, 12 (2012), pp. 1138–1147.

[203] K. V. Emtsev, F. Speck, Th. Seyller, L. Ley, and J. D. Riley. "Interaction, growth, and ordering of epitaxial graphene on SiC {0001} surfaces: A comparative photoelectron spectroscopy study", *Physical Review B* **77**, 15 (2008), p. 155303.

[204] P. Lauffer, K. V. Emtsev, R. Graupner, T. Seyller, L. Ley, S. A. Reshanov, and H. B. Weber. "Atomic and electronic structure of few-layer graphene on SiC (0001) studied with scanning tunneling microscopy and spectroscopy", *Physical Review B* **77**, 15 (2008), p. 155426.

[205] N. Srivastava, G. He, R. M. Feenstra, P. J. Fisher, et al. "Comparison of graphene formation on C-face and Si-face SiC (0001) surfaces", *Physical Review B* **82**, 23 (2010), p. 235406.

[206] J. Hass, R. Feng, J. E. Millán-Otoya, X. Li, M. Sprinkle, P. N. First, W. A. De Heer, E. H. Conrad, and C. Berger. "Structural properties of the multilayer graphene/4 H- Si C (000 1^{-}) system as determined by surface X-ray diffraction", *Physical Review B* **75**, 21 (2007), p. 214109.

[207] J. Hass, F. Varchon, J-E. Millan-Otoya, M. Sprinkle, N. Sharma, W. A. de Heer, C. Berger, P. N. First, L. Magaud, and E. H. Conrad. "Why multilayer graphene on 4H-SiC (0001) behaves like a single sheet of graphene", *Physical Review Letters* **100**, 12 (2008), p. 125504.

[208] J. Hass, W. A. De Heer, and E. H. Conrad. "The growth and morphology of epitaxial multilayer graphene", *Journal of Physics: Condensed Matter* **20**, 32 (2008), p. 323202.

[209] F. Varchon, R. Feng, J. Hass, X. Li, B. N. Nguyen, C. Naud, P. Mallet, J-Y. Veuillen, C. Berger, E. H. Conrad, et al. "Electronic structure of epitaxial graphene layers on SiC: effect of the substrate", *Physical Review Letters* **99**, 12 (2007), p. 126805.

[210] C. Riedl, C. Coletti, T. Iwasaki, A. A. Zakharov, and U. Starke. "Quasi-free-standing epitaxial graphene on SiC obtained by hydrogen intercalation", *Physical Review Letters* **103**, 24 (2009), p. 246804.

[211] G. T. Williams. "Monitoring in-situ processing of solid surfaces with real-time x-ray photoelectron spectroscopy". Ph.D. thesis. Aberystwyth, 2011.

[212] A. G. Shard. "Detection limits in XPS for more than 6000 binary systems using Al and Mg Kα X-rays", *Surface and Interface Analysis* **46**, 3 (2014), pp. 175–185.

[213] G. Bussetti, C. Goletti, P. Chiaradia, and T. Derry. "Optical gap between dangling-bond states of a single-domain diamond C(111)-2 $\times$ 1 by reflectance anisotropy spectroscopy", *Europhysics Letters (EPL)* **79**, 5 (2007), p. 57002.

[214] *AIMPRO.abinitio*. `aimpro.ncl.ac.uk`. website. Apr. 2010.

[215] Z. X. Shen. *Angle-Resolved Photoemission Spectroscopy*. `https://arpes.stanford.edu/research/tool-development/angle-resolved-photoemission-spectroscopy`. Date Accessed: 15/07/2019. Stanford University, CA., 2019.

[216] C. Bena and L. Simon. "Dirac point metamorphosis from third-neighbor couplings in graphene and related materials", *Physical Review B* **83** (11 2011), p. 115404.

[217] J. L. McChesney, A. Bostwick, T. Ohta, T. Seyller, K. Horn, J. González, and E. Rotenberg. "Extended van Hove Singularity and Superconducting Instability in Doped Graphene", *Physical Review Letters* **104** (13 2010), p. 136803.

[218] National Institute of Standards and Technology (NIST). *NIST Standard Reference Database 82: NIST Electron Effective-Attenuation-Length Database*. `https://www.nist.gov/srd/nist-standard-reference-database-82`. 2009.

[219] K. Fuchs. "The conductivity of thin metallic films according to the electron theory of metals", *Mathematical Proceedings of the Cambridge Philosophical Society*. Vol. 34. 1. 1938, pp. 100–108.

[220] E. H. Sondheimer. "The mean free path of electrons in metals", *Advances in Physics* **1**, 1 (1952), pp. 1–42.

[221] E. Machlin. *An introduction to aspects of thermodynamics and kinetics relevant to materials science*. Elsevier, 2010.

[222] Z. Nishiyama. "X-ray investigation of the mechanism of the transformation from face centered cubic lattice to body centered cubic", *Science Reports of Tohoku University* **23** (1934), p. 637.

[223] G. Wassermann. "Influence of the α–γ transformation of an irreversible Ni steel onto crystal orientation and tensile strength", *Archiv für das Eisenhüttenwesen* **16** (1933), pp. 647–651.

[224] C. A. Swarts and J. D. Dow. "X-ray line shapes of metals: Exact solutions of a final-state interaction model", *Physical Review B* **72**, 15 (2005), p. 155119.

[225] M. C. Biesinger. *X-ray Photoelectron Spectroscopy (XPS) Reference Pages*. `http://www.xpsfitting.com/`. website. 2018.

[226] Thermo Fisher. *XPS Simplified: Carbon*. `https://xpssimplified.com/elements/carbon.php`. website. 2020.

[227] A. Varykhalov, J. Sánchez-Barriga, P. Hlawenka, and O. Rader. "Massless Dirac fermions in epitaxial graphene on Fe (110)", *arXiv preprint arXiv:1212.6866* (2012).

[228] G. Giovannetti, P. A. Khomyakov, G. Brocks, V. M. Karpan, J. Van den Brink, and P. J. Kelly. "Doping graphene with metal contacts", *Physical Review Letters* **101**, 2 (2008), p. 026803.

[229] Y. Takano, M. Nagao, I. Sakaguchi, M. Tachiki, T. Hatano, K. Kobayashi, H. Umezawa, and H. Kawarada. "Superconductivity in diamond thin films well above liquid helium temperature", *Applied Physics Letters* **85**, 14 (2004), pp. 2851–2853.

[230] D. Nečas and Klapetek P. *Gwyddion*. `http://gwyddion.net/`. website. Nov. 2019.

[231] E. Gheeraert, P. Gonon, A. Deneuville, L. Abello, and G. Lucazeau. "Effect of boron incorporation on the "quality" of MPCVD diamond films", *Diamond and Related Materials* **2**, 5-7 (1993), pp. 742–745.

[232] Y. G. Wang, S. P. Lau, B. K. Tay, and X. H. Zhang. "Resonant Raman scattering studies of Fano-type interference in boron doped diamond", *Journal of Applied Physics* **92**, 12 (2002), pp. 7253–7256.

[233] V. Mortet, Z. V. Živcová, A. Taylor, O. Frank, P. Hubík, D. Trémouilles, F. Jomard, J. Barjon, and L. Kavan. "Insight into boron-doped diamond Raman spectra characteristic features", *Carbon* **115** (2017), pp. 279–284.

[234] M. Bernard, A. Deneuville, and P. Muret. "Non-destructive determination of the boron concentration of heavily doped metallic diamond thin films from Raman spectroscopy", *Diamond and Related Materials* **13**, 2 (2004), pp. 282–286.

[235] S. Gupta, O. A. Williams, and E. Bohannan. "Electrostatic force microscopy studies of boron-doped diamond films", *Journal of Materials Research* **22**, 11 (2007), pp. 3014–3028.

[236] G. T. Williams, S. P. Cooil, O. R. Roberts, S. Evans, D. P. Langstaff, and D. A. Evans. "High temperature photoelectron emission and surface photovoltage in semiconducting diamond", *Applied Physics Letters* **105**, 6 (2014), p. 061602.

[237] T. Yokoya, E. Ikenaga, M. Kobata, H. Okazaki, K. Kobayashi, A. Takeuchi, A. Awaji, Y. Takano, M. Nagao, I. Sakaguchi, et al. "Core-level electronic structure evolution of heavily boron-doped superconducting diamond studied with hard x-ray photoemission spectroscopy", *Physical Review B* **75**, 20 (2007), p. 205117.

[238] W. E. Moddeman, A. R. Burke, W. C. Bowling, and D. S. Foose. "Surface oxides of boron and $B_{12}O_2$ as determined by XPS", *Surface and Interface Analysis* **14**, 5 (1989), pp. 224–232.

[239] T. Hu, L. Steihl, W. Rafaniello, T. Fawcett, D. D. Hawn, J. G. Mashall, S. J. Rozeveld, C. L. Putzig, J. H. Blackson, W. Cermignani, et al. "Structures and properties of disordered boron carbide coatings generated by magnetron sputtering", *Thin Solid Films* **332**, 1-2 (1998), pp. 80–86.

[240] H. Künzli, P. Gantenbein, R. Steiner, and P. Oelhafen. "Deposition and characterization of thin boron-carbide coatings", *Fresenius' Journal of Analytical Chemistry* **346**, 1-3 (1993), pp. 41–44.

[241] L. G. Jacobsohn, R. K. Schulze, M. E. H. Da Costa, and M. Nastasi. "X-ray photoelectron spectroscopy investigation of boron carbide films deposited by sputtering", *Surface Science* **572**, 2-3 (2004), pp. 418–424.

[242] C. Vincent, H. Vincent, H. Mourichoux, and J. Bouix. "Characterization by XPS and SEM of reactive chemical vapour deposited boron carbide on carbon fibre", *Journal of Materials Science* **27**, 7 (1992), pp. 1892–1900.

[243] I. Jiménez, D. G. J. Sutherland, T. Van Buuren, J. A. Carlisle, L. J. Terminello, and F. J. Himpsel. "Photoemission and x-ray-absorption study of boron carbide and its surface thermal stability", *Physical Review B* **57**, 20 (1998), p. 13167.

[244] Z-H. Sheng, H-L. Gao, W-J. Bao, F-B. Wang, and X-H. Xia. "Synthesis of boron doped graphene for oxygen reduction reaction in fuel cells", *Journal of Materials Chemistry* **22**, 2 (2012), pp. 390–395.

[245] A. C. Ferrari. "Raman spectroscopy of graphene and graphite: disorder, electron–phonon coupling, doping and nonadiabatic effects", *Solid State Communications* **143**, 1-2 (2007), pp. 47–57.

[246] A. C. Ferrari and D. M. Basko. "Raman spectroscopy as a versatile tool for studying the properties of graphene", *Nature Nanotechnology* **8**, 4 (2013), p. 235.

[247] Y. Hishiyama, H. Irumano, Y. Kaburagi, and Y. Soneda. "Structure, Raman scattering, and transport properties of boron-doped graphite", *Physical Review B* **63**, 24 (2001), p. 245406.

[248] T. Hagio, M. Nakamizo, and K. Kobayashi. "Studies on X-ray diffraction and Raman spectra of B-doped natural graphite", *Carbon* **27**, 2 (1989), pp. 259–263.

[249] Y. A. Kim, K. Fujisawa, H. Muramatsu, T. Hayashi, M. Endo, T. Fujimori, K. Kaneko, M. Terrones, J. Behrends, A. Eckmann, et al. "Raman spectroscopy of boron-doped single-layer graphene", *ACS Nano* **6**, 7 (2012), pp. 6293–6300.

[250] S. Hüfner, G. K. Wertheim, and J. H. Wernick. "XPS core line asymmetries in metals", *Solid State Communications* **17**, 4 (1975), pp. 417–422.

[251] F. Fromm, M. H. Oliveira Jr, A. Molina-Sanchez, M. Hundhausen, J. M. J. Lopes, H. Riechert, L. Wirtz, and T. Seyller. "Contribution of the buffer layer to the Raman spectrum of epitaxial graphene on SiC (0001)", *New Journal of Physics* **15**, 4 (2013), p. 043031.

[252] L. M. Malard, M. A. A. Pimenta, G. Dresselhaus, and M. S. Dresselhaus. "Raman spectroscopy in graphene", *Physics Reports* **473**, 5-6 (2009), pp. 51–87.

[253] C. Riedl, C. Coletti, and U. Starke. "Structural and electronic properties of epitaxial graphene on SiC (0001): a review of growth, characterization, transfer doping and hydrogen intercalation", *Journal of Physics D: Applied Physics* **43**, 37 (2010), p. 374009.

[254] L. I. Johansson, R. Armiento, J. Avila, C. Xia, S. Lorcy, I. A. Abrikosov, M. C. Asensio, and C. Virojanadara. "Multiple π-bands and Bernal stacking of multilayer graphene on C-face SiC, revealed by nano-Angle Resolved Photoemission", *Scientific Reports* **4** (2014), p. 4157.

[255] A. C. Ferrari, J. C. Meyer, V. Scardaci, C. Casiraghi, M. Lazzeri, F. Mauri, S. Piscanec, D. Jiang, K. S. Novoselov, and S. Roth. "Raman spectrum of graphene and graphene layers", *Physical Review Letters* **97**, 18 (2006), p. 187401.

[256] A. Reina, H. Son, L. Jiao, B. Fan, M. S. Dresselhaus, Z. Liu, and J. Kong. "Transferring and identification of single-and few-layer graphene on arbitrary substrates", *The Journal of Physical Chemistry C* **112**, 46 (2008), pp. 17741–17744.

[257] Y. Zhang, L. Zhang, and C. Zhou. "Review of chemical vapor deposition of graphene and related applications", *Accounts of Chemical Research* **46**, 10 (2013), pp. 2329–2339.

[258] Y. Wang, Y. Zheng, X. Xu, E. Dubuisson, Q. Bao, J. Lu, and K. P. Loh. "Electrochemical delamination of CVD-grown graphene film: toward the recyclable use of copper catalyst", *ACS nano* **5**, 12 (2011), pp. 9927–9933.

[259] S. Unarunotai, Y. Murata, C. E. Chialvo, H-S. Kim, S. MacLaren, N. Mason, I. Petrov, and J. A. Rogers. "Transfer of graphene layers grown on SiC wafers to other substrates and their integration into field effect transistors", *Applied Physics Letters* **95**, 20 (2009), p. 202101.

[260] M. M. Lucchese, F. Stavale, E. H. M. Ferreira, C. Vilani, M. V. O. Moutinho, R. B. Capaz, C. A. Achete, and A. Jorio. "Quantifying ion-induced defects and Raman relaxation length in graphene", *Carbon* **48**, 5 (2010), pp. 1592–1597.

[261] L. G. Cançado, A. Jorio, E. H. M. Ferreira, F. Stavale, C. A. Achete, R. B. Capaz, M. V. O. Moutinho, A. Lombardo, T. S. Kulmala, and A. C. Ferrari. "Quantifying defects in graphene via Raman spectroscopy at different excitation energies", *Nano Letters* **11**, 8 (2011), pp. 3190–3196.

[262] A. J. Pollard, B. Brennan, H. Stec, B. J. Tyler, M. P. Seah, I. S. Gilmore, and D. Roy. "Quantitative characterization of defect size in graphene using Raman spectroscopy", *Applied Physics Letters* **105**, 25 (2014), p. 253107.

[263] Y/ Ahn, H. Kim, Y-H. Kim, Y. Yi, and S-I. Kim. "Procedure of removing polymer residues and its influences on electronic and structural characteristics of graphene", *Applied Physics Letters* **102**, 9 (2013), p. 091602.

[264] C. Gong, H. Carlo Floresca, D. Hinojos, S. McDonnell, X. Qin, Y. Hao, S. Jandhyala, G. Mordi, J. Kim, L. Colombo, et al. "Rapid selective etching of PMMA residues from transferred graphene by carbon dioxide", *The Journal of Physical Chemistry C* **117**, 44 (2013), pp. 23000–23008.

[265] M. Her, R. Beams, and L. Novotny. "Graphene transfer with reduced residue", *Physics Letters A* **377**, 21-22 (2013), pp. 1455–1458.

[266] G. Deokar, J. Avila, I. Razado-Colambo, J-L. Codron, C. Boyaval, E. Galopin, M-C. Asensio, and D. Vignaud. "Towards high quality CVD graphene growth and transfer", *Carbon* **89** (2015), pp. 82–92.

[267] G. Beamson, A. Bunn, and D. Briggs. "High-resolution monochromated XPS of poly (methyl methacrylate) thin films on a conducting substrate", *Surface and Interface Analysis* **17**, 2 (1991), pp. 105–115.

[268] C. Girardeaux and J-J. Pireaux. "Analysis of Poly (methyl methacrylate)(PMMA) by XPS", *Surface Science Spectra* **4**, 2 (1996), pp. 134–137.

[269] S. Tougaard. "Improved XPS analysis by visual inspection of the survey spectrum", *Surface and Interface Analysis* **50**, 6 (2018), pp. 657–666.

[270] G. Beamson and D. Briggs. *High Resolution XPS of Organic Polymers: The Scienta ESCA300 Database*. Wiley, 1992.

[271] P. Louette, F. Bodino, and J-J. Pireaux. "Poly(vinyl alcohol) (PVA) XPS reference core level and energy loss spectra", *Surface Science Spectra* **12**, 1 (2005), pp. 106–110.

[272] A. Eckmann, A. Felten, A. Mishchenko, L. Britnell, R. Krupke, K. S. Novoselov, and C. Casiraghi. "Probing the nature of defects in graphene by Raman spectroscopy", *Nano Letters* **12**, 8 (2012), pp. 3925–3930.

[273] J-H. Lee, E. K. Lee, W-J. Joo, Y. Jang, B-S. Kim, J. Y. Lim, S-H. Choi, S. J. Ahn, J. R. Ahn, M-H. Park, et al. "Wafer-scale growth of single-crystal monolayer graphene on reusable hydrogen-terminated germanium", *Science* **344**, 6181 (2014), pp. 286–289.

[274] A. Patil, G. Lopez, M. Foxe, I. Childres, C. Roecker, J. Boguski, I. Jovanovic, and Y. P. Chen. "Graphene field effect transistors for detection of ionizing radiation", *IEEE Nuclear Science Symposuim & Medical Imaging Conference*. 2010, pp. 674–676.

[275] A. J. Pollard, K. R. Paton, C. A. Clifford, and E. Legge. *Good Practice Guide No. 145: Characterisation of the Structure of Graphene*. `https://www.npl.co.uk/special-pages/guides/gpg145_graphene.pdf`. Date Accessed: 22/11/2018. National Physical Laboratory (UK), 2017.